

1996

Remote Sensing Of Suspended Sediment

LAVENDER, SAMANTHA JANE

<http://hdl.handle.net/10026.1/2119>

<http://dx.doi.org/10.24382/4508>

University of Plymouth

All content in PEARL is protected by copyright law. Author manuscripts are made available in accordance with publisher policies. Please cite only the published version using the details provided on the item record or document. In the absence of an open licence (e.g. Creative Commons), permissions for further reuse of content should be sought from the publisher or author.

Remote Sensing Of Suspended Sediment

by

SAMANTHA JANE LAVENDER

A thesis submitted to the University of Plymouth
in partial fulfilment for the degree of

DOCTOR OF PHILOSOPHY

Institute Of Marine Studies
Faculty of Science

in collaboration with the

Plymouth Marine Laboratory

LIBRARY STAMP

June 1996

LIBRARY STORE

REFERENCE ONLY

UNIVERSITY OF PLYMOUTH	
Item No.	900 3063108
Date	28 NOV 1996
Class No.	T 551.4609 L AV
Contl. No.	X703379282
LIBRARY SERVICES	

90 0306310 8



ABSTRACT

REMOTE SENSING OF SUSPENDED SEDIMENT

by

SAMANTHA JANE LAVENDER, BSc Hons.

A remote sensing near infrared suspended sediment algorithm is developed from first principles and applied to Compact Airborne Spectrographic Imagery (CASI) data flown over the Humber Estuary. Laboratory measurements were used as the basis for the algorithm development, with the resulting spectra indicating that the ideal wavelength for a suspended sediment algorithm is the near infrared. The resulting algorithm took the form of a waveband ratio which was subsequently validated with a semi-analytical water optics model based on the absorption/scattering properties of the optically active constituents. The model was then used to derive a global water-leaving radiance algorithm, which is independent of the sediment type. The algorithm was applied to the CASI data collected during August and September 1993, and the resulting SPM maps were compared with contemporaneous *in-situ* measurements. The *in-situ* measurements include calculations of the diffuse attenuation coefficient (K_d), which was correlated with the SPM concentration. Further developments to the algorithm through the use of an atmospheric correction are outlined.

LIST OF CONTENTS

Abstract	i
Contents	ii
List Of Figures	vi
List Of Tables	x
Acknowledgements	xi
Authors Declarations	xiii
Chapter 1: Introduction	1
1.1 Aims And Objectives	1
1.2 Land-Ocean Interaction Study (LOIS)	1
1.3 Thesis Overview	2
1.4 Compact Airborne Spectral Imager (CASI)	4
Chapter 2: Optical Properties	6
2.1 Optics Definitions.....	6
2.1.1 The Properties Of Light	7
2.1.2 Inherent Optical Properties	12
2.1.3 Apparent Optical Properties	15
2.2 Effects Of The Medium	16
2.2.1 Absorption	16
2.2.2 Scattering	18
2.3 Optics Modelling	21
2.3.1 In-Water Optics	22
2.3.1.1 Water	24
2.3.1.2 Dissolved Organic Matter	24
2.3.1.3 Phytoplankton	26
2.3.1.4 Suspended Sediment	29

2.3.2 Atmospheric Optics	30
2.3.2.1 Main Equation	31
2.3.2.2 Attenuation of the solar irradiation	32
2.3.3 Air/Water Interface Optics	39
2.3.3.1 Reflection By The Sea Surface	39
2.3.3.2 Normalised Water-Leaving Radiance	41
2.4 Summary	43
Chapter 3: Laboratory Experiments	44
3.1 Previous Work	44
3.2 Method	45
3.3 Data Processing	48
3.4 Data Analysis	50
3.5 Discussion	55
Chapter 4: Field Experiments	58
4.1 The Geography Of The Humber Coastal Zone	58
4.1.1 The Holderness Coast	58
4.1.2 The Humber Estuary	58
4.2 Field Campaigns	61
4.3 Fieldwork Protocol	63
4.4 Calibration	65
4.4.1 In-Water Constituents	65
4.4.2 Light Sensors	68
4.5 Ground Data Processing	70
4.5.1 QUBIT and UOR	70
4.5.2 Profiling Reflectance Radiometer (PRR)	70
4.5.3 Calculation of K_d 's	72

4.6 Results	74
4.6.1 Comparison of different sensors for each track	74
4.6.2 Comparison of K_d values	80
4.7 Summary	86
Chapter 5: Algorithm Development	88
5.1 Previous Research.....	88
5.2 Laboratory Experiments	90
5.3 Semi-Analytical Model	94
5.4 Atmospheric Effects	96
5.5. Waveband Positions	102
Chapter 6: Airborne Radiometry	105
6.1 Aircraft Overflights	105
6.2 Image Processing	113
6.3 Image Investigation	114
6.3.1 Pixel Size	114
6.3.2 Comparison of nadir lines for contemporaneous imagery	115
6.3.2.1 Transaxial Imagery	115
6.3.2.2 Humber Approaches	116
6.4 Results	117
6.4.1 Imagery validation	117
6.4.1.1 August Humber Approaches	119
6.4.1.2 September Humber Approaches	119
6.4.1.3 September Transaxial	123
6.4.2 Spectral Radiance Comparison	128
6.5 Discussion	128
Chapter 7: Conclusion And Discussion	129

7.1 Sediment Algorithm 129

7.2 Algorithm Validation 130

7.3 *In-situ* Measurements 130

7.4 Further Work 131

References 132

Appendix 1: Acronyms And Symbols 143

Appendix 2: CASIGO Software 146

Appendix 3: Published Papers 151

LIST OF FIGURES

Figure Number		Page
Figure 2-1	a) The electronic spectrum and b) an expansion of the optical spectrum	8
Figure 2-2	Lambert's Law	9
Figure 2-3	Reflectance	11
Figure 2-4	Absorption	13
Figure 2-5	Volume scattering	13
Figure 2-6	Volume scattering functions for different water types, using data from Petzold (1972)	20
Figure 2-7	Water a) backscattering and b) absorption calculated using values taken from Smith and Baker (1981), for the wavelength range 400 to 800 nm, and Palmer and Williams (1974) for the near infrared beyond this.	25
Figure 2-8	DOM absorption calculated using Equation 2-34.	25
Figure 2-9	Phytoplankton pigment absorption using values taken from Prieur and Sathyendranath (1981).	27
Figure 2-10	Chlorophyll backscattering calculated from Equation 2-38.	27
Figure 2-11	Suspended sediment backscattering calculated from Equation 2-39.	30
Figure 2-12	Fresnel reflectance calculated using Equation 2-73.	41
Figure 3-1	Particle size distribution for the different sediment and algal stocks determined by Malvern Sizer.	46
Figure 3-2	The reflectance difference caused by placing a white disk on the bottom of the tank during the Wash sediment suspensions.	49
Figure 3-3	The relationship between the reflectance difference (at 600 nm) and sediment concentration, with the dotted line indicating the sediment concentration at which the actual depth exceeds the penetration depth.	49
Figure 3-4	Spectral reflectance for different concentrations of Brough sediment.	51
Figure 3-5	Spectral reflectance for different concentrations of Cleethorpes sediment.	51
Figure 3-6	Spectral reflectance for different concentrations of Easington sediment.	52
Figure 3-7	Spectral reflectance for different concentrations of Wash sediment.	52
Figure 3-8	A comparison of the calculated reflectance for the fine fraction (less than 10 μ m) at the different sediment types at a concentration of 20 mg/l.	53
Figure 3-9	A comparison of the calculated reflectance for the different size fractions of the Exe sediment at a concentration of 20 mg/l.	53
Figure 3-10	The relationship between the wavelength of maximum reflectance and concentration of suspended matter for all the sediment data, with the dotted line indicating the 170 mg/l concentration level.	54
Figure 3-11	The relationship between the wavelength of maximum	54

	sediment fraction (less than 10 μm).	
Figure 3-12	Spectral reflectance for different concentrations of phytoplankton with a water base.	56
Figure 3-13	Spectral reflectance for different concentrations of phytoplankton with a suspended sediment base.	56
Figure 3-14	Spectral reflectance at different DOM concentrations.	57
Figure 4-1	The Holderness coast and Humber estuary.	59
Figure 4-2	Vertical distribution of the current velocities and SPM at Middle Shoal over a tidal cycle in the neap, mid and spring phases (data taken from BTDB, 1978).	62
Figure 4-3	Plot of typical survey vessel track	63
Figure 4-4	Calibration of SPM for the a) blue transmissometer, b) nephelometer and c) short path transmissometer with the circled data points being excluded from the regression.	67
Figure 4-5	The calibrations to chlorophyll- <i>a</i> for a) fieldwork 1 and b) combined fieldwork 2 and 3, with the circled data points being excluded from the regression.	69
Figure 4-6	Calibration graph for salinity (all fieldworks) with the data points surrounded by a circle being excluded from the regression and the straight line represents x equal to y .	69
Figure 4-7	Side view of the PRR-600 indicating the depth offsets.	71
Figure 4-8	Plot of SPM (black line), $K_d[550]$ (red line) and $K_d[632]$ (blue line) for a) the whole and b) the plume region of September 1st Track 1.	73
Figure 4-9	Humber Estuary continuous data for June 30th Track 1. Blue lines represent QUBIT data, black lines UOR data and red symbols bottle samples.	75
Figure 4-10	Humber Estuary continuous data for June 30th Track 2. Blue lines represent QUBIT data, black lines UOR data and red symbols bottle samples.	76
Figure 4-11	Humber Estuary continuous data for August 4th Track 1. Blue lines represent QUBIT data, black lines UOR data (except SPM where black is 490 nm and green the short path transmissometer) and red symbols bottle samples.	78
Figure 4-12	Humber Estuary continuous data for August 4th Track 2. Blue lines represent QUBIT data, black lines UOR data (except SPM where black is 490 nm and green the short path transmissometer) and red symbols bottle samples.	79
Figure 4-13	Humber Estuary continuous data for September 1st Track 1. Blue lines represent QUBIT data, black lines UOR data (except SPM where black is 490 nm and green the short path transmissometer) and red symbols bottle samples.	81
Figure 4-14	Humber Estuary continuous data for September 1st Track 2. Blue lines represent QUBIT data, black lines UOR data (except SPM where black is 490 nm and green the short path transmissometer) and red symbols bottle samples.	82
Figure 4-15	$K_d[850]$ regressions against SPM as determined by a) transmissometer. b) short path transmissometer and c) nephelometer for: UOR August (blue squares); UOR September (red circles); PRR August (clear squares); PRR September (clear circles).	84
Figure 4-16	$K_d[632]$ regressions against SPM as determined by a)	85

	transmissometer. b) short path transmissometer and c) nephelometer for: UOR August (blue squares); UOR September (red circles); PRR August (clear squares); PRR September (clear circles).	
Figure 4-17	Along track PRR K_d 's for a) August compared to SSM and b) September compared to the UOR K_d 's with c) spectral plot comparing the UOR (squares and left-hand values on the x-axis) and PRR (circles) K_d 's for September.	87
Figure 5-1	Spectral reflectance for a) waveband 11 and b) waveband 12 plotted against SPM for all the tank data with the different symbols representing sediment suspensions. The squares are for fine suspensions, triangles for medium suspensions, circles for coarse suspensions and hourglasses for unfractionated suspensions (see Section 3.2 for further details), and the colours have no meaning except for the clarity of the diagram.	92
Figure 5-2	Plot of waveband 11 versus waveband 12. The squares are for fine suspensions, triangles for medium suspensions, circles for coarse suspensions and hourglasses for unfractionated suspensions (see Section 3.2 for further details), and the colours have no meaning except for the clarity of the diagram.	93
Figure 5-3	Waveband ratio against SPM. The squares are for fine suspensions, triangles for medium suspensions, circles for coarse suspensions and hourglasses for unfractionated suspensions (see Section 3.2 for further details), and the colours have no meaning except for the clarity of the diagram.	93
Figure 5-4	Plot of: a) waveband ratio versus SPM for the fine fraction only; b) reflectance waveband ratio versus SPM for the model; c) normalized water-leaving radiance waveband ratio for the model.	95
Figure 5-5	Rayleigh attenuation derived from Equations 2-54 and 2-55 for an altitude of 10000 feet.	97
Figure 5-6	Atmospheric absorption by ozone (squares), water vapour (triangles) and permanent gases (circles).	97
Figure 5-7	Plot of the a) regression of solar irradiance waveband 12 versus waveband 11 and b) plot of the solar waveband ratio versus waveband 12.	99
Figure 5-8	Effect of the solar waveband ratio on the a) L_{wn} ratio and b) constants where the squares represent A, the circles B and triangles C.	101
Figure 5-9	SPM map for September 1st Flightline 6.	103
Figure 5-10	Effect of changing the a) waveband width and b) waveband position on the L_{wn} waveband ratio.	104
Figure 6-1	Proposed Aircraft Flightlines	105
Figure 6-2	Flightline positions for the August Fieldwork	106
Figure 6-3	Flightline positions for the September fieldwork	107
Figure 6-4	Axial flightlines (from left to right): September Fl 3; September Fl 6; August Fl 7.	109
Figure 6-5	Transaxial flightlines (from left to right): August Fl 6; August Fl 5; September Fl 2; September Fl 8; September Fl 9.	110
Figure 6-6	Humber Approaches at 5000 feet (from left to right): September Fl 4; September Fl 5; August Fl 2; August Fl 3; August Fl 4.	111
Figure 6-7	Humber Approaches (from left to right): August Fl 8; August Fl	112

	9; September Fl 1.	
Figure 6-8	Nadir plots for September 1st Fl 8 (red) and 9 (blue), showing the sensor radiance at 645.8 and 865 nm plus the near infrared waveband ratio.	115
Figure 6-9	Nadir plots for August 4th flightlines 3 (red) and 4 (blue).	117
Figure 6-10	Nadir plots for September 1st flightlines 1 (red), 4 (blue) and 5 (black).	118
Figure 6-11	Position of flightlines 1, 4 and 5 on September 1st.	118
Figure 6-12	Plot of nadir line a) waveband 12 sensor radiance and b) sensor radiance waveband ratio for August 4th Fl 8, with the survey vessel position marked by a dotted line.	120
Figure 6-13	Plot of near infrared waveband ratio radiance (square symbols) and bathymetry (solid line) for August 4th Fl 8, with the survey vessel position marked by a dotted line.	120
Figure 6-14	Thermal imagery contemporaneous with September 1st a) Fl 1, b) Fl 4 and c) Fl 5. The survey vessel is the black dot near the center of each image.	122
Figure 6-15	Plot of waveband 12 sensor radiance (solid line) and calculated SPM (square symbols) for September Fl 1, with the survey vessel position marked by a dotted line.	122
Figure 6-16	SPM maps for September flightlines 1, 4 and 5 (from right to left).	124
Figure 6-17	Plot of bathymetry (solid line) and waveband 12 sensor radiance for September a) Fl 2 and b) Fl 9.	125
Figure 6-18	Plot of bathymetry (solid line) and calculated SPM (dotted line) for September a) Fl 2 and b) Fl 9.	125
Figure 6-19	Regression of waveband 12 versus the sensor radiance waveband ratio for September Fl a) 2 and b) 9.	126
Figure 6-20	Comparison of the wavelength spectra for: a) August flightlines 3 (triangles) and 4 (squares) at 5 km (dotted line) and 10 km (solid line) b) September flightlines 1 (squares), 4 (triangles) and 5 (circles) at 10 km (dotted line) and 15 km (solid line). c) September flightlines 8 (triangles) and 9 (squares) at 14 km (dotted line) and 18 km (solid line).	127
Figure 6-21	Comparison of the wavelength spectra for: a) August with measurements at 5000 feet (circles), Fl 8 2000 feet (triangles), Fl 9 2000 feet (squares) and at the sea-surface (upside-down triangles). b) September with measurements at 10000 feet (circles), 5000 feet (triangles) and at the sea-surface (squares).	129
Figure A2-1	Display window for the casigo module	146
Figure A2-2	CASI image plan and side view for geometric correction	148
Figure A2-3	Display window for the colour composite module	148
Figure A2-4	Display window for the SPM module	150

LIST OF TABLES

Table Number		Page
Table 4-1	Along track measurements made with the relevant sensor packages on each fieldwork.	64
Table 4-2	Linear regression equations for the suspended sediment calibrations	66
Table 4-3	Linear regression equations for the chlorophyll- <i>a</i> calibrations.	68
Table 4-4	Linear regression equations for the salinity calibrations.	68
Table 4-5	Vessel tracks during the three fieldwork periods.	70
Table 4-6	Sensor derived SPM and $K_d(550)$ regressions.	80
Table 4-7	Sensor derived SPM and $K_d(632)$ regressions.	83
Table 5-1	Comparison between the CASI, UOR and PRR-600 wavebands.	91
Table 5-2	Linear relationship between the SPM coefficients and solar irradiance.	100
Table 5-3	Solar irradiance input to SPM algorithm.	100
Table 6-1	Aircraft flightline details	108
Table 6-2	Calculated pixel and swath widths, from Equation 6-1, with a SFOV of 35 degrees.	114
Table 6-3	Contemporaneous ground data for August flightlines 4, 8 and 9. Time and position data from the QUBIT system, and SPM data from the calibrated nephelometer.	121
Table 6-4	Contemporaneous ground data for September flightlines 1, 4 and 5. Time and position data from the QUBIT system, and SPM data from the calibrated transmissometer.	121

ACKNOWLEDGEMENTS

I would like to take this opportunity to express my heartfelt thanks and gratitude, to all the people who have given me both support and assistance in producing this thesis.

Particular thanks must go to both my supervisors, Professor Keith Dyer (University of Plymouth) and Dr Jim Aiken (Plymouth Marine Laboratory), for their continuing advice , encouragement, support and guidance which kept me going throughout the last three and a quarter years.

I am also indebted to both Dr Tony Bale and Gerald Moore (Plymouth Marine Laboratory), without whom this work would have been much more stressful. Tony was wonderful in his support, specifically his assistance in organizing and active participation in the laboratory experiments and fieldwork trips. Whilst Gerald was a source of inspiration and new ideas. Michael Moore (an MSc student in 1993) for his participation in both the fieldwork and laboratory experiments.

I must thank the master and survey officer of "Sea Vigil" for their help in deploying and retrieving instruments. The National Rivers Authority (now Environmental Agency), in particular Nick Holden and Richard Saull, have been a vital element, as without their provision of CASI data there would be no imagery.

For the technical and computing assistance and facilities in this thesis, I would like to thank NERC Equipment Pool For Field Spectroscopy (EPFS) for providing the Spectron SE590 which was used in ground truthing. Dr Kevin Morris (PML) and Steve Groom (Remote Sensing Data Analysis Service) both formerly of the NERC Remote Sensing & GIS Unit for access to the facilities and assistance. I would also like to acknowledge Steve for introducing me to the topic of atmospheric correction.

I must also thank Dr Derek Pilgrim (UoP), for allowing me to use the Marine Optics Laboratory and computer equipment within it. In addition Derek has offered me tremendous support, guidance and honest opinions ever since my degree project which began the chain of events culminating in this thesis.

I would like to thank Sean Nicholson (NERC Computing Services) for his encouragement and patience in allowing me the time and facilities to finish. My husband, Andy, for his support throughout both my student and working life.

There are many other people, too numerous to individually mention, who have given me both advice and support. To these people I would like to say a big thank you.

AUTHOR'S DECLARATION

At no time during the registration for the degree of Doctor of Philosophy has the author been registered for any other University award.

This study was financed with the aid of a studentship from the Natural Environment Research Council, and carried out in collaboration with Plymouth Marine Laboratory.

Tony Bale and Michael Moore provided assistance during the laboratory experiments and Gerald Moore formulated the semi-analytical model from which the Suspended Particulate Matter algorithm was developed.

Publications or presentation of other forms of scientific work (including those under my maiden name of Hudson):

Aiken J., Hudson, S.J. and Vessey, J.P. 1994. The measurement of optical attenuation in sea water. *Proceedings of Oceans 94*, Ostates, 2, 689-693.

Bale, A.J., Tocher, M.D., Weaver, R., Hudson, S.J. and Aiken, J. 1994. Laboratory measurements of the spectral properties of estuarine suspended particles. *Netherlands Journal of Aquatic Ecology*, 28, 237-244.

Hudson, S.J., Moore, G.F., Bale, A.J., Dyer, K.R. and Aiken, J. 1994. An operational approach to determining suspended sediment distributions in the Humber estuary by airborne multi-spectral imagery. *Proceedings of the First International Airborne Remote Sensing Conference and Exhibition, Strasbourg*, Vol. III, 3, 10-20.

Aiken, J., Hudson, S., Moore, G. and Bottrell H. 1995. Further development of airborne remote sensing techniques. *Preliminary report to the National Rivers Authority*.

Hudson, S. 1996. The Plymouth Correction Experiment. *Proceedings of the First SeaWiFS Exploitation Initiative (SEI) Team Meeting*. NASA Tech. Memo. 104566, Vol. 33, Eds.

Hooker, S.B. and Firestone, E.R., NASA Goddard Space Flight Center Greenbelt, Maryland, 20-22.

Aiken, J., Moore, G., Bottrell, H. and Lavender, S. 1996. Further Development Of Airborne Remote Sensing Techniques: Atmospheric correction of CASI data and retrieval of suspended particulate matter concentrations in coastal waters. *Third report to the National Rivers Authority.*

Morris, K.P., Robinson M-C., Youngs, K.J., Lavender, S.J., and Murphy, R.J. 1996. Integration of CASI data and sea-truth measurements in the coastal zone, Proceedings of the 2nd Airborne Remote Sensing Conference and Exhibition, San Francisco, USA. (to be published).

Presentations given:

NERC Airborne Remote Sensing Conference, Nottingham, 1993. (Poster)

First Airborne Remote Sensing Conference and Exhibition, Strasbourg, 11-15th September 1994. (Poster)

First LOIS RACS(C) Workshop, Bristol, September 1994. (Talk)

Holderness Sediment Regime Workshop, Liverpool, September 1994. (Talk)

SeaWiFS Exploitation Initiative Meeting, Southampton, January 1995. (Talk)

SIRREX 4 (SeaWiFS *In-situ* Optical Instrument Calibration Workshop), National Institute Of Standards and Technology (NIST), Washington, May 1995. (Talk)

LOIS Annual Conference, Plymouth, March 1996. (Talk)

Signed S. J. Lavender

Date 3/6/96

1. INTRODUCTION

1.1 Aims And Objectives

This thesis was undertaken with the aid of a Natural Environment Research Council (NERC) studentship, as part of the Land-Ocean Interaction Study (LOIS). The aim was to develop a near infrared water-leaving radiance model which can calculate suspended sediment concentrations in Case 2 waters, which would aid in the interpretation of airborne remote sensing imagery and determination of sediment fluxes in the Humber estuary and associated coastal zone.

Suspended sediment fluxes can be quantified through a combination of mooring measurements, shipborne surveys and both satellite and airborne remote sensing imagery. The mooring measurements and shipborne surveys provide *in-situ* measurements, whilst remote sensing allows the contemporaneous mapping of parameters over a large area, but can only provide a 'surface' value. In a wider context, remote sensing provides a means of mapping water quality which is important for organisations such as the National Rivers Authority (NRA) who need to monitor large areas in a short time span.

1.2 Land-Ocean Interaction Study (LOIS)

The over-riding objective of LOIS is the development of simulation models from a detailed, comprehensive and integrated factual base. One of the major parts is the River-Atmosphere-Coast Study (RACS). The aims are (LOIS, 1992):

- a) quantifying hydrodynamical transports and processes affecting transformations, interactions and fates of particles, biogeochemically important elements and representative contaminants from land sources to the coastal zone,
- b) providing the first integrated environmental data base of a UK coastal region covering seasonal cycles and interannual variability and incorporating measurements of fluxes of materials and rates of biological productivity,

- c) generating a new quantitative understanding of estuarine and coastal processes controlling the fluxes and reactivities of both natural and anthropogenic materials,
- d) providing integratable models of these processes as building-blocks for comprehensive coastal zone system models which will realistically predict the effects of future environmental change.

Remote sensing provides LOIS with the capability of monitoring large areas, such as the Humber Estuary, in a matter of hours which could not be achieved using conventional measurements. By using airborne remote sensing, areas can be covered at pre-determined regular intervals to coincide with tidal events. It also enables the integration of the different components of LOIS e.g. land, coast and sea as the Compact Airborne Spectrographic Imager (CASI) can be programmed for wavebands and saturation levels enabling the optimum configuration to be achieved for each application. Satellite observations, using the Sea viewing Wide Field-of-view Sensor (SeaWiFS), will provide measurements of a larger area, but at a reduced resolution of 1.13 km (Hamilton *et al.*, 1993). This will occur twice a day at times determined by the satellites orbit and the coverage will depend on cloud cover. The turning of observed radiances into quantitative values for parameters such as suspended sediment concentration requires an atmospheric correction, and the algorithm must then be calibrated against measurements or a mathematical model.

A quantitative suspended sediment algorithm will contribute towards the aims of points a and c, allowing the comprehensive mapping of sea surface sediment distributions both in the estuary and coastal zone. A major benefit of airborne remote sensing will be the mapping of sediment distributions over a tidal cycle. When integrated with current velocities measured by moorings, fluxes can be calculated.

1.3 Thesis Overview

Optical remote sensing utilises the electromagnetic radiation spectrum between 400 and

1000 nm, with the visible radiation being in the range 400 to 700 nm and the near infrared being from 700 to 1000 nm. The water-leaving radiance can be used to detect and quantify the organic and inorganic material suspended or dissolved in the water column.

Chapter 2 introduces the optical theory, which is applied in the latter chapters. In estuarine and coastal waters the total suspended matter can be divided into two fractions, suspended particulate matter (SPM) and phytoplankton. The dissolved organic material (DOM) results from land runoff or biological degradation, and has been also called gelbstoff or yellow substance. The effect of these materials on the water-leaving radiance, depends on their absorption and scattering properties, which vary non-linearly with wavelength. The equations used to calculate these properties are given in Section 2.3.1.

To fully understand the effect of suspended sediment on the water-leaving radiance, the other in-water components have to also be quantified and modelled, as the signals are superimposed on one another and interact in a non-linear way. In the first instance, a set of laboratory measurements were used to study the effect of each component, as the conditions and concentrations could be controlled (see Chapter 3). The tank experiments were used to characterise the reflectance resulting from the different sediment concentrations and types, and the biogenic effects of DOM and phytoplankton. The data were examined both as full spectra (Chapter 3) and discrete wavebands (Chapter 5), which corresponded to those flown by CASI and the SeaWiFS satellite. It was shown that the ratio of two near infrared bands (SeaWiFS bands 7 and 8) was related to the suspended sediment concentration, and did not vary with sediment type (see Figure 5-4). This was in contrast to the visible wavelength region where the different sediment types produced different spectral shapes due to their colour (see Figure 3-8).

An analytical water-optics model was developed to validate the tank experiments and derive a general solution that would be applied to satellite and airborne imagery (Chapter 5). This compares to previous research, which involved choosing a retrieval variable by statistical means and then linearly regressing it against the *in-situ* SPM samples. For the tank experiments, the model was based on the reflectance equation, which relates the above water reflectance to the water mass optical properties. This was converted to normalised

water-leaving radiance (see Equation 2-75) for application to the CASI imagery, as this includes the effect of differing amounts of solar irradiance in each waveband.

Three fieldwork surveys of the Humber estuary were performed in June, August and September 1993. The calibration of the *in-situ* sensors and calculation of key variables is described in Chapter 4.

Airborne remote sensing, using the Compact Airborne Spectrographic Imager (CASI), took place during the August and September surveys. Three flightlines were flown at heights of 10 000, 5 000 and 2 000 feet on three transects; Axial, Transaxial and Humber Approaches (see Chapter 6). Comparison of the contemporaneous imagery shows the stability of the near infrared waveband ratio (see Section 6.3.2). Key physical variables and in-water optical properties were measured from the research vessel placed under the Humber Approaches flightline. The comparison of these two sets of measurements is termed imagery validation and is discussed in Section 6.4.

The previous chapters are discussed in Chapter 7 and conclusions are drawn about the SPM algorithm. The chapter then discusses further research, which would make the algorithm more accurate.

1.4 Compact Airborne Spectrographic Imager (CASI).

Water targets have lower reflectances than land targets, 2-7% compared to 10-50%, which necessitates a sensor with a greater signal-to-noise ratio (SNR) and hence improved performance (Hamilton *et al.*, 1993). The Compact Airborne Spectrographic Imager (CASI) is a 'pushbroom' imager, which splits the beam of received radiation onto a two dimensional Charge-Coupled Detector (CCD) array resulting in several co-registered images, each representing a waveband. It operates over a 430 to 870 nm wavelength range with a resolution of 2.8 to 2.9 nm, and the swath width has 512 pixels spread over the 35 degree field-of-view (FOV). The spatial resolution depends on the altitude, ground speed and integration time, but is typically in the 2 to 10 metres range. The dynamic range is 12 bits (i.e. a resolution of 1 in 4096 of the saturation radiance).

CASI can operate in either spatial or multispectral mode. In multispectral mode the operator selects 39 separate pixels across the FOV or portion thereof and in spatial mode the operator selects 12 non-overlapping spectral bands specifying wavelength and bandwidth (Anger *et al.*, 1994). The spatial mode was chosen as this research covered a large area.

Being an aircraft sensor, CASI is continually developing in response to new demands and so the above specifications are only applicable to the instrument flown. In the full LOIS campaign the CASI sensor has an increased dynamic range of 16 bits, 15 wavebands in spatial mode and a lumigen coating to improve the blue end response (Anger *et al.*, 1994).

2. OPTICAL PROPERTIES

This chapter defines, from first principles, the atmospheric, marine and remote sensing optical properties used in the following chapters. It uses the same scientific notation in each case, so that the reader can easily move from one discipline to the other.

2.1 Optics Definitions

In this section the optics definitions which are relevant to both the aquatic and atmospheric mediums will be explained. The nature of light is first discussed from a historical point of view.

The first quantitative scientific research into the nature of light was carried out by Alhazen, who in around 1000 AD showed that the angle of incidence, for a reflected ray of light, was equal to the angle of reflection. In 1627 Willebrod Snell formulated Snell's Law (see Equation 2-36), and the prevalent theory for the nature of light was the corpuscular theory, a particle theory devised by Isaac Newton. However, Robert Hook and Christian Huygens performed experiments that supported the wave rather than particle-like nature of light, which were further supported by the theoretical work of James Clerk Maxwell in the mid 1800's. With Thomas Young's work on the interference of light and the work of David Brewster on reflection, refraction and polarisation, the wave theory became more prominent. In 1818 Augustin Fresnel explained diffraction using wave theory, which effectively ended the corpuscular theory.

In 1893 Wilhelm Wien formulated his blackbody radiation displacement law and in 1900 Lord Rayleigh used electromagnetic wave theory to explain the long-wave portion of the blackbody spectrum. However Max Planck formulated a statistical explanation for blackbody radiation (Planck's Law), that same year, which gave birth to the quantum theory. The implication of Planck's Law was that the Electromagnetic Radiation (EMR) was made up of particle-like energy packets called photons or quanta and had discrete energy levels, which could be explained by probability. A beam of light would consist of a continual stream of these photons. The photons were used to emphasise the quantized or

statistical properties of light, while waves were used to emphasise the time-averaged effects of the EMR.

In 1909 Albert Einstein explained wave-particle duality which was discussed further by Niels Bohr who called it complementarity. He recognised that classical physicists were always successful in applying either waves or particles to solving a problem, but never both. When the interaction of radiation with matter was explored the particle aspect was used, but when propagation was being explored the wave aspect was used. Thus Bohr's principle states that the wave and particle aspects of radiation are complementary: one or the other may be used, but never both together.

2.1.1 The Properties Of Light

Light is a radiant flux of energy (power which is defined as energy, Joules, per second), Φ , and has the units of Watts (W):

$$\text{Power } (\Phi) = \text{Js}^{-1} = \text{W} \quad (2-1)$$

Radiation within the electromagnetic spectrum varies in frequency, which is inversely related to wavelength in accordance with Equation 2-2, in which the speed of light (c) remains constant in a given medium.

$$\text{wavelength}(\lambda) = \frac{\text{speed}(c)}{\text{frequency}(\nu)} \quad (2-2)$$

The units of wavelength are normally nanometres (nm) for visible light and Hertz (Hz) or inverse seconds (s^{-1}) for frequency. Wavelength may also be converted to wavenumber (κ) which has units of inverse centimetres (cm^{-1}):

$$\text{wavenumber}(\kappa) = \frac{2\pi}{\text{wavelength}(\lambda)} \quad (2-3)$$

The bandwidth of the optical spectrum is only a small part of the full electromagnetic

spectrum, which increases in wavelength from gamma rays through to radio waves (see Figure 2-1). Within the optical spectrum the waveband from 400 nm (violet) to 700 nm (deep red), which the human eye is sensitive to, is called light.

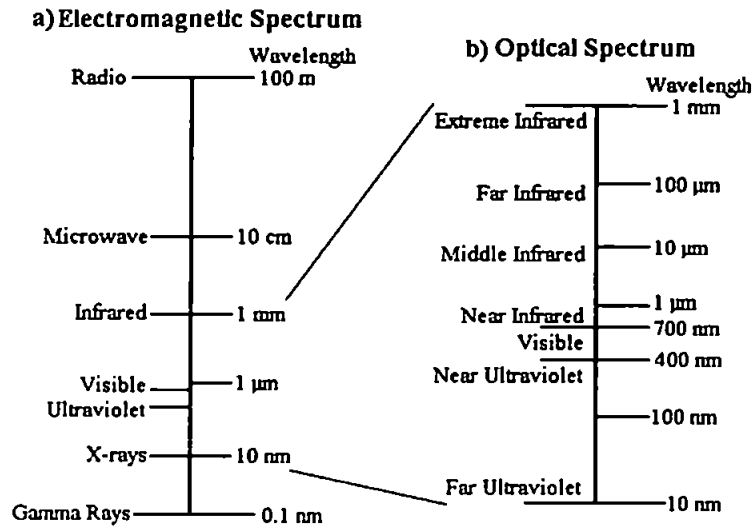


Figure 2-1: a) The electromagnetic spectrum and b) an expansion of the optical spectrum

Electromagnetic waves occur in short wave trains or bursts, with each burst carrying radiant energy (ϵ) as given by Equation 2-4 where ν is the frequency of the wave.

Alternatively, Equation 2-4 can describe the energy in one photon of a particular frequency, ν .

$$\epsilon = h \cdot \nu \quad (2-4)$$

Planck's constant (h) equals $6.625 \cdot 10^{-34}$ joule seconds (Js), so the amount of energy present in one photon or a short wave burst increases as the frequency increases. From Equation 2-4 it can be shown that the energy decreases as the wavelength increases from blue through green to red.

There are two radiometric quantities which describe the radiant field, irradiance and radiance. Irradiance deals with a diffuse flux of light, while radiance is a directional flux or beam. Radiance, L , is defined as the power per unit solid angle per unit area per unit wavelength, resulting in units of watts per steradian per square centimetre per nanometer

($\text{W sr}^{-1} \text{cm}^{-2} \text{nm}^{-1}$). A steradian is defined as the solid angle at the apex of a cone and is the ratio of the projected area to the radius squared, since the surface of a sphere is $4\pi r^2$ there are 4π steradians in a sphere.

The direction of the incident radiation is conventionally taken as normal to the surface, so to calculate the value at other angles we use Lambert's law (see Figure 2-2). As the emitted radiation falls off with θ_n (the nadir angle), the 'projected' surface area also falls off at the same rate. This means the radiance emitted by a Lambertian surface is constant with respect to θ_n .

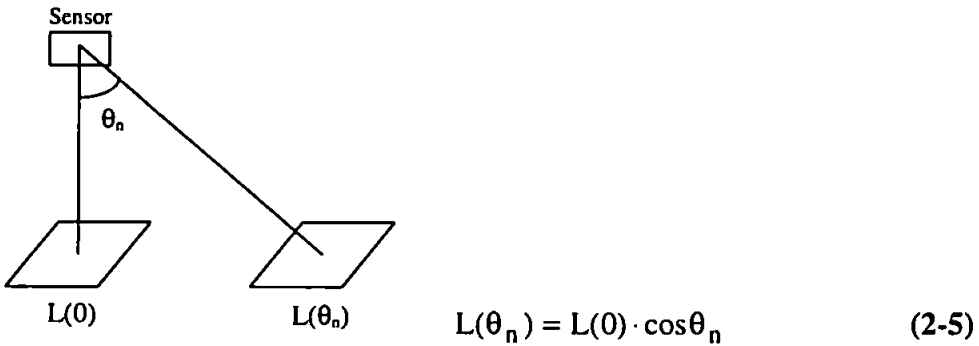


Figure 2-2: Lambert's Law

Radiance is a function of its direction, from a vertical (as defined by Lambert's Law) and horizontal plane, and is therefore defined in terms of the zenith (θ) and azimuth (ϕ) angles respectively. The zenith angle is measured between the light beam and upward vertical, while the nadir angle is measured between the light beam and downward vertical. The azimuth angle is that between the vertical plane incorporating the light beam and some other specified vertical plane, normally the sun. This gives radiance the notation $L(\theta, \phi)$.

Irradiance, E , is defined as the incident radiant power per unit area per unit wavelength, giving it units of watts per square centimetre per nanometer ($\text{W cm}^{-2} \text{nm}^{-1}$). For in-water optics we are interested in both the upwelling and downwelling light fields, and the total irradiance field can be divided into these two components (see Equation 2-6).

$$E(\lambda, z) = E_d(\lambda, z) + E_u(\lambda, z) \quad (2-6)$$

The downwelling vector irradiance, $E_d(\lambda, z)$, is the downwelling flux incident per horizontal unit area (see Equation 2-7). The zenith angle, θ , is measured from 0 to π and the azimuth angle, ϕ , is measured from 0 to 2π .

$$E_d(\lambda, z) = \int_{2\pi} L(\lambda, z, \theta, \phi) \cdot \cos\theta \cdot d\omega \quad (2-7)$$

The ideal vector irradiance sensor would be a horizontally orientated cosine collector, with an acceptance angle of 180 degrees and the flux striking the sensor would be normalised by $\cos(\theta)$. The greatest response would occur when the light flux is normal to the surface, as the cosine of zero is unity, and when the light flux was horizontal there would be no response as the cosine of 90 degrees is zero. This cosine response can be achieved by using an opal glass, which transmits only an amount of light roughly proportional to the cosine of the angle made by the incident light (Jerome, 1973). The PRR-600 (see Section 4.5) uses such a downwelling cosine collector.

The scalar irradiance, $E_o(\lambda, z)$, is independent of the zenith angle of incidence and is the integral of the radiance distribution at a point over all the directions. The downwelling scalar irradiance, $E_{od}(\lambda, z)$, can be obtained from Equation 2-8.

$$E_{od}(\lambda, z) = \int_{2\pi} L(\lambda, z, \theta, \phi) \cdot d\omega \quad (2-8)$$

Hemispherical scalar irradiance can be measured using a hemispherical or 2π collector, as used on the Oceanographic Recorder (Aiken & Bellan, 1990), for both upwelling and downwelling scalar irradiance. Small errors occur due to the loss of light with a nearly horizontal path, although in the case of the Oceanographic Recorder larger errors are produced by shading from the towed body.

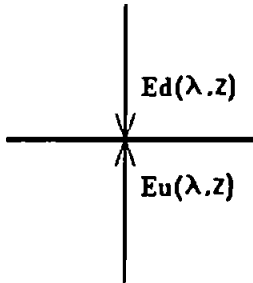
Photosynthetically Available Radiation (PAR) irradiance, $^{\circ}E_o(z)$, is the quantum scalar irradiance measured in the 400 to 700 nm photosynthetic waveband (see Equation 2-9). We may also use $^{\circ}E_{od}(\lambda)$ and $^{\circ}E_{ou}(\lambda)$ for the 2π downwelling and upwelling PAR.

$$^{\circ}E_o(\lambda, z) = \int_{\lambda=400}^{700} \int_{4\pi} L_q(\lambda, z, \theta, \phi) \cdot d\lambda \cdot d\omega \quad (2-9)$$

The average cosine for downwelling light, $\bar{\mu}_d(\lambda, z)$, provides information about the angular structure of the light field and is calculated by dividing the downwelling vector irradiance by the downwelling scalar irradiance:

$$\bar{\mu}_d(\lambda, z) = \frac{E_d(\lambda, z)}{E_{od}(\lambda, z)} \quad (2-10)$$

Reflectance, $R(\lambda, z)$, is the ratio of upwelling irradiance to downwelling irradiance (see Figure 2-3). This ratio describes the flux of light across a boundary, which is not a solid surface but a certain point in space e.g. a depth of 5 metres. The alternative term, used to describe the light being reflected off a solid surface is reflectivity.



$$R(\lambda, z) = \frac{E_u(\lambda, z)}{E_d(\lambda, z)} \quad (2-11)$$

Figure 2-3 : Reflectance

From Equation 2-11 it can be seen that reflectance is dimensionless and is therefore commonly converted to a percentage value. We can also have scalar irradiance reflectance, R_o , which is the ratio of the upwelling to downwelling scalar irradiance. This is related to the conventional irradiance reflectance through the average cosine of the light field (Equation 2-10).

As the remote sensing sensor will measure the upwelling radiance rather than irradiance, reflectance can be converted to remote sensing reflectance, $R_{rs}(\lambda, z)$, which is the ratio of

upwelling radiance to downwelling irradiance (see Equation 2-12). In converting the upwelling radiance to upwelling irradiance we need an additional π steradians factor.

$$R_{rs}(\lambda, z) = \frac{L_u(\lambda, z) \cdot \pi}{E_d(\lambda, z)} \quad (2-12)$$

The reflectance, just above the water surface, is calculated from Equation 2-13 where $F_0(\lambda)$ is the instantaneous solar irradiance, $L_w(\lambda, z)$ is the water-leaving radiance and θ is the solar zenith angle. In the underwater situation π is often replaced by the irradiance-to-radiance ratio, Q , which approximates 4.5 and varies with the angular dependant scattering of water molecules (Gordon & Clark, 1981).

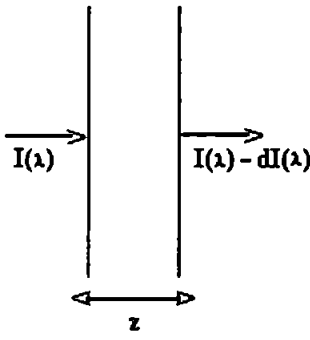
$$R_{+0}(\lambda) = \frac{L_w(\lambda) \cdot \pi}{F_0(\lambda) \cdot \cos\theta} \quad (2-13)$$

2.1.2 Inherent Optical Properties

The inherent optical properties are independent of the ambient light field. They specify the probability of events occurring and are only dependent on the substances in the medium and not the geometric structure of the light field, and so provide a means of modelling light propagation. It should also be noted that they apply to a single scattering situation, where each photon interacts with only one particle and the effect of several particles will be additive.

The total absorption coefficient, $a(\lambda)$, is the absorption loss resulting from the radiance being propagated through an infinitesimally narrow layer of absorbing, but non-scattering, medium divided by the thickness of that layer (see Equation 2-14 and Figure 2-4). It is given units of per metre (m^{-1}).

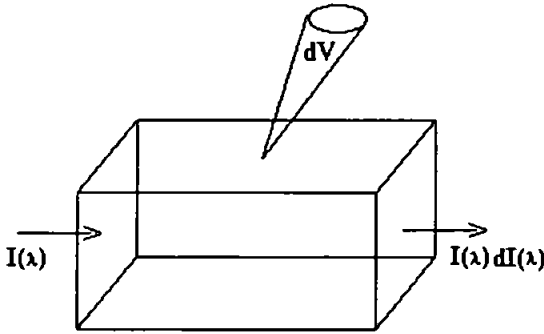
The volume scattering function, $\beta(\lambda, z, \sigma)$, depends not only on the degree of scattering but also the angular distribution of the scattered flux. Therefore, it is defined as the radiant



$$dI(\lambda, z) = a(\lambda, z) \cdot I(\lambda)$$

$$\Rightarrow a(\lambda, z) = \frac{dI(\lambda, z)}{I(\lambda)} \quad (2-14)$$

Figure 2-4: Absorption



$$\beta(\lambda, z, \sigma) = \frac{dI(\lambda, z, \sigma)}{I(\lambda, z) \delta V} \quad (2-15)$$

Figure 2-5: Volume scattering

intensity scattered in a given direction, σ , from a volume element, δV , illuminated by a parallel beam of light, per unit of incident irradiance onto the cross-section of the volume, and per unit volume (see Equation 2-15 and Figure 2-5).

To get a scattering term similar to the absorption coefficient, i.e. without a directional component, the volume scattering function is integrated over all the angles (0 to 4π) becoming the total volume scattering coefficient $b(\lambda, z)$, see Equation 2-16. This also has units of per metre (m^{-1}).

$$b(\lambda, z) = \int_{4\pi} \beta(\lambda, z, \sigma) \cdot d\omega \quad (2-16)$$

The total scattering coefficient can be divided up into its two components: the forward-scattering, b_f , and backscattering, b_b , coefficients (see Equation 2-17). These relate directionally to the upwelling and downwelling light fields, with the backscattering coefficient representing the downwelling light scattered in the upwelling direction.

$$b(\lambda, z) = b_f(\lambda, z) + b_b(\lambda, z) \quad (2-17)$$

The normalised volume scattering function, $\beta^*(\lambda, z, \sigma)$, describes the angular distribution of the scattering (see Equation 2-18).

$$\beta^*(\lambda, z, \sigma) = \frac{\beta(\lambda, z, \sigma)}{b(\lambda, z)} \quad (2-18)$$

In atmospheric correction, we use the single scattering phase function, $P^*(\lambda, \theta, \phi)$, as shown by Equation 2-19 with functions having units of per steradian (sr^{-1}).

$$P^*(\lambda, \theta, \phi) = \frac{4\pi \cdot \beta(\lambda, \theta, \phi)}{b(\lambda)} \quad (2-19)$$

Direct field measurements of the absorption and scattering coefficients are not easy, so we choose instead to measure the volume (beam) attenuation coefficient, $c(\lambda, z)$, using a beam transmissometer. This is commonly performed at 680 nm i.e. in the red wavelength region, but there are also blue (490 nm) and green transmissometers (550 nm) available.

Attenuation is the fraction of energy removed from a beam by both absorption and scattering per unit distance (see Equation 2-20).

$$c(\lambda, z) = a(\lambda, z) + b(\lambda, z) \quad (2-20)$$

The single scattering albedo, $\omega_0(\lambda, z)$, gives the probability that a photon will be scattered rather than absorbed (see Equation 2-21).

$$\omega_0(\lambda, z) = \frac{b(\lambda, z)}{c(\lambda, z)} \quad (2-21)$$

The backscattering probability, $b_b(\lambda, z)$, (Gordon *et al.*, 1988) or backscattering ratio (Morel, 1988) gives the probability that the photon will be backscattered and is defined as:

$$\underline{b}_b(\lambda, z) = \frac{b_b(\lambda, z)}{c(\lambda, z)} \quad (2-22)$$

2.1.3 Apparent Optical Properties

These properties change with the light field as well as the in-water constituents, and so are affected by parameters such as the solar zenith angle. The subsurface downwelling irradiance diminishes in an approximately exponential manner with increasing depth, and is wavelength dependent because of the wavelength dependence of the absorption and scattering functions. The rate of decrease can be quantified by calculating the diffuse attenuation coefficient, $K(\lambda)$, which has units of per metre (m^{-1}) which is the same as the beam attenuation coefficient. We calculate the diffuse attenuation coefficient from Beer-Lambert's law (see Equation 2-23), where z is the depth.

$$E(\lambda, z) = E(\lambda, 0) \cdot \exp[-K(\lambda) \cdot z] \quad (2-23)$$

This can be rearranged to give Equation 2-24, where $K(\lambda)$ would be the negative slope of line for a graph of depth versus log irradiance.

$$\Rightarrow \frac{E(\lambda, z_2)}{E(\lambda, z_1)} = \exp[-K(\lambda) \cdot dz]$$

$$\Rightarrow \ln \left[\frac{E(\lambda, z_2)}{E(\lambda, z_1)} \right] = -K(\lambda) \cdot dz$$

$$\Rightarrow d \ln[E(\lambda)] = -K(\lambda) \cdot dz$$

$$\Rightarrow K(\lambda) = -\frac{d}{dz} \ln[E(\lambda)] \quad (2-24)$$

The diffuse attenuation coefficient is generally expressed in terms of the upwelling or downwelling light flux i.e. $K_u(\lambda)$ and $K_d(\lambda)$ respectively. As we will also use scalar irradiance sensors we will have scalar diffuse attenuation coefficients, $K_{ou}(\lambda)$ and $K_{od}(\lambda)$.

The penetration depth or depth from which 90% of the light returns to the surface, $z_{90}(\lambda)$, can be calculated from the downwelling diffuse attenuation coefficient (Gordon & McCluney, 1975), see Equation 2-25.

$$z_{90}(\lambda) = \frac{1}{K_d(\lambda)} \quad (2-25)$$

The optical depth, $\zeta(\lambda)$, is a function of $K_d(\lambda)$ and the geometric depth, z , (see Equation 2-26).

$$\zeta(\lambda) = K_d(\lambda) \cdot z \quad (2-26)$$

2.2 Effects of the Medium

The effects of the medium upon light propagation can be divided into the scattering and absorption components.

2.2.1 Absorption

When a photon passes within the vicinity of a molecule there is a finite probability that it will be captured and the amount of energy in the molecule will increase by that in the photon. The effect will depend on the wavelength of the incident radiation which is related to the energy, see Equation 2-4. The simplest form of atomic absorption causes an electron to move to a higher electron level, which is at an increased distance from the nucleus. The energy in a molecule has electronic energy levels associated with the electrons of its component atoms and also quantized vibrational and rotational energy levels, so it can be considered part rotational, part vibrational and part electronic. Vibrational energy levels

are associated with oscillations in the atom-atom bond distances and rotational energy levels arise from the rotation of molecules in space. A molecule can only have one of a discrete series of energy levels. The energy increments corresponding to an electronic change in level, these are large in comparison to the vibrational energy increments which in turn are larger than the rotational energy increments.

Photons in the visible range have sufficient energy, when absorbed, to bring about transformations from one energy level to another. In the visible wavelength region water absorption involves not electronic excitation but molecular vibration. Within a complex molecule such as chlorophyll there is usually more than one possible energy transition that can occur.

Excitation energy can be lost by re-emission of radiation, this process is known as fluorescence. In living, photosynthesising algal cells only about 1% of the absorbed light is lost in this way.

The complex refractive index is needed if we are going to consider that particle absorption (Jerlov, 1976), this obeys Equation 2-27 (Nanu & Robertson, 1993).

$$m = n - ik \quad (2-27)$$

Where n is the refractive index of the particle relative to the surrounding medium and k is the extinction index which is equal to $r\lambda/4\pi$ where r is the particle radius.

Particle absorption can cause a variation in reflectance. For example, quartz-rich sediments have a much lower reflectance in the near-infrared region than clay-rich sediments (Whitlock *et al.*, 1977). Iron oxides selectively reflect red light and absorb green light (Curran, 1985), while other pigments can affect the reflectance in the blue and green wavelengths, but will only affect reflectance in the red and near infrared when they are present in extremely high concentrations (Stumpf & Pennock, 1989). In general, the fine particles behave primarily as scatterers, while the coarser particles tend to absorb radiation in the visible wavelengths (Novo *et al.*, 1989).

2.2.2 Scattering

Scattering occurs when a photon interacts with a molecule or particle and undergoes a change in direction. Scattering varies in magnitude and direction not only with the amount of particulate matter, but also with the particle size relative to the incident radiation wavelength and the index of refraction for the scattering material. This holds true whether it be suspended particulate matter in the sea or aerosols in the atmosphere.

In nature, there will not be a single particle size but a range or size distribution. For suspended sediment and aerosols the size distribution is due to the settling out of larger particles which depends on the turbulence in the medium. For the permanently suspended sediment in the Humber we will be mainly dealing with mud, which is classed as the material with a diameter of less than $63\mu\text{m}$ and comprises of a mixture of silt and clay (McCave, 1987).

Aerosols are solid and/or liquid particles suspended in the air, whose concentration varies considerably with time and space. They get into the atmosphere by essentially two mechanisms: detachment by the wind stress; and the condensation and sublimation of gases. Once there, they form water vapour nuclei and undergo a complicated process of growth (which depends on many parameters e.g. water vapour content, pressure and temperature). As a result, aerosol particles range from diameters of 10^{-7} cm (clusters of molecules) to about 0.1 cm (raindrops). The size distributions of aerosols are generally very similar, due to the mechanisms of coagulation and precipitation. However, industrial areas may be an exception to the rule because the aerosols are generated from gas to liquid conversions in the boundary layer. Scattering depends on the relative size of the particle radius (r) to the wavelength of incident radiation:

- (i) Molecular or Rayleigh, $r \ll \lambda$
- (ii) Mie, $\lambda/10 < r < 10\lambda$
- (iii) Isotropic, $r \gg \lambda$

According to Rayleigh theory, any particle in a light field induces a dipole by the electrical

vector of the field. As the dipole oscillates, at the frequency of the exciting radiation, it emits radiation of the same frequency in all directions i.e. scattered light. Density fluctuation scattering is named Molecular or Rayleigh scattering according to the medium, as Rayleigh theory is only applicable to gases. The division between Rayleigh and Mie theory occurs when the particle is one tenth the size of the incident wavelength (Maul, 1985).

The Rayleigh volume scattering function, $\beta_r(\lambda, \sigma)$, describes the scattering by air molecules where N is the number of molecules per unit volume and σ is the angle of the incident radiation.

$$\beta_r(\lambda, \sigma) = \frac{\pi^2(m^2 - 1)^2}{2N\lambda^4} (1 + \cos^2 \sigma) \quad (2-28)$$

When Equation 2-28 is substituted into the scattering phase function, see Section 2.1.2, we get Equation 2-29 (Zibordi *et al.*, 1990) where as much light is scattered forward as back.

$$P_r^*(\sigma) = \frac{3}{4} (1 + \cos^2 \sigma) \quad (2-29)$$

The Mie theory of scattering applies to spherical particles and is valid for any particle size and radiation wavelength (Van de Hulst, 1957). It calculates the power scattered from a randomly polarised beam (of unit intensity) into a unit steradian, by a single particle of radius r and complex refractive index m . However, these Mie calculations are complex to use and form a slowly converging series, so need a lot of computing power to run in real time. Therefore, they are only used when the particle radius is of the same order as the incident radiation wavelength.

Isotropic or non-selective scattering is independent of wavelength and causes the flux to be scattered mainly in the forward direction. At visible wavelengths in the atmosphere this type of scattering occurs in thick clouds or fog. Scattering by these 'large' particles is comprised of three phenomena: diffraction, refraction and reflection. The diffraction is

determined by the size and shape of the particle, whereas refraction and reflection depend upon the composition which is characterised by the relative refractive index.

Mie scattering is also characterised by an angular distribution predominantly in the forward direction. In the ocean, 50% of the scattered light may lie between the scattering angles of 0 and 5 degrees (Maul, 1985). This can explain why the upwelling light may be only 5% of the incident radiation. If the solar beam is not vertical and there are large scattering angles we can still get significant scatter in a backwards (away from the water surface) direction (Kirk, 1983).

The volume scattering function shows that the scattering at small angles is crucial when determining the total scattering coefficient, as the scattering is predominately in the forward direction (see Figure 2-6). This forward scattering is determined chiefly by the size of the particles, with the shape having very little influence and the composition having fairly little influence (Jerlov, 1976). Therefore, it is the backscattering that varies with these factors, and as this is an important term in the calculation of reflectance these effects need to be understood. Volume scattering function values in the atmosphere are much smaller than in the ocean, which means we can see further above than in the water.

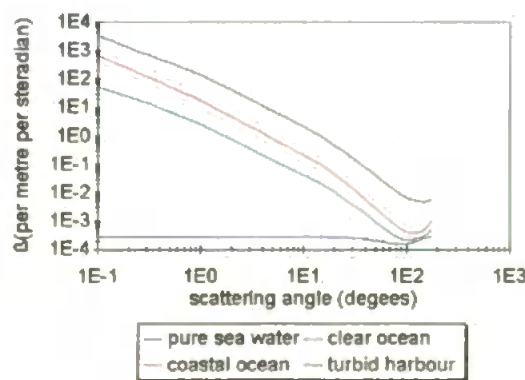


Figure 2-6: Volume scattering functions for different water types, using data from Petzold (1972).

The aerosol scattering phase function, $P_s^*(\sigma)$, can be approximated by fitting an analytical expression (Irvine, 1965) to the Mie theory of scattering, which significantly reduces the number of computations. The two term Henry-Greenstein (TTHG) function, see Equation 2-30, is normally used for this curve fitting procedure where a , g_1 and g_2 (the asymmetry

factors) depend on the incident radiation wavelength and particle size distribution. Gordon *et al.* (1983) used values of 0.962, 0.713 and 0.759 respectively.

$$P_a^*(\sigma) = \frac{(1 - g_1^2)a}{(1 + g_1^2 - 2g_1\cos\sigma)^{1.5}} + \frac{(1 - g_2^2)(1 - a)}{(1 + g_2^2 + 2g_2\cos\sigma)^{1.5}} \quad (2-30)$$

Aranuvachapun (1986) showed that the variation in the scattering phase function due to changes in the aerosol size distribution is larger than that due to the change in wavelength. The TTHG and thus the asymmetry factors are therefore assumed to be independent of wavelength, in the visible and near-infrared. The TTHG is accurate for a smoothly varying phase function (small number of large particles), but as the number of large particles increases the phase function becomes more variable and the TTHG becomes less accurate (Aranuvachapun, 1985).

Both Rayleigh and Mie theory depend upon the mean particle separation distance being greater by a factor of 3 or more than the particle radius (Maul, 1985). If this is always the case we would have independent or single scattering, if not we have multiple scattering.

When water molecules scatter light, a small proportion of the scattered photons (when interacting with the scattering molecule) lose a small amount of energy and so become shifted in wavelength. These appear in the scattered light field as emission bands, occurring at wavelengths other than that of the exciting light, and are referred to as Raman scattering. A particularly strong Raman emission shows up 100 nm to the longer wavelength side of the excitation source (Kirk, 1983). However, water Raman scattering is normally considered negligible for waters with SPM as the main component (Carder *et al.*, 1993).

2.3 Optics Modelling

In this section the theory developed in the previous two sections will be applied to the three cases: in-water, atmospheric and air/sea interface.

2.3.1 In-Water Optics

The most appropriate parameter to model or measure, for the light field just above the water surface is reflectance, $R_{+0}(\lambda)$. This is wavelength dependent and can be determined by the inherent properties (Gordon *et al.*, 1975) as well as the ratio of upwelling to downwelling light (as seen in Section 2.1.1).

$$R_{+0}(\lambda) = 0.33 * \frac{b_b(\lambda)}{b_b(\lambda) + a(\lambda)} \quad (2-31)$$

The value of 0.33 accounts for the passage of light through the sea-surface interface, so without it we get the sub-surface reflectance. It is not in reality a constant, and will vary with the radiance distribution and volume scattering function. It takes a value of 0.3244 when the sun is at the zenith and 0.3687 for a uniform sky, but the variation from the chosen value of 0.33 never exceeds 5% and only slightly varies throughout the commonly used part of the electromagnetic spectrum. Therefore, the error in assuming it is a constant is normally considered insignificant (Morel & Prieur, 1977).

The absorption and backscattering coefficients relating to each group of substances, present in the water, are expressed as a product of the substances concentration and corresponding specific absorption. Each group is in fact made up of several substances (often present in differing proportions) with slightly different properties, so the specific absorption curve for each group will be subject to a certain amount of variability (Prieur & Sathyendranath, 1981). However, it is often sufficiently accurate to consider each group as a routinely measured parameter. The concentration of chlorophyll-*a* is used to represent the phytoplankton, suspended particulate matter (SPM) is used to represent non-chlorophyllous particles and Dissolved Organic Matter (DOM) is used to represent the Coloured Dissolved Organic Matter (CDOM) or gelbstoff.

The total backscattering and absorption coefficients for a body of water can therefore be calculated by summing the contributions from each of the specific in-water constituents (see Equation 2-32 and Equation 2-33), where the subscripts in Equation 2-32 represent

water, DOM, chlorophyll-*a* and SPM respectively.

$$a(\lambda) = a_w(\lambda) + a_y(\lambda) \cdot y + a_{ch}(\lambda) + a_s(\lambda) \cdot s \quad (2-32)$$

$$b_b(\lambda) = 0.5 \cdot b_w(\lambda) + b_{bch}(\lambda) + b_{bs}(\lambda) \cdot s \quad (2-33)$$

The factor of 0.5 in the water backscattering term (Equation 2-33) converts the scattering values to backscattering values, and can be applied because of the symmetry of the volume scattering function (Morel, 1974). The chlorophyll absorption and backscattering terms do not have concentration terms in Equation 2-32 and Equation 2-33, because they have a non-linear relationship with concentration (see Section 2.2.3).

Equation 2-33 describes a monodisperse system with particles of a given refractive index scattering light, so that the scattered light can be assumed to have the same wavelength as the incident light. There is also no multiple scattering and so the particles are independent i.e. the intensities of the light scattered by each particle can be summed so that the total scattering is proportional to the number of particles. However, experimental volume scattering functions tend to exhibit the distinctive properties of a polydisperse system, being a smoothed rather than the oscillatory curve that would be expected in a monodisperse system (see Section 2.2.4).

Chlorophyll-*a* and DOM fluorescence are not covered by this model, as their effects on the reflectance of Case 2 sediment laden waters are much smaller in magnitude when compared to the sediment backscattering.

In clear oceanic waters (Case 1) reflectance is a function of: absorption by algal pigments, detritus and low concentrations of (aquatic) humus at short wavelengths; absorption by water molecules at long wavelengths; scattering by water molecules at short wavelengths; Raman scattering at intermediate wavelengths; fluorescence by humus at shorter wavelengths; fluorescence by algal pigments at longer wavelengths.

While in suspended sediment laden coastal waters (Case 2) these effects still occur, but the analysis becomes more complicated due to the; backscattering from particles, which

becomes the dominant scattering factor as it can give values up to 1000 times greater than the backscattering of oceanic waters (Decker, 1993); greater absorption at shorter wavelengths by high concentrations of humus and tripton; decrease in the contribution of water molecule scattering, Raman scattering and fluorescence by aquatic humus and algal pigments.

These additional effects in Case 2 waters make the development of algorithms more complex as the absorption/scattering effects are superimposed and there are non-linear relationships between concentration and reflectance.

2.3.1.1 Water

Water scatters strongly in the blue region (Novo *et al.*, 1989) with a decreasing influence towards the near infrared (see Figure 2-7a).

Water absorption causes a significant decrease in the reflectance values beyond 550 nm, and results in the absorption coefficient being dominated by the absorption of water in this region (Carder *et al.*, 1993). The spectral absorption rises in magnitude until it peaks at around 760 nm then decreases slightly until 813 nm where it begins to rise rapidly (see Figure 2-7b).

2.3.1.2 Dissolved Organic Matter

There are many dissolved substances in the sea, but for optics modelling only the dissolved organic matter (DOM) is considered significant. This group of substances causes a significant absorption in the ultraviolet and blue wavelengths relative to those in the red (see Figure 2-8). In coastal waters, the organic material is made up mainly of humic and fulvic acids, which are either present in the soil and become leached out by rainwater or are the result of the decomposition of biological materials by bacteria. This group is also regularly referred to as gelbstoff, yellow substance or Dissolved Organic Carbon (DOC), which is the largest and most often measured component.

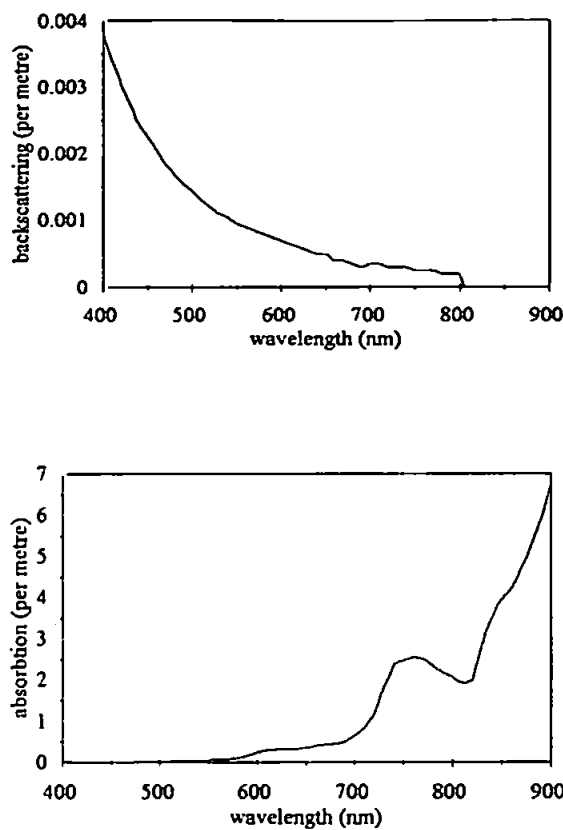


Figure 2-7: Water a) backscattering and b) absorption values taken from Smith and Baker (1981), for the wavelength range 400 to 800 nm, and Palmer and Williams (1974) for the near infrared beyond this.

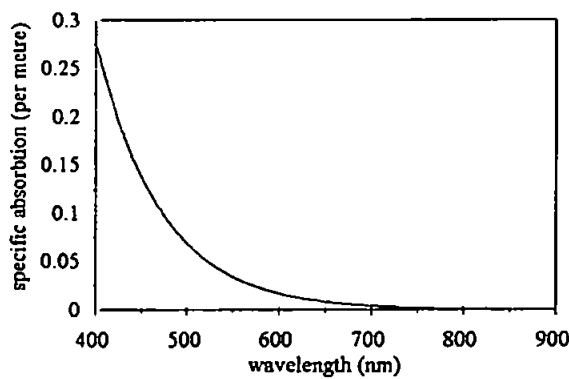


Figure 2-8: DOM absorption calculated using Equation 2-34.

The equation for the absorption of DOM (see Equation 2-34) relates the wavelength required to absorption measurements at a standard wavelength e.g. 375 nm (Ferrari & Tassan, 1991). Standard wavelengths of 340, 440 (Davie-Coley & Vant, 1987) or 450 nm (Carder *et al.*, 1989) may also be used. Values for k are of the order of 0.014 nm^{-1} (Bricaud *et al.*, 1981), and vary with the proportion of humic and fulvic acids. For the 440 nm standard wavelength the value of absorption coefficients goes from 0.02 m^{-1} in 'ocean desert' areas, remote from terrestrial sources, to 1.6 m^{-1} in the Baltic Sea which is dominated by DOM (Bricaud *et al.*, 1981).

$$a_y(\lambda) = a_y(375) \exp(-k(\lambda - 375)) \quad (2-34)$$

DOM can show a parallel and an inverse relationship with salinity, due to relatively DOM-rich fresh waters being diluted by the DOM-poor marine waters (Mantoura & Woodward, 1983). The riverine DOM can also be correlated with river flow indicating that the source is soil-derived inputs. However, in populated catchments there can be an inverse relationship (Stumm & Morgan, 1981) because of sewage outfalls. Maximum concentrations of marine DOM tend to occur in the summer (coinciding with less turbid waters and therefore a greater probability of high chlorophyll concentrations) whilst in winter concentrations correspond to the background level found in oceanic waters (Mantoura & Woodward, 1983).

2.3.1.3 Phytoplankton

The phytoplankton pigment absorption spectral curve (shown in Figure 2-9) has chlorophyll absorption peaks at 440 and 675 nm, a phaeophytin peak at 410 nm and a carotenoid shoulder at 480 nm (Prieur & Sathyendranath, 1981). It is dependent not only on the optical properties of the phytoplankton cells, but also the packaging effect (Haardt & Maske, 1987). This is a consequence of the pigment molecules, not being uniformly distributed, but contained within discrete packages: chloroplasts, within cells, within cell colonies. This lessens the effectiveness with which the cells collect light from the prevailing field (Kirk, 1983).

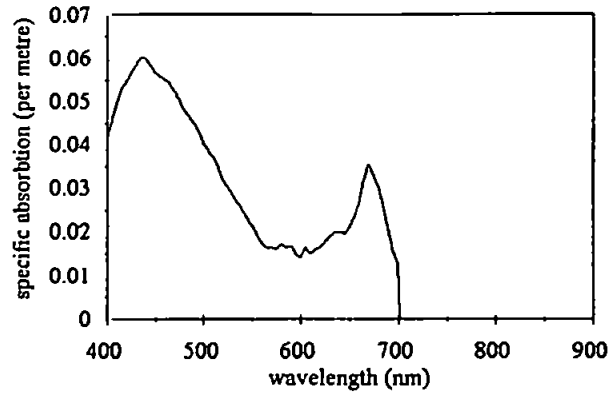


Figure 2-9: Phytoplankton pigment absorption using values taken from Prieur and Sathyendranath (1981).

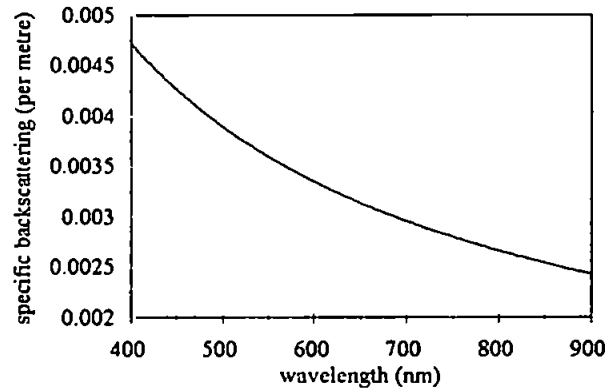


Figure 2-10: Chlorophyll backscattering calculated from Equation 2-38.

An equation for the absorption of chlorophyll-*a*, for concentrations less than 10 mg m^{-3} , (Prieur & Sathyendranath, 1981) is given in Equation 2-35, where a_{Ch}^* is the normalised spectral absorption coefficient of phytoplankton pigment and Ch is the chlorophyll concentration (mg m^{-3}).

$$a_{\text{ch}}(\lambda) = a_{\text{c}}^*(\lambda) \cdot 0.06 \text{ Ch}^{0.62} \quad (2-35)$$

The backscattering of chlorophyll is strongest in the blue region, with a decreasing influence through the spectra towards the near infrared (see Figure 2-10) and can be evaluated from Equation 2-36.

$$b_{bCh}(\lambda) = \underline{b}_b(\lambda) \cdot b(550) \quad (2-36)$$

For the detrital fraction of the biological particulate matter the scattering varies approximately inversely with wavelength (Morel, 1973) when the size distribution function obeys a Junge law with the exponent -4. When living algae with a relatively narrow size distribution are superimposed a peak may be present. The shape of the volume scattering function for the detrital marine particles leads to an almost constant \underline{b}_b of about 2% (Morel, 1973). Experimentally algal cells exhibit very low $\underline{b}_b(\lambda)$ values (Bricaud *et al.*, 1983), which is fully supported by theory (Bricaud & Morel, 1986). The spectral variation in $\underline{b}_b(\lambda)$ for algae, is mainly determined by the algal pigment absorption. In eutrophic waters, the chlorophyll concentration is about 100 mg l⁻¹, and the backscattering ratio reaches a value of about 0.2% (Yu-Hwan Ahn *et al.*, 1992).

The backscattering of chlorophyll at 550 nm, $b(550)$, is statistically related to the chlorophyll concentration through Equation 2-37 (Morel, 1980).

$$b(550) = b^0 Ch^{0.62} \quad (2-37)$$

Where b^0 ranges from 0.12 to 0.45 m⁻¹, with a mean value of around 0.3 m⁻¹ (Gordon & Morel, 1983). This variation is due to changes in scattering resulting from different species and variations in the associated detrital particles (Gordon, 1994). The non-linear character of the equation reflects a relative change in the proportions of true algae to non-algal (detrital or heterotrophic) particles as the phytoplankton concentration increases.

So the overall equation for the chlorophyll backscattering coefficient, can now be expanded to give Equation 2-38 (Morel, 1988). This equation can account for a change from an oligotrophic situation (abundant detritus) to an euphotic situation (algal cells are predominant).

$$b_{bCh}(\lambda) = \underline{b}_b(\lambda) \cdot b(550) = 0.30 Ch^{0.62} (2 \cdot 10^{-3} + 2 \cdot 10^{-2} (0.5 - 0.25 \log Ch) (550/\lambda)) \quad (2-38)$$

Chlorophyll fluorescence depends on the physiological state of the algae and the environmental conditions present at that time (Bricaud *et al.*, 1983). It can be used to predict photosynthesis and therefore primary production. About 1% of the light a photosynthesising cell absorbs is re-emitted as fluorescence, with a fluorescence peak occurring at approximately 683 nm. This peak does not have a constant magnitude for a constant chlorophyll concentration, in different phytoplankton species, due to the packaging effect (Yu-Hwan Ahn *et al.*, 1992), which was explained at the start of this section.

2.3.1.4 Suspended Sediment

Suspended sediment (both organic and inorganic) strongly backscatters radiation, and in turbid conditions overwhelms the reflectance signal of phytoplankton pigments and DOM absorption (Bukata *et al.*, 1985). However, high levels of phytoplankton pigments and DOM can have a suppressing effect on the observed reflectance spectra in certain wavebands (Lathrop, 1992).

The backscattering of suspended sediment is inversely related to wavelength, being strong in the blue and then decreasing in influence through the spectrum (see Figure 2-11).

A suspended sediment backscattering equation (see Equation 2-39) has been derived from the particle-dominated normalised volume scattering function, determined by Petzold (1972) for the turbid waters of San Diego Harbour, and also used in the work of Whitlock *et al.* (1981).

$$b_{bs}(\lambda) = 0.006144 + 15.764 * [\frac{1}{\lambda}] \quad (2-39)$$

Equation 2-39 shows that scattering is inversely related to wavelength in sediment dominated waters, which was also noted by Kirk (1983).

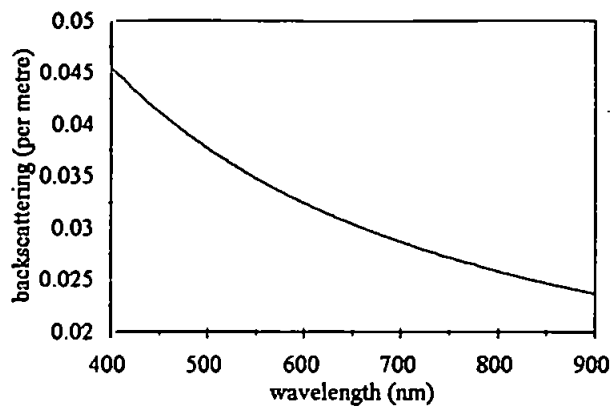


Figure 2-11: Suspended sediment backscattering calculated from Equation 2-39.

2.3.2. Atmospheric Optics

Atmospheric correction is very important for both aircraft and satellite sensors as only 5 to 10% of the signal originates from the water. It is not feasible to be constantly measuring all the atmospheric parameters necessary, so models have to make broad assumptions, particularly about aerosols. In the oceanic situation, we have Case 1 water (dominated by photosynthetic pigments) where the optical properties of the water are smoothly varying and as the area is a long way from land the aerosol contribution can be considered constant, models have been reasonably successful. However, in the Case 2 waters (dominated by suspended sediment) which are present in the Humber estuary and coastal zone the water parameters and aerosol properties exhibit large variations over small spatial scales. Consequently modified models need to be considered whereby the aerosol variations can be assumed and corrected for. Depending on the wind direction, the proportions of each aerosol type (continental, marine and anthropogenic) will vary. The relative humidity will control the size of many of the aerosols, as they grow by adsorption of water molecules. So there needs to be either measurements of the atmosphere, taken concurrently with the images, to determine the aerosol parameters or determination of the parameters from the images themselves. Also, it is not always necessary to perform the same degree of atmospheric correction, depending on the wavebands being used, as it may increase the

possibility of errors and processing time (important if the method is to be used operationally).

2.3.2.1 Main Equation

The spectral radiance received at a remote sensor can be written as a linear sum of the contributions, where: h_0 is the altitude of the sensor; $L_p(\lambda, h_0)$ is the path radiance; $L_{sky-g}(\lambda, h_0)$ is the sky- glitter radiance; $L_{sun-g}(\lambda, h_0)$ is the sun-glitter radiance; $L_{ws}(\lambda, h_0)$ is the water-leaving radiance entering the sensor (see Equation 2-40).

$$L_s(\lambda, h_0) = L_p(\lambda, h_0) + L_{sky-g}(\lambda, h_0) + L_{sun-g}(\lambda, h_0) + L_{ws}(\lambda, h_0) \quad (2-40)$$

The radiance entering the sensor is related to the water-leaving radiance just above the surface, $L_w(\lambda)$, where $t_d(\lambda, h_0)$ is the diffuse transmittance of the atmosphere (see Equation 2-41).

$$L_{ws}(\lambda, h_0) = L_w(\lambda) \cdot t_d(\lambda, h_0) \quad (2-41)$$

Diffuse rather than direct transmittance is used as a proportion of the pixel's radiance originates from neighboring pixels and it can be calculated from Equation 2-42 (Gordon *et al.*, 1983) where $\tau_r(\lambda)$ is the Rayleigh optical depth, see Equation 2-51, and $\tau_{03}(\lambda)$ is the ozone optical depth, see Equation 2-46.

$$t_d(\lambda) = \exp \left(\frac{\frac{\tau_r(\lambda)}{2} + \tau_{03}(\lambda)}{\cos \theta} \right) \quad (2-42)$$

The path radiance can be split into its Rayleigh, $L_r(\lambda, h_0)$, and aerosol, $L_a(\lambda, h_0)$, scattering components (see Equation 2-43). This is only exact for a single-scattering atmosphere, i.e. there is no Rayleigh-aerosol interaction.

$$L_p(\lambda, h_0) = L_r(\lambda, h_0) + L_a(\lambda, h_0) \quad (2-43)$$

In adapting the CZCS atmospheric correction model (Gordon and Castano, 1987) for SeaWiFS, the radiance terms were replaced with reflectance terms because the new sensors will be calibrated for reflectance rather than radiance. It is not difficult to perform this conversion for satellite data, and the definition of reflectance was used as Equation 2-12. However, it is much more difficult in airborne remote sensing as there is a proportion of the atmosphere above as well as below the aircraft. The SeaWiFS model also added a Rayleigh-aerosol interaction term, giving the equation:

$$R_s(\lambda, h_0) = R_r(\lambda, h_0) + R_a(\lambda, h_0) + R_{ra}(\lambda, h_0) + t_d(\lambda) \cdot L_w(\lambda) \quad (2-44)$$

2.3.2.2 Attenuation of the solar radiation

The attenuation of solar irradiance by scattering and absorption, as a function of wavelength, is defined through the optical thickness of each of the atmospheric constituents. In the visible and near-infrared regions the main constituents are the permanent gases (nitrogen, carbon dioxide, oxygen and argon), aerosols, ozone and water vapour.

For aircraft data the optical thickness of a constituent, x , must take account of the detection altitude, see Equation 2-45, where the scale height factor, $H_x(h_0)$, depends on the altitude and assumes that the constituents are vertically homogeneous (Zibordi *et al.*, 1990).

$$\tau_x(\lambda, h_0) = H_x(h_0) \cdot \tau_x(\lambda) \quad (2-45)$$

The bottom layer of the atmosphere, called the troposphere, extends from the earth's surface to about 10 km and contains about 80% of the atmosphere's mass and 90% of the water vapour and aerosols. Therefore, a plane flying at or above this altitude will have all of these components below its sensors. In contrast, the main ozone concentration is situated between 20 and 50 km i.e. it is situated above the aircraft and only affects the downwelling solar irradiance.

1) Atmospheric Absorption

From 1814 to 1817 Joseph Fraunhofer observed dark lines in the solar spectrum that now bear his name, and in 1860 Robert Bunsen and Kirchhoff explained Fraunhofer's lines as absorption due to gases in and above the solar photosphere. The atmospheric absorption will be divided into its separate absorbing components, which can be defined in terms of their optical depths.

a) Ozone

In the visible wavelength region the atmosphere is almost transparent with only a small amount of attenuation by ozone, with the ozone optical depth being given by Equation 2-46 where $K_{03}(\lambda)$ is the spectral absorption coefficient in units of cm^{-1} (Vigroux, 1953) and C_{03} is the ozone concentration in units of cm (Lacis & Hansen, 1974). The scale height is given by Equation 2-47 (Zibordi *et al.*, 1990).

$$\tau_{03}(\lambda, h_0) = H_{03}(h_0) \cdot C_{03} \cdot K_{03}(\lambda) \quad (2-46)$$

$$H_{03}(h_0) = 1 - \frac{1.0183}{(1 + 0.0183 \exp(h_0 / 5))} \quad (2-47)$$

b) Water Vapour

The water vapour optical depth, $\tau_w(\lambda, h_0)$, is given by Equation 2-48 (Iqbal, 1983) where $K_w(\lambda)$ is the water vapour absorption coefficient with units of cm^{-1} (Leckner, 1978) and C_w is the water-vapour concentration with units of cm. The scale height factor is given by Equation 2-49 (Reitan, 1963), with b_0 being dependent on the concentration which ranges from 0.30 to 0.95 km^{-1} and T_d being the dew point temperature in degrees Celsius, see Equation 2-50 (Tomasi, 1984).

$$\tau_w(\lambda, h_0) = H_w(h_0) \cdot ((0.2385 K_w(\lambda) \cdot C_w) / ((1 + 20.07 K_w(\lambda) \cdot C_w)^{0.45})) \quad (2-48)$$

$$H_w(h_0) = 1 - \exp(-b_0 \cdot h_0) \quad (2-49)$$

$$b_0 = \exp(-((\ln C_w - 0.061 T_d) + 0.715) / 0.983)) \quad (2-50)$$

2) Atmospheric scattering

The atmospheric scattering can be divided into its two main components, Rayleigh and aerosol scattering. Rayleigh scattering is caused by the molecules in the atmosphere, as where aerosol scattering is caused by the particles or aerosols.

a) Rayleigh

The Rayleigh optical depth is given by Equation 2-51 where z is the altitude, $\rho(z)$ is the air density and k_s is given by Equation 2-52 with: N being the number of molecules per unit volume; n being the refractive index of the gas; δ being the depolarization factor. Thus the Rayleigh optical depth is proportional to the King Factor (see Equation 2-53).

$$\tau_r = \int k_s \rho(z) dz \quad (2-51)$$

$$k_s = \frac{8\pi^3}{3} \frac{(n^2-1)^2}{\lambda^4 N} \left(\frac{6+3\delta}{6-7\delta} \right) \quad (2-52)$$

$$\tau_r \propto \left(\frac{6+3\delta}{6-7\delta} \right) \quad (2-53)$$

Hansen & Travis (1974) used a depolarization factor of 0.031 to obtain the most accurate approximation of the Rayleigh scattering optical thickness for the permanent gases, see Equation 2-54 (Teillet, 1990). The total optical depth approximation (Hansen & Travis, 1974) is defined by Equation 2-55.

$$\tau_r(\lambda) = H_r(h_0) * (0.0085669 * \lambda^{-4} (1 + (0.0113 * \lambda^{-2}) + (0.00013 * \lambda^{-4}))) \quad (2-54)$$

$$H_r(h_0) = 1 - \exp(-0.118h_0 - 0.00116(h_0^2)) \quad (2-55)$$

To get an optical thickness at any surface pressure, $\tau_r^*(\lambda)$, other than the standard atmospheric pressure, P_0 , which is equal to 1013.25 mb we can use Equation 2-56. If a standard atmospheric pressure of 1013 mb is assumed, it would cause a maximum error of $\pm 5\%$ (Andre & Morel, 1989).

$$\tau_r^*(\lambda) = \frac{P}{P_0} \tau_r(\lambda) \quad (2-56)$$

b) Aerosols

In the visible and near infrared wavelength regions the aerosols are expected to dominate the Rayleigh scattering. The maximum aerosol scattering occurs when the aerosol particle diameter is approximately the same as the radiation wavelength and is a function of the aerosol size, shape and index of refraction. Therefore, to calculate the single and multiple scattering phase functions, measurements of the number densities of aerosol particles, aerosol light scattering and aerosol size spectrum are needed. To make an assessment of the aerosol contribution we need one waveband to assess the aerosol magnitude and a second waveband to assess the wavelength dependence, in addition to rules governing the spectral variation, in order to relate the aerosol contribution to other wavebands (Gordon & Wang, 1994).

If we have a power-law type size distribution, the aerosol optical thickness can be calculated from Angstrom's Law (see Equation 2-57), where B is the Angstrom exponent which is related to the size distribution (see Equation 2-58) and A is proportional to the total number of aerosol particles (Greg & Carder, 1990). Sturm (1981) put A equal to 0.05 and B equal to 1. Equation 2-57 is an adaptation of the Angstrom empirical formulae (Angstrom, 1964), for aerosol extinction, within a clear atmosphere above a continent where the aerosol particles are small (0.04-0.1 μm and 0.1-0.3 μm) compared to the wavelength. It may be used if the influence of the coastal aerosol size distribution is very similar to that of continental aerosols which are typically smaller and have a higher concentration than marine aerosols (Maul, 1985). Equation 2-57 requires that slight inhomogenities in the size distribution and scattering phase function do not significantly affect the optical depth, which is valid when the concentration of large aerosol particles (> 0.1 μm) is low and decreases rapidly with size.

$$\tau_a(\lambda) = A \cdot \lambda^{-B} \quad (2-57)$$

$$B = \lambda^n \quad (2-58)$$

When the particle size becomes comparable to the wavelength accuracy decreases (Aranuvachapun, 1985). Quenzel (1970) suggested that Angstrom's Law may not describe the particle size distribution when the aerosol optical depth shows an increase with wavelength i.e. B is less than zero.

It can be assumed that the aerosols reside in the boundary layer, but the reflectance cannot be computed since its optical characteristics depend on the variable composition. Groom (1989) took the correction for scale heights from Guzzi *et al.* (1987), but no scale height correction was applied to aerosols as the aircraft was above the boundary layer. Guzzi *et al.* (1987) used Angstrom's Law to account for the varying altitude of an airborne platform (see Equation 2-59), where the scale height factor is defined by Equation 2-60.

$$\tau_a(\lambda, h_0) = H_a(h_0) \cdot A \cdot \lambda^{-B} \quad (2-59)$$

$$H_a(h_0) = 1 - \exp\left(\frac{-h_0}{H_p}\right) \quad (2-60)$$

The scale height, H_p , is equated to 0.97/1.4 for the first 5 km of the atmosphere according to Penndorf (1954). Zibordi *et al.* (1990) used Equations 2-59 and 2-60, but for clean air conditions (up to an altitude of 3.7 km) put H_p equal to 1.2 km (Elterman, 1968). Singh (1992) used values of $H=1.2$ km, $A=0.1$ and $B=1.3$ (Colwell, 1983) for continental aerosols.

The single scattering albedo can be related to Equation 2-61, where the relative humidity (RH) is a percentage and the air-mass type (AM) goes from 1 to 10 with 1 being marine aerosols (Shettle & Fenn, 1979) and 10 being continental (Bird & Riordan, 1986).

$$\omega_a = (-0.0032 \cdot AM + 0.972) \exp(3.06^{-4} \cdot RH) \quad (2-61)$$

Zibordi *et al.* (1990) derived the single scattering albedo from the ratio of the aerosol scattering to absorption:

$$\omega_a(\lambda) = \frac{\tau_a(\lambda, h_0)}{\tau_{aa}(\lambda, h_0)} \quad (2-62)$$

So the albedo depends strongly on the aerosol optical characteristics and size determination, which is assumed to be independent of wavelength in the visible and near infrared. For maritime aerosols, Deepak & Gerber (1983) set $\omega_a(\lambda)$ to 1.

Groom (1989) fitted the power law curve to the near infrared data, where water reflectance is at a minimum. This gave very unstable estimates for the Angstrom exponent possibly due to calibration problems and so a fixed value of -1 was used.

The single scattering approximation for the aerosol reflectance component, $R_{as}(\lambda)$, is given by Equation 2-63 where θ_0 is the zenith angle for the sensor - pixel geometry (Gordon *et al.*, 1983).

$$R_a(\lambda) = \frac{\tau_a(\lambda) \cdot \omega_a(\lambda) \cdot p_a(\theta, \theta_0, \lambda)}{4 \cos \theta \cdot \cos \theta_0} \quad (2-63)$$

$$p_a(\theta, \theta_0, \lambda) = P_a^*(\sigma^-, \lambda) + [\rho(\theta) + \rho(\theta_0)] P_a^*(\sigma^+, \lambda) \quad (2-64)$$

Where $\rho(\theta)$ is the Fresnel reflectance at the air-sea interface and $P_a^*(\sigma, \lambda)$ is the aerosol scattering phase function. The term involving σ^- provides the contribution due to photons backscattered to the sensor from the atmosphere without reaching the sea surface. σ^+ accounts for photons scattered in the atmosphere towards the sea surface (sky radiance) and then specularly reflected from the surface into the SFOV ($\rho(\theta)$ term) as well as those which are specularly reflected from the sea surface and then scattered by the atmosphere into the SFOV ($\rho(\theta_0)$ term). With the scattering angles corresponding to:

$$\cos \sigma_{\pm} = \pm \cos \theta \cos \theta_0 - \sin \theta \sin \theta_0 \cos (\phi - \phi_0) \quad (2-65)$$

In the CZCS model, the dark pixel method was used to obtain an Angstrom exponent (see Equation 2-66), with an extrapolation using Equation 2-67 (Groom, 1988).

$$\epsilon(\lambda_i, \lambda_j) = \frac{R_a(\lambda_i)}{R_a(\lambda_j)} = \frac{\omega_a(\lambda_i) \cdot \tau_a(\lambda_i) \cdot p_a(\theta, \theta_0, \lambda_i)}{\omega_a(\lambda_j) \cdot \tau_a(\lambda_j) \cdot p_a(\theta, \theta_0, \lambda_j)} \quad (2-66)$$

$$\epsilon(\lambda_i, \lambda_j) = \left(\frac{\lambda_i}{\lambda_j} \right)^{-n} \quad (2-67)$$

It was assumed that the water-leaving radiance equaled zero and the ratio of the aerosol reflectances in the two wavebands, i and j , are constant over a scene, even in the presence of spatial inhomogeneities in aerosol concentration. Although the optical depth spectra does exhibit a strong dependence with wavelength, the ratio of optical depths at different wavelengths may not be constant (if large aerosols are present) and Equation 2-67 would no longer be valid. But results would still support the use of (Gordon, 1978):

$$\epsilon(\lambda) = \frac{\tau(\lambda)}{\tau(750)} \quad (2-68)$$

For SeaWiFS the extrapolation (Equation 2-66) was not considered valid, as the near infrared wavebands are too far away from the visible wavebands to give a good extrapolation (Gordon, 1994). A more accurate method was needed, because the goal was to recover water-leaving reflectance with an error of no more than 5%. The extrapolation was improved by deriving a set of look-up tables based on different aerosol and in the future an experimental database will be added (Gordon, 1994).

SeaWiFS procedure will derive multiple scattering from another set of look-up tables. So to estimate $\epsilon(768,865)$ we assume the aerosol belongs to a given model (i^{th} model) and then solve the radiative transfer equation and derive the aerosol and Rayleigh-aerosol reflectance to provide $\epsilon_i(768,865)$. An average ϵ value is then calculated for a large number of likely models (according to Equation 2-69) and the derived value of $\epsilon(768,865)$ is used to estimate $\epsilon(\lambda,865)$ for all the other wavebands. In general, the derived value will fall between two of the N aerosol models (which have pre-calculated look-up tables), so we then assume that $\epsilon(768,865)$ will fall between the two models in the same manner.

$$\varepsilon(765,865) = \frac{1}{N} \sum_{i=1}^N \varepsilon_i(765,865) \quad (2-69)$$

Then another look-up table derives the aerosol plus Rayleigh-aerosol reflectance from the Rayleigh-aerosol reflectance we perform. The aerosol calculations are performed for each pixel (Gordon and Evans, 1993).

2.3.3 Air/Water Interface Optics

The irradiance, incident on the water surface, is composed of diffuse and direct solar radiation, both of which may be reflected from or transmitted through the water surface. So in attempting to measure the water-leaving radiance, $L_w(\lambda)$, with a downward facing spectrometer we actually measure:

$$L_t(\lambda) = L_w(\lambda) + L_{\text{sky-g}}(\lambda) \quad (2-72)$$

where $L_{\text{sky-g}}(\lambda) = \rho(\theta) \cdot L_{\text{t-sky-g}}(\lambda)$ with $\rho(\theta)$ being the Fresnel reflectance and $L_{\text{t-sky-g}}(\lambda)$ being the total sky-glitter radiance.

2.3.3.1 Reflection By The Sea Surface

The sea surface interface is assumed to be a Lambertian surface, which is a diffuse or isotropic reflector, and applies in calm sea conditions. The solar radiation interacts with the top layer, causing backscattering and absorption to take place, which results in the incident radiation losing its angular dependence. Therefore the backscattered radiation only carries the properties of the material with which it last interacted, and is not affected by the angle of the incident radiation. In contrast, a non-Lambertian surface, which is an anisotropic diffuse reflector, would have the intensity of reflected radiation affected by the sun-target-sensor geometry.

Surfaces can be specular or bi-directionally specular, with reflection at a smooth plane boundary between two transparent medium of different refractive index being known as specular reflection. The water's surface is treated as specular, and is therefore smooth with respect to wavelength.

The relative proportions of the sub-surface and water surface reflectance detected by the sensor, as total reflectance, varies according to the viewing geometry. If the solar zenith angle is greater than 50°, the surface reflectance starts to make a significant contribution to the total signal detected by the sensor (Curran, 1987). This dependence of reflection, at the surface, on the solar zenith angle (θ) of the incident light is described by the Fresnel equation (see Equation 2-73).

$$\rho(\theta) = 0.5 \left(\frac{\sin^2(\theta - \theta_r)}{\sin^2(\theta + \theta_r)} \right) + 0.5 \left(\frac{\tan^2(\theta - \theta_r)}{\tan^2(\theta + \theta_r)} \right) \quad (2-73)$$

Where the refracted angle, θ_r , is itself determined by θ according to Snell's Law (see Equation 2-74).

$$\frac{\sin\theta}{\sin\theta_r} = \frac{n}{n_r} \quad (2-74)$$

Here n_r and n are the refraction indices of the water and air respectively and the ratio of these indices can be given a value of 1.33 (for salt and fresh water, at normal ambient temperatures and for light within the photosynthetic range). We can therefore obtain an estimate of the reflected radiance from the solar zenith angle (see Figure 2-12).

The diffuse and direct components of specular reflection are dealt with separately in atmospheric correction models. The direct solar radiation reflected by the water surface is known as sun glitter, which can be minimised by viewing the water surface either vertically or at predetermined angles away from the sun (Clarke & Ewing, 1974). The diffuse solar radiation reflected at the surface is called skylight, and increases with decreasing wavelength at the expense of the sun glitter (Gordon *et al.*, 1988). So the surface reflection

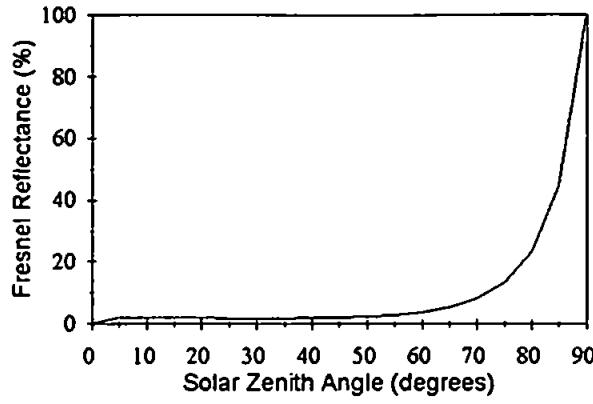


Figure 2-12: Fresnel Reflectance calculated using Equation 2-73.

must be built into the atmospheric correction model, as otherwise the water-leaving radiance will be overestimated.

2.3.3.2 Normalised Water-Leaving Radiance

The normalised water-leaving radiance, i.e. the water-leaving radiance that would be measured by a sensor placed above the water surface if the Sun was at the zenith and the atmosphere was absent, can be related to the in-water constituents via the sub-surface reflectance as in Equation 2-75 (Gordon *et al.*, 1988). This is useful as it allows different data sets to be compared. It can also be used instead of reflectance in developing in-water algorithms.

$$L_{wn}(\lambda) = \frac{(1 - \rho(\theta))(1 - \rho)F_0(\lambda,0) \cdot R_{-0}(\lambda)}{Q \cdot n_w^2(1 - R_d(\lambda) \cdot R_{-0}(\lambda))} \quad (2-75)$$

Where n_w is the ratio of the refracted indices for air and water, as present on the right hand side of Snell's Law (Equation 2-74) and $R_d(\lambda)$ is the water-air reflectance for totally diffuse irradiance $\cong 0.48$. Q is the underwater irradiance-to-radiance ratio $E_u(\lambda) / L_u(\lambda)$, which is only weakly dependent on wavelength. This would be set as π for a Lambertian reflector, but from the work of Bricaud & Morel (1987) the actual value may be closer to

4.5. $R_{-0}(\lambda)$ is the sub-surface reflectance just below the surface and $F_0(\lambda)$ is the mean extraterrestrial solar irradiance.

The Fresnel reflectance, $\rho(\theta)$, of the sea surface integrated over all the incident angles can be taken as 0.021 for the visible spectrum. Whitlock *et al.* (1981) assumed a value of 0.02. The Fresnel albedo due to the specular reflection of the sun and skylight, $\underline{\rho}$, ranges from 0.021 for a nadir sun to 0.064 for a solar zenith angle of 60 degrees, and totally diffuse skylight has a value of 0.066 (also from Gegg & Carder 1990). So we get a mean value of 0.043. Both $\rho(\theta)$ and $\underline{\rho}$ can be considered independent of wind speed (or sea state), from Austin (1974) and Priesendorfer & Mobley (1986) or Plass *et al.* (1975) respectively.

To derive the relationship between the sub-surface and above-surface remote sensing reflectance Equation 2-75 was rearranged:

$$L_{wn}(\lambda) = \frac{(1 - \rho(\theta))(1 - \underline{\rho})F_0(\lambda)}{n_w^2(1 - R_d(\lambda) \cdot R_{-0}(\lambda))} \cdot \frac{R_{-0}(\lambda)}{Q}$$

$R_{rs-0}(\lambda) = \frac{R_{-0}(\lambda)}{Q}$ was then substitute into the right hand side (RHS) of the above equation:

$$\Rightarrow L_{wn}(\lambda) = \frac{(1 - \rho(\theta))(1 - \underline{\rho})F_0(\lambda)}{n_w^2(1 - R_d(\lambda) \cdot R_{-0}(\lambda))} \cdot R_{rs-0}(\lambda)$$

$L_{wn}(\lambda) = \frac{F_0(\lambda)}{E_d(\lambda)} \cdot L_w(\lambda)$ was then substituted into the left hand side (LHS):

$$\Rightarrow \frac{F_0(\lambda)}{E_d(\lambda)} \cdot L_w(\lambda) = \frac{(1 - \rho(\theta))(1 - \underline{\rho})F_0(\lambda)}{n_w^2(1 - R_d(\lambda) \cdot R_{-0}(\lambda))} \cdot R_{rs-0}(\lambda)$$

$R_{rs+0}(\lambda) = \frac{L_w(\lambda)}{E_d(\lambda)}$ was substituted into the LHS and $F_0(\lambda)$ cancels out from both sides:

$$\Rightarrow R_{rs+0}(\lambda) = \frac{(1 - \rho(\theta))(1 - \rho)}{n_w^2(1 - R_d(\lambda) \cdot R_{-0}(\lambda))} \cdot R_{rs-0}(\lambda)$$

Assuming that $R_{-0}(\lambda)$ is small, as in Case 1 waters when it has a maximum value of 0.08 to 0.1, then $(1 - R_d(\lambda) \cdot R_{-0}(\lambda))$ will tend to unity. Typical data for n_w , $\rho(\theta)$ and ρ were inserted giving the approximation:

$$R_{rs+0}(\lambda) \approx 0.529 \cdot R_{rs-0}(\lambda) \quad (2-76)$$

In Case 2 waters, where the sub-surface reflectance is much greater, $(1 - R_d(\lambda) \cdot R_{-0}(\lambda))$ was substituted with $(1 - R_d(\lambda) \cdot Q \cdot R_{rs-0}(\lambda))$ as the sub-surface reflectance in this equation can not be considered negligible:

$$R_{rs+0}(\lambda) \approx \frac{0.529 \cdot R_{rs-0}(\lambda)}{(1 - 2.16 \cdot R_{rs-0}(\lambda))} \quad (2-77)$$

2.4 Summary

The equations derived in this chapter were applied to the experimental data (see Chapters 4 and 6) and used for the mathematical model (see Chapter 5).

3. LABORATORY EXPERIMENTS

In this chapter, laboratory experiments are reported that were used to determine the most appropriate optical wavebands for the suspended sediment algorithm and the optical effects of the other two optically active constituents. By simulating the 'real' environment in the laboratory the variables can be reduced and concentrations controlled.

3.1 Previous Work

Previous experiments to characterize suspended sediment reflectance with a laboratory tank arrangement, used either specific wavebands (Bhargava & Mariam, 1990, 1991a & 1991b and Choubey & Subramanian, 1991) or the full wavelength spectra (Witte *et al.*, 1982, Novo *et al.*, 1989, Tocher, 1992, Krijgsman, 1994 and Bale *et al.*, 1994). The aim of this series of experiments, was to simulate the water-leaving radiance that would result from different concentrations and sources of suspended sediment and also to investigate the spectral signals arising from the other optically active in-water parameters: phytoplankton and DOM.

In general, previous research concluded that reflectance increased with SPM (Bhargava & Mariam, 1990, 1991a & 1991b, Choubey & Subramanian, 1991, Novo *et al.*, 1989, Tocher, 1992 and Bale *et al.*, 1994). Bhargava & Mariam (1990, 1991a & 1991b) demonstrated that higher correlation coefficients / lower standard errors were observed in the 700 to 900 nm range and Tocher (1992) showed that the visible spectra was affected by sediment colour, whilst 804.3 nm remained unaffected. However, Choubey & Subramanian (1991) concluded that the spectral characteristics depend largely on the mineral composition, colour and sediment size rather than concentration with the shorter wavelengths being more useful. Novo *et al.* (1989) concluded that fine grained sediments may exhibit a more uniform spectral strength of correlation between SPM and reflectance.

3.2 Method

The laboratory arrangement is described by Bale *et al.* (1994) in Appendix 1. To obtain the large volume of natural suspended sediment needed, a thin surface layer of sediment was collected from the intertidal areas of interest and suitable size fractions were elutriated according to Stokes Law, see Equation 3-1 where: v is the particle settling velocity (ms^{-1}); g is the gravitational acceleration (ms^{-2}); ρ_1 is the density of the particle (kgm^{-3}); ρ_2 is the density of the liquid (kgm^{-3}); μ is the viscosity of the liquid (Nsm^{-2}).

$$v = \frac{1}{18} g \frac{\rho_1 - \rho_2}{\mu} d^2 \quad (3-1)$$

Four regions around the Humber estuary were selected: the eroding cliff at Easington on the Holderness Coast; the beach at Cleethorpes; near the turbidity maximum at Brough; and the Wash. These sediment types are combined within the Humber plume and each has a different composition. Each sediment was homogeneously suspended, using tap water, in a settling column (1.2 m in height and 0.3 m in diameter). After 3 h the top metre was siphoned off and mixed with Kalgon, a defloculant, before being left to stand overnight.

Settling was used in preference to sieving as it creates more natural size fractions, and were used in preference to dry sieved soil samples as used by Bhargava & Mariam (1990, 1991a & 1991b). The use of tap water and addition of a defloculant prevented sediment flocculation, which occurs in the estuarine environment, but will only have a small effect on the application of results as the flocs tend to sink below the penetration depth.

The maximum particle diameter, for the final suspensions, was calculated as approximately $10.2 \mu\text{m}$ from Equation 3-1. The actual size distribution was determined by using a Malvern (laser) particle sizer, see Figure 3-1. The Cleethorpes, Easington and Wash sediment suspensions had particles with the largest size band being from 7.9 to $10.1 \mu\text{m}$, while Brough had 31% of its particles larger than this size band. The presence of particles greater than the calculated maximum particle diameter, in the Brough sediment stock, indicates that flocculation may have occurred. The algal stock shows a different size

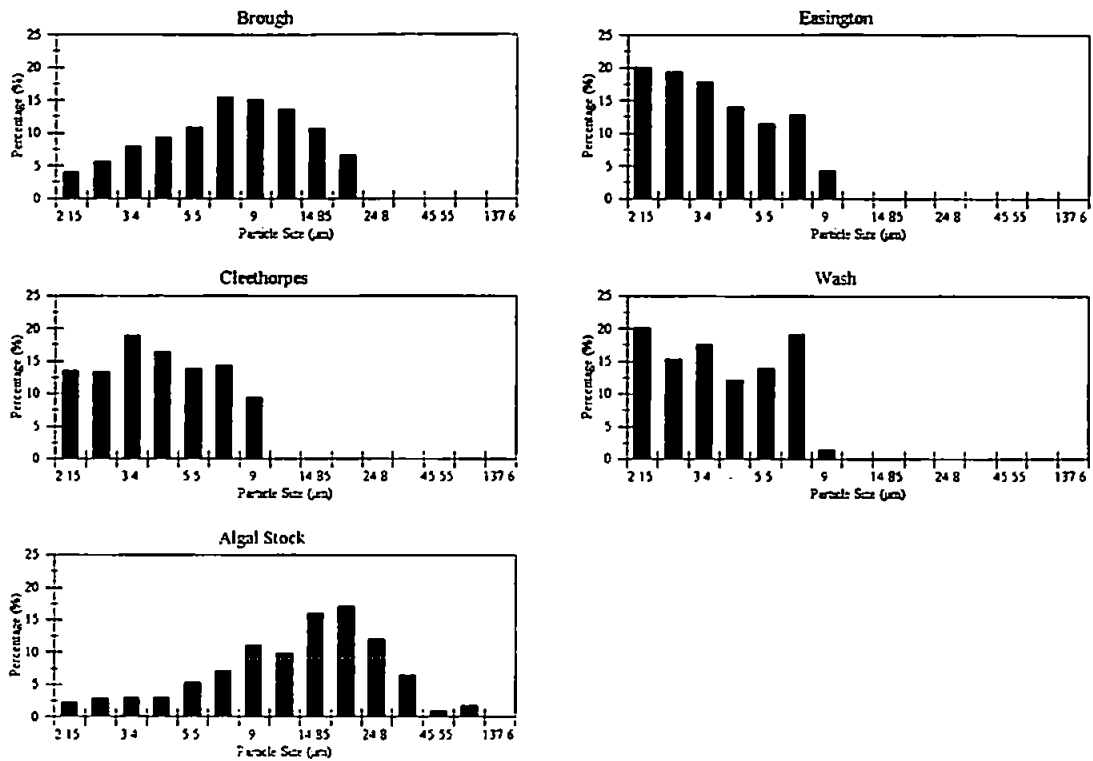


Figure 3-1: Particle size distribution for the different sediment and algae stocks determined by Malvern sizer.

distribution, with the phytoplankton cells having a larger mean size. From the Wentworth-size classification (Dyer, 1986) the particles were a mixture of silt and clay with size distributions in the range of 63.5 µm to 2 µm and 2 µm to 0.5 µm respectively.

At the start of the experiment for each sediment type the tank was filled with tap water, which was flushed through the tap for several minutes before filling the tank, so that the pipes were flushed of stagnant water. Four spectra were measured and the resulting average 'water' spectra were used to subtract the water surface reflectance and bottom effect, which on average resulted in a reflectance value of 0.4% for the 400 to 800 nm wavelength range. Samples were taken to determine the concentration of chlorophyll-*a* and suspended sediment and verify that these factors did not vary significantly between each experiment.

The chlorophyll sample was filtered through Whatman GF/F filter pads before the pigments were extracted with acetone. The chlorophyll-*a* concentration was determined

spectrophotometrically after the method of Parsons *et al.* (1984). The Dissolved Organic Carbon (DOC) concentration was measured using CO₂ following UV photo-oxidation as described by Mantoura & Woodward (1983).

The SPM concentration was determined gravimetrically, by filtering a known volume of the sample through a pre-weighed tared Whatman GF/C filter pad, and then re-weighing the dried pad plus particulate matter. A Malvern Laser Particle Sizer was used to measure the particle size distribution in 15 bands between 1.9 and 188 µm. The amount of suspended matter contained within the tap water was very small (less than 1 mg/l) when compared to the sediment concentrations being used in the experiments.

A volume of the sediment suspension was added to the tank of water until it reached the required concentration, as measured by a calibrated Partec suspended solids meter, whereas in Bale *et al.* (1994) the initial suspensions were diluted to obtain several concentration levels. The suspended sediment concentrations were chosen to reflect those which would normally be found in the coastal zone: 10, 20, 40, 60 and 100 mg/l. Four spectra were taken for each concentration and a sample removed, which was immediately filtered to obtain the actual suspended sediment concentration, organic fraction of the suspension and chlorophyll-*a* concentration. The Cleethorpes and Easington sediments had a large proportion of coarse sediment in the collected sample, and so there was an insufficient amount of suspended sediment in the stock to reach the final two concentrations. Despite the removal of samples and addition of stock the water level in the tank was kept constant, so as to provide constant surface illumination conditions.

A phytoplankton experiment was conducted using the final suspended sediment concentration of the Cleethorpes suspension (27.63 mg/l) as a base. A laboratory mixed algae culture (principally *Phaeodactylum tricornutum* and *Tetracelmis suecica*) was added to obtain increasing concentrations and the resulting wavelength spectra measured. This was then repeated with a base of tap water, and the addition of a large volume of Cleethorpes suspended sediment at the end to act as a comparison to the first set of reflectance spectra. The freshwater conditions and hence potential cell lysis were not considered significant as the reflectance spectra were used only to look at non-quantitative spectral effects.

The third experiment involved a tap water base and an increasing concentration of DOC, obtained from the particle-free and organic rich water of an upland stream (Bale *et al.*, 1994).

The 'bottom effects' were quantified by placing a white disk on the bottom of the tank, within the SFOV. Figure 3-2 shows the bottom effect for the Wash sediment suspension, calculated by subtracting the measured reflectance without the disk from that with the disk. The two lower concentrations (8.79 and 17.36 mg/l) show a significant difference in reflectance, suggesting that the penetration depth was greater than the tank depth. This difference is wavelength dependent, reducing in the near infrared as water absorption starts to increase (see Figure 2-9). The bottom effects at 600 nm, for all the sediment concentration levels, were plotted against the suspended load in order to determine the concentration above which the bottom had no detectable influence. Figure 3-3 shows this to be at about 30 mg/l for a white reflecting bottom, but this concentration level will be smaller for the actual tank as the bottom would be absorbing rather than reflecting light.

3.3 Data Processing

The water-leaving radiance spectra and corresponding reference (white panel) files were processed by the SMENU program (Rollins, 1992) and spectral reflectance values were calculated. The spectra were corrected for wavelength variations using solar irradiance measurements taken at the start of each experiment. The software used Equation 3-2 to calculate the above-surface reflectance, $R_{+0}(\lambda)$, where $L_r(\lambda)$ is the measured reference panel radiance and $R_r(\lambda)$ is the known reference panel reflectance (Rollins, 1992).

$$R_{+0}(\lambda) = \frac{L_w(\lambda)}{L_r(\lambda)} \times R_r(\lambda) \quad (3-2)$$

The four reflectance spectra, calculated for each concentration level, were then carefully examined before being averaged so that any suspect spectra could be examined. This averaging process reduced the signal to noise ratio (SNR), and so gave a more

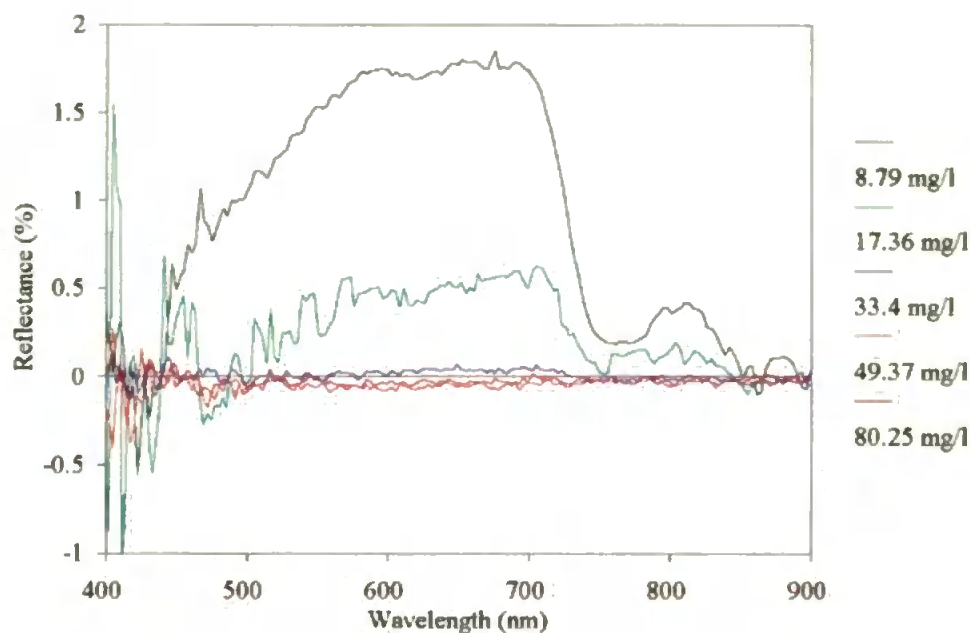


Figure 3-2: The reflectance difference caused by placing a white disk on the bottom of the tank during the Wash sediment suspensions.

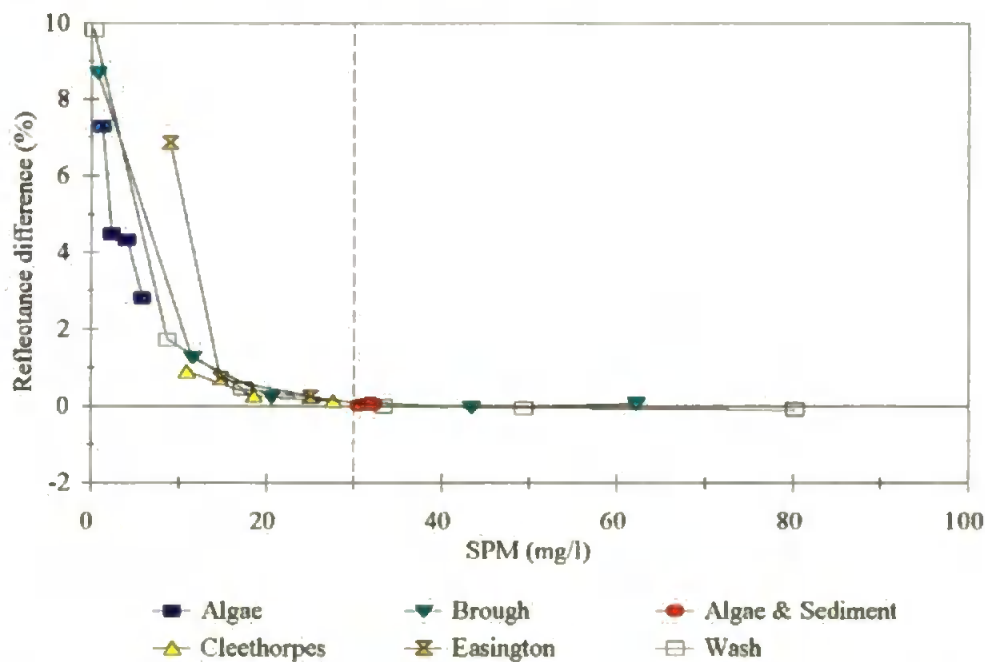


Figure 3-3: The relationship between the reflectance difference (at 600 nm) and sediment concentration, with the dotted line indicating the sediment concentration at which the actual depth exceeds the penetration depth.

representative spectral shape. The average tap water reflectance was then subtracted from each of the averaged concentration spectra.

3.4 Data Analysis

The different sediment types showed increasing reflectance, over the whole spectral range, with an increase in concentration, see Figures 3-4 to 3-7. This agrees with previous research (Bhargava & Mariam, 1991b) and is the result of an increase in backscattering, due to an increase in the number of particles, which is not compensated for by a proportional increase in absorption.

In the visible wavelengths (400 to 700 nm), the different sediment types produced different spectra and levels of calculated reflectance for a suspended sediment concentration of around 20 mg/l, see Figure 3-8. This is explained by the different mineralogy which influences the spectral shape. Over the concentration range used the reflectance values peak between 500 and 700 nm, drop off to a minima at approximately 750 nm, followed by a peak at approximately 800 nm. The first peak, in the visible range, indicates the sediment colour while the second peak in the near infrared wavelength region is the result of a decrease in water absorption (see Figure 2-9).

By comparing the reflectance spectra, from the work of Tocher (1992), for different sediment size fractions it can be seen that the particle size is very important in determining the amount of light reflected (see Figure 3-9). This is because the smaller the particle the greater the surface area to volume ratio and hence scattering ability.

The wavelength of maximum reflectance was determined for all the tank results and plotted against SPM, see Figure 3-10. The results show that there are three data groups. Between 550 nm and 650 nm the maximum wavelength appears to increase with SPM, but the groups at around 700 and 800 nm have a maximum wavelength that is constant with SPM. These latter two groups mainly include samples with an SPM of greater than 170 mg/l, the exceptions are the unfractionated Tamar and Exe sediments. So by using the fine fractions and an SPM range of 0 to 170 mg/l a more robust relationship is achieved, see Figure 3-11.

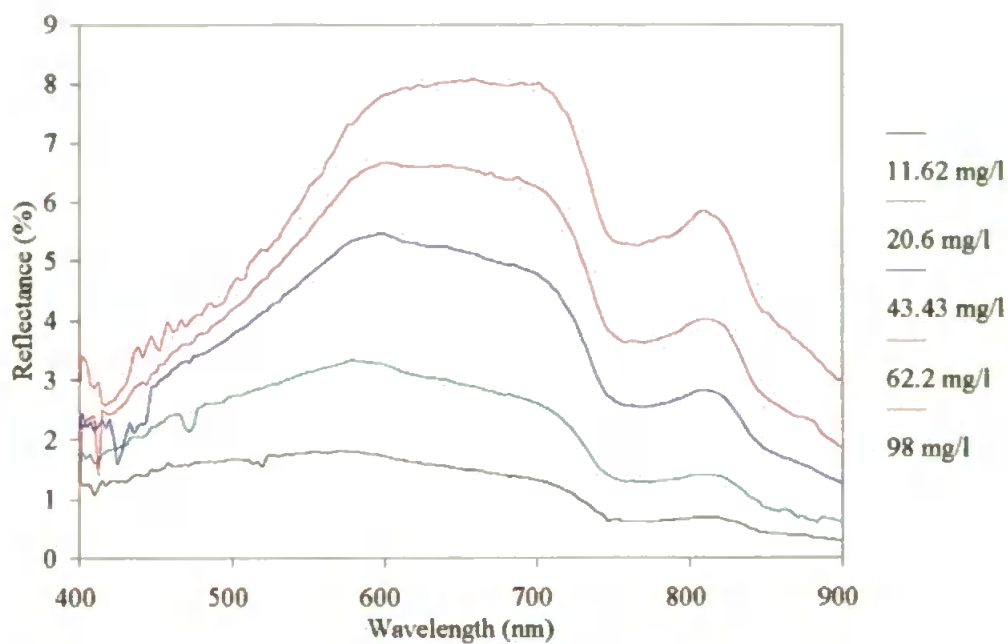


Figure 3-4: Spectral reflectance for different concentrations of Brough sediment.

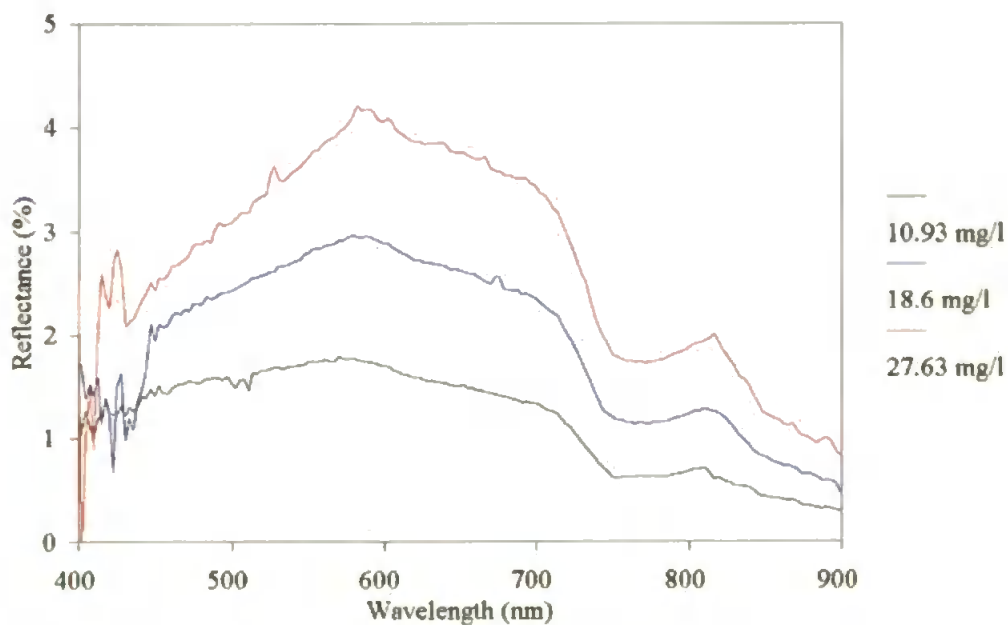


Figure 3-5: Spectral reflectance for different concentration of Cleethorpes sediment.

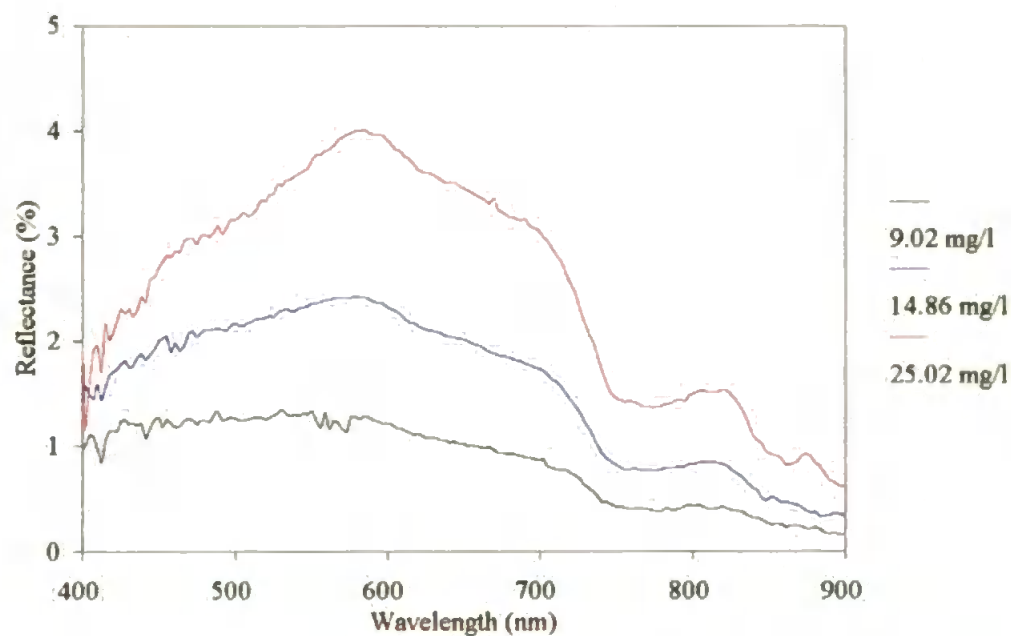


Figure 3-6: Spectral reflectance for different concentration of Easington sediment.

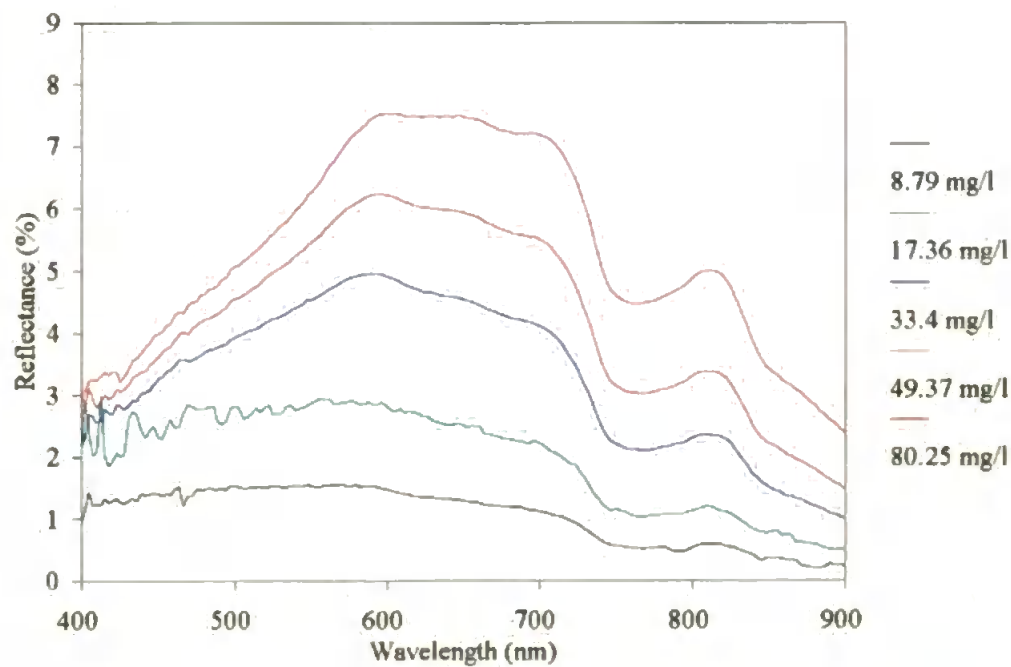


Figure 3-7: Spectral reflectance for different concentrations of Wash sediment.

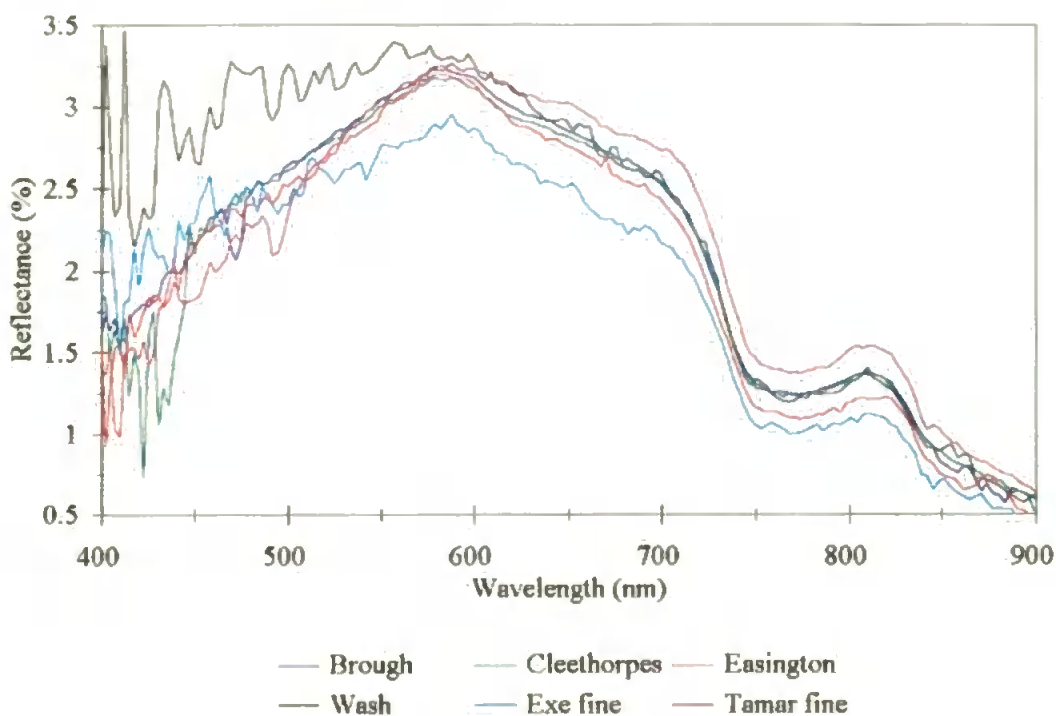


Figure 3-8: A comparison of the calculated reflectance for the fine fraction (less than 10 μm) of the different sediment types at a concentration of 20 mg/l.

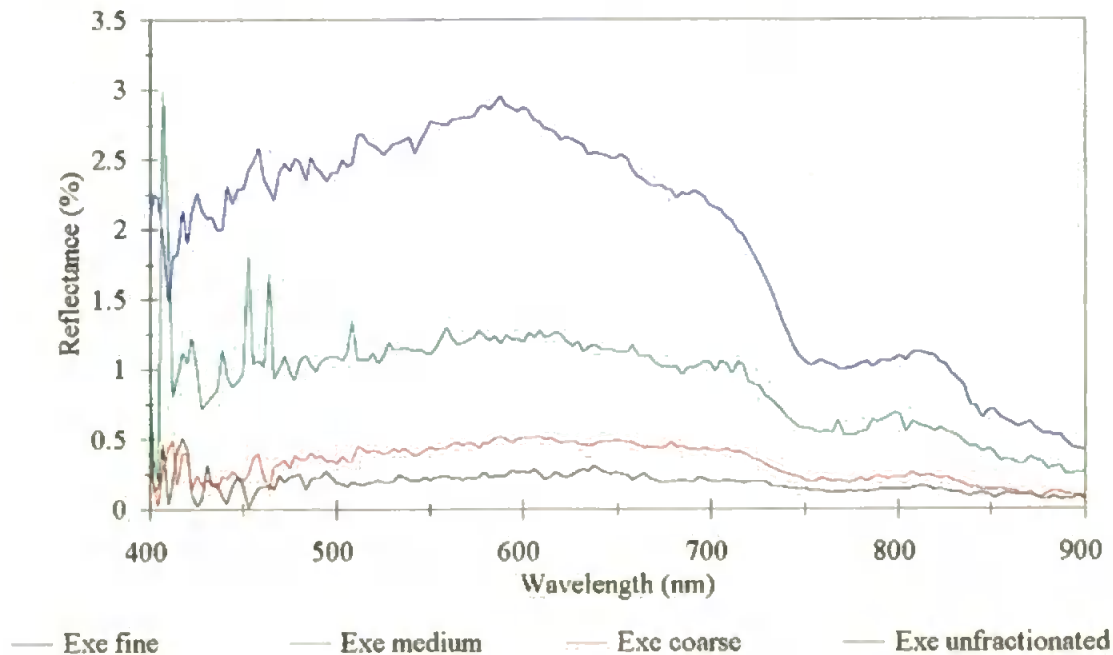


Figure 3-9: A comparison of the calculated reflectance for the different size fractions of the Exe sediment at a concentration of 20 mg/l.

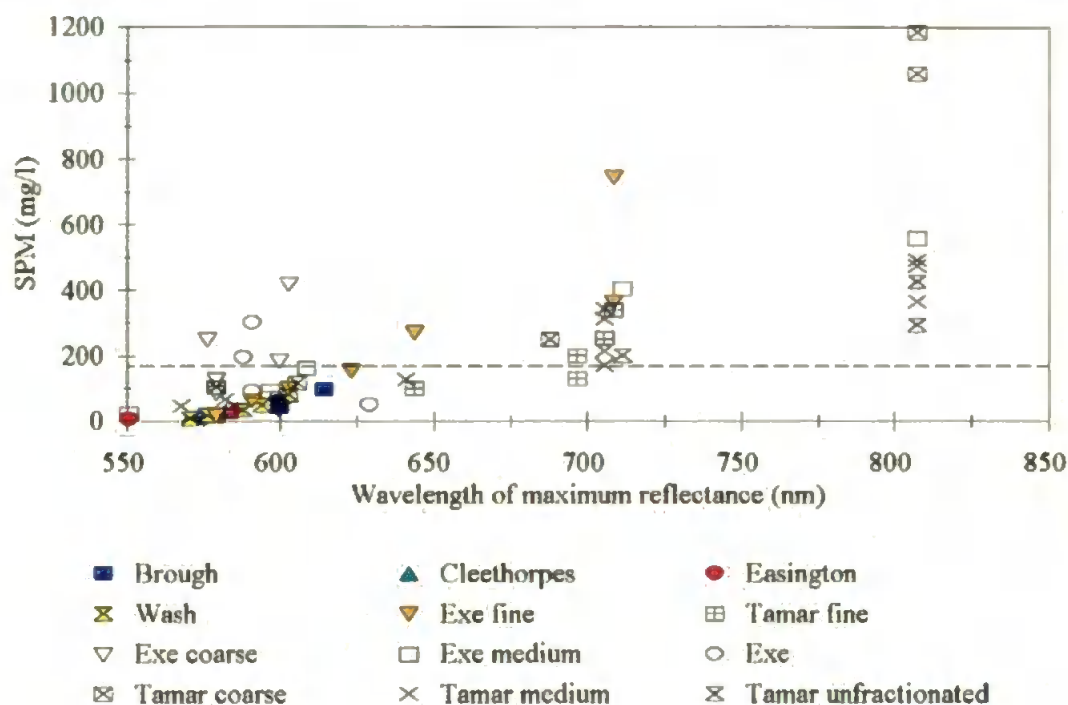


Figure 3-10: The relationship between the wavelength of maximum reflectance and concentration of suspended matter for all the sediment data, with the dotted line indicating the 170 mg/l concentration level.

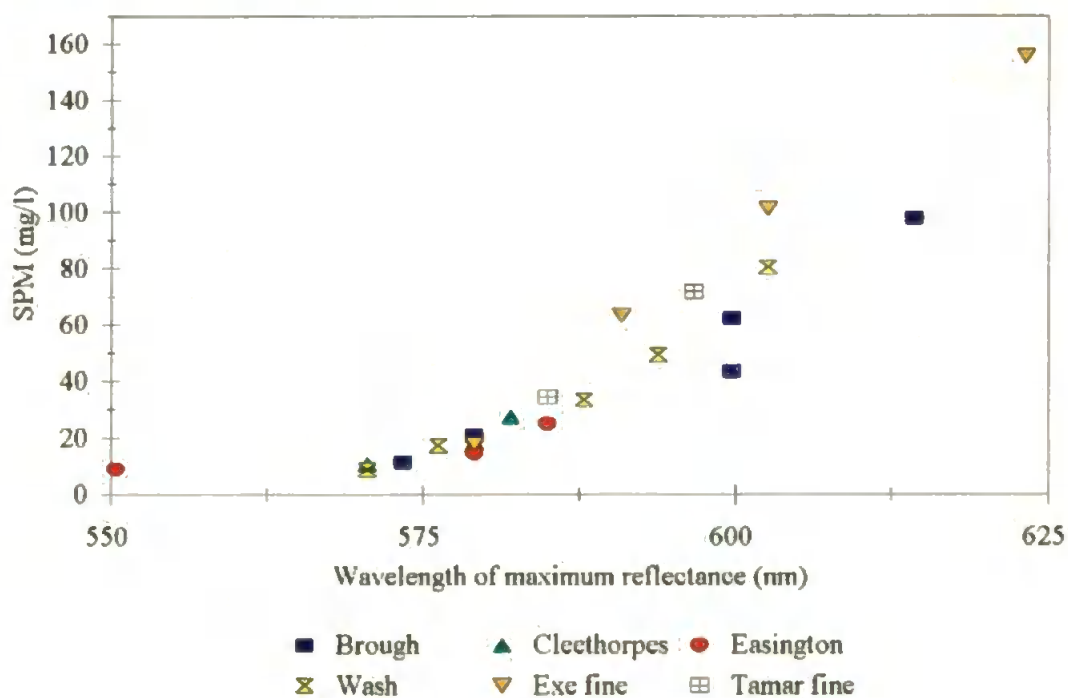


Figure 3-11: The relationship between the wavelength of maximum reflectance and concentration of suspended matter for the fine sediment fraction (less than 10 µm).

The DOC and phytoplankton experiments clearly showed that these constituents affect the signal up to about 700 nm, with both strongly absorbing light especially in the blue region, see Figures 3-12 to 3-14. Similar results were shown by Witte *et al.* (1982), who commented that the addition of humic material produced large decreases between 400 and 720 nm but between 730 and 760 nm there was a negligible effect. This means that above 700 nm only suspended sediment and water influence the reflectance spectra.

In the near infra red region the reflectance signal has a much more robust relationship with the suspended sediment concentration, despite the absolute signal and relative changes being smaller in magnitude than those seen in the visible range, see Figures 3-4 to 3-7. Bhargava & Mariam (1990) also notes the importance of the near infrared signal. Bale *et al.* (1994) replaced the sediment concentration with the target area (Ta), a function of the net cross-sectional area and suspended sediment concentration. The reflectance (at 804 nm), resulting from the different Exe and Tamar size fractions, came together to form a power relationship, see Equation 3-3.

$$Ta = 25.437 * R_{+0}(804)^{1.466} \quad (3-3)$$

3.5 Discussion

The laboratory suspended sediment spectra show there is: increasing reflectance with increasing SPM; decreasing reflectance as the size fraction increases; different sediment types have different spectral shapes in the visible wavelength region.

When DOM and phytoplankton are present, absorption affects the spectra below 700 nm. Therefore the wavelengths above 700 nm (near infrared) are only influenced by suspended sediment and water giving a robust relationship between SPM and reflectance. This disagrees with Choubey & Subramanian (1991), but their research only used two sediment types and four wavebands and so conflicts with the results of Krijgsman (1994) who concluded that the spectra should be measured at a high wavelength resolution as a small number of preset wavebands may be invariant to concentration variations of the mixture.

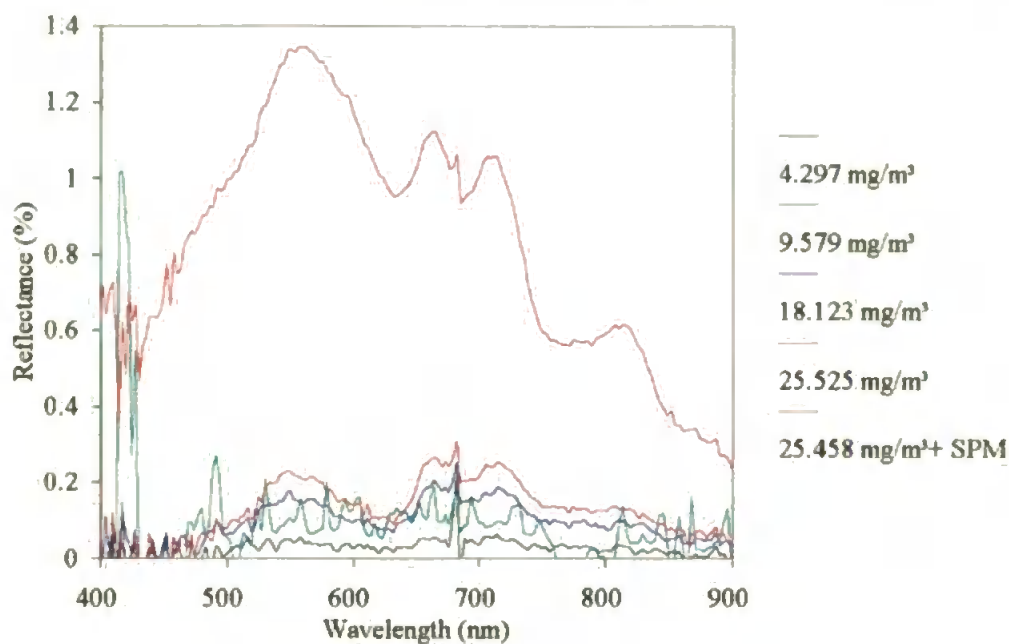


Figure 3-12: Spectral reflectance for different concentrations of phytoplankton with water base.

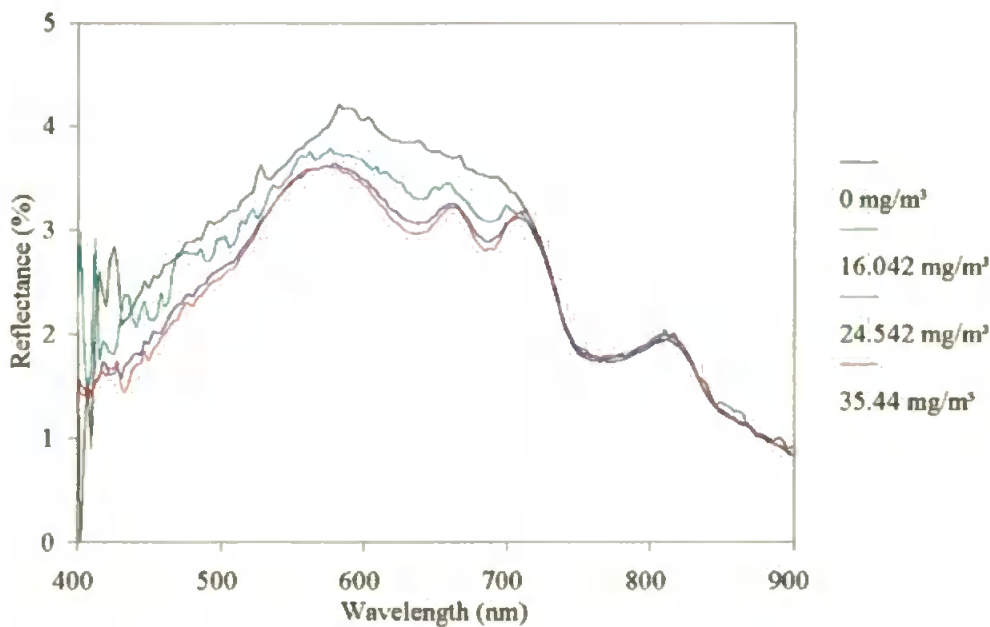


Figure 3-13: The spectral reflectance for different concentrations of phytoplankton with a suspended sediment base.

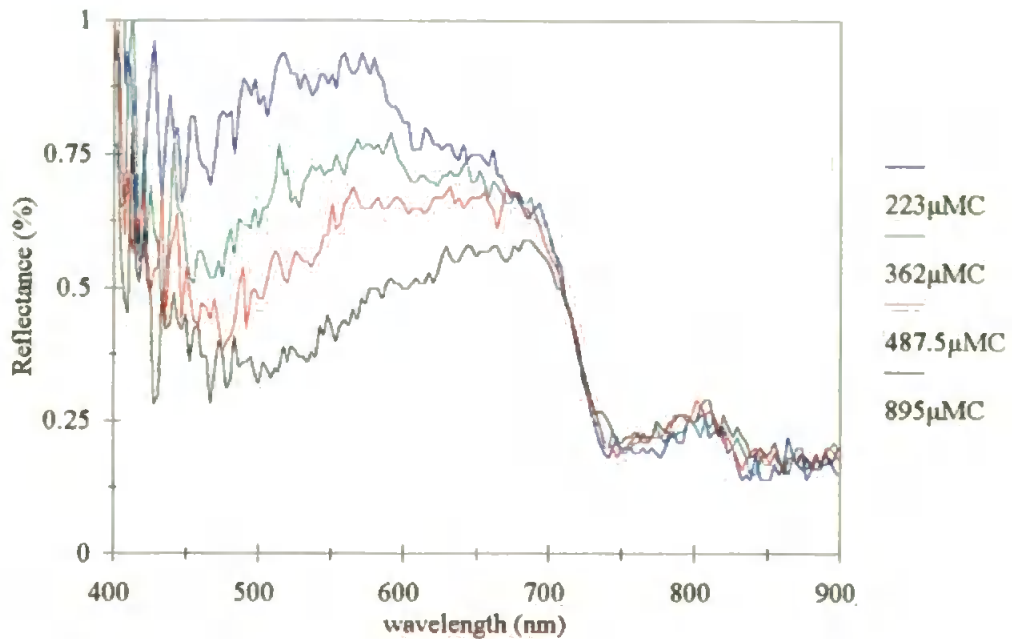


Figure 3-14: Spectral reflectance of different DOM concentrations.

In-situ optical work by Amos & Topliss (1985), showed a peak at around 670 nm in the multispectral irradiance, in response to the suspended lithic material. Both relative and absolute increases in inorganic SPM produced a shift towards longer (red) wavelengths, which was also noted by Collins & Pattiaratchi (1984). Ritchie *et al.* (1976) showed, with surface spectral measurements, that the reflectance maximum was at 550 nm for low SPM concentrations and shifted to 600 nm for higher concentrations. Morel & Prieur (1977) noted that the reflectance curves for Case 2 waters were convex between 400 and 560 nm, with a maximum at 560 nm. The sediment fractions used in this research had a reflectance maxima that increased from 550 to 650 nm with SPM concentration.

4. FIELD EXPERIMENTS

In this chapter the ground data will be calibrated and processed so that it can be compared to the airborne remote sensing imagery (Chapter 6). Section 4.1 describes the fieldwork area and dynamics of the Humber estuary. A description of the three fieldwork experiments and sensors presented in Section 4.2, with the fieldwork protocol in Section 4.3. In Section 4.4 the sensors are calibrated and data processed, with the different instruments being combined and products calculated in Section 4.5. Section 4.6 discusses the fieldwork results and Section 4.7 summarizes the chapter.

4.1 The Geography Of The Humber Coastal Zone

4.1.1 The Holderness Coast

The Holderness coast is 60 km long extending from the sand and shingle spit of Spurn Head in the South to the chalk promontory of Flamborough Head in the North (see Figure 4-1). The coastline consists of rapidly eroding, 10 to 20 m high, Pleistocene glacial till cliffs (Curran *et al.*, 1987). The sand and gravel fractions are the main source of beach materials, whilst the silts and clays are carried offshore as sediment plumes (Pringle, 1985). These plumes appear to move southwards, due to wave action and tidal currents, with the suspended sediment being lost offshore or deposited in the lee of Spurn point (Curran *et al.*, 1987). The eroded material consists of 67% mud and dominates the East Coast sediment flux, with the ratio of cliff to fluvial supply, Humber Estuary and Wash, being 7:1 (McCave, 1987).

4.1.2 The Humber Estuary

The Humber is the largest estuary on the East Coast of England with a total drainage area of around 250 000 km², equal to approximately one fifth of England's land area (Arnett, 1991). The average freshwater flow is 250 m³s⁻¹, more than three times the volume

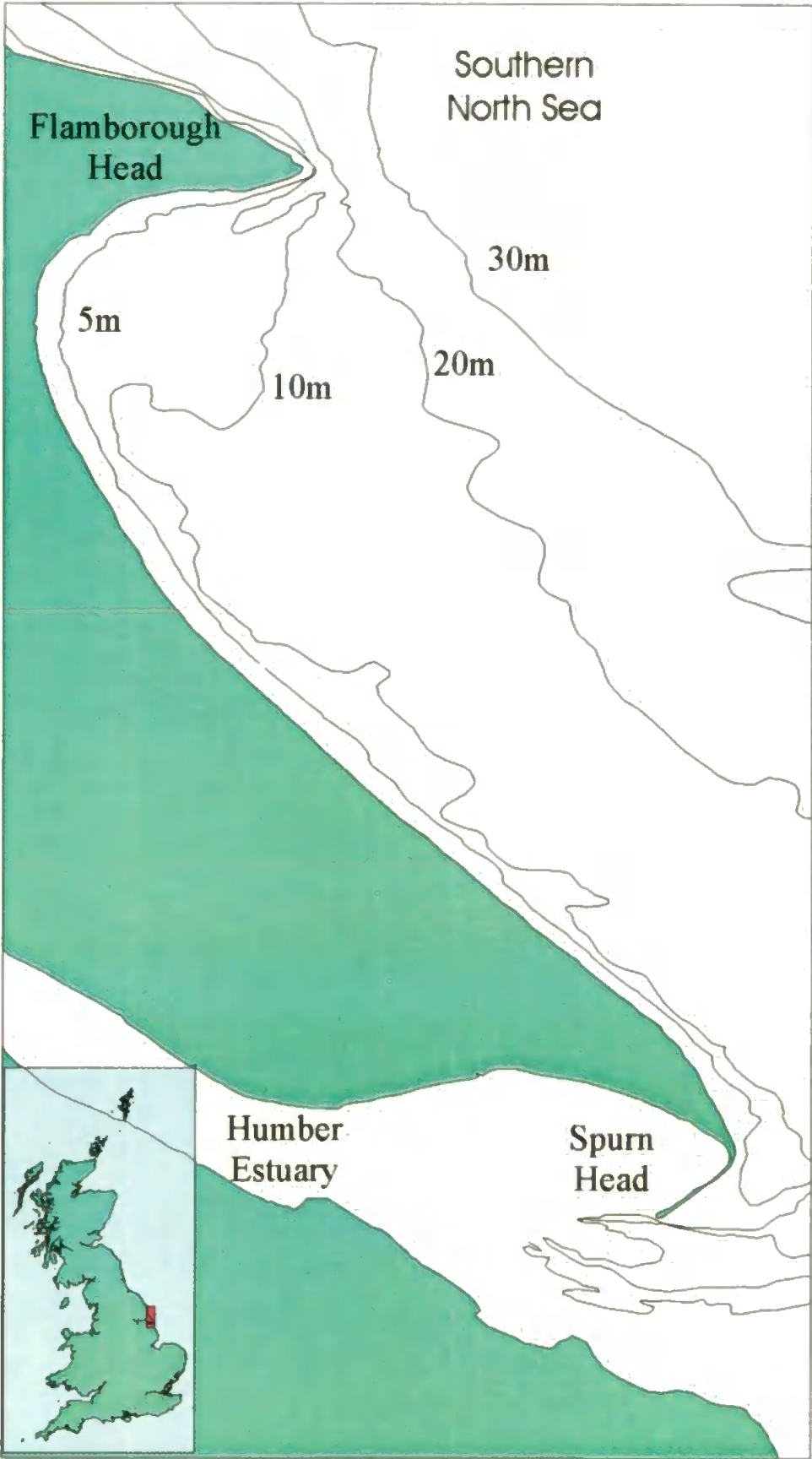


Figure 4-1: The Holderness Coast and Humber Estuary.

discharged by the River Thames (The Quality Of The Humber Estuary, 1993). From Trent Falls, the confluence of the Ouse and Trent, to the mouth at Spurn Point the Humber measures about 62 km and the width increases from 1 to over 8 km (Barr *et al.*, 1990).

The Humber is a macrotidal estuary, with the flood and ebb tides being of approximately equal duration in the outer estuary. As the water flows upstream it becomes increasingly restricted by the narrowing banks, which lengthens the period of the ebb tide (Denman, 1979) and causes an increase in the high water level from the lower to upper estuary. On spring tides the amplitude is over 7 m in range and the current velocities are between 2 and 3 ms⁻¹ (Barr *et al.*, 1990), whilst on neap tides the amplitude is 3 m.

The estuary has a relatively small vertical salinity gradient, with variations of less than 5 ppt (Denman, 1979), and a pronounced longitudinal gradient (Barr *et al.*, 1990). The lower Trent, Aire, Don and Ouse are warmed by the discharge of cooling water causing a significant temperature gradient from upstream to the mouth. The warmest temperatures are usually found during August, frequently co-incident with low river flow (Greenpeace, 1982).

The current velocities on the ebb tide are less than on the flood, and near the bed there is a residual current caused by the vertical mixing of salt/fresh water which can penetrate inland to the Humber bridge (Arnett, 1991). The stronger currents on the flood cause a preferential movement of sediment towards the head of the estuary, due to the current established by the movement of saline water along the bed (The Quality Of The Humber Estuary, 1993). In addition the slack water period at high water is longer than at low water, enabling a greater proportion of material to settle to the bed. So the pollutant inputs, coming from the diverse array of industries along the banks (Arnett, 1991), may move upstream rather than out to sea.

A salinity gradient occurs between the North and South banks, below Immingham, with the Coriolis force causing saltier water to flow inland along the North bank and fresher water to flow seawards along the South bank (Arnett, 1991). This results in well defined salinity/temperature fronts, parallel to and on either side of the estuary. The fronts are marked by an accumulation of foam and floating debris, and a discontinuity in the water colour (caused by differences in the SPM concentration). There is also a well defined

plume, extending out into the North Sea, which has fronts defined by the surface jet of fresher water impinging on the saltier water.

The suspended sediment originates mainly from the North Sea rather than fluvial input, because of tidal asymmetry and a tendency for freshwater to float on the surface causing the fluvial sediment to be transported seaward (The Quality Of The Humber Estuary, 1993). The concentration at a particular point is determined largely by the current velocities. High velocity currents re-suspend the material deposited at slack water causing concentrations to vary by an order of magnitude over a tidal cycle (The Quality Of The Humber Estuary, 1993). There is a vertical stratification with concentrations being greater at the bed, see Figure 4-2.

The residual suspended sediment fluxes are small when compared to the total ebb and flood flux, with the estuary discharging about 100 Kt of fluvial sediment a year (McCave, 1987). Between Kingston Upon Hull (referred to hereafter as Hull) and Grimsby there is a single channel, whilst below Grimsby, at the mouth, the single channel turns into a three channel system.

There is a complex distribution of bottom sediments with deposits becoming finer towards the banks, and coarser sands and gravels occurring in the central channels where stronger currents exist. At high water, when there are small tidal velocities, only the finest material can be transported, creating large areas of mud flats. This is particularly evident in Spurn Bight, which is an area 12 km long and 4 km wide, reached only by the top metre of the flooding tide and not affected by strong tidal currents and waves.

4.2. Field Campaigns

Through collaboration with the National Rivers Authority (NRA), aircraft overflights occurred at the start and end of their August 1993 survey. The fieldwork used the NRA survey vessel 'Sea Vigil', which was moored in Hull Marina and so had access restricted to two hours either side of high water. To best utilize the time available continuous measurements were performed along a track extending from Hull Marina to the Humber

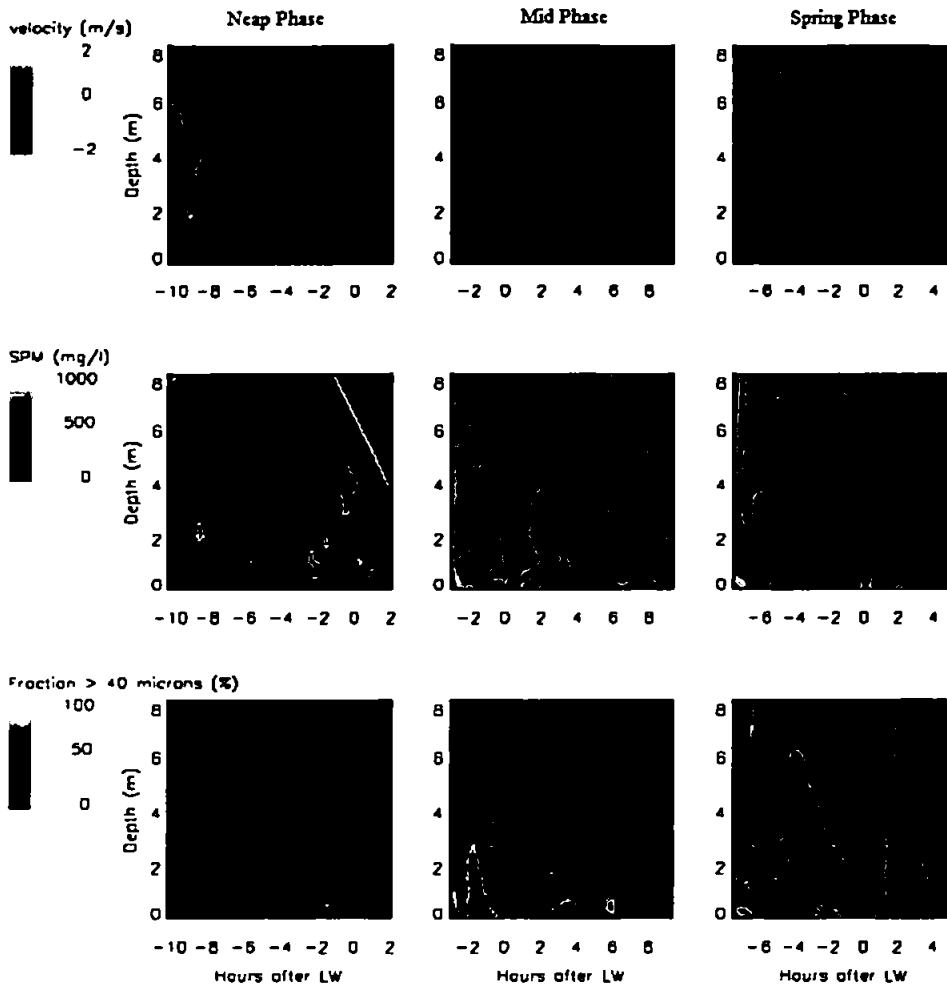


Figure 4-2: Vertical distribution of the current velocities and SPM at Middle Shoal over a tidal cycle in the neap, mid and spring phases (data taken from BTDB, 1978).

Light Float (see Figure 4-3). Vertical light profiling was carried out outside the estuary where the water was much clearer, giving better optical data.

The first fieldwork was not scheduled for overflights, and on the 30th June there was very poor visibility and calm sea conditions. The Undulating Oceanographic Recorder (UOR) was deployed outside the marina and towed a track, at an average depth of 4 m, out to the Humber Light Float (about 10 miles offshore). Vertical optical profiles were measured using the Profiling Reflectance Radiometer (PRR-600), after which the UOR was towed back with two further stops for vertical profiles.

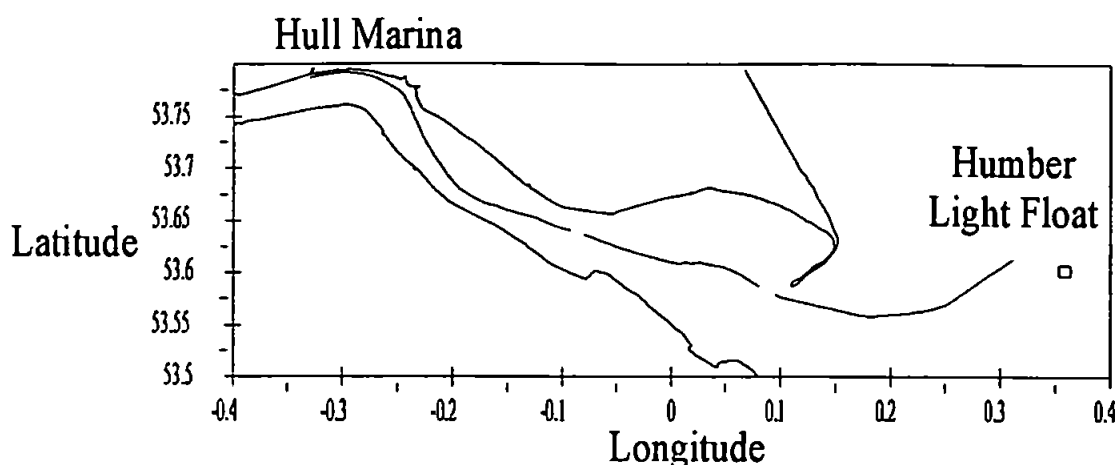


Figure 4-3: Plot of a typical survey vessel track.

For the second fieldwork (4 August), the diving shute was removed from the UOR so that it towed shallower, at a depth of 2 to 3 m. The 4th August began sunny with calm conditions, but in the afternoon (when overflights occurred) there was low cloud preventing flights at 10000 feet. The vessel was positioned under flightline 3 (see Figure 6-1), sampling continuously, during the aircraft overflights.

On the third fieldwork (1 September), the UOR was placed in the water downstream of Hull Marina and was towed out past Spurn Head, at a depth of 2 to 3 m, to a position under the Humber Approaches flightline. The UOR was left in the water while the overflights took place, which gave co-incident PRR and UOR data. Once the overflights had occurred the UOR was towed to and around the Humber Light Float then back to Hull Marina.

4.3. Fieldwork Protocol

Ground truth measurements were obtained using the vessel's water quality monitoring system, a fixed depth UOR and instruments logged using a couple of laptop personal computers (see Table 4-1).

The vessel was equipped to continuously measure in-water parameters using an Aquatracker (placed in a flow-through cell) and separate Turner chlorophyll fluorescence sensor. The Aquatracker measured salinity, temperature, turbidity and dissolved oxygen. However, the dissolved oxygen probe was not calibrated and the data has not been

Table 4-1 : Along track measurements made with the relevant sensor package on each fieldwork

PACKAGE	PARAMETER	FIELDWORK
QUBIT & UOR	Salinity	June, August & September
QUBIT & UOR	Temperature	June, August & September
QUBIT & UOR	Chlorophyll Fluorescence	June, August & September
QUBIT	Position	June, August & September
QUBIT	Nephelometer	August & September
UOR	Transmissometer (blue)	June, August & September
UOR	Short Path Transmissometer	August & September
UOR	Underwater Light Sensors	June, August & September
Laptop + Spectron SE590	Solar Irradiance (Spectra)	June, August & September
Laptop + Biospherics sensor	Solar Irradiance (PAR)	August & September
Laptop + PRR-600	Underwater Light Profiling	June, August & September

processed. The data was logged, together with position and time, using the onboard QUBIT system. The intake pipes were at a depth of about 1 m and situated either side of the boat, with the Turner intake pipe on the starboard side. Calibration bottle samples were taken from the Turner overflow pipe, so correspond well in both depth and time to the continuous system.

The UOR carried salinity, temperature, SPM (blue transmissometer, 490 nm, plus short path transmissometer) and chlorophyll fluorescence sensors together with hemispherical light sensors. This logged every 4 s compared to the QUBIT system which logged every 10 s, resulting in a comparatively noisier UOR trace (see Figures 4-9 to 4-14).

During the fieldwork period samples were taken at 20 minute intervals, with additional sampling during the overflight period. The volumes filtered varied from 400 to 3000 ml depending on the SPM concentration. The filter papers were refrigerated so that the organic matter would not degrade with time.

To supplement the vessel's along track measurements a fixed depth UOR was towed behind the vessel, at an average depth of 2 to 3 m. This instrument measured salinity, temperature, chlorophyll fluorescence, beam transmission (blue), beam transmission (near infra-red) and upwelling/downwelling scalar irradiance in 6 wavebands (see Table 5-1).

Downwelling solar irradiance was measured periodically, over the wavelength spectra from 400 to 900 nm, using the Spectron SE-590 (described in the laboratory experiments, see Chapter 3) and continuously by a PAR sensor. Both sensor heads were placed on the cabin roof to avoid instrument shading by structures on the boat.

The Profiling Reflectance Radiometer (PRR-600) was lowered over the sun facing side of the vessel when the aircraft was overhead, and at other significant sites, in order to calculate the water-leaving radiance. The instrument has 7 downwelling vector irradiance sensors and 7 upwelling radiance sensors (see Table 5-1) plus a depth and temperature sensor. This instrument was designed for ocean deployment so has a 200 m depth range and -5 to 35°C temperature scale, causing digitization limitations in the Humber.

4.4. Calibration

4.4.1. In-Water Constituents

The three data sets (UOR, QUBIT and bottle samples) for each track were numerically merged into one file using the time of day (TOD) variable which has units of decimal hours. This accounted for the different logging rates, the QUBIT logged every 10 s and UOR every 4 s, and the sensor packages not starting at the same time. The QUBIT and UOR timing was checked by comparing the merged salinity values, at the sharp frontal changes, which occurred axially along the estuary. The difference in depth between the two sensors (QUBIT inlet pipe 1 m and UOR 3 to 4 m) did not cause a significant difference in the readings, indicating that the water was vertically homogeneous. As the bottle samples were taken from the Turner overflow and synchronized with the QUBIT clock they were also merged at the correct time points.

Suspended sediment and chlorophyll-*a* concentrations were determined, from the bottle samples, as described in Section 3.3.1. The salinity samples were calibrated against IAPSO standard sea water using a precision salinometer.

The blue wavelength transmissometer (see Table 4-1) was converted from volts to transmission (T) using the factory and in-air values, which remained the same throughout

the three fieldwork experiments. The transmission was then converted to the beam attenuation coefficient (c), using Equation 4-1, where 0.25 m is the path length.

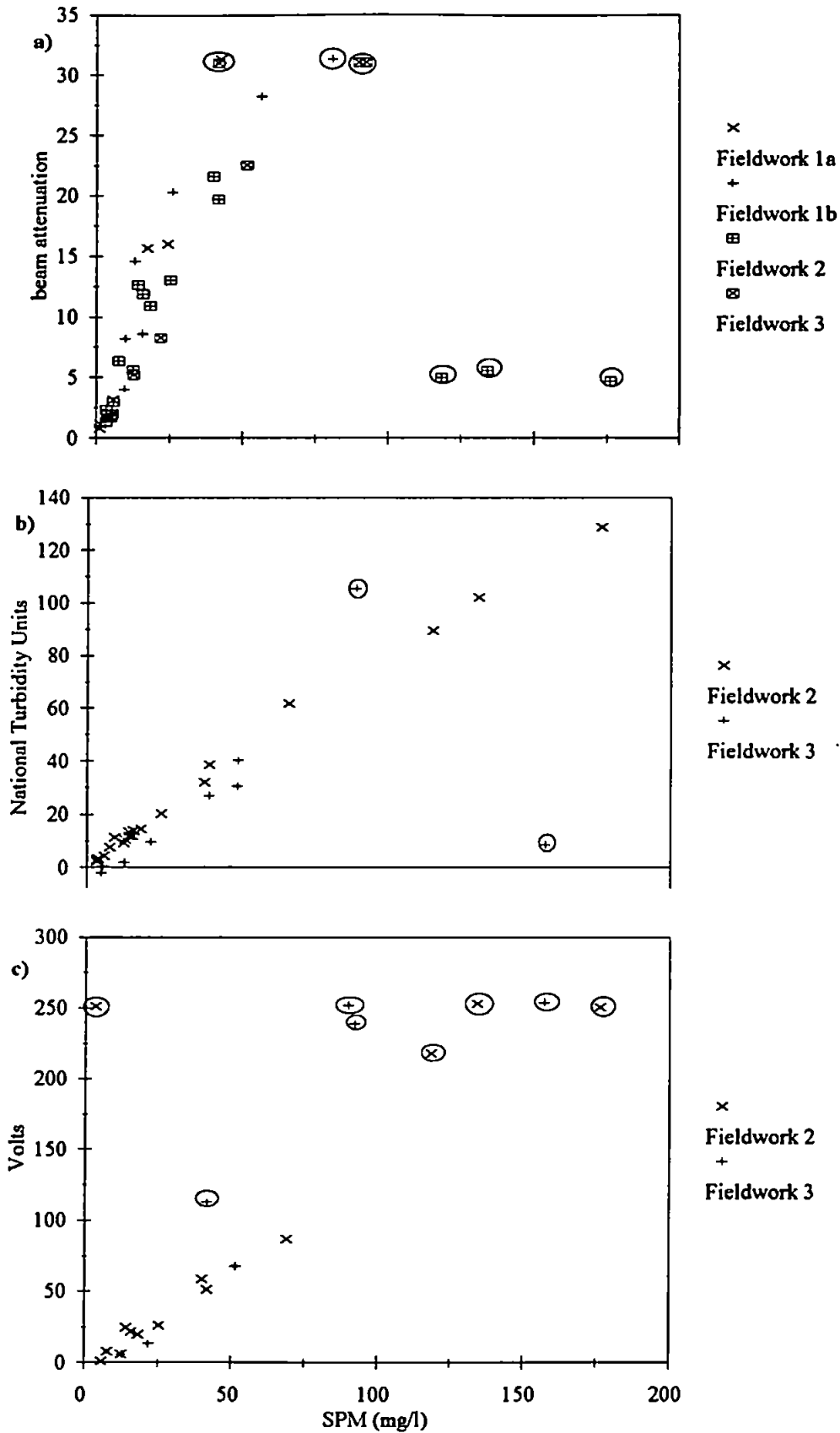
$$c(\lambda) = \frac{-\ln T(\lambda)}{0.25} \quad (4-1)$$

The suspended sediment concentrations, obtained from the bottle samples, were then regressed against the attenuance values, see Figure 4-4a. This was also done for the nephelometer (which had uncalibrated units of NTU) and short path transmissometer (which was in units of volts), see Figures 4-4b and 4-4c. The data sets from the three fieldworks were combined to give a large data set for each instrument, although the nephelometer and short path transmissometer were not used on the first fieldwork. It can be seen that both transmissometers saturated above about 75 mg/l giving a constant sensor reading with increasing concentrations beyond this, see Figures 4-4a and 4-4c. Data points above the sensors saturation level or significantly different from the general trend were excluded from the regression (circled in Figure 4-4) as they would have significantly altered the calibration equations. The linear regression equations (given in Table 4-2) were applied to the underway data to obtain a continuous measurement of SPM.

Table 4-2: Linear regression equations for the suspended sediment calibrations.

	x-coefficient	constant	r^2
Blue Transmissometer	1.85578	-0.76818	0.974
Nephelometer	1.313585	0.231163	0.985
Short Path Transmissometer	0.68168	5.491038	0.955

The chlorophyll fluorescence measurements were linearly regressed against the bottle samples to convert the data to the concentration of chlorophyll-*a*, see Figure 4-5. This was done separately for each fieldwork, as the first fieldwork had much higher phytoplankton levels and the sensor sensitivity was adjusted to reduce noise after the first fieldwork. The June UOR chlorophyll fluorescence data produced a very good regression, but the August and September data was much poorer. This difference resulted from the smaller chlorophyll-*a* concentrations and a degradation of the bottle samples, with both data sets showing high levels of breakdown pigments (see Table 4-3). So the global calibration (derived from previous research) was used for August and September. The



Turner system produced very poor regressions, because the UOR system has optical filters to remove the effects of sediment and DOM.

Table 4-3: Linear regression equations for the chlorophyll-*a* calibrations.

	x-coefficient	constant	r^2
UOR fluorescence sensor (First Fieldwork)	0.017	2.299	0.937
UOR fluorescence sensor (2nd and 3rd)	-0.00639	0.64259	0.393
Global Calibration	-0.03104	1.15	

The salinity samples compared very well with both the UOR and QUBIT sensor systems, see Figure 4-6, and so the original values were consequently uncorrected (see Table 4-4).

Table 4-4: Linear regression equations for the salinity calibrations.

	x-coefficient	constant	r^2
UOR sensor (All Fieldworks)	1.01587	-0.51605	0.997
QUBIT sensor (All Fieldworks)	1.033031	-0.68101	0.996

4.4.1. Light Sensors

The UOR 2π -collectors, 6 upwelling and downwelling, were calibrated both spectrally and radiometrically at Plymouth Marine Laboratory (PML). Readings were obtained at several distances from a standard intensity calibrated lamp for each 2π -collector. A best fit of Equation 4-2 was applied to the data, E_{su} , to determine the calibration coefficients. The constants A & B are non-linearity corrections, C is determined by the sensor sensitivity and D is the slope of the line.

$$E_s = \log(A + B \cdot \log(E_{su})) + \exp(C + D \cdot \log(E_{su})) \quad (4-2)$$

The spectral calibration was performed with a spectrometer, giving the middle wavelength and half width maximum (see Table 5-1).

The Spectron (SE-590) was calibrated by the NERC Equipment Pool for Field Spectroscopy (EPFS). The PRR-600 had been recently acquired and so the manufacturer's calibration was relied upon. The PAR sensor was relatively calibrated to the Spectron (SE-590) as it was used to determine changes in the downwelling solar irradiance.

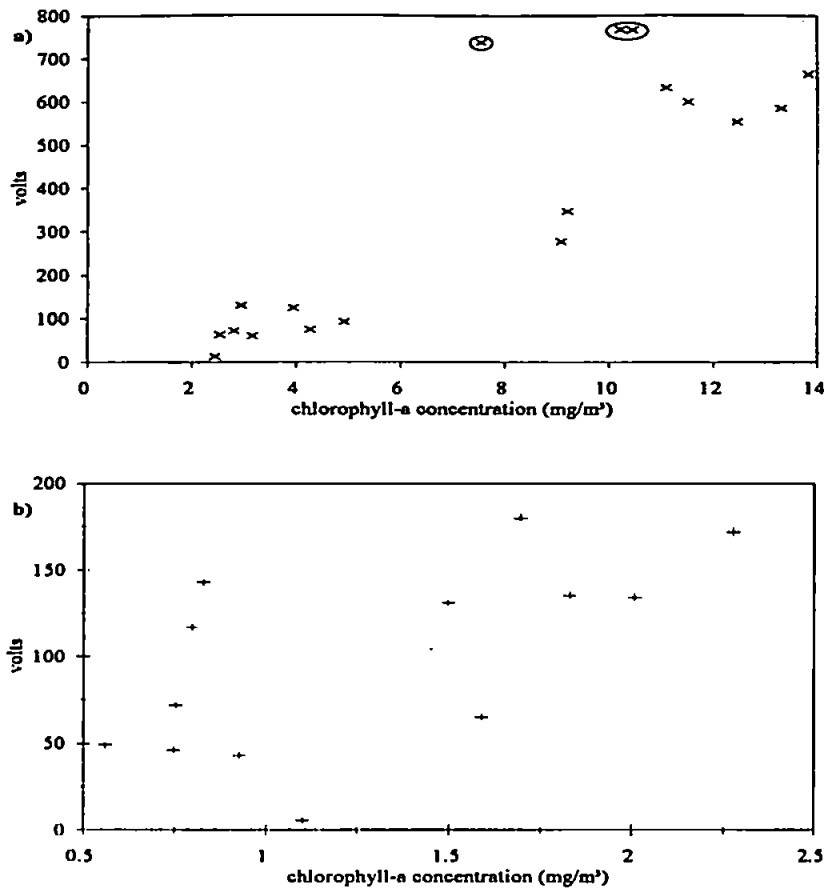


Figure 4-5: The calibrations of chlorophyll-*a* for a) fieldwork 1 and b) combined fieldwork 2 and 3, with the circled data points being excluded from the regression.

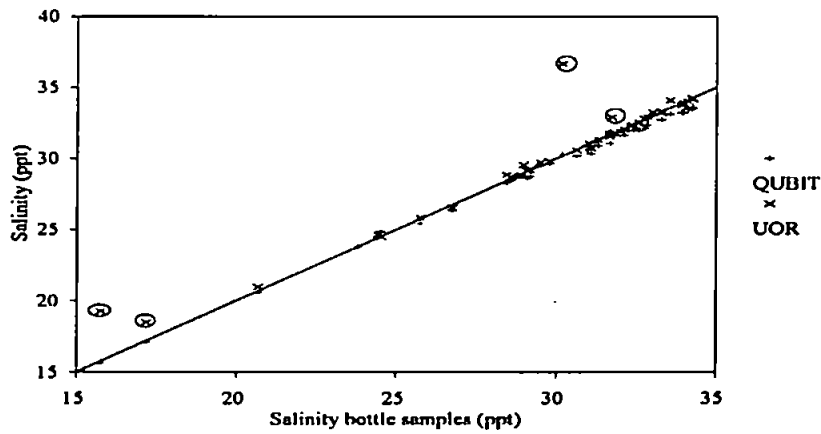


Figure 4-6: Calibration graph for salinity. Circled data points are excluded from the regression and the straight line represents x equal to y .

4.5. Ground Data Processing

4.5.1. QUBIT and UOR

All the cruise tracks proceeded axially along the estuary from Hull to Spurn Head, and then turned north east and headed out towards the Humber light buoy, see Figure 4-3. Track 1 was in the outward direction, from the estuary to the buoy and track 2 occurred on the return journey.

Table 4-5: Vessel tracks during the three fieldwork periods.

Date (Track)	Start Time (\pm LW Spurn)	Start Position	End Time (\pm LW Spurn)	End Position
30/06/93 (1)	05:11 (-3.54)	53.726 0.346	09:01 (+0.28)	53.606 0.362
30/06/93 (2)	10:10 (+1.44)	53.506 0.320	14:10 (+5.43)	53.735 -0.332
04/08/93 (1)	08:23 (-5.44)	53.692 -0.232	11:02 (-2.79)	53.598 0.328
04/08/93 (2)	12:18 (-1.52)	53.605 0.328	13:25 (-0.40)	53.623 0.177
01/09/93 (1)	09:58 (-2.91)	53.675 -0.218	12:38 (-0.23)	53.572 0.242
01/09/93 (2)	13:35 (+0.72)	53.567 0.240	17:26 (+4.57)	53.620 -0.265

4.5.2. Profiling Reflectance Radiometer (PRR-600)

In this research a similar method was adopted to that of Hamilton *et al.* (1993). In that work, with Biospherical Instruments MER-1048 profiling radiometer, the data were binned to 1 m depth averages and corrected for ship shadow and other artifacts. Ship effects were defined as a deviation in the upper 10 to 20 m of the optical profile not correlated with a change in the chlorophyll-*a* concentration or beam attenuation coefficient. These included ship shadow (light intensities lower than expected) or ship reflectance (light intensities greater than expected), and at stations where effects were identified the upper portion of the profile was replaced with the extrapolated curve derived from the lower unaffected portion.

Some optical casts were smoothed to remove intensity variations caused by: wave focusing; the ship's motion; instrument tilt and roll. Wave focusing occurs with the convex part focusing the downwelling light and the concave part de-focusing the light, but the upwelling light remains unaffected (Kirk, 1994). Clouds affect both the upwelling and downwelling light in the whole profile.

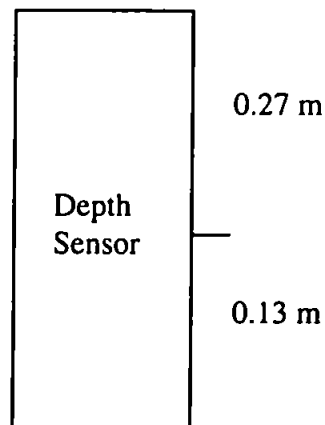
In the research of Hamilton *et al.* (1993), each spectral channel was corrected individually using interactive software, and no corrections were made to channels that did not possess clear artifacts. The diffuse attenuation coefficients were used to propagate the shallowest upwelling irradiance measurements to the surface, after which they were converted to water-leaving radiance using Equation 4-3 (Hamilton *et al.*, 1993).

$$L_w(\lambda) = (0.98/1.79) * L_u(\lambda, 0-) \quad (4-3)$$

The data files were exported from the PRR-READ program (Biospherical Instruments) in comma separated form and then imported into a spreadsheet (Quattro Pro). Extra columns were included to calculate the actual depths of the upwelling and downwelling sensor heads, see Figure 4-7. The downward and upward parts of the cast were separated at the lowest recorded depth, and the downward cast was sorted for depth. The above-surface data were then removed.

Two groups of light data values were selected, for each wavelength, with each group having the same depth and similar light levels. The negative gradient, of the line joining the logarithm of the two resulting average values, was the diffuse attenuation coefficient for the downwelling irradiance sensors (see Equation 2-24) and the beam attenuation

Downwelling Light Sensors



Upwelling Light Sensors

Figure 4-7: Side view of the PRR-600 indicating the depth offsets.

coefficient for the upwelling radiance sensors. These attenuation coefficients were used to extrapolate the shallowest light data values to the surface, and the water-leaving radiance was calculated using two methods:

- 1) Multiply the sub-surface upwelling radiance by a factor of 0.547 (see Equation 4-20).
- 2) Calculate the sub-surface reflectance, using Equation 2-12, and multiply by 0.529 (see Equation 2-76) to get the above-surface reflectance. Then calculate the water-leaving radiance by multiplying the above-surface reflectance by the downwelling solar irradiance (from the Spectron) and dividing by π , a re-arrangement of Equation 2-12.

4.5.3 Calculation of the K_d 's

Underway measurements of K_d were made by comparing the normalized downwelling above-surface PAR, $E_{od}(\lambda, z)^*$, adjusted for the air-water interface, with the normalized UOR downwelling scalar irradiance, $^oE_{od}^*$, at a fixed depth according to Equation 4-4.

$$K_d(\lambda) = -1 \cdot \left[\frac{(E_{od}(\lambda, z)^* - ^oE_{od}^*)}{z} \right] \quad (4-4)$$

During the September overflights, when the UOR was just below the surface (about 7 cm), the PAR and UOR sensors were normalized by dividing the measured value by the average measurement taken over a 36 minute period.

Figure 4-8a shows the September track 1 values for the short path transmissometer derived SPM, $K_d(550)$ and $K_d(632)$ sensors. Figure 4-8b shows an expansion of the steep gradient at the edge of the plume. $K_d(632)$ provides data when the short path transmissometer is saturated, although its relationship to SPM may no longer be linear, whereas $K_d(550)$ is only measurable from about 0.15° Longitude onwards (outside of the estuary mouth) when the SPM concentration is less than about 160 mg/l.

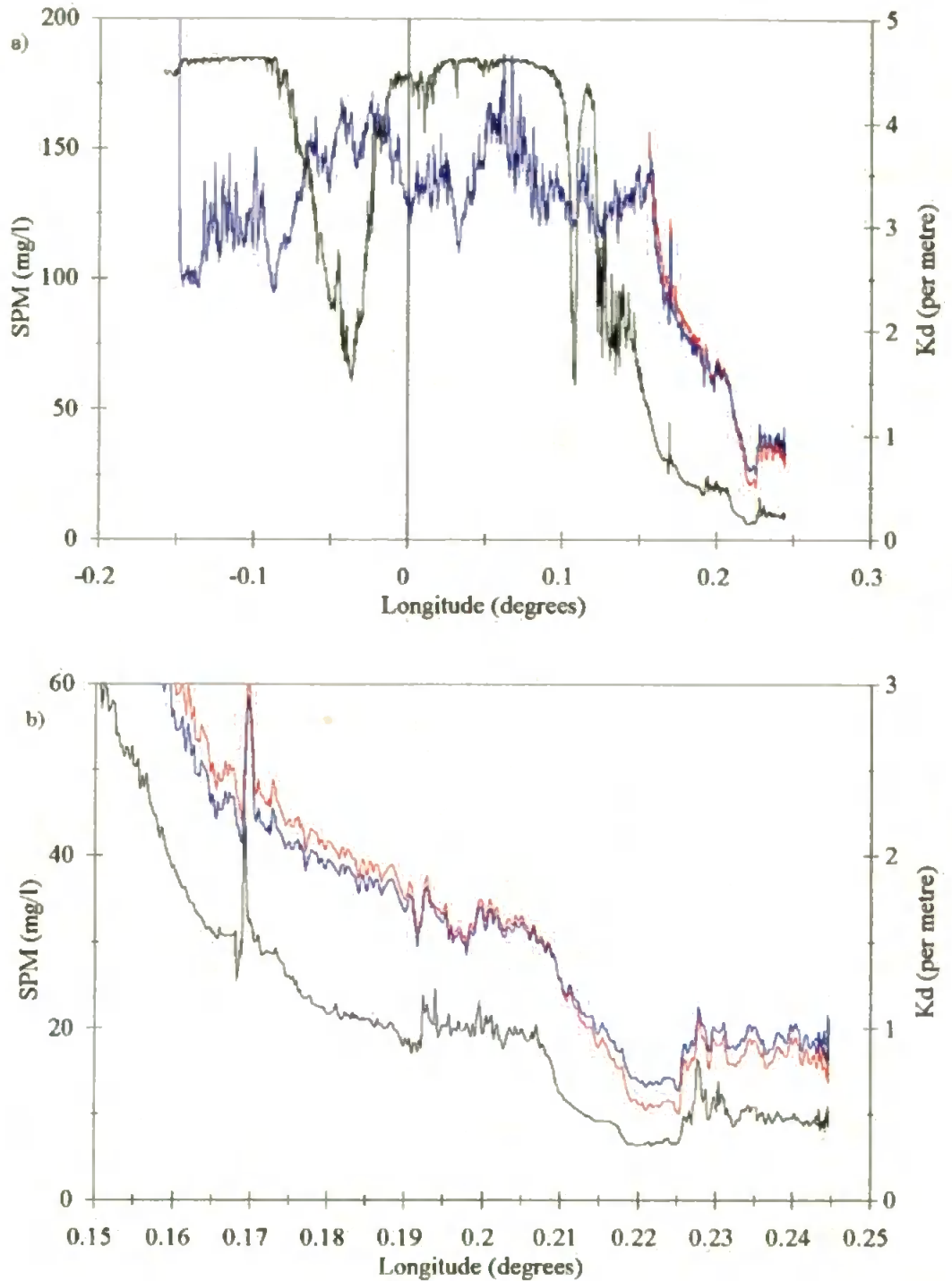


Figure 4-8: Plot of SPM (black line), $K_d[550]$ (red line) and $K_d[632]$ (blue line) for a) the whole and b) the plume region of September 1st Track 1.

4.6 Results

4.6.1 Comparison Of Different Sensors For Each Track

During the June fieldwork the UOR salinity data was relatively higher than the QUBIT data, but for the August and September fieldwork it was lower. This was not due to a change in the temperature offset as the UOR temperature readings were always relatively lower than the QUBIT readings. Thus it was probably due to the relative depth of the readings, as the QUBIT inlet pipe was at 1 m while the UOR was deeper than this in June, but at around the same depth in August and September. The salinity samples, taken from the Turner overflow pipe compared well to the QUBIT, which could again indicate the different depths of the two sensors being the cause of the difference.

1) June

Track 1 started three and a half hours before and ended half an hour after low water (LW), see Table 4-5. There was a strong temperature front (at approximately 0.23 degrees of longitude) in both the UOR and QUBIT trace, see Figure 4-9b. After the front the decrease became more rapid, indicating that this is a front within the temperature plume. The salinity graph (Figure 4-9a) does not show such a sharp change in gradient at the front.

Track 2 represents the return tow from the Humber Light Buoy back to Hull, beginning a third of the way through LW and ending just before high water (HW), see Table 4-5. The temperature graph (Figure 4-10b) shows many features, but not a single distinct front as in track 1. However, the expanded scale of the salinity trace (Figure 4-10a) highlights a front within the estuary, at approximately -0.25 degrees of longitude.

The UOR had a transmissometer (490 nm) and the QUBIT system a nephelometer (see Table 4-1). Initially, the nephelometer experienced stability problems and was adjusted at 5.386 GMT, after which valid data was obtained (start of the SPM plot in Figure 4-9d). The nephelometer also had a lack of sensitivity at low suspended sediment concentrations, due to the reliance on particle backscatter (see track 1 after 0.1 degrees of longitude). During track 2 problems occurred at longitudes of less than -0.1 degrees.

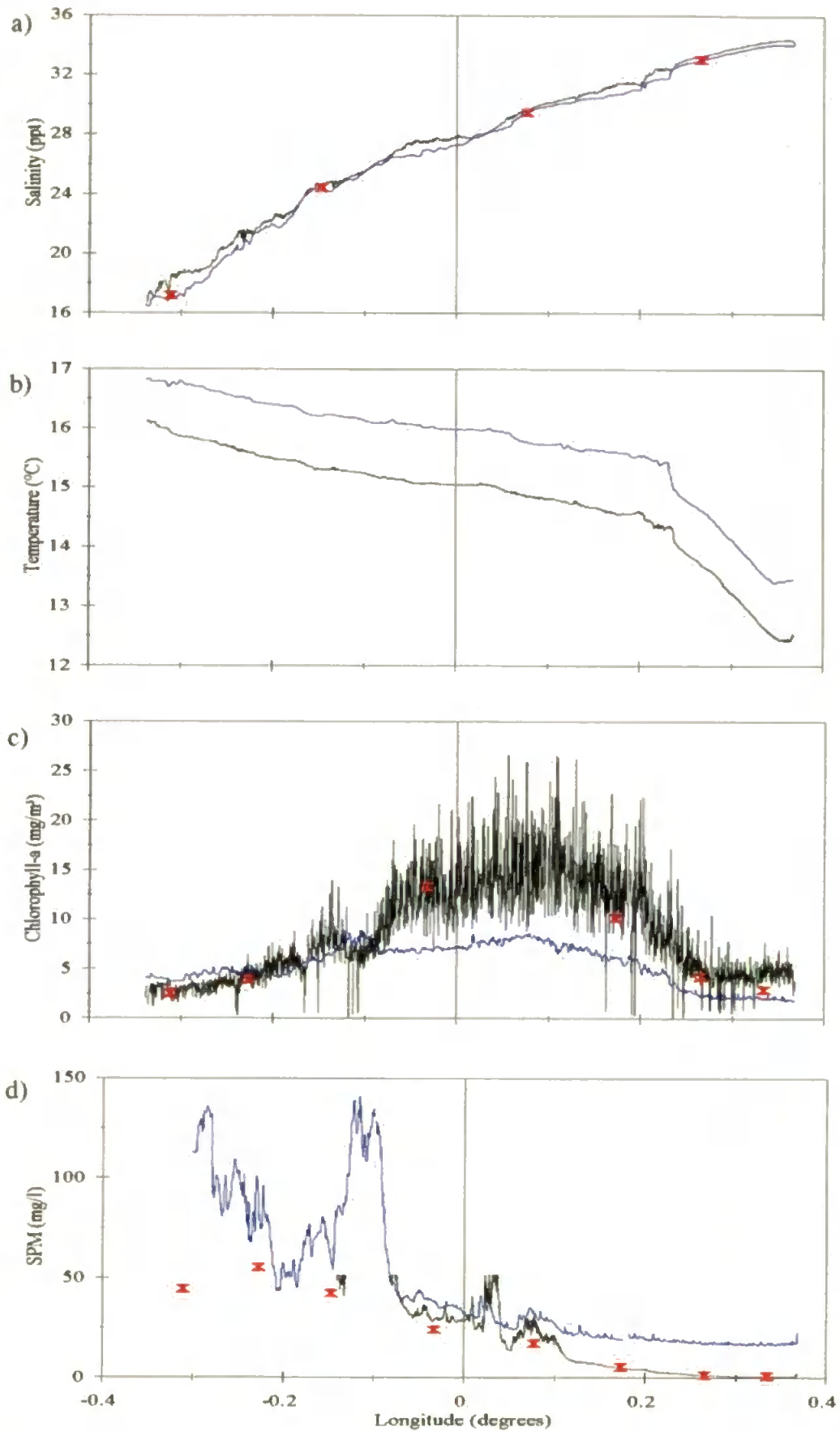


Figure 4-9: Humber Estuary continuous data for June 30th Track 1. Blue lines represent QUBIT data, black lines UOR data and red symbols bottle samples.

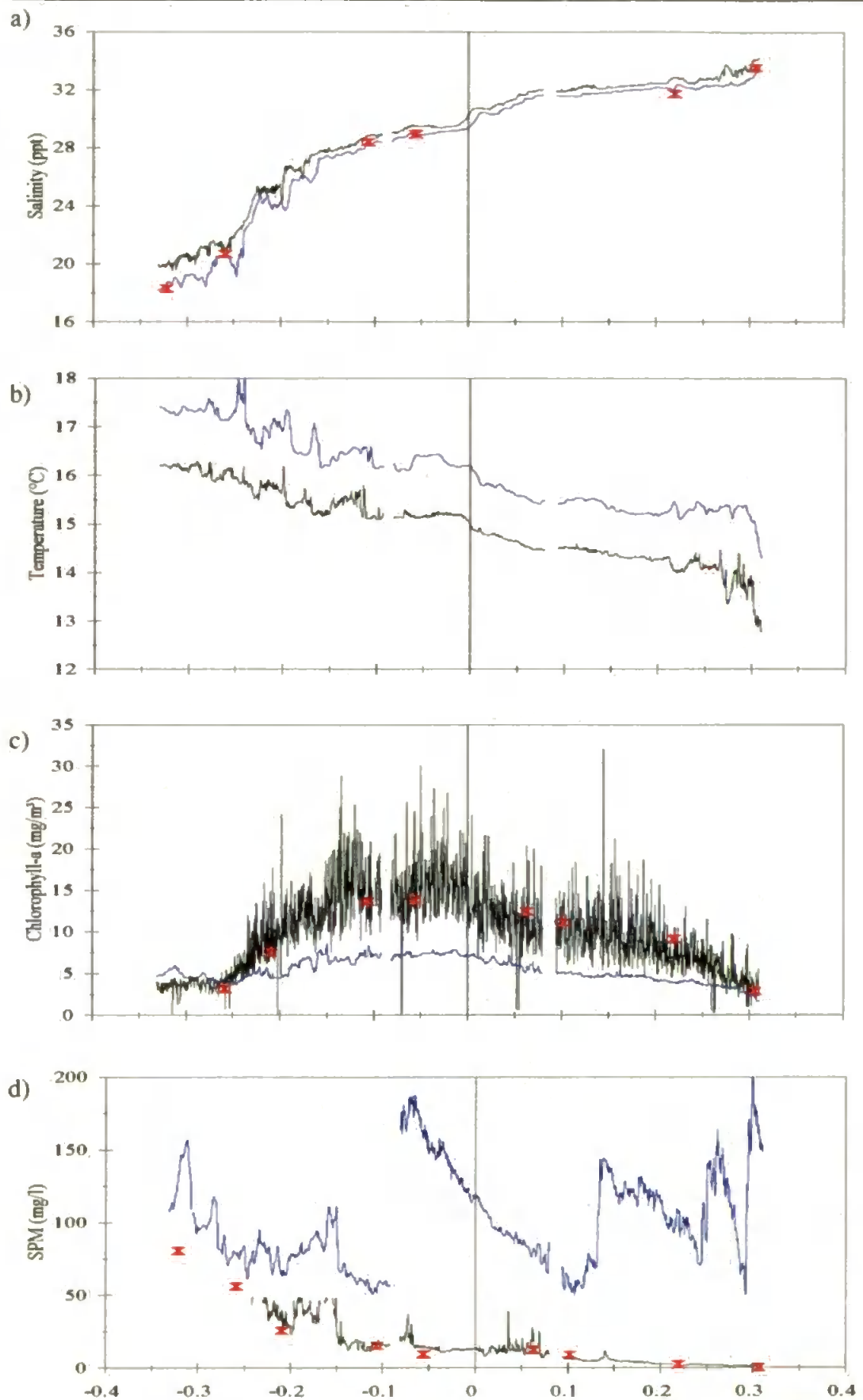


Figure 4-10: Humber Estuary continuous data for June 30th Track 2. Blue lines represent QUBIT data, black lines UOR data and red symbols bottle samples.

During track 1, the estuary was very turbid, causing the transmissometer to saturate at concentrations of greater than 50 mg/l until approximately -0.10 degrees of longitude (at the mouth of the estuary), when the nephelometer showed a sharp drop in suspended sediment concentration (Figure 4-9d). The trace shows several strong sediment structures until approximately 0.1 degrees of longitude, just before Spurn Head, after which there was a steady decrease. The chlorophyll sensors showed a pronounced phytoplankton bloom (predominantly *Phaeocystis*) in track 1 and 2, which was spread out by the tide in the intervening period (see Figures 4-9c and 4-10c).

2) August

The UOR towed shallower than in June (generally less than 1 m). During track 1 the temperature trace, between 0 and 0.25 degrees of longitude, shows a different water mass to that on either side (see Figure 4-11b). This change was also reflected by the salinity (Figure 4-11a) and SPM (Figure 4-11d), and is consistent with observations indicating that the vessel entered a more turbid body of water bordered by fronts with associated foam lines. There was no phytoplankton bloom, as in June, although the QUBIT system trace showed peaks which are in response to changes in SPM (see Figure 4-11c).

Track 1 also shows that the UOR and QUBIT salinity values are very similar until the front, at 0 degrees of longitude, after which the UOR reads lower (i.e. less saline water). This indicates that the UOR was shallower than the effective QUBIT depth and the less vertically homogeneous water. The temperature trace for the UOR was consistently lower (i.e. cooler water), and had a smaller difference after 0 degrees of longitude.

Track 2 covers the period while waiting for the overflights, during which time the vessel drifted in a westerly direction i.e. landwards. A particularly strong frontal structure was crossed at 0.2 degrees of longitude which shows up as: a drop in salinity (Figure 4-12a); a rise in temperature (Figure 4-12b); a rise in SPM (Figure 4-12d).

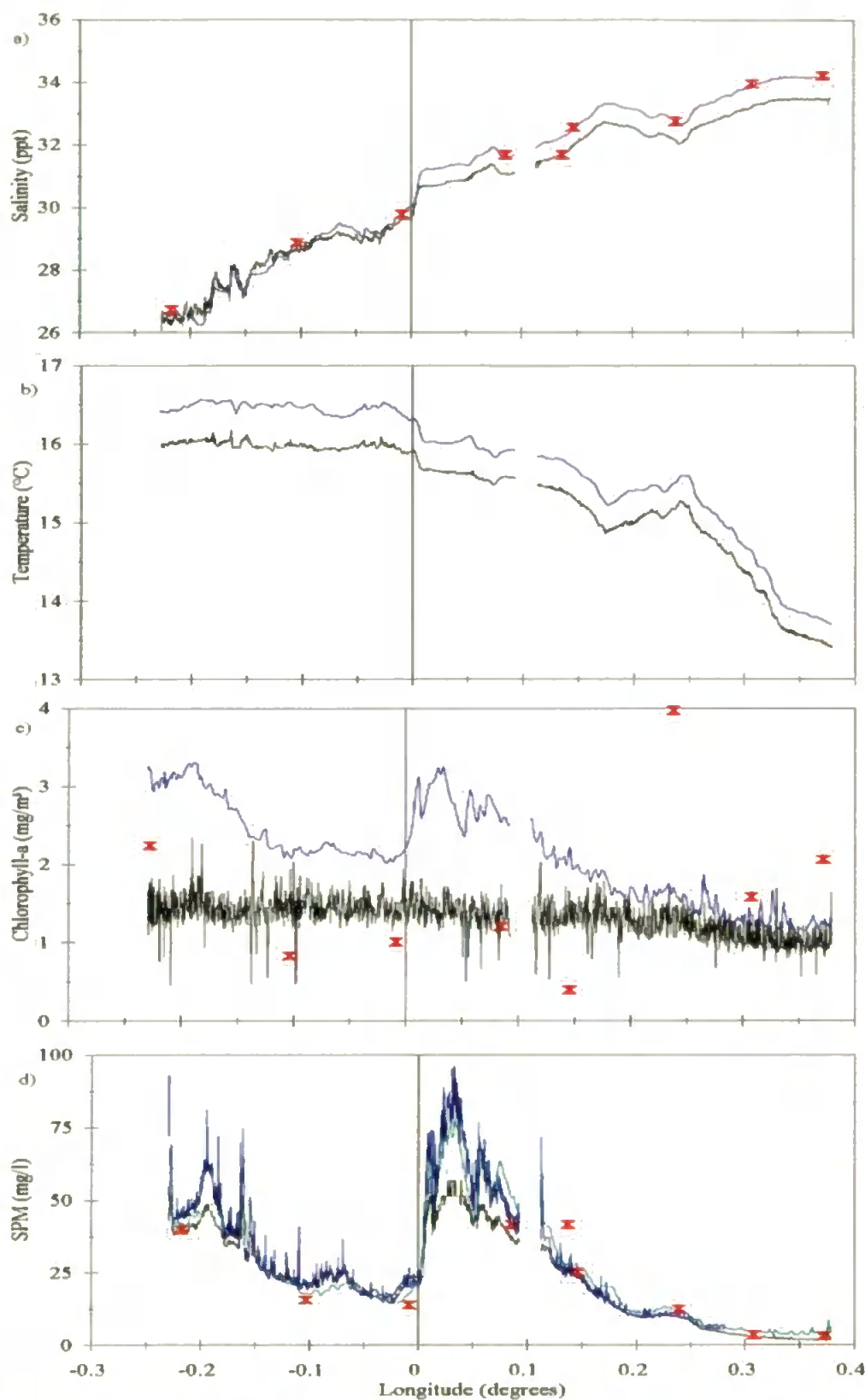


Figure 4-11: Humber estuary continuous data for August 4th Track 1. Blue lines represent QUBIT data, black lines UOR (except SPM where black is the 490 nm and green the short path transmissometer) and red symbols the bottle samples.

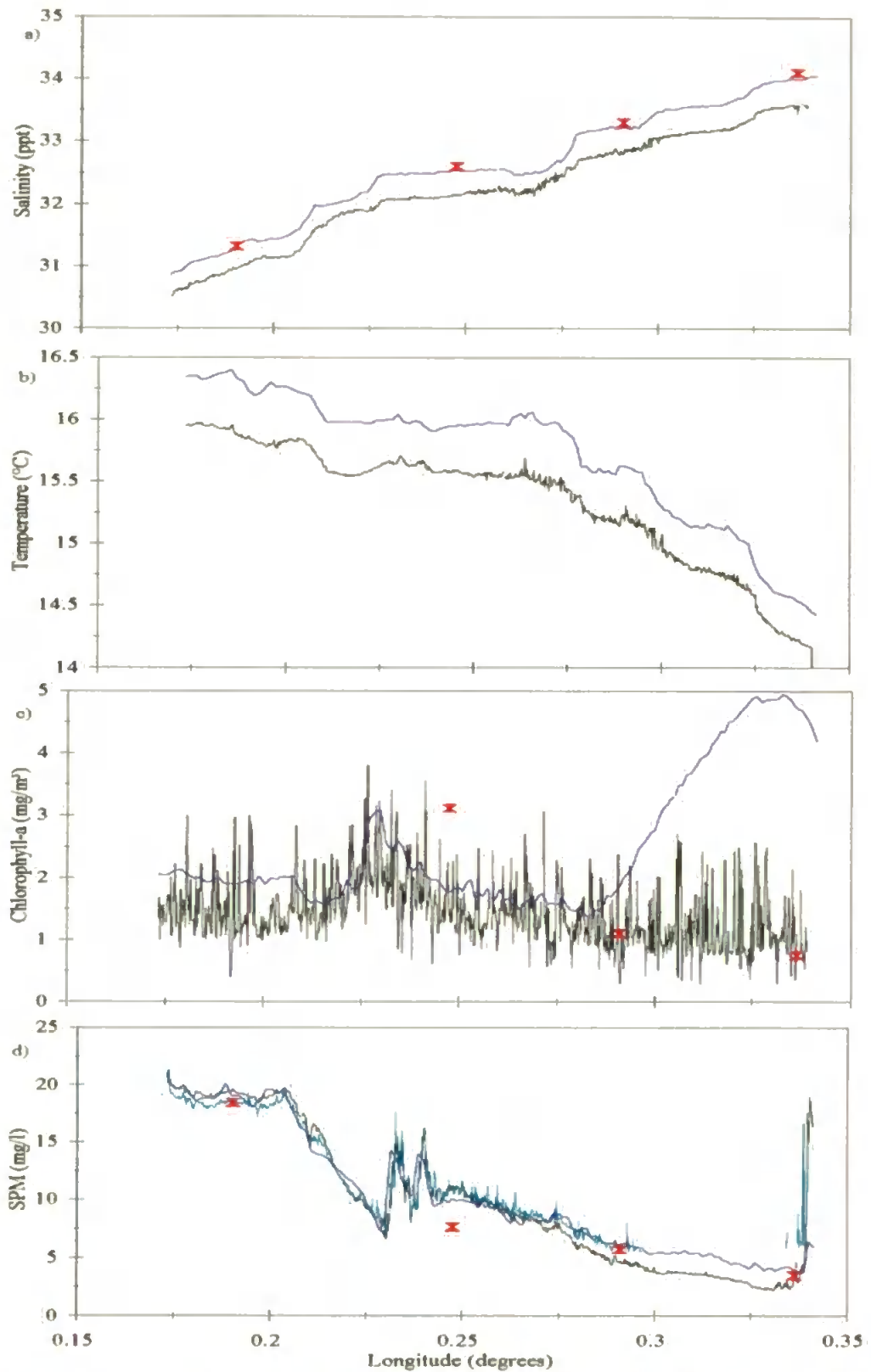


Figure 4-12: Humber Estuary continuous data for August 4th Track 2. Blue lines represent QUBIT data, black lines UOR (except SPM where black is the 490 nm and green the short path transmissometer) and red symbols the bottle samples.

3) September

The UOR and QUBIT salinity traces for track 1 had similar values (see Figure 4-13a), with no fronts, but a wide peak from about -0.1 to 0.05 degrees of longitude. This does not appear in the temperature trace, which shows a gradual decline with increasing longitude (see Figure 4-13b). However, the QUBIT temperature trace shows more structure than the UOR trace. The UOR chlorophyll-*a* concentrations were low and constant, while the QUBIT chlorophyll-*a* again varied with SPM. All the SPM sensors could not cope with the high suspended sediment concentrations and saturated below 200 mg/l.

Track 2 shows greater structure with a strong salinity front at 0.05 degrees of longitude (see Figure 4-14a), which does not show up in the temperature trace (Figure 4-14b) but is coincident with a large SPM peak (Figure 4-14c). At 0.23 degrees of longitude the salinity began rising indicating another weaker front, which also appeared as falling values in the temperature trace and a leveling off in the SPM trace (Figure 4-14d).

4.6.2 Comparison of K_d values

Both the $K_d(550)$ and $K_d(632)$ values were highly correlated with derived SPM (see Figures 4-15 and 4-16), although the equations varied for each derived SPM were different (see Table 4-6 and 4-7).

Table 4-6: Sensor derived SPM and $K_d(550)$ regressions.

Sensor (Month)	X-Coefficient	Constant	R^2
Model	0.097	0.394	
Blue Transmissometer (Aug.)	0.124	-0.272	0.72
Blue Transmissometer (Sept.)	0.079	0.086	0.97
Short Path Transmissometer (Aug.)	0.109	-0.012	0.97
Short Path Transmissometer (Sept.)	0.152	0.076	0.97
Nephelometer (Aug.)	0.122	-0.287	0.87
Nephelometer (Sept.)	0.099	0.486	0.98

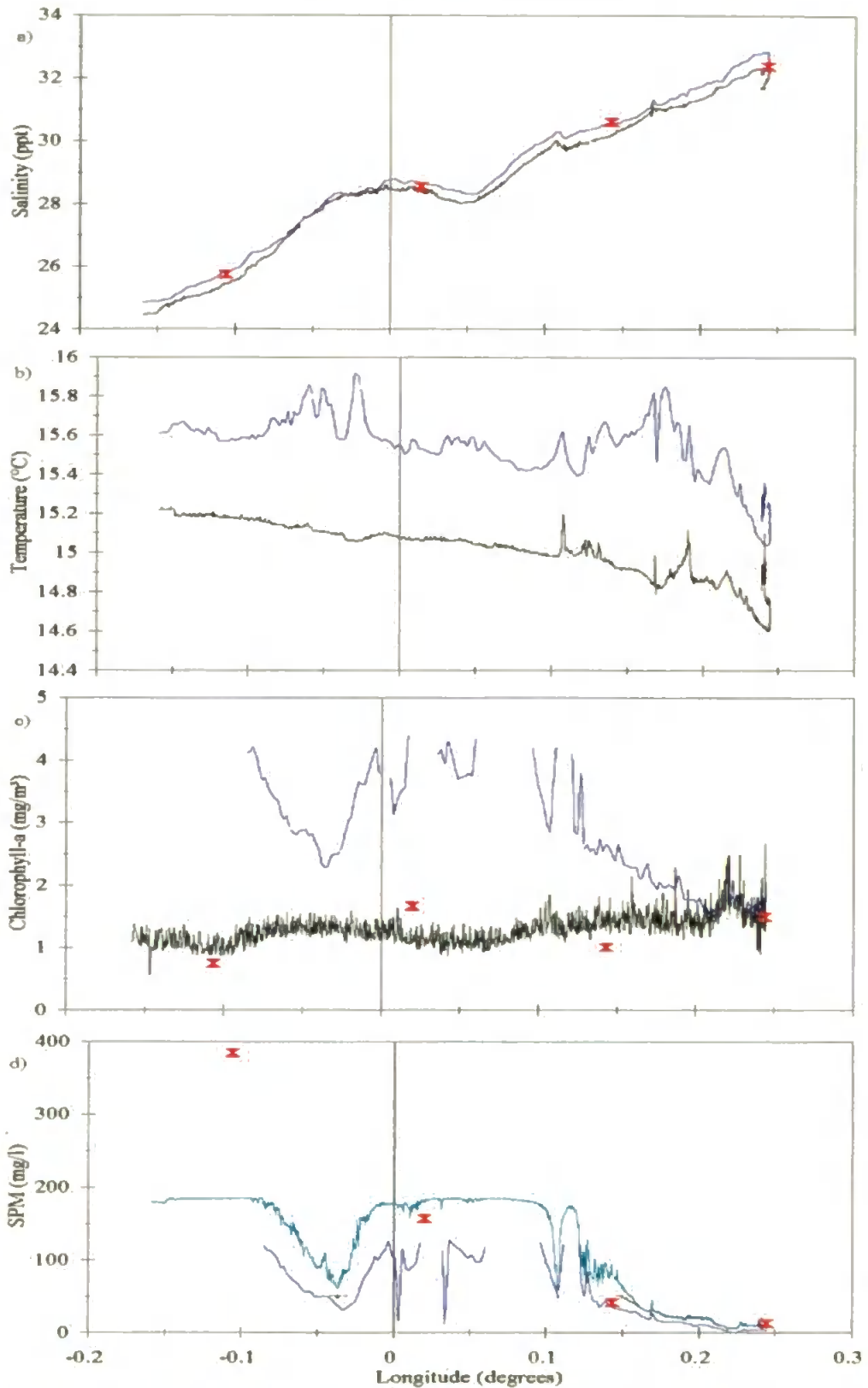


Figure 4-13: Humber estuary continuous data for September 1st Track 1. Blue lines represent QUBIT data, black lines UOR (except SPM where black is the 490 nm and green the short path transmissometer) and red symbols the bottle samples.

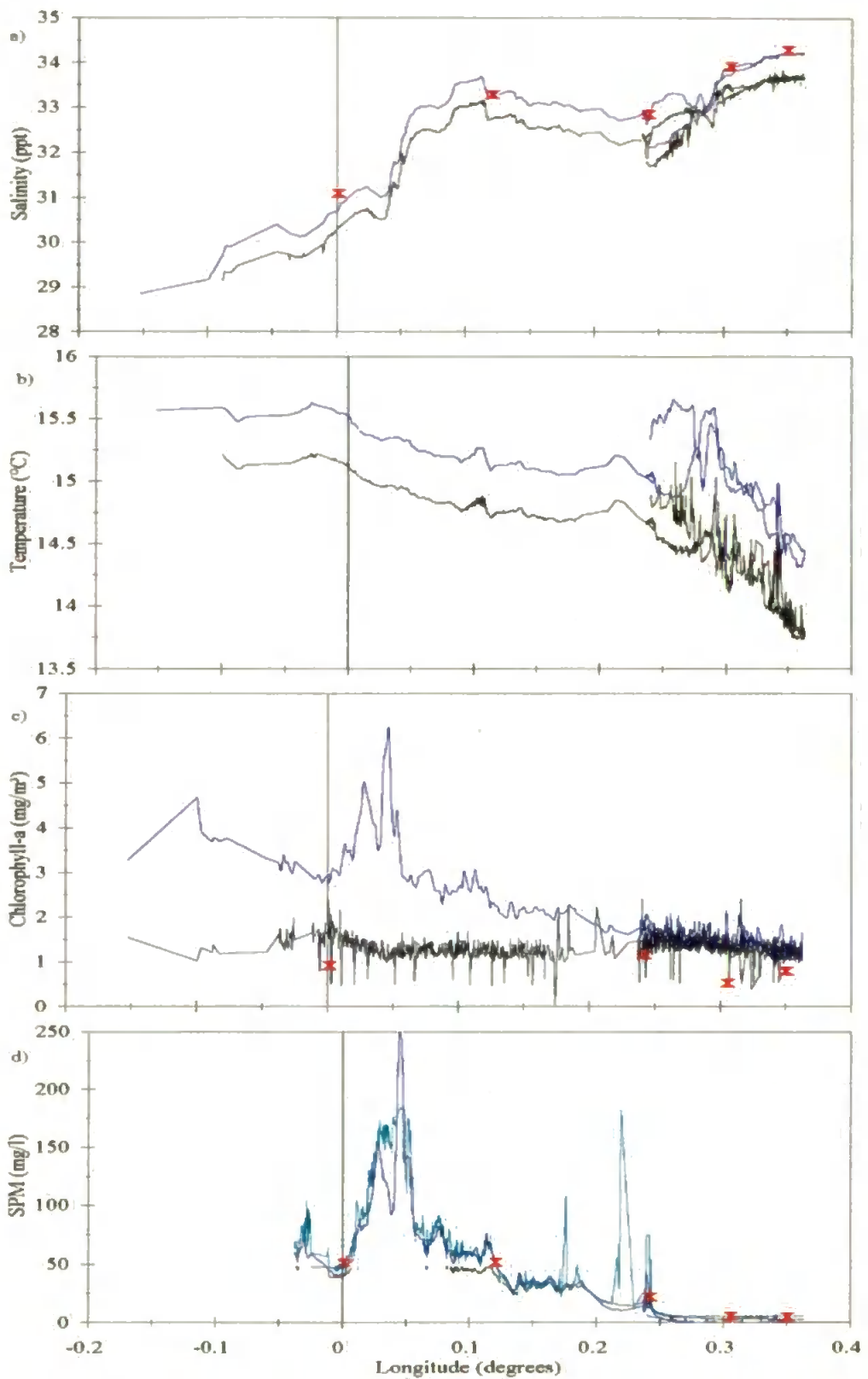


Figure 4-14: Humber estuary continuous data for September 1st Track 2. Blue lines represent QUBIT data, black lines UOR (except SPM where black is the 490 nm and green the short path transmissometer) and red symbols the bottle samples.

Table 4-7: Sensor derived SPM and $K_d(632)$ regressions.

Sensor (Month)	X-Coefficient	Constant	R^2
Model	0.093	0.287	
Blue Transmissometer (Aug.)	0.106	-0.080	0.83
Blue Transmissometer (Sept.)	0.067	0.289	0.97
Short Path Transmissometer (Aug.)	0.067	0.305	0.97
Short Path Transmissometer (Sept.)	0.089	0.281	0.95
Nephelometer (Aug.)	0.100	0.052	0.85
Nephelometer (Sept.)	0.089	0.588	0.97

In general the September regressions have higher coefficients and R^2 than August. The poorest sensor R^2 for both wavelengths are for the August blue transmissometer values which have a limited SPM range. The August $K_d(550)$ data have negative constants. A comparison can also be made with modelled values which were calculated using the formulation of Kirk (1984), in terms of the apparent optical properties, with a DOM concentration of $4 \mu\text{MC}$ and chlorophyll-*a* concentration of 3 mg/m^3 .

The validity of this method was determined by calculating the effect of deviations in the parameters. This involved calculating the average value and standard deviation of the depth, normalised PAR and normalised downwelling scalar irradiance (632 nm) for September Track 1. $K_d(632)$ was then calculated using the average values and then each parameter was varied by its standard deviation. A 31% change in $K_d(632)$ was caused by varying the normalised downwelling irradiance, 11% by the depth and 2% by the normalised PAR. So the errors in the $K_d(632)$ regression were most influenced by changes in the downwelling irradiance.

Figure 4-17 shows a comparison of the PRR K_d values with the SPM for August (as the UOR was not kept in the water during the overflight period) and both sets of K_d values for September. The August $K_d(665)$ value changed its relative magnitude within the spectra, before 14.90 GMT was between $K_d(510)$ and $K_d(560)$ for four of the five profiles, but after this it was first at the same level as $K_d(560)$ then gradually increased until it became greater than $K_d(510)$. At the end of September track 1 the $K_d(560)$ was relatively higher still, between $K_d(443)$ and $K_d(488)$. This position shift was borne out by the UOR data at $K_d(632)$ which was greater than or at the same level as $K_d(520)$ and the $K_d(490)$ drops to

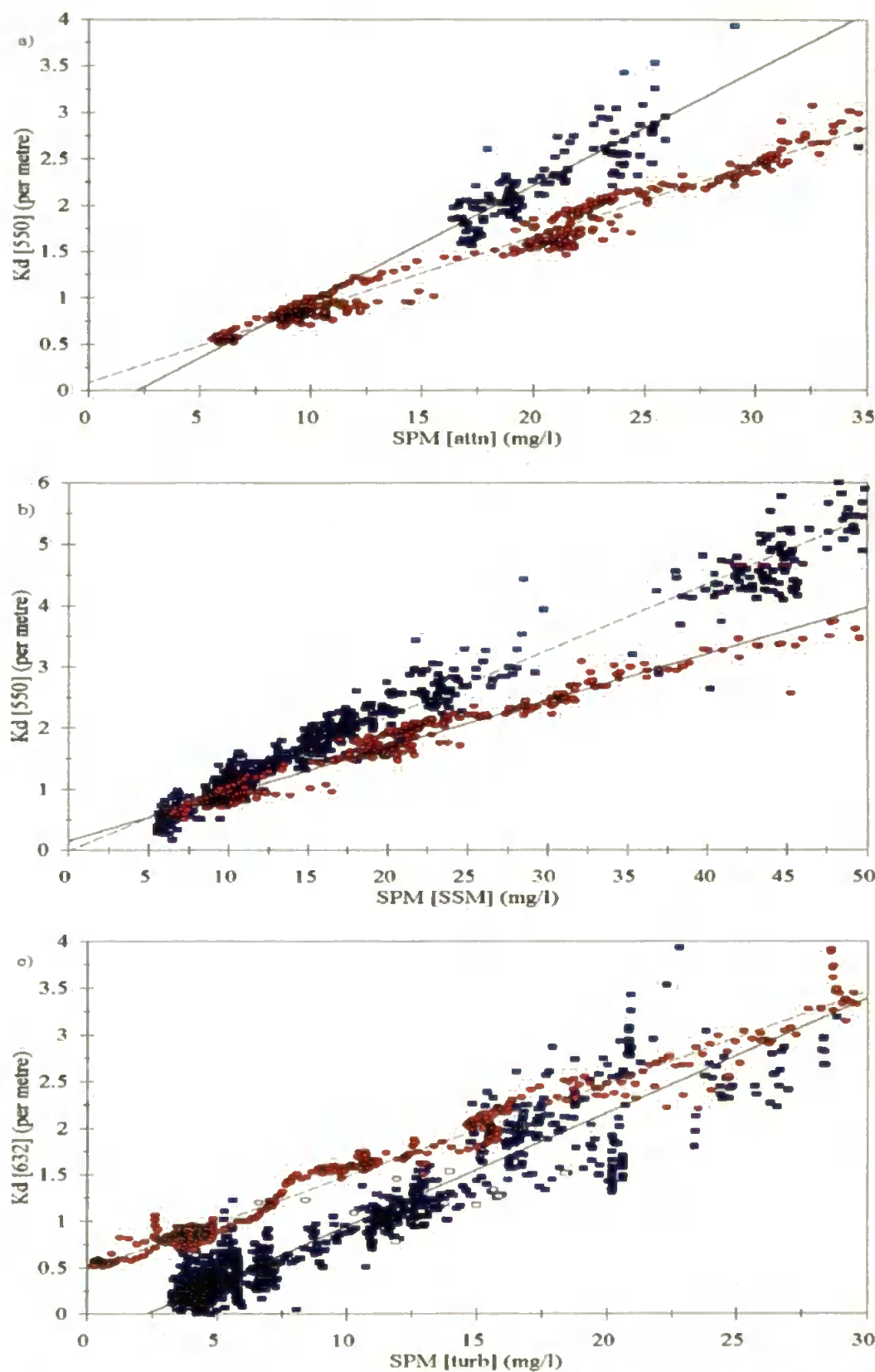


Figure 4-15: K_d [550] regressions against SPM as determined by a)transmissometer, b) short path transmissometer and c) nephelometer for: UOR August (blue squares); UOR September (red circles); PRR August (clear squares); PRR September (clear circles).

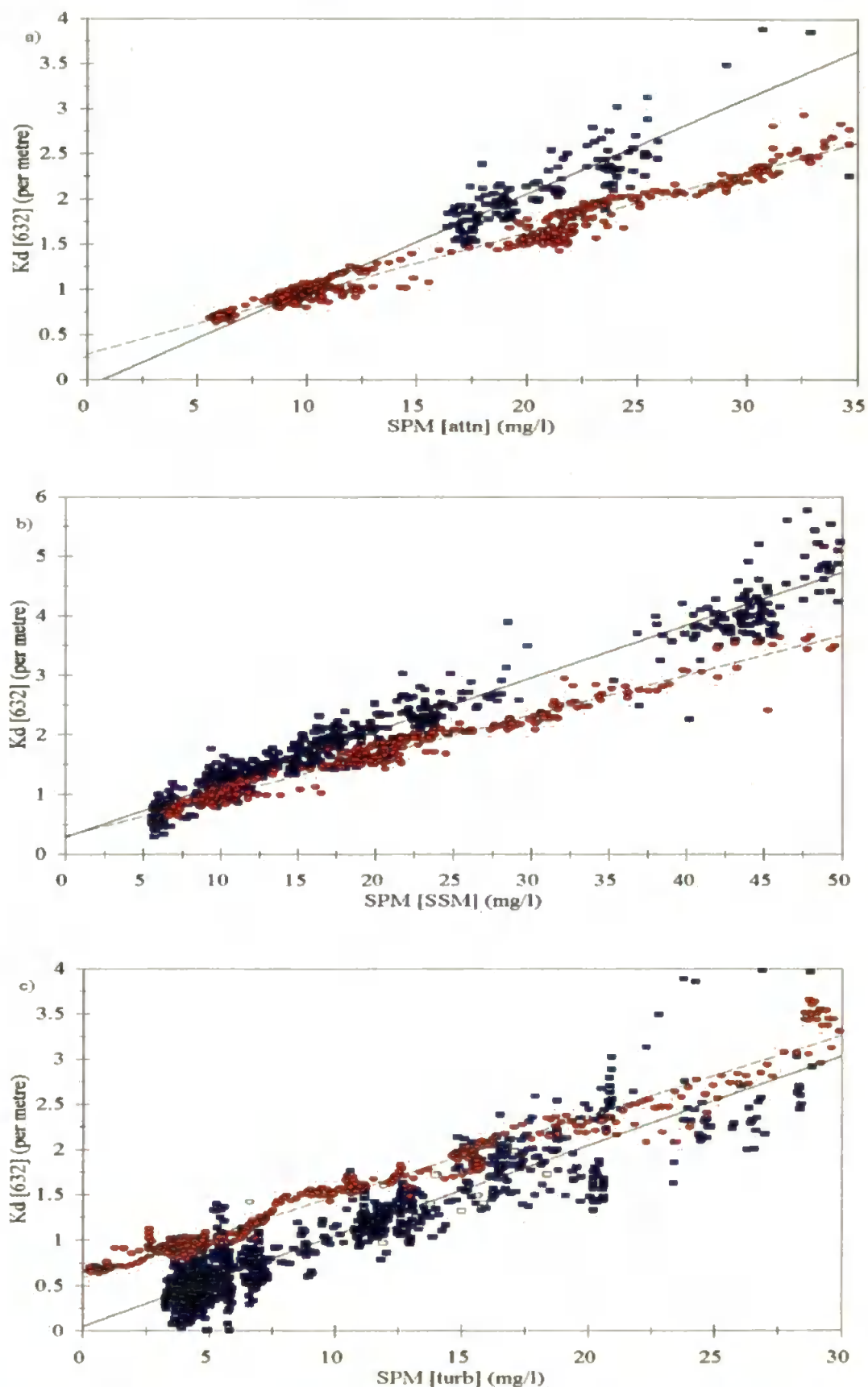


Figure 4-16: K_d [632] regressions against SPM as determined by a) transmissometer, b) short path transmissometer and c) nephelometer for: UOR August (blue squares); UOR September (red circles); PRR August (clear squares); PRR September (clear circles).

this level (less than unity) on several occasions. The relative increase in the UOR $K_d(665)$ values can be attributed to an increase in the SPM concentration, resulting from the passage of the survey vessel into the Humber plume front. Figure 4-17b and c show a spectral comparison between the UOR and PRR, with both curves having a minima at $K_d(550)/K_d(560)$ although the PRR curve was flatter overall.

4.7 Summary

This chapter presented the ground data, starting at the collection and proceeding through the calibration and processing with the light sensors being calibrated to radiometric units (see Section 4.4.1) and *in-situ* data calibrated to biogenic or geophysical parameters (see Section 4.4.2). As two sensor packages (UOR and QUBIT) measured key parameters, a comparison of the data was carried out (see Section 4.6.1) which indicated that the:

- a) salinity values were similar for both packages
- b) QUBIT temperature values were always higher than the UOR values
- c) UOR chlorophyll-*a* calculations were most reliable
- d) nephelometer provided the most reliable SPM data in high concentration areas (>75 mg/l) and the blue transmissometer provided the most reliable values at low SPM concentrations (<75 mg/l), but no sensor performed reliably above 175 mg/l.

Section 4.5.3 described how K_d values were calculated for the UOR and section 4.6.2 compared these values with the SPM measurements (derived from the *in-situ* optical sensors) and derived PRR K_d values (see Section 4.5.2). The results showed that the $K_d(550)$ and $K_d(632)$ values were highly correlated with derived SPM. August gave the lowest correlation coefficients and yielded negative constants, which may be caused by the September normalization. The PRR values are consistently within the spread of the UOR values.

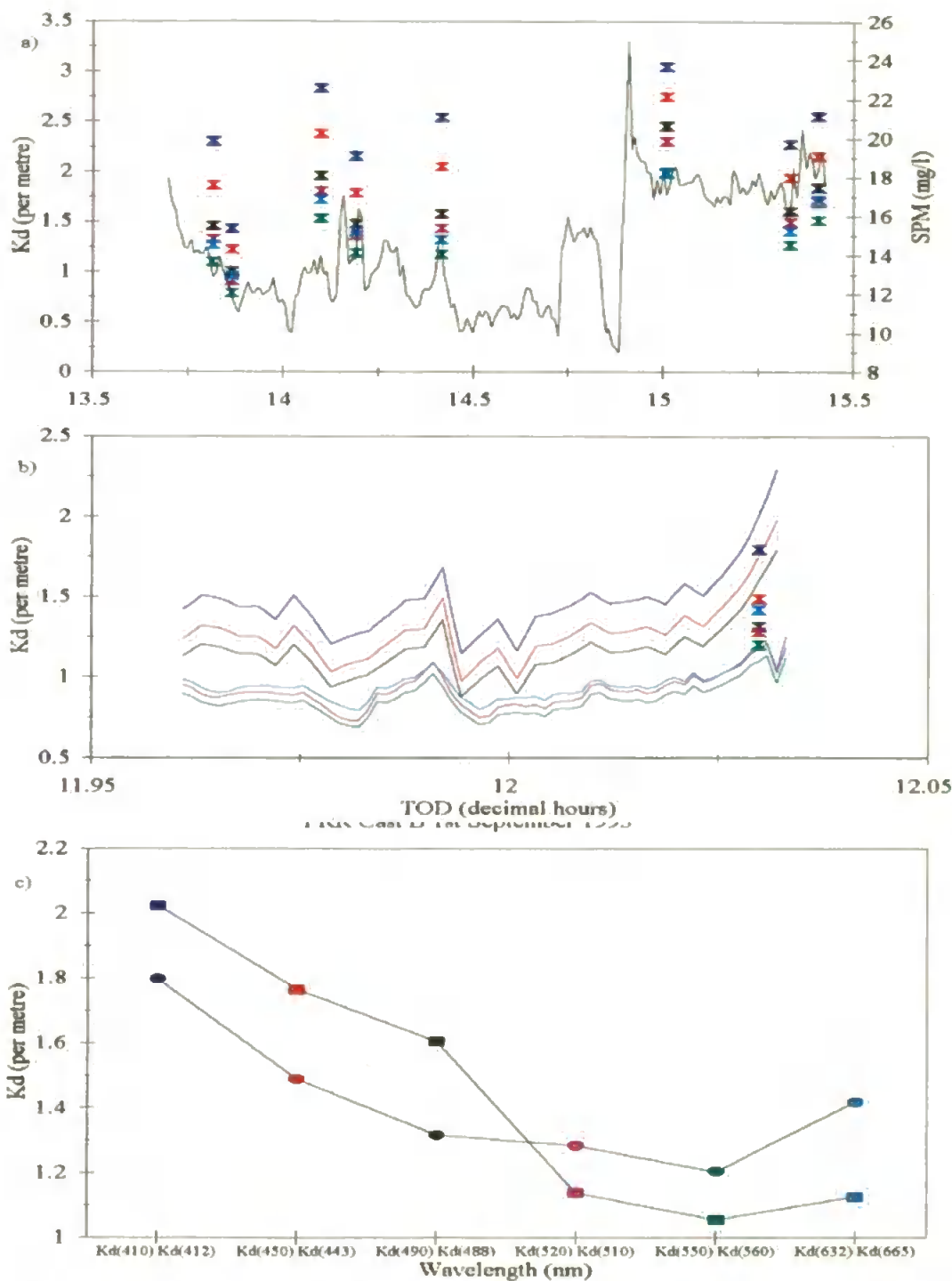


Figure 4-17: Along track PRR K_d values for a) August compared to SSM and b) September compared to the UOR K_d values, with c) spectral plot comparing the UOR (squares and left-hand values on the x-axis) and PRR (circles) K_d values for September. In all three figures the coloured symbols represent the wavelengths, see figure c for the colour key.

5. ALGORITHM DEVELOPMENT

5.1 Previous Research

Water colour measurements can provide information on the concentration of optically active substances present in the surface layer of the sea. The quantitative determination of these substances, such as chlorophyll-*a* (Ch) and suspended sediment (s), can be performed using retrieval variables, X , by empirical correlation with reflectance $R(\lambda)$ or reflectance ratios $\frac{R(\lambda_1)}{R(\lambda_2)}$, see Equation 5-1 (Tassan, 1988).

$$X = f [R(\lambda)] \quad (5-1)$$

The retrieval variables are usually inserted into a logarithmic expression, the retrieval algorithm, such as Equation 5-2 (Tassan, 1988) with parameters A and B being inferred from *in-situ* measurements.

$$\log [Ch, s] = A + B \cdot \log [X] \quad (5-2)$$

The retrieval variable must be highly sensitive to the retrieved parameter and relatively insensitive to other optically active matter, and may utilize two or more wavebands. Equations 5-3 and 5-4 demonstrate Coastal Zone Color Scanner (CZCS) sediment retrieval variables (Tassan, 1988).

$$X = [R(550) - R(670)]^a [R(520) / R(550)]^b \quad (5-3)$$

$$X = [R(520) + R(550)]^c [R(520) / R(550)]^d \quad (5-4)$$

Retrieval variables often include waveband ratios as they can suppress solar angle and atmospheric effects (Amos & Topliss, 1985), and may also cancel out effects caused by the sensor tilt angle and FOV (Morel & Prieur, 1977). However, waveband ratios cannot provide information on scattering and absorption and hence discriminate between different absorbing agents, so multispectral methods should be examined (Morel & Prieur, 1977).

The waveband combinations used in sediment algorithms are normally chosen by statistical means e.g. the highest coefficient of determination and/or the lowest root mean square error (Ritchie & Cooper, 1988) or the 'least squares' best-fit equation (Amos & Topliss, 1985 and Mitchelson *et al.*, 1986). When the suspended particulate matter (SPM) concentration is linearly regressed against the retrieval variable there is often a large spread of values around the line of best fit. This poor correlation can be partially attributed to atmospheric optical effects, as a complete atmospheric correction should be performed first.

The regression technique assumes there is no error in the measurement of SPM and that the error in the sensor reflectance $R_s(\lambda)$ is unrelated to the SPM error (Whitlock *et al.*, 1982). If this is incorrect the Daniel and Wood's Criteria should be applied, where the standard deviation in the sensor reflectance must be equal to or greater than 3.16 times the standard deviation in the SPM data noise $N(\lambda)$: $\sigma_{R_s(\lambda)} \geq 3.16 \sigma_{N(\lambda)}$ (Whitlock *et al.*, 1982). The regression coefficient should be supplemented by other statistical confidence tests e.g. the standard deviation and F-test as used by Liedtke *et al.* (1995).

Statistical techniques should only be applied under controlled environmental conditions: water depth greater than penetration depth (see Section 2.1.2); constant vertical concentration gradient within the penetration depth; ground truth synchronous with the remote sensing; several validation points. The assumption that SPM is the only factor controlling the retrieval variable may not be valid, as the water constituents have non-linear optical relationships and each varies differently with wavelength (see Chapter 2). The resulting algorithm may only apply to the particular site and also that particular time, inducing large errors (well beyond acceptance limits) in appreciably different water masses (Tassan, 1988).

There are problems matching a point concentration, measured by the vessel, to a sensor value as this requires a geometric correction and the SPM concentration may vary rapidly with time. In previous research the ground data collection did not occur at the same time as the overflights e.g. Ritchie & Cooper (1988). The depth at which SPM is measured should be related to the diffuse attenuation coefficient of the remote sensing wavelength (see Section 2.1.2), as different wavelengths penetrate to differing depths. Mitchelson *et*

al. (1986) used an approximate penetration depth ($1/K$), which in Case 2 waters is as near to the surface as possible.

Simpson & Brown (1987) and Mitchelson *et al.* (1986) used optical measurements at the sea surface, which should be identical to those in a remote sensed image provided that the optical characteristics of the sensors and field-of-view are similar (or area of water is homogeneous) and the radiometric calibration and atmospheric correction are performed.

Doerffer (1979) used an inverse modeling technique, based on the two flow model of Joseph (1950), which derived reflectance from the suspended sediment, chlorophyll-*a* and DOM concentrations (computed from the optical properties of the individual substances). For the particular case of the Elbe Estuary, Doerffer (1979) demonstrated that the reflectance at 650 nm was related to SPM with little dependence on the chlorophyll-*a* and DOM concentrations.

In this research the simulated sensor wavebands, derived from laboratory reflectance spectra (see Chapter 3), were used to determine the best combination of wavebands for the retrieval variable. A semi-analytical model was used to derive a general algorithm, which was compared to the ground data as a final validation.

5.2 Laboratory Experiments

The reflectance spectra were binned into the CASI wavebands (Table 5-1) by assuming that the waveband shape was linear. Wavebands 11 and 12, which approximate SeaWiFS bands 7 and 8, were chosen as they are situated in the near infrared region, which the laboratory research predicts to have a robust relationship with SPM. To examine the relationship, each waveband was plotted against SPM concentration (see Figure 5-1). The two wavebands produce similar graphs for each sediment suspension, although waveband 11 has relatively higher reflectance levels. The sediment suspensions become grouped according to their different size fractions, with an increase in the particle size causing a decrease in reflectance for the same concentration.

Table 5-1: Comparison of the CASI, UOR and PRR-600 wavebands, with the midpoint shown in brackets.

CASI	UOR	PRR-600
	368-455 (410)	407-417 (412)
433-453 (443)	430-485 (450)	438-448 (443)
480-500 (490)	466-504 (490)	485-495 (490)
500-520 (510)	504-561 (520)	505-515 (510)
545-565 (555)	536-583 (550)	555-565 (550)
610-636 (623)	618-635 (623)	
637-660 (648.5)		
660-680 (670)		660-670 (665)
680-685 (682.5)		PAR/678-688 (683)
690-710 (700)		
716-740 (728)		
745.1-755.8 (750.5)		
845-885 (865)		

The waveband relationship was then examined by plotting one waveband against the other (see Figure 5-2). The results showed an exponential curve which again diverged for different size fractions.

A waveband ratio (waveband 12 over 11) was then tried as it reduces contamination from: changes in the solar irradiance; sensor view angle; waveband inaccuracies (see Section 5.5). By plotting the waveband ratio against SPM an inverse exponential curve was created (see Figure 5-3), which indicates that the waveband ratio sensitivity decreases as the concentration increases. This decrease in sensitivity also occurs in the single waveband plots (Figure 5-1) and results in a cut off point of 1000 mg/l being applied to calculated SPM maps (see Figure 5-9). By using a waveband ratio rather than single waveband the of the algorithm sensitivity to particle size was reduced, as seen by the reduced spread of the different size fraction curves in Figure 5-3 as compared to 5-1.

Curran (1987) concluded that the flattening of the SPM versus $L_w(\lambda)$ curve, at high sediment concentrations, to form an asymptote has led to the assumption that the

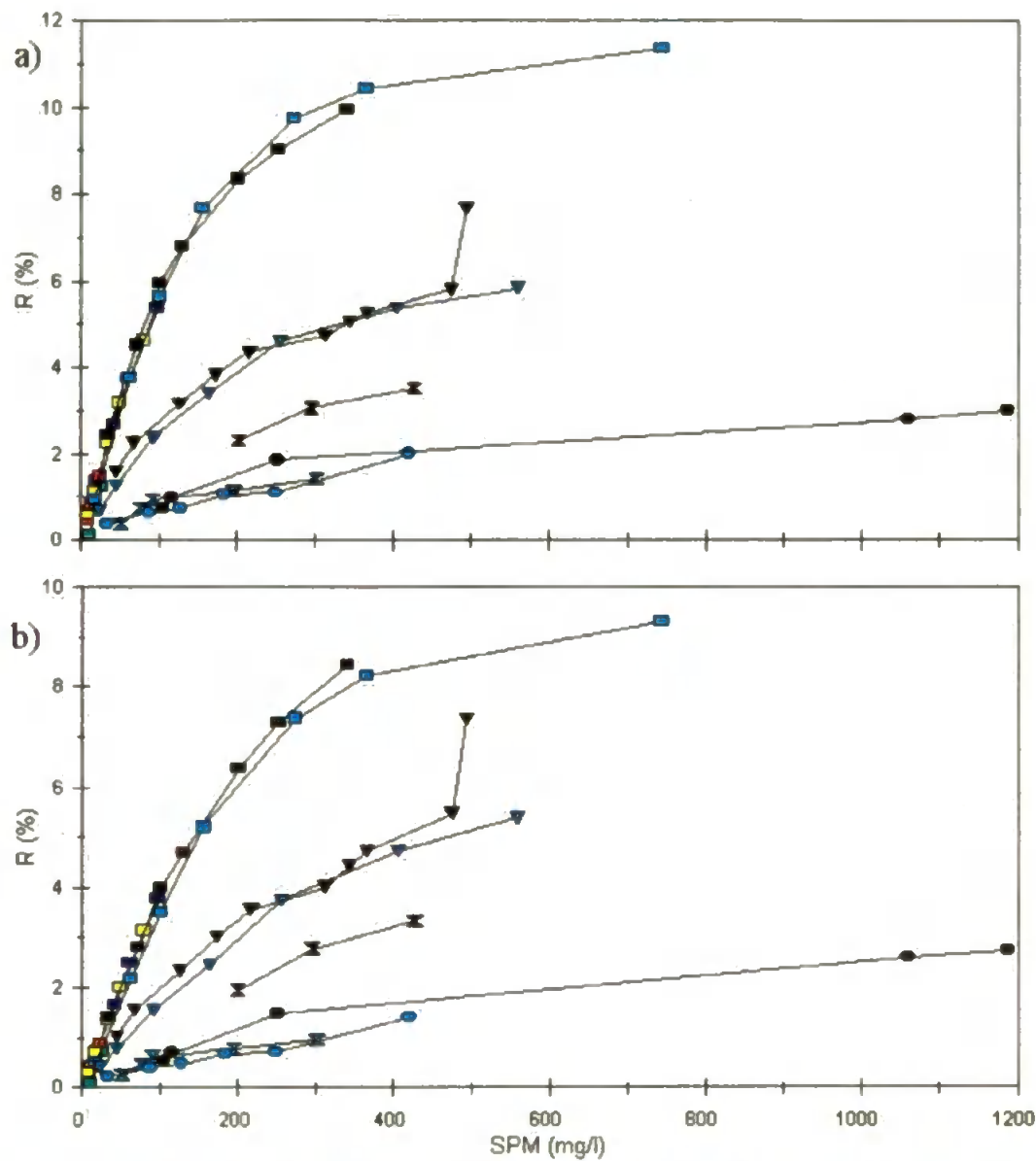


Figure 5-1: Spectral reflectance for a) waveband 11 and b) waveband 12 plotted against SPM for all the tank data with the different symbols representing sediment suspensions. The squares are for fine suspensions, triangles for medium suspensions, circles for course suspensions and hourglasses for unfractionated suspensions (see Section 3.2 for further details), and the colours have no meaning except for the clarity of the diagram.

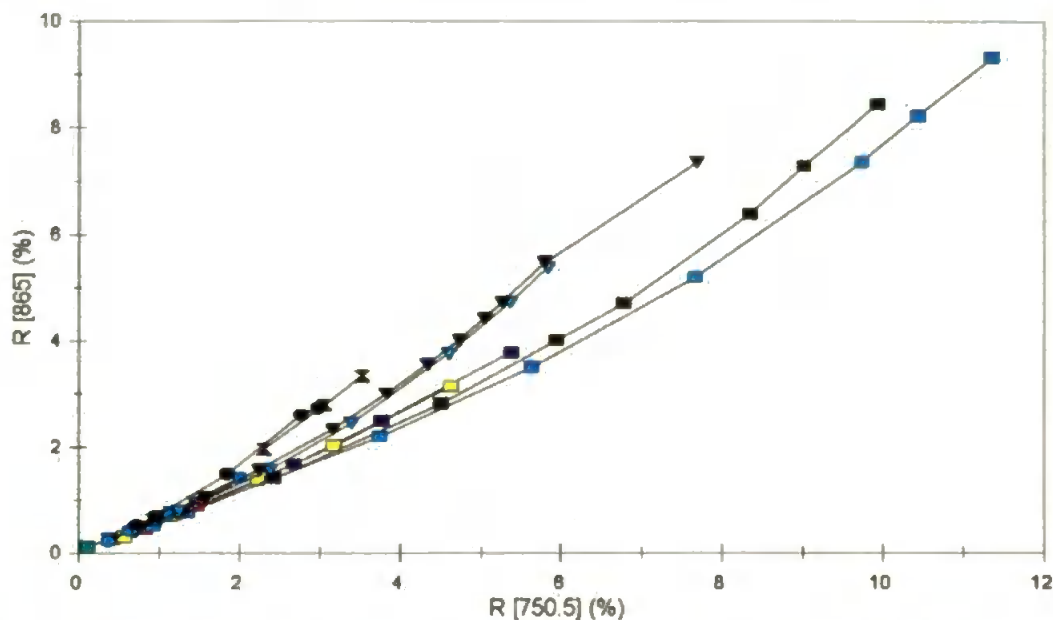


Figure 5-2: Plot of waveband 11 versus waveband 12. The squares are for fine suspensions, triangles for medium suspensions, circles for course suspensions and hourglasses for unfractionated suspensions (see Section 3.2 for further details), and the colours have no meaning except for the clarity of the diagram.

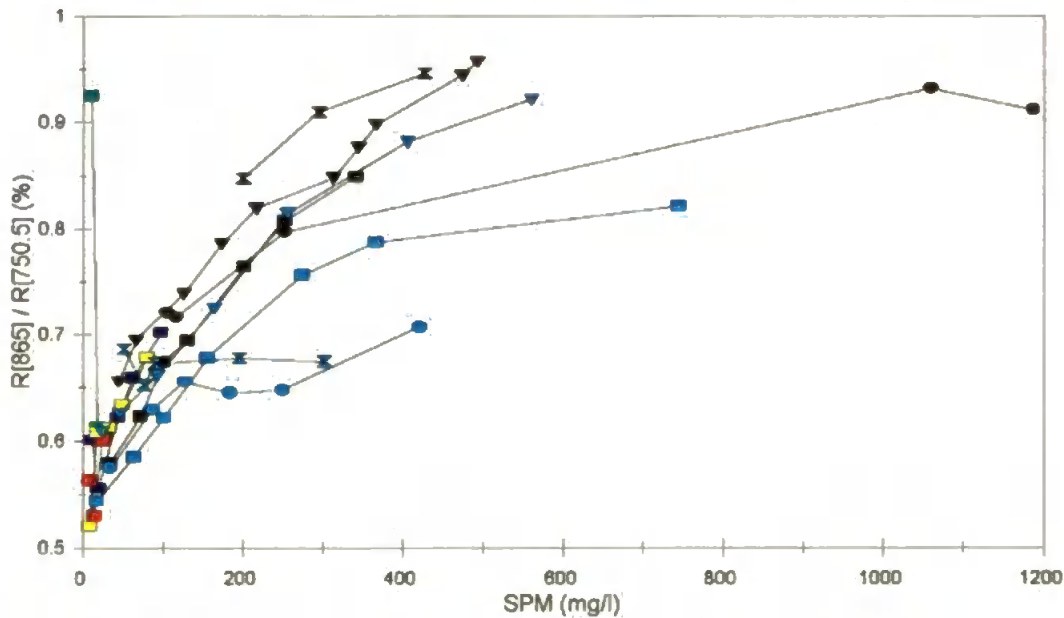


Figure 5-3: Plot of near infrared reflectance waveband ratio against SPM. The squares are for fine suspensions, triangles for medium suspensions, circles for course suspensions and hourglasses for unfractionated suspensions (see Section 3.2 for further details), and the colours have no meaning except for the clarity of the diagram.

relationship is logarithmic. Previous studies (Ritchie *et al.*, 1983 and Whitlock *et al.*, 1981) indicated that the water-leaving radiance reached a maximum as the suspended sediment concentrations increased causing low estimates at high concentrations. However there was a decrease in sensitivity at longer wavelengths, in the red and near infrared where the penetration depth is shallower. So the near infrared can differentiate a greater range of SPM concentrations, but will be insensitive at low concentrations.

The greatest divergence in the sediment suspensions occurred for the coarse and medium fractions, which are unlikely to remain in the top 0.2 m of the water column (the approximate penetration depth for the near infrared wavebands) under normal conditions. So from the remote sensing perspective only the fine fraction should to be considered further.

5.3 Semi-analytical model

A semi-analytical model was constructed to validate the laboratory experiments and develop a global algorithm, as opposed to a specific algorithm from a regression technique. The model was based on the reflectance equation, see Equations 2-31, 2-32 and 2-33 or Section 2.2 in Hudson *et al.* 1994 Appendix 3.

The model produced a near infrared reflectance waveband ratio that behaved in the same manner as the laboratory fine sediment fraction, see Figure 5-4a and b. The model's reflectance equation was then replaced by the normalised water-leaving radiance equation (see Equation 2-75), which relates the SPM algorithm to the aircraft imagery waveband ratio, w_r . An SPM algorithm (see Equation 5-5) was then derived from the water-leaving radiance curve, see Figure 5-4c.

$$\text{SPM (mg / l)} = A * \left(\frac{w_r - B}{1 - C \cdot w_r} \right) \quad (5-5)$$

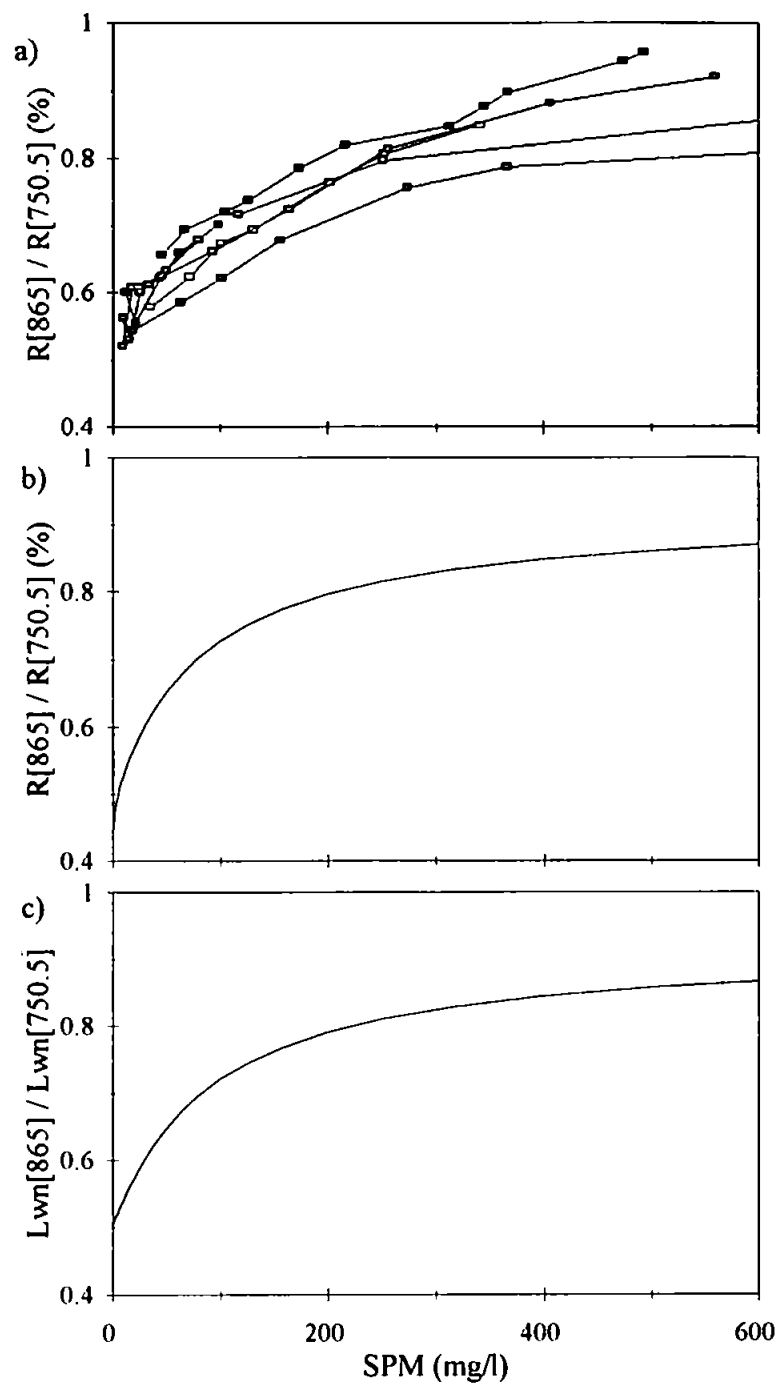


Figure 5-4: Plot of: a) waveband ratio versus SPM for the fine fraction only; b) reflectance waveband ratio versus SPM for the model; c) normalised water-leaving radiance waveband ratio for the model.

The constants (A, B and C) are related to the level of solar irradiance. So in the case of normalised water-leaving radiance the extraterrestrial solar irradiance figures were used, which resulted in constants of 141.46, 0.381 and 1.415. The constants are also used to restrict the input water-leaving radiance waveband ratio range, so that the asymptote is not reached (see Equation 5-9 in Section 5.4.1), resulting in a maximum SPM of 1000 mg/l.

5.4 Atmospheric Effects

The development of a Case 2 atmospheric correction is beyond the scope of this thesis and forms the basis of further research (see Section 7.4). Instead a correction for the atmospheric attenuation was applied, from solar irradiance measurements obtained by the spectrometer on the research vessel (see Section 4.4.1). The solar irradiance would be preferably measured on the aircraft, but these data were not available and so ground level values were used instead.

Initially the SPM algorithm (Equation 5-5) was applied to a radiometrically calibrated image (see Figure 5 in Hudson *et al.* 1994 in Appendix 3). The resulting SPM map masked out (by producing negative SPM values) features such as uncovered inter-tidal areas or land targets whose waveband ratio exceeded the acceptable range, and clouds or vessels (including the wake) which may also saturate the sensor.

However, the resulting sediment map was contaminated by an atmospheric component as an atmospheric correction was not used. As the Rayleigh attenuation in the near infrared is small when compared to the visible region (see Figure 5-5) and the two wavebands were not directly situated on absorption features (see Figure 5-6), the contamination can be assumed to be due primarily to aerosols. The waveband ratio will reduce the effects of solar irradiation intensity and sensor-pixel geometry, and the atmospheric contamination can be summarised by Equation 5-6.

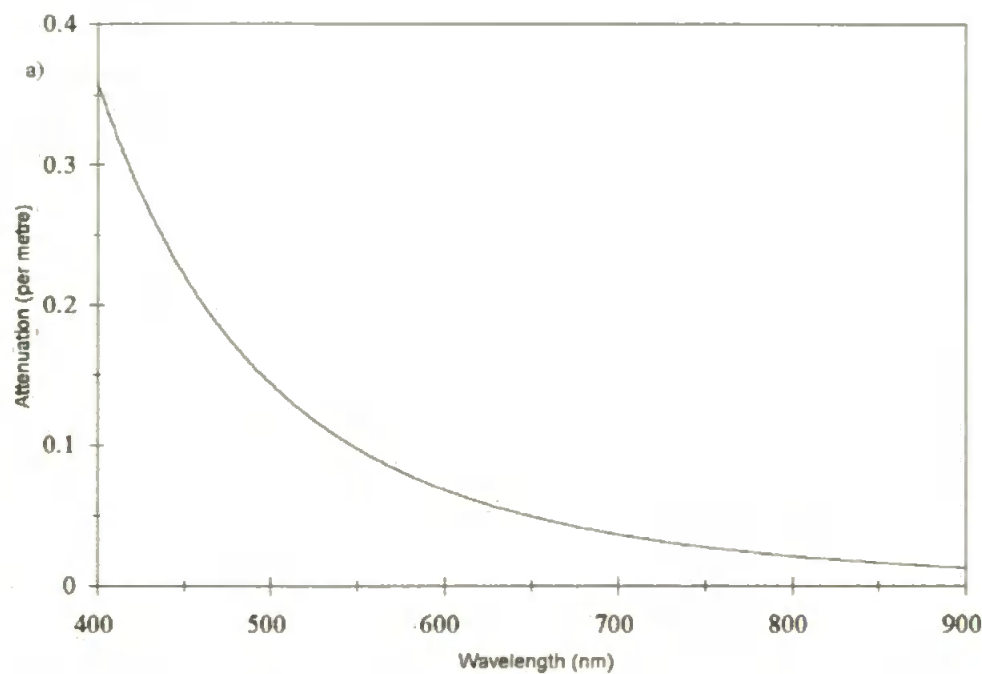


Figure 5-5: Rayleigh attenuation derived from Equations 2-54 & 2-55 with an altitude of 10000 feet.

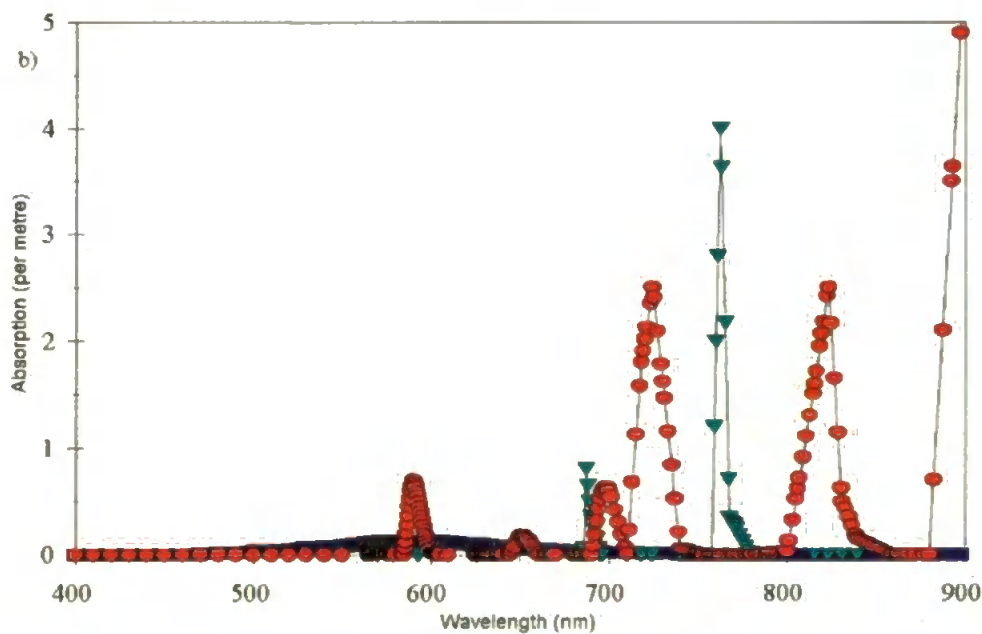


Figure 5-6: Atmospheric absorption by ozone (squares), water vapour (triangles) and permanent gases (circles).

$$SPM \approx f\left(\frac{L_w[865] + L_a[865]}{L_w[750.5] + L_a[750.5]}\right) \quad (5-6)$$

Two assumptions can be made about the atmospheric contamination:

(a) The atmospheric component varies smoothly when compared to the water signal as the structures seen in the images clearly originate from the water (see Figures 6-4 to 6-7).

(b) The atmospheric component must be small when compared to the water-leaving radiance, at high SPM concentrations, as there is no apparent across-scan variation in the imagery. This is despite the increased path length at greater scan angles causing an increased atmospheric radiance (see Figure 5 Hudson *et al.*, 1994). However, as the SPM decreases, this effect becomes apparent.

As no direct measurements of the atmospheric signal were made, the ground level downwelling solar irradiance will be used as an indirect measure. The downwelling solar irradiance, as measured by the Spectron cosine head, was binned into the CASI wavebands, in the same manner as for the laboratory spectra. The relationship between waveband 11 and 12 was examined and appears to show a constant linear relationship over varying conditions (see Figure 5-7a which has an r^2 of 0.999). However, if the solar waveband ratio is plotted against waveband 12 the relationship shows a greater amount of scatter (see Figure 5-7b), due to small deviations not being apparent in Figure 5.7a. Therefore there was no robust relationship between the solar waveband ratio and waveband 12.

However, it must be noted that by measuring the solar irradiance only the effects of aerosol forward scattering are observed, which is the larger but least wavelength-dependent component of the total aerosol scattering. The aircraft sensor will have the water-to-aircraft signal affected by atmosphere, which will include aerosol backscattering and would therefore vary with aerosol type and concentration (see Section 2.3.2.2).

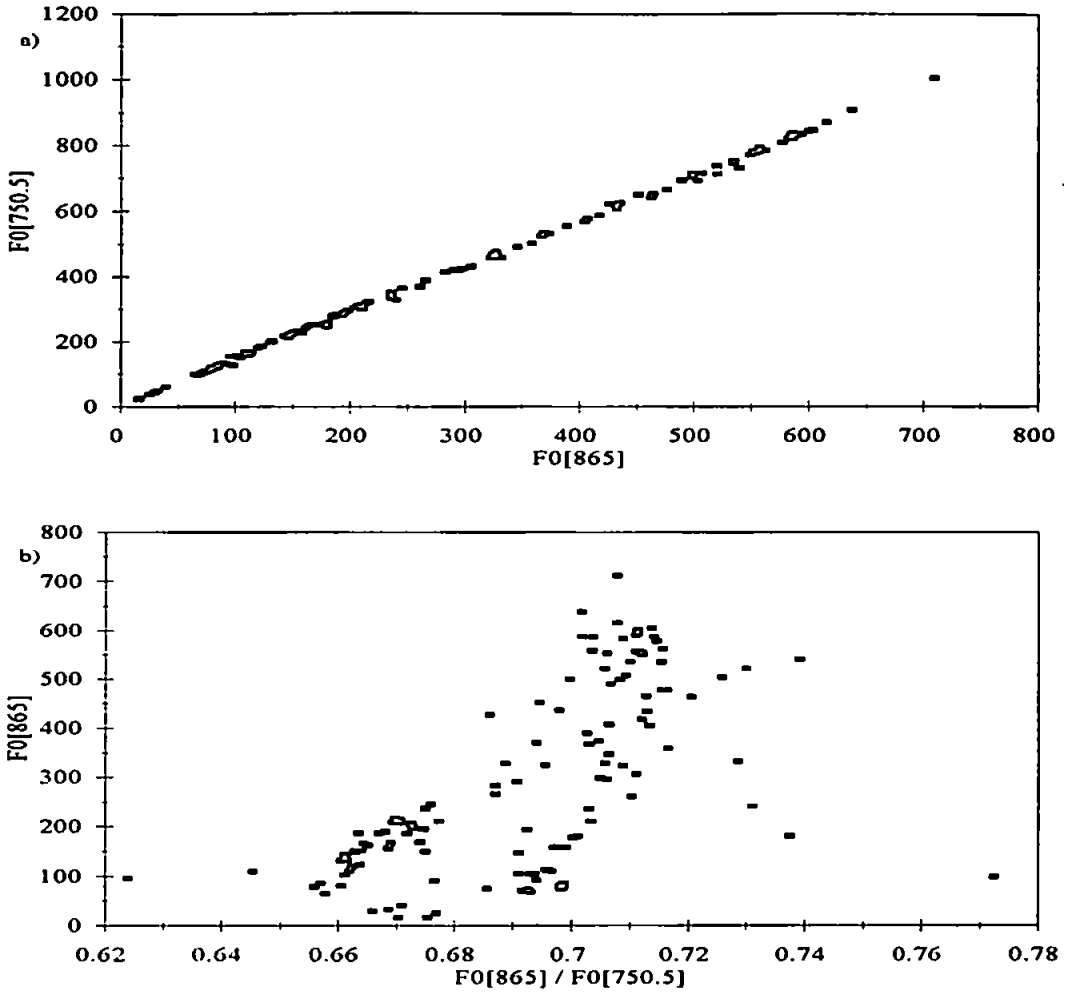


Figure 5-7: Plot of the a) regression of solar irradiance waveband 12 versus waveband 11 and b) plot of solar waveband ratio versus waveband 12.

The SPM algorithm was modified (see Equation 5-7) to include the solar waveband ratio, sr , and the effect (on the water-leaving radiance ratio to SPM relationship) of varying the solar irradiance can be seen in Figure 5-8a, where an increase in the downwelling irradiance causes an increase in the water-leaving radiance ratio and hence decrease in the predicted SPM concentration.

$$SPM = sr \cdot A \left(\frac{wr - B}{1 - C \cdot wr} \right) \quad (5-7)$$

Chapter 5 - Algorithm Development

The next stage was to quantify the effect of the solar waveband ratio on the coefficients (A, B and C). The coefficient values were calculated for a solar waveband ratio ranging from 0.65 to 0.8 in 0.01 increments and plotted on Figure 5-8b. The coefficients were then regressed against the solar waveband ratio, which required an average of 48 iterations, to obtain the best non-linear fit equations and resulted in a linear relationship (see Table 5-2).

Table 5-2: Linear relationship between the SPM coefficients and solar irradiance.

Coefficient	x-coefficient	constant	r^2
A	-186.864	268.921	0.995
B	0.498	0.000	1.000
C	-2.078	3.009	0.997

To apply these results to the fieldwork experiments, the solar waveband ratios for each solar irradiance measurements (taken approximately every 20 minutes during the overflight days) were calculated and fieldwork estimates of the average SPM algorithm coefficients were made (see Table 5-3).

Table 5-3: Solar irradiance input to SPM algorithm.

Data Type	Solar Ratio	A	B	C	Max Ratio	Min Ratio
Extraterrestrial	0.773	124.566	0.384	1.404	0.713	0.384
Average June	0.685	143.996	0.332	1.620	0.618	0.332
Average August	0.688	140.435	0.342	1.580	0.633	0.342
August Overflight	0.708	136.625	0.352	1.538	0.650	0.352
Average September	0.714	135.483	0.355	1.525	0.656	0.355

The downwelling solar irradiance will also determine the amount of water-leaving radiance, so the coefficients also affect the limits of the water-leaving ratio. The maximum and minimum ratio limits can be calculated from Equations 5-8 and 5-9 respectively, and resulting fieldwork values for these limits are given in Table 5-3.

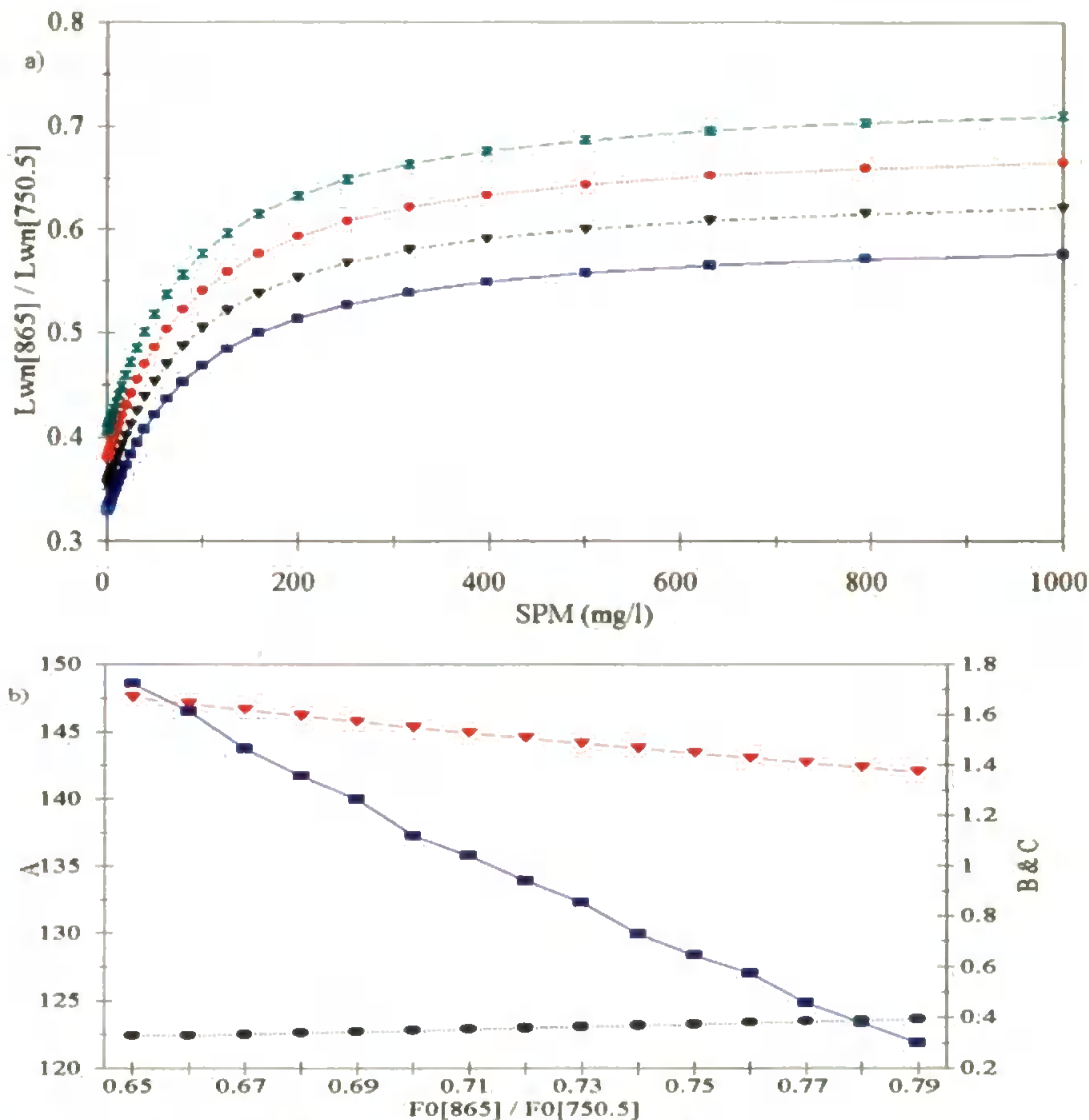


Figure 5-8: Effect of the solar irradiance waveband ratio on:

- a) L_{wn} ratio where the symbols represent a change in the ratio from 0.65 (squares) to 0.8 (hourglasses) in 0.5 increments.
- b) constants where the squares represent coefficient A, circles coefficient B and triangles coefficient C.

$$1 - C \cdot r_{\max} = 0 \quad \Rightarrow \quad r_{\max} = \frac{1}{C} \quad (5-8)$$

$$r_{\min} - B = 0 \quad \Rightarrow \quad r_{\min} = B \quad (5-9)$$

The SPM algorithm using the extraterrestrial ratio was applied to flightline (Fl) 6 and compared to the SPM algorithm using the measured September solar waveband ratio (see Figure 5-9). The false colour composite (wavebands 12, 11 and 7) highlights the sediment features, which include streak patterns approximately one third of the way down the image and a complex pattern around Spurn Head. The right hand side of all three images are brighter, due to the effects of atmospheric scattering.

If the downwelling solar irradiance ratio (at aircraft level) is known for each swath line the constants can be calculated exactly. This facility is available on the NERC aircraft, which has a solar irradiance head, but not the NRA aircraft which was used for this research.

5.5 Waveband positions

When CASI is operated in spatial mode, several CCD elements (with an individual resolution of approximately 2 nm) are averaged to obtain a waveband. The individual CCD elements will have a Gaussian distribution and so the waveband will not have a linear shape, as assumed in Section 5.2, and the position of central wavelength may also vary. The non-linear effect of the CCD elements, on the SPM algorithm, were examined by shifting the position and varying the band width of wavebands 11 and 12 (see Figure 5-10). In both situations, the effect of changing the waveband positions and size on the SPM algorithm appears to be negligible.



Figure 5-9: September 1st Flightline 6 showing:

- a) False Colour Composite (wavebands 12, 11 and 7).
- b) SPM map using the extraterrestrial solar ratio.
- c) SPM map using the average September solar ratio.

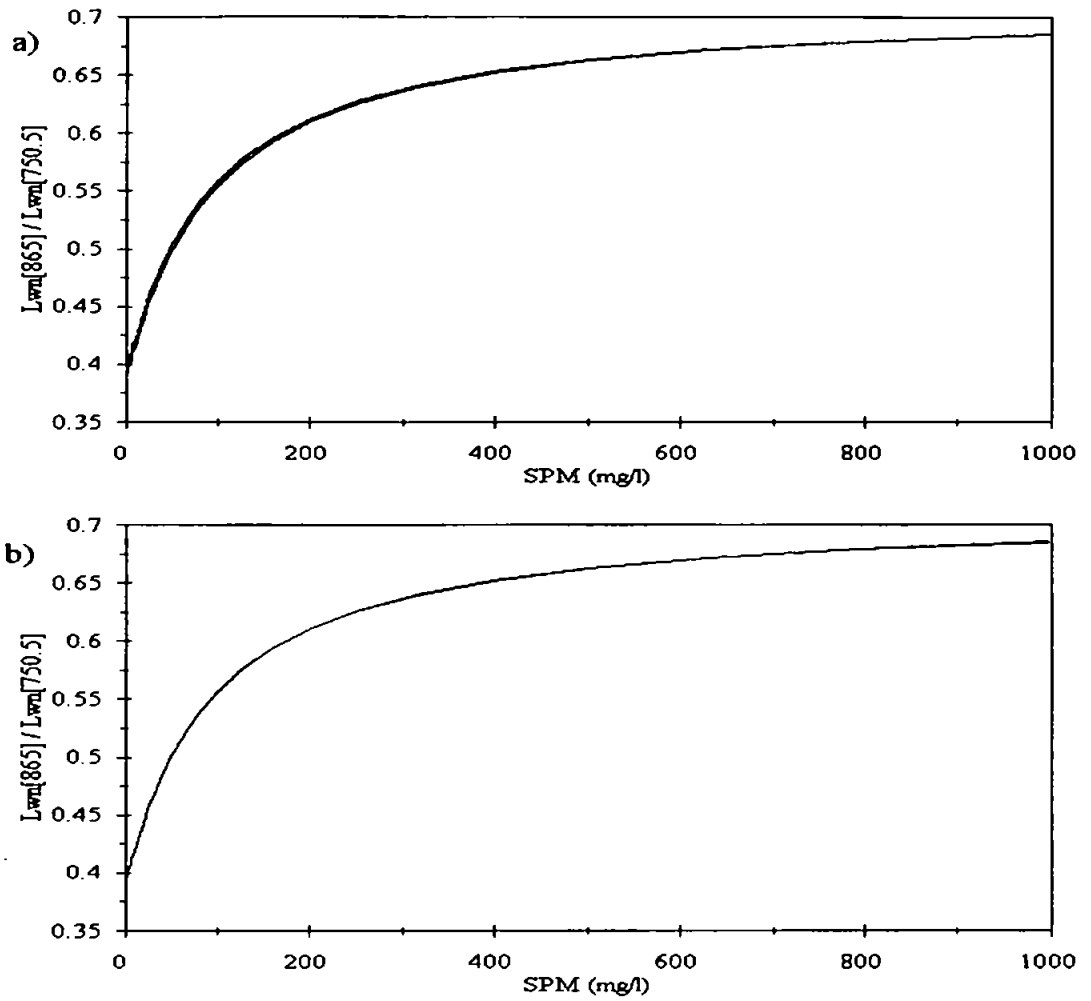


Figure 5-10: The effect, on the L_{wn} ratio, of changing the :

- a) position of wavebands 11 and 12 from their actual position, by 2 nm in both directions, in 0.5 nm steps.**
- b) width of wavebands 11 and 12 from the assumed widths to the width minus 1.5 nm in 0.5 nm intervals.**

6. AIRBORNE RADIOMETRY

Section 6.1 describes the proposed and actual overflights, and section 6.2 describes the processing software with further details being given in Appendix 2. Section 6.3 compares the contemporaneous imagery, which were flown at several heights. In Section 6.4 the imagery is validated by applying the SPM algorithm and then comparing the results with ground data, and also by comparing sensor radiance spectra. Section 6.5 summarizes the previous sections.

6.1 Aircraft Overflights

CASI overflights occurred on the 4th August and 1st September. The planned tracks were Fl 1 being flown axially along the estuary from North Killingholme Haven to the Chequer No 3 Buoy passing over Bull Sand Fort, see Figure 6-1. This was so that Fl 1 would show the sediment structure along the estuary and out into the plume. The second Fl was from the Oil Depot on the southern shore to Kilnsea in the north, and crosses Fl 1 at Bull Sand Fort and show the lateral variations at the estuary mouth. Fl 3 was from the Oil Depot to the Humber Light Buoy and would show the plume, crossing over Fl 1, and extending out into the clear water at the Humber Buoy. The flightlines would be flown sequentially at altitudes of 2000, 5000 and 10000 ft to aid in the development of an atmospheric correction.

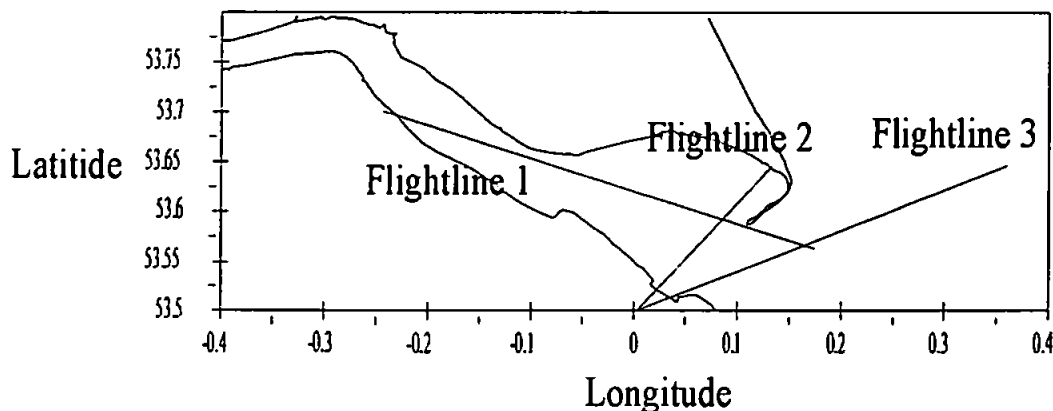


Figure 6-1: Proposed aircraft flightlines.

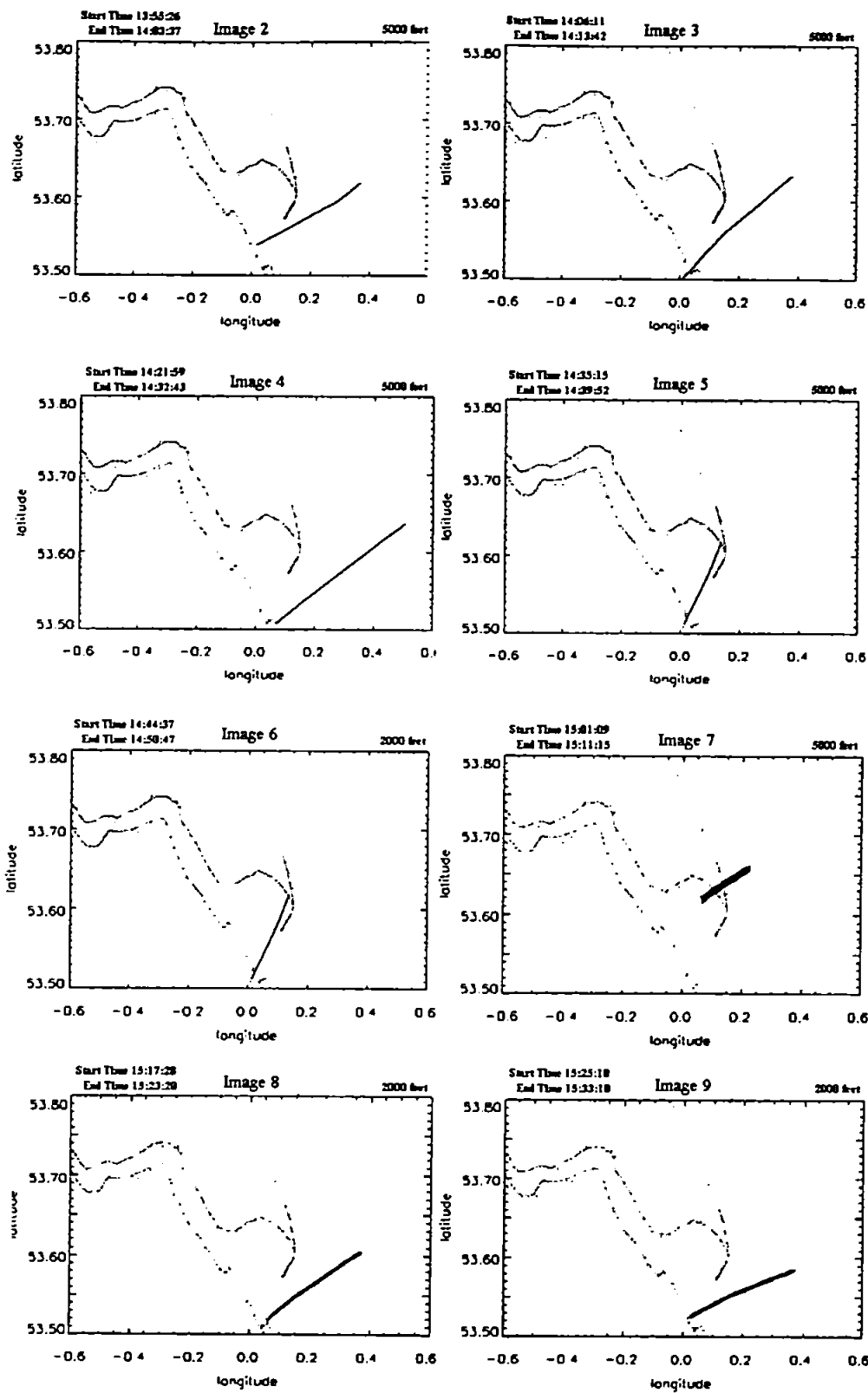


Figure 6-2: Flightline positions for the August Fieldwork

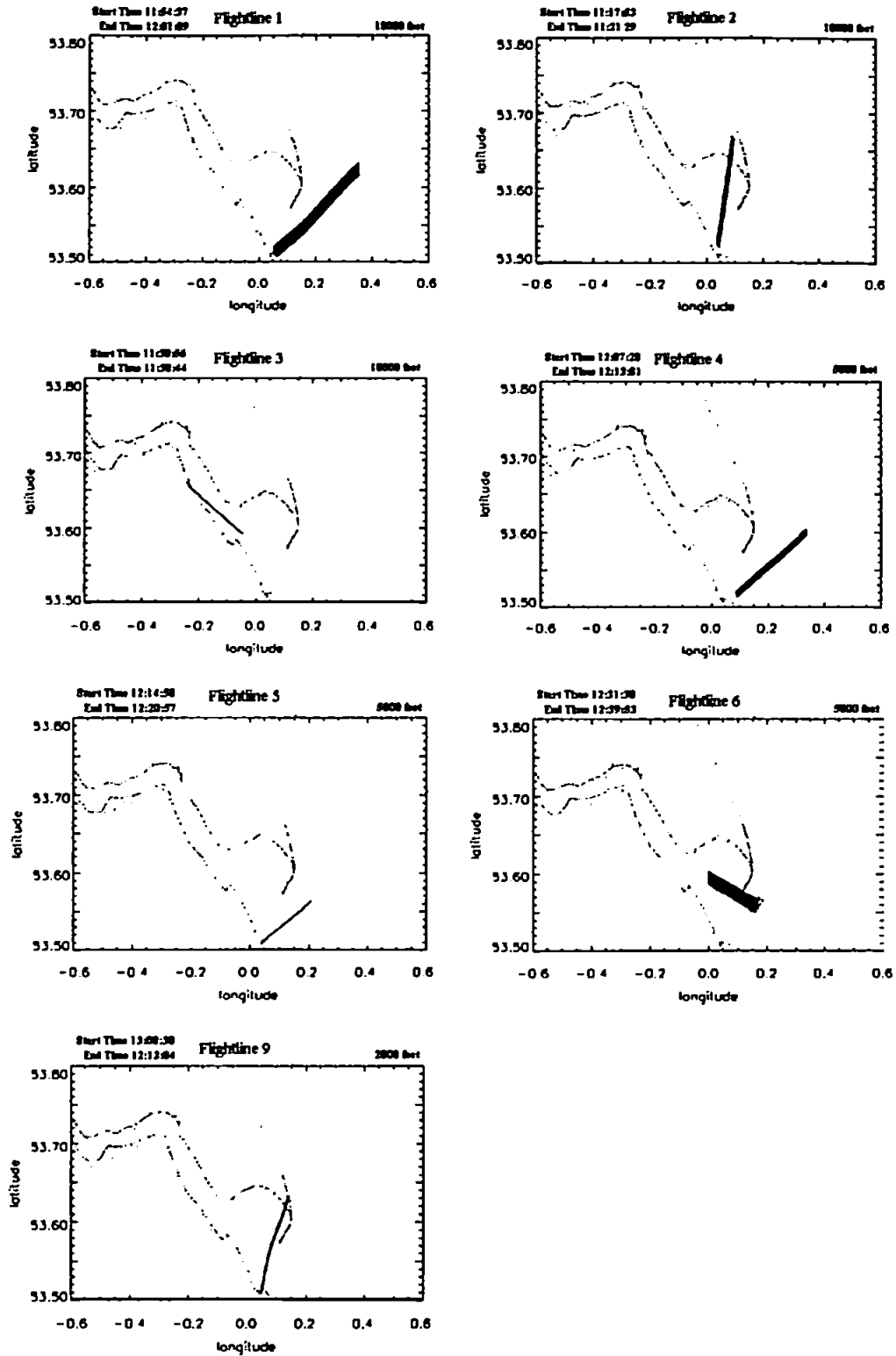


Figure 6-3: Flightline positions for the September Fieldwork.

In total 8 flightlines were flown in August and 8 in September, see Table 6-1. On 4 August there was low cloud so the aircraft only flew at heights of 2000 and 5000 ft, and there was also some cloud below the aircraft which can be seen in the imagery. On 1 September there was a small amount of cumulus cloud, present over the land on flightline (Fl) 2 and small amounts in Fl 1. The flights on 4 August were flown later than planned so were not at high water (see Table 6-1).

Table 6-1: Aircraft flightline details.

LINE Name (Altitude)	4th August			1st September		
	Start Time (Heading)	Time ± LW	No.	Start Time (Heading)	Time ± LW	No.
Axial (10000)				11:30:56 (115)	-1.35	3
Axial (5000)	15:01:07 (124)	+1.20	7	12:31:30 (295)	-0.34	6
Transaxial (10000)				11:17:53 (200)	-1.57	2
Transaxial (5000)	14:35:15 (041)	+0.77	5	12:58:12 (030)	+0.10	8
Transaxial (2000)	14:44:37 (225)	+0.92	6	13:08:28 (212)	+0.27	9
Humber Approaches (10000)				11:54:37 (060)	-0.96	1
Humber Approaches (5000)	13:55:26 (248)	+0.10	2	12:07:28 (252)	-0.74	4
	14:06:11 (062)	+0.28	3	12:14:58 (062)	-0.62	5
	14:13:42 (250)	+0.55	4			
Humber Approaches (2000)	15:17:18 (070)	+1.47	8			
	15:25:10 (259)	+1.57	9			

The flightlines varied in position from those planned (see Figures 6-2 and 6-3). The axial flightlines are not overlapping, so cannot be compared to each other, and August Fl 3 suffers from roll distortion despite a roll correction being applied (see Figure 6-4).

Figures 6-4 to 6-7 display the flightlines as true colour composites using wavebands 7, 3 and 1 (see Table 5-1). The axial flightlines indicate there are high SPM concentrations in the upper estuary. The GPS for August Fl 7 appears to be incorrect and August Fl 6 appears to have the same GPS data as Fl 5 which is incorrect (see Figure 6-5). September

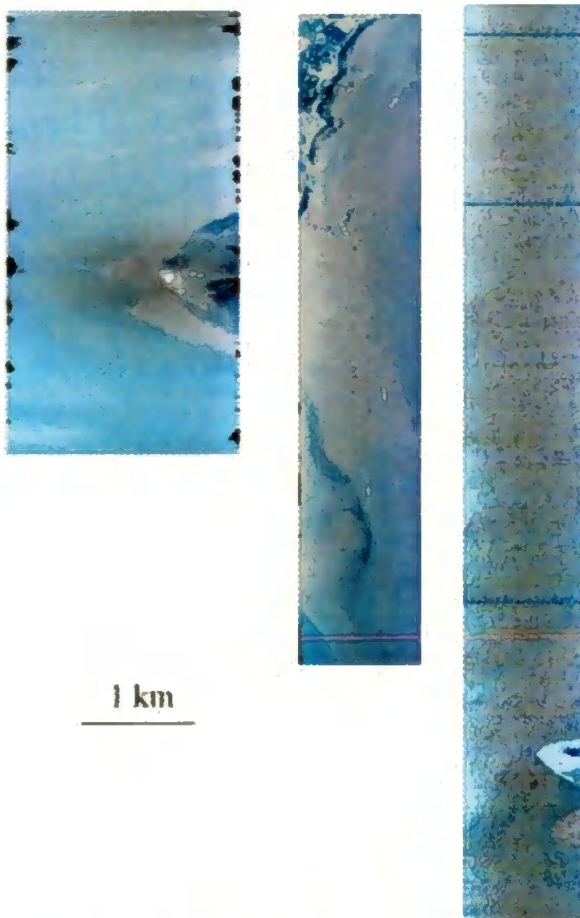


Figure 6-4: Axial flightlines (from left to right): September Fl 3; September Fl 6; August Fl 7.

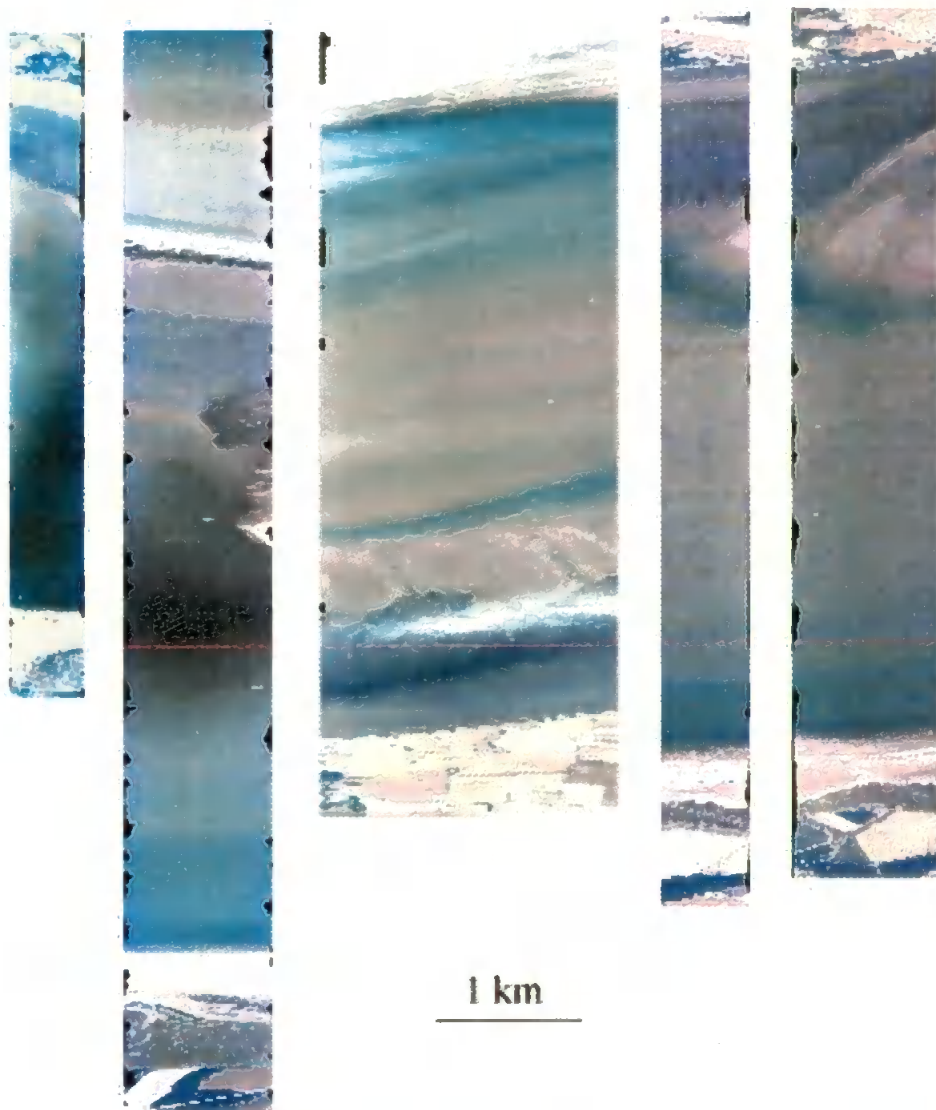


Figure 6-5: Transaxial flightlines (from left to right): August FI 6; August FI 5; September FI 2; September FI 8; September FI 9.

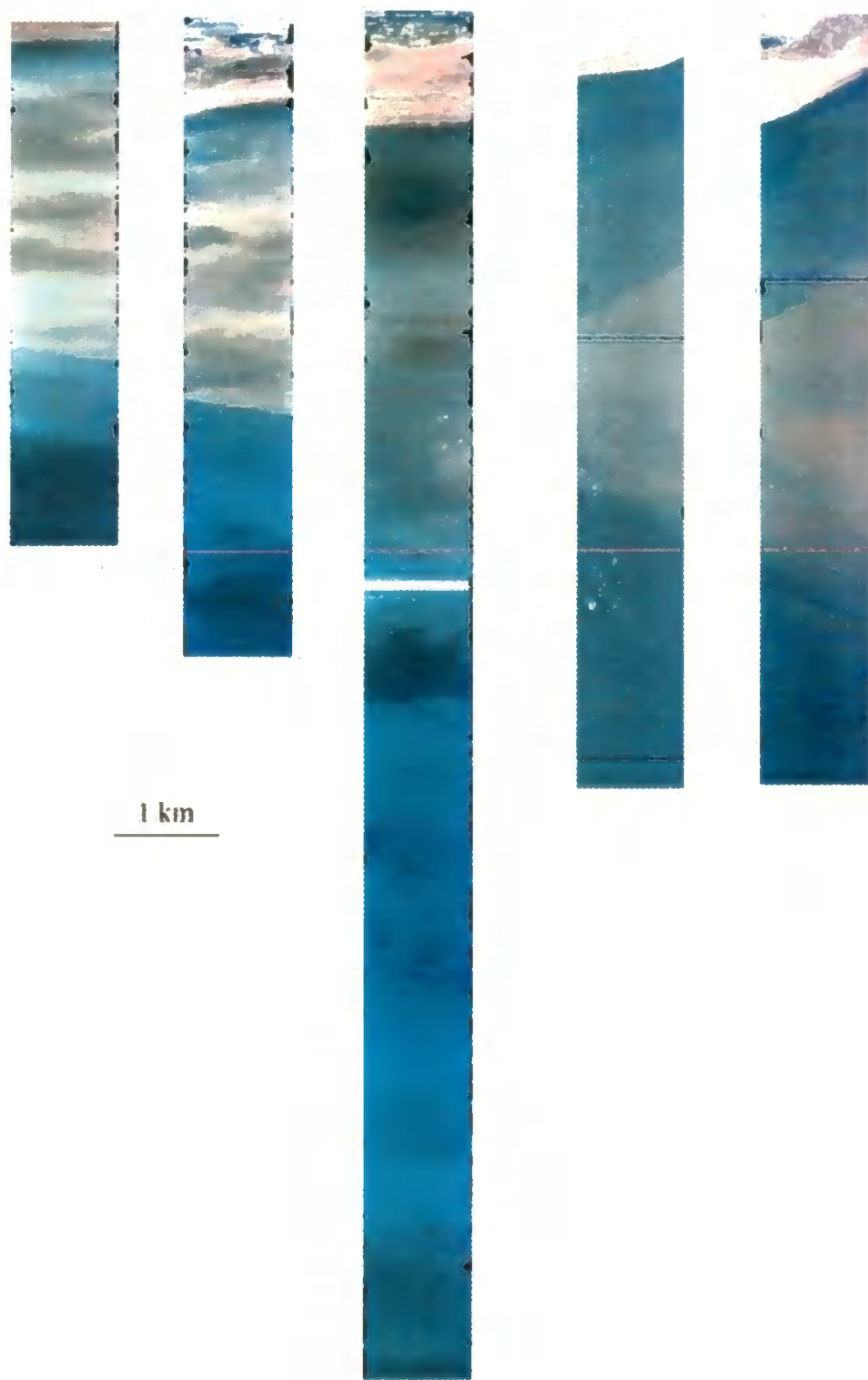


Figure 6-6: Humber Approaches at 5000 ft (from left to right): September Fl 4; September Fl 5; August Fl 2; August Fl 3; August Fl 4.



Figure 6-7: Humber Approaches (from left to right): August Fl 8; August Fl 9; September Fl 1.

fl 8 has no gps data (so is not shown in Figure 6-3). September flightlines 4 and 5 clearly show the Humber plume, but August flightlines 2 and 3 are obscured by a significant amount of cloud contamination. August Fl 4 shows the northern edge of the plume, but the southern edge is obscured. September Fl 1 has a large amount of cloud at the northern end.

The aircraft overflowed the vessel during the Humber Approaches flightlines, so there is good positioning of data points and highly accurate geometric correction was not needed.

6.2 Image Processing

The imagery was calibrated to radiance units ($\mu\text{W}/\text{cm}^2/\text{sr}/\text{nm}$) and then roll corrected by the NRA using the PC Borstadt software. At Plymouth, the processing was carried out using a custom program written in Interactive Data Language (IDL), this allowed high level programming with subroutines already built in for commonly used tasks such as image display (see Appendix 2). A 'C' program was written to convert the imagery from the supplied format (Easypace) which was pixel-interleaved, to a raw (unsigned 16-bit integer) band interleaved form with a separate ancillary file containing details of the image size and GPS data. This was then incorporated into a batch processing system which created: sediment maps; true colour composites; false colour composites. A program (ssample) was used to sub-sample the 16 bit imagery by a factor of 8 to give quick-look and test data, which enabled programs to run much faster.

The interactive IDL program (see Appendix 2) allowed the user to input data files and then scale, display and output results in the desired form. A colour table was created to display the suspended sediment maps in the NASA colour palette.

The sediment map function used the sediment algorithm as derived, in Mathcad, for the specific near infrared wavebands. The false colour composite includes two near infrared wavebands (12 and 11) and a visible waveband (7) as these are best at highlighting the suspended sediment distribution. The true and false colour composites were automatically

scaled between 0 and 4000 Digital Number (DN), as water targets cannot have a DN of greater than 4000 or $L_s(\lambda)$ of greater than $4 \mu\text{W}/\text{cm}^2/\text{sr}/\text{nm}$.

6.3 Image Investigation

6.3.1. Pixel Size

The across swath pixel size is determined by the Sensor Field-Of View (SFOV) and altitude, according to Equation 6-1, and the Swath Width would be the pixel width multiplied by the total number of pixels (512).

$$\text{Pixel Width} = \frac{\text{Altitude} \cdot \tan\left(\frac{\text{SFOV}}{2}\right)}{256} \quad (6.1)$$

For the altitudes flown the pixel widths would be as given in Table 6-2. So the Swath Width at 5000 ft is around 2.5 times that at 2000 ft, and the width at 10000 ft is around 2.0 times that at 5000 ft.

Table 6-2: Pixel width and swath width are calculated from Equation 6-1, with a SFOV of 35 degrees and given to 3dp.

Altitude (ft)	Pixel Width (m)	Swath Width (m)
10000	3.754	1922.061
5000	1.877	961.031
2000	0.751	384.421

The pixel length (along track direction) is determined by the aircraft speed and integration time. This will not be dependent on altitude, leading to non-square pixels. To compare imagery, the pixel number is converted to: degrees of latitude; degrees of longitude; distance from the land/sea interface (km). All three are calculated from the GPS data using a geometric correction model (see Appendix 2).

6.3.2 Comparison of nadir lines for contemporaneous imagery

6.3.2.1 Transaxial Imagery

September flightlines 8 and 9 were flown about 9.5 minutes apart after LW (see Table 6-1). Fl 8 had no GPS data, so only a visual position fix can be made. They appear to be over the same water as the sand banks at the top look similar (see Figure 6-5). Fl 9 has water in the top right-hand corner, because of the different altitudes, of 5000 and 2000 ft respectively, which result in Fl 8 being 2.5 times the width of Fl 9 (see Section 6.3.1). Both flightlines have similar water-leaving radiance values, with the area covered by water being from 12 to 19 km along the flight path, for both wavebands (given in Figure 6-8). The Fl 8 radiance

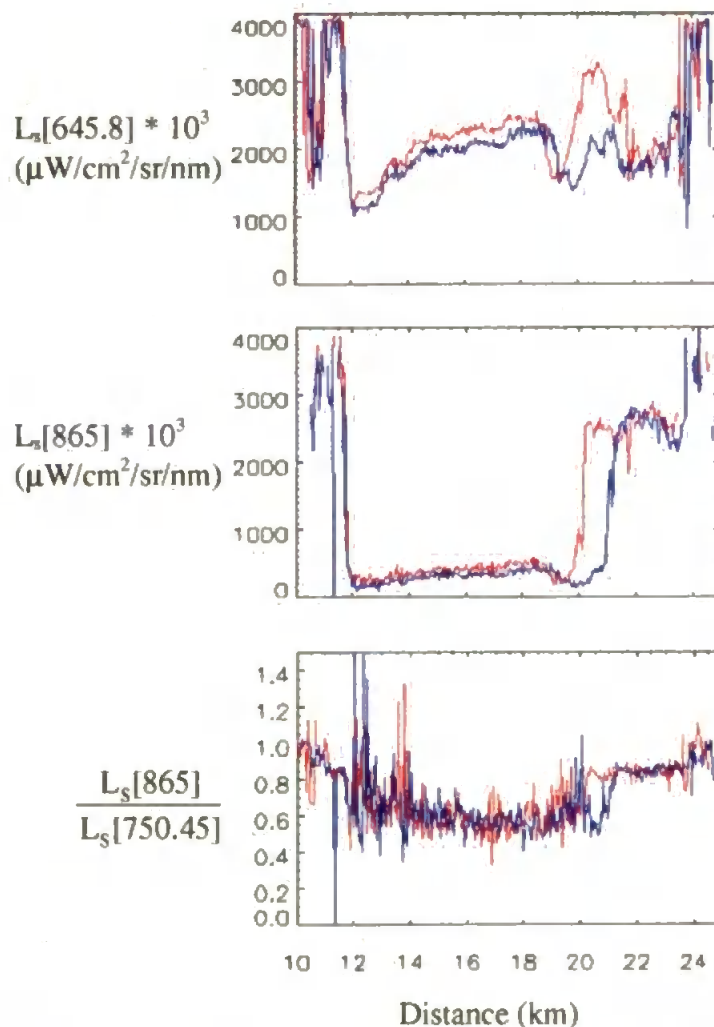


Figure 6-8: Nadir plots for September 1st flightlines 8 (red) and 9 (blue), showing the sensor radiance at 645.8 and 865 nm plus the near infrared waveband ratio.

has slightly higher values than Fl 9, due to the increased atmospheric signal because of the higher altitude. If flown on the same track Fl 8 has less water pixels, see the start of the northern shore, than 9 indicating that the water level has risen which would be consistent with the tidal height changing, and as Spurn Head has a gently sloping beach a small change in the tidal height will affect a large area. The waveband ratio is noisy, but the two flightlines only vary significantly with the different land/sea interfaces on the northern shore.

6.3.2.2 Humber Approaches

August flightlines 3 and 4 were flown at the same altitude (5000 ft) and around a quarter of an hour apart after LW (see Table 6-1). Fl 4 is longer in length, but has smaller pixels (5.354 m as compared to 8.031 m) in along track direction. This is because of the different orientations relative to the wind (see Table 4-1). Fl 3 also suffers from haze in the plume area (distance of 5 to 17 km along the flight path), resulting in much higher values in waveband 6 and slightly higher values in waveband 12, and the waveband ratio is significantly lower (see Figure 6-9).

September flightlines 1, 4 and 5 were flown at altitudes of 10000, 5000 and 5000 ft respectively. There were flown three quarters of an hour, a quarter of an hour and eight minutes before LW, within 20 minutes of each other (see Table 6-1). Fl 1 suffers from a small amount of cloud (see Figure 6-7), while flightlines 4 and 5 suffer from a large amount of haze (see Figure 6-6). Fl 1 has greater radiance values in both wavebands, due to its higher altitude (see Figure 6-10). Fl 4 doesn't have the sloping northern edge of 1 and 5, between approximately 8 and 16 km, but is the same afterwards. This is due to a navigation difference, see Figure 6-11, where Fl 4 is flown to the south east of Fl 1 and 5. Fl 1 shows greater structure, between 2 and 8 km, due to clouds between 5000 and 1000 ft. The southern fronts of the plume are more defined (at 4 and 6 km) than the northern edge, with a change in radiance of 0.4 and 0.5 respectively for waveband 11 (865 nm). The waveband ratio is less noisy in Fl 1.

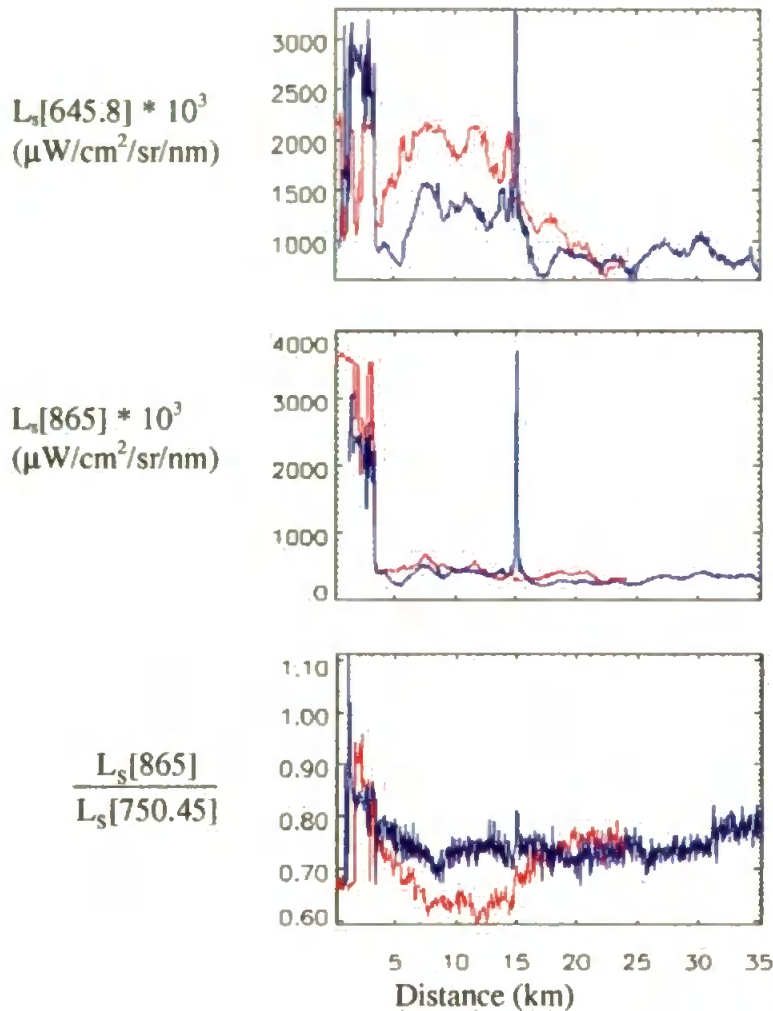


Figure 6-9: Nadir plots for August 4th flightlines 3 (red) and 4 (blue).

6.4 Results

6.4.1 Imagery validation

Airborne and satellite sensors are primarily validated by comparing the water-leaving radiances with the atmospherically corrected sensor radiances. The comparison of sensor-derived biogeochemical values with *in-situ* measurements is the secondary validation which gives confidence in the combined atmospheric correction and biogeochemical algorithm (Aiken & Moore, 1994). An estimated surface value is not directly comparable with satellite or airborne imagery because of the pixel size and inherent averaging, it is

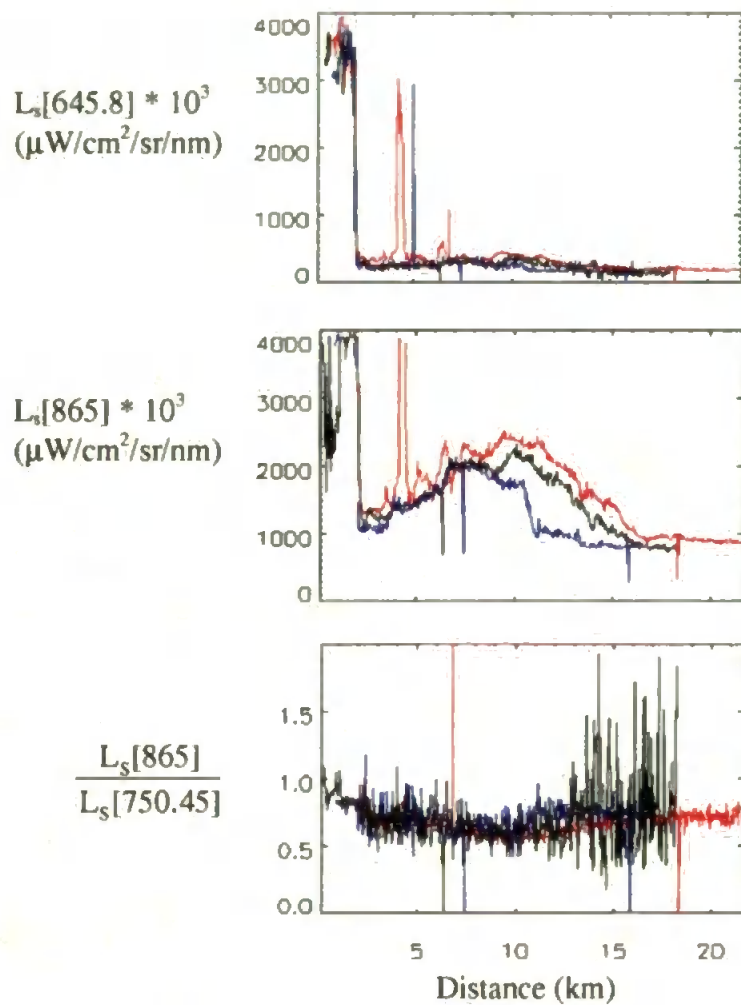


Figure 6-10: Nadir plots for September 1st flightlines 1 (red), 4(blue) and 5(black).

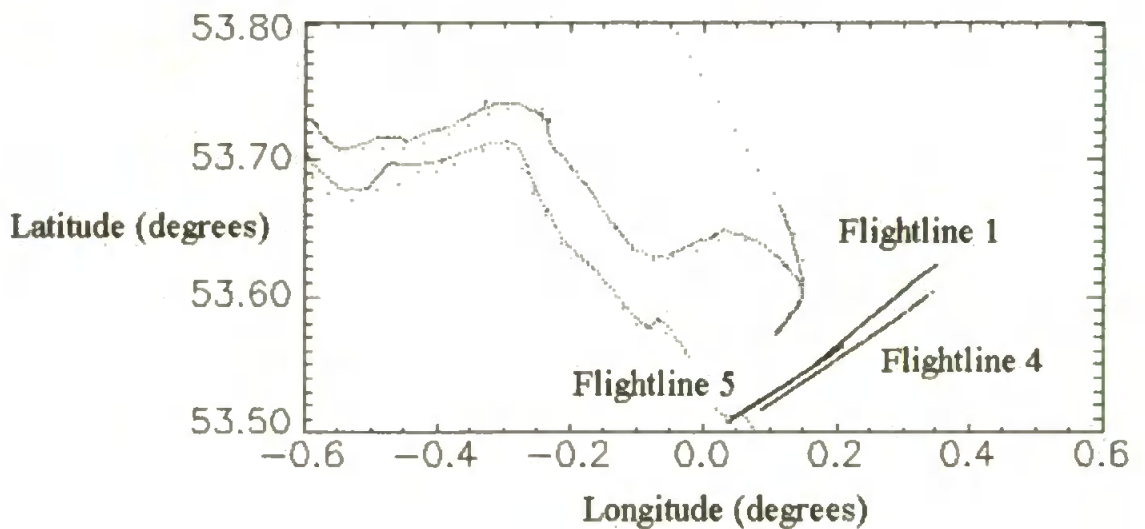


Figure 6-11: Position of September 1st flightlines 1, 4 and 5.

necessary to know the spatial variability around the measurement site. Airborne imagery can provide an intermediate value between the ground data and satellite imagery.

In this research contemporaneous airborne imagery has been compared to the ground data using the geometric position of the survey vessel on the imagery and as given on the thermal video (September only). This leads to several possible SPM values, so for each the average and standard deviation has been calculated for an enclosing 20 value block of pixels around the vessel.

6.4.1.1 August Humber Approaches

The August ground data (Figure 4-8) indicates that the survey vessel was positioned on a front during the overflight period. This front is also shown, by the change in the sensor radiance values, when plotting the Fl 8 nadir line radiance (see Figure 6-12). The graph also shows that the main sediment plume with the high SPM concentrations was to the east of the vessel, therefore the SPM concentration in this region was very low, ranging from 10 to 14 mg/l for the overflight periods (see Table 6-3). These low SPM values result in poor algorithm performance, as the water-leaving radiance waveband ratio data falls outside of the accepted limits (see Figure 6-13) due to the higher atmospheric contamination. On the resulting SPM maps we get good plume definition, but the regions with low SPM concentrations are rather noisy and do not produce a consistent SPM prediction.

6.4.1.2 September Humber Approaches.

In September both CASI and thermal video imagery were acquired. The survey vessel was, as with the August data, located on the edge of the plume at the northern end of the flightline. The position as given by the geometrically corrected image was 53.5768 N 0.2377 E, and on the thermal image (see Figure 6-14a) was 53.5794 N 0.2395 E. By comparing these positions with the ground data we get three sets of ground data to compare with Fl 1, see Table 6-4. The vessel's position, as given by Fl 4, was 53.5692 N 0.2484 E and the thermal imagery (see Figure 6-14b) gives 53.5677 N 0.2437 E as the position (see Table 6-4). There is no GPS data for the vessel in Fl 5, but the thermal image (see Figure 6-14c) gives the position as 53.5715 N 0.2324 E.

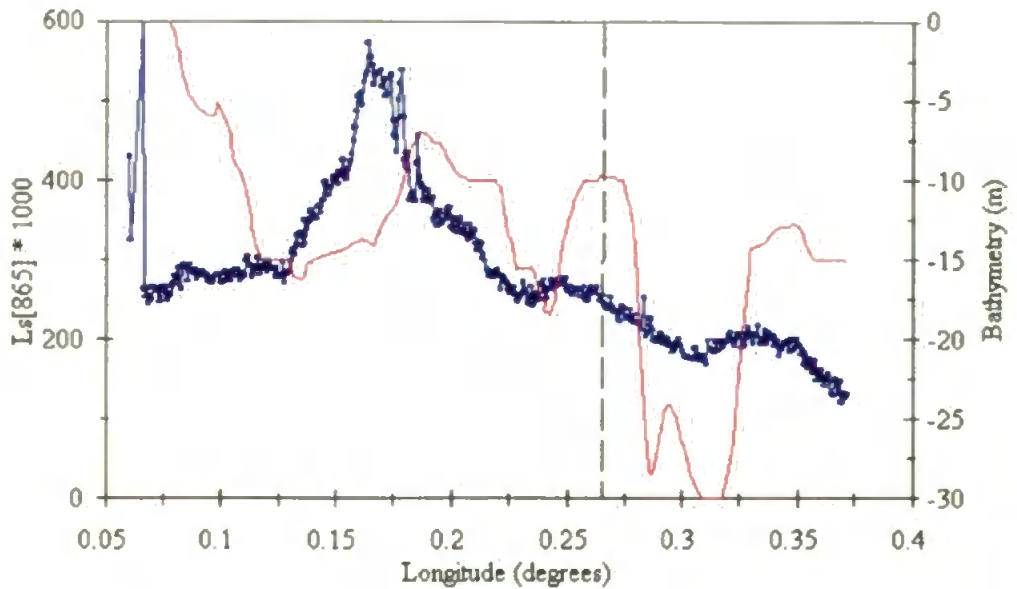


Figure 6-12: Plot of waveband 12 radiance (square symbols) and bathymetry (solid line) for August 4th Fl 8, with the survey vessel position marked with a dotted line.

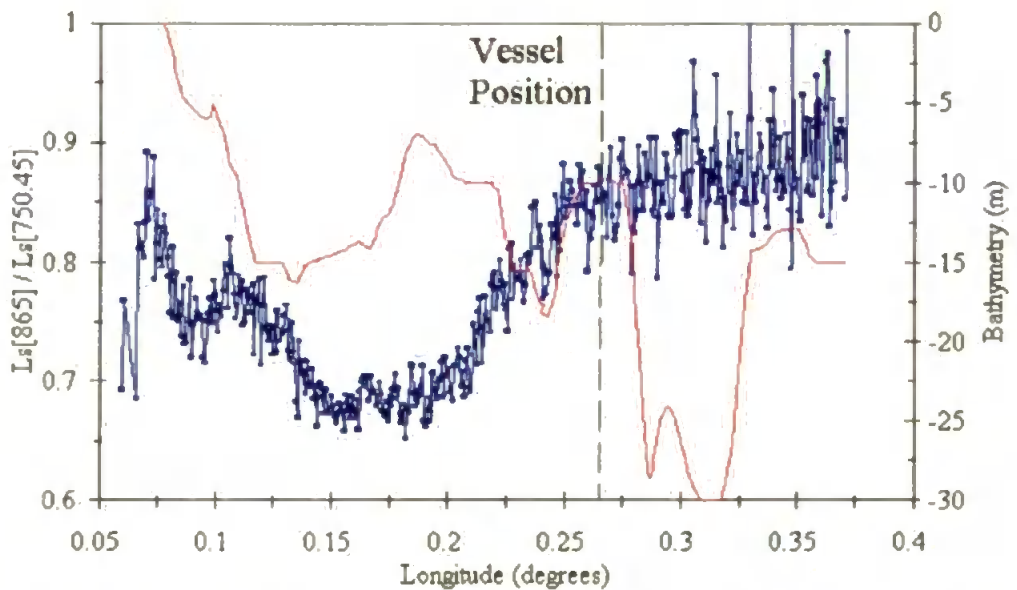


Figure 6-13: Plot of infrared waveband ratio radiance (square symbols) and bathymetry (solid line) for August 4th Fl 8, with the survey vessel position marked by a dotted line.

Table 6-3: Contemporaneous ground data with August Fl 4, 8 and 9. Time and position data from the QUBIT system, and SPM data from the calibrated nephelometer.

Time (GMT)	Latitude (N)	Longitude (E)	SPM (mg/l) [average /standard deviation]
Fl 4			
14.017	53.5603	0.2385	10.14 [12.26/0.99]
14.025	53.5613	0.2390	10.04 [12.30/1.00]
14.033	53.5627	0.2392	11.85 [12.34/1.02]
Fl 8			
14.817	53.5645	0.2320	14.90 [13.63/2.54]
14.825	53.5643	0.2318	14.77 [14.14/3.50]
14.833	53.5640	0.2320	13.70 [14.35/3.68]
Fl 9			
14.592	53.5672	0.2358	11.35 [11.20/1.98]
14.600	53.5673	0.2357	10.80 [11.21/0.49]
14.608	53.5673	0.2352	11.02 [11.22/0.49]
14.617	53.5672	0.2348	10.68 [11.24/0.49]

Table 6-4: Contemporaneous ground data for September Fl 1, 4 and 5. Time and position data from the QUBIT system, and SPM data from the calibrated transmissometer.

Time (GMT)	Latitude (N)	Longitude (E)	SPM (mg/l) [average/standard deviation]
Fl 1			
11.920	53.5531	0.2377	9.61 [9.53/0.32]
11.930	53.5538	0.2395	9.15 [9.46/0.34]
11.973	53.5586	0.2444	9.07 [9.11/0.27]
Fl 4			
12.051	53.5674	0.2404	13.19 [12.20/1.14]
12.153	53.5689	0.2392	11.00 [11.01/0.31]
12.177	53.5692	0.2395	10.59 [10.51/0.13]
12.184	53.5692	0.2397	10.38 [10.47/0.12]
12.197	53.5692	0.2396	10.67 [10.58/0.19]
Fl 5			
11.893	53.5514	0.2324	09.00 [10.67/1.00]
12.298	53.5704	0.2400	10.42 [10.49/0.06]
12.390	53.5715	0.2407	10.16 [10.00/0.18]
12.394	53.5715	0.2407	09.96 [9.93/0.19]

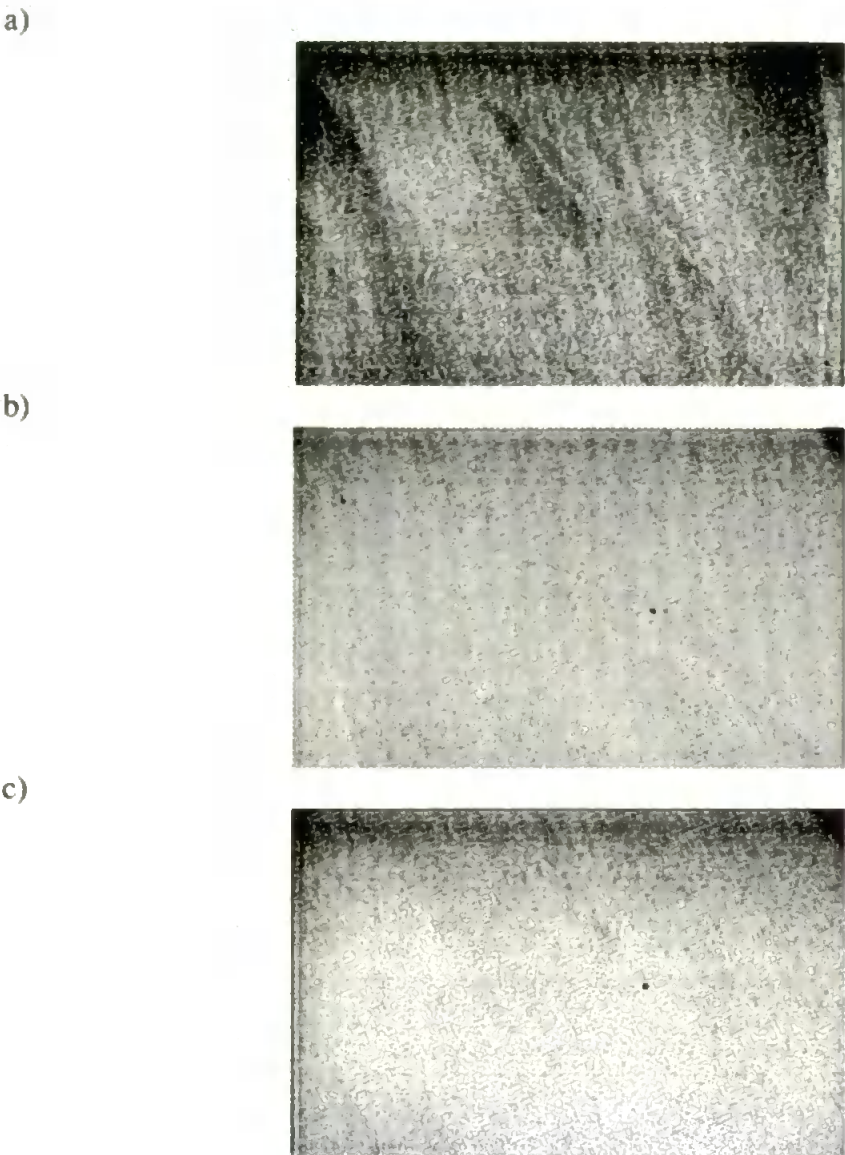


Figure 6-14: Thermal imagery contemporaneous with September 1st a) Fl 1, b) Fl 4 and c) Fl 5. The survey vessel is the black dot near the centre of each image.

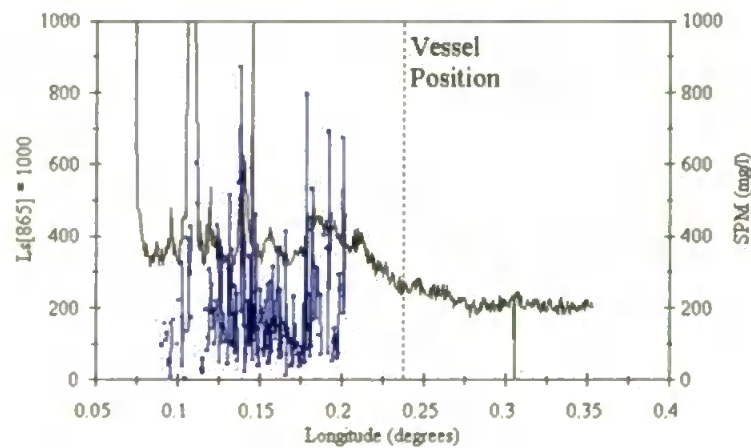


Figure 6-15: Plot of waveband 12 radiance (solid line) and calculated SPM (square symbols) for September Fl 1, with the survey vessels position marked by a dotted line.

By plotting the nadir line waveband 12 radiance and calculated SPM against longitude, for Fl 1, it is shown that the algorithm is working in the plume area (see Figure 6-15), but not at the vessel which was outside of the plume. This can also be seen by looking at the resulting SPM maps (see Figure 6-16). The maps indicate that there is a higher plume SPM concentration in Fl 1 as compared to Fl 4 and 5. They also show that the survey vessel was beyond the plume (in Case 1 water) where the algorithm is failing.

6.4.1.3 September Transaxial

There was unfortunately no contemporaneous ground data for this imagery, but we can compare September Fl 2 and 9. Fl 2 had much higher SPM concentrations, due to the overflight time related to the tidal cycle, as can be seen from looking at the waveband 12 radiance (see Figure 6-17). Fl 2 waveband 12 radiance also shows a good correlation with bathymetry.

When the calculated SPM was plotted instead of the waveband 12 radiance, Fl 2 displayed a reduced amount of noise and the correlation with bathymetry was improved (see Figure 6-18). When the sensor waveband radiance ratio was plotted against the waveband 12 radiance, the waveband ratio increased with an increasing waveband 12 radiance for Fl 2, but Fl 9 was less definitive (see Figure 6-19). The correlation between the waveband ratio and waveband 12 radiance is indicative of Case 2 water (with the water signal dominating), while an increasing waveband ratio with no increase in radiance indicates Case 1 waters (with a dominant atmospheric signal). Alternatively an increasing waveband 12 radiance with a constant waveband ratio indicates a land target.

Figure 6-20 shows a comparison of the wavelength spectra for the three sets of concurrent flightlines. August Fl 3 and 4 spectra are from the landward side and inside the plume (see Figure 6-9 for the nadir distance plots), September Fl 1, 4 and 5 spectra are from within and the seaward side of the plume (see Figure 6-10) and September Fl 8 and 9 spectra are from the southern and northern shores (see Figure 6-8). The September plume spectra (dotted lines) have a similar waveband 11/12 (750/865 nm) slope with altitude, suggesting that the water signal is larger than the atmospheric signal. Whereas the other spectra have a significant variation in this gradient indicating that the atmospheric signal is dominant.

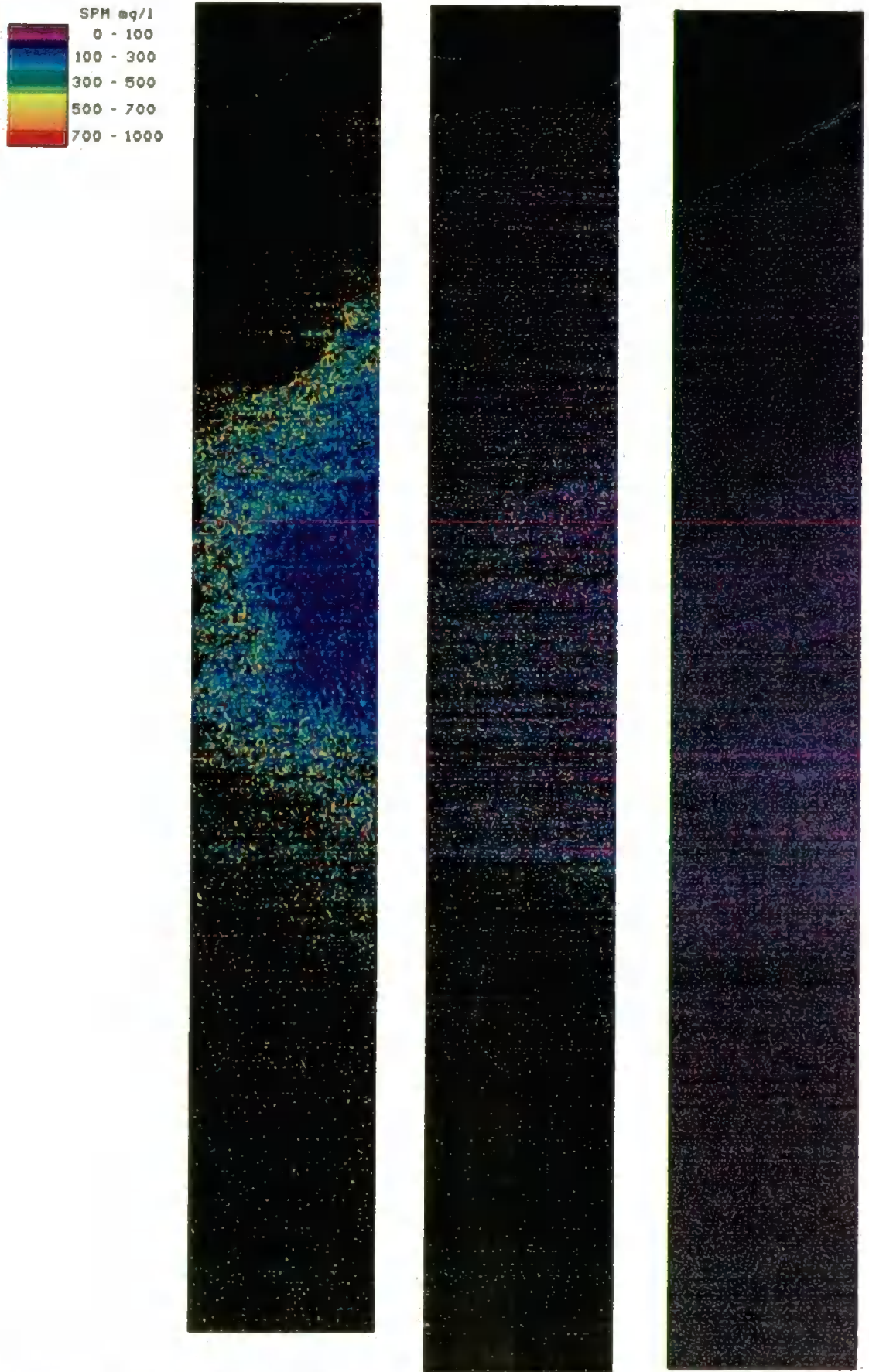


Figure 6-16: SPM maps for September flightlines 1, 4 and 5 (from left to right).

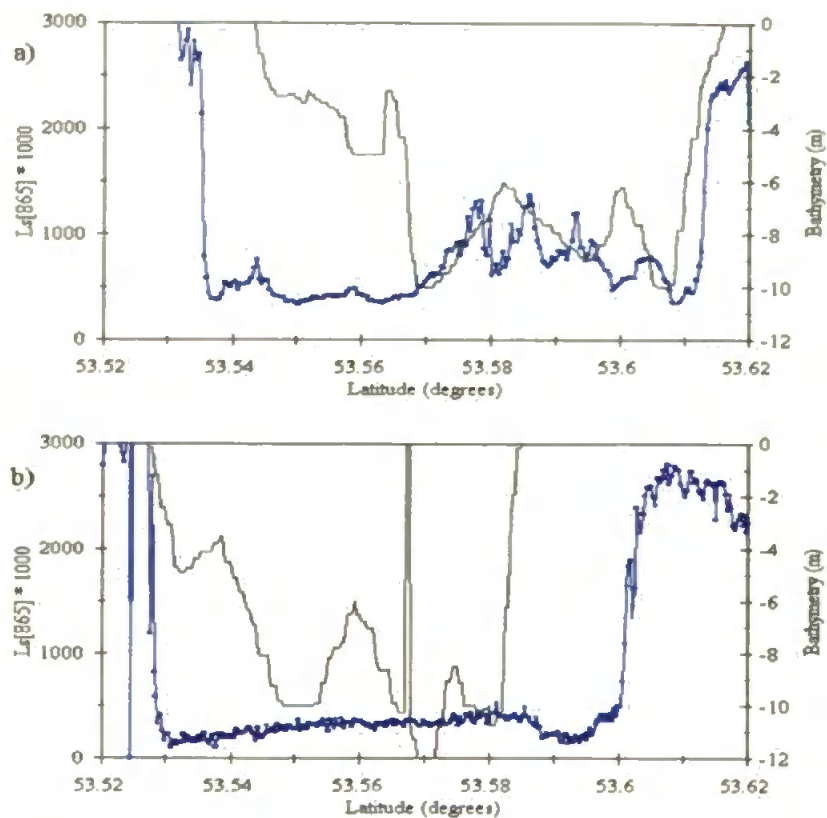


Figure 6-17: Plot of bathymetry (solid line) and waveband 12 radiance (dotted line) for September a) F1 2 and b) F1 9.

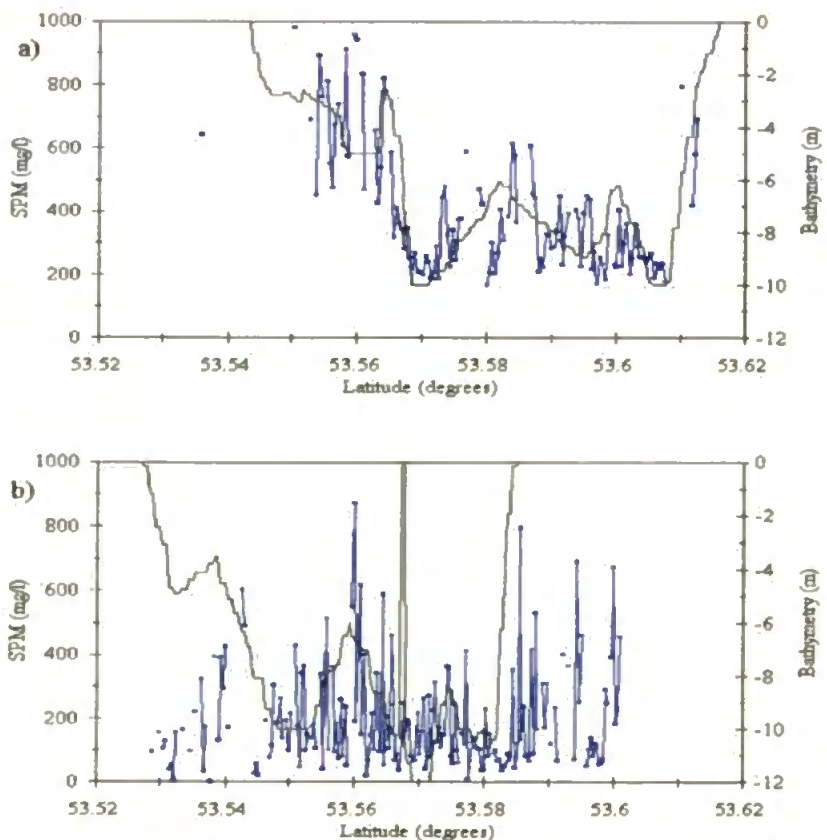


Figure 6-18: Plot of bathymetry (solid line) and calculated SPM (dotted line) for September a) F1 2 and b) F1 9.

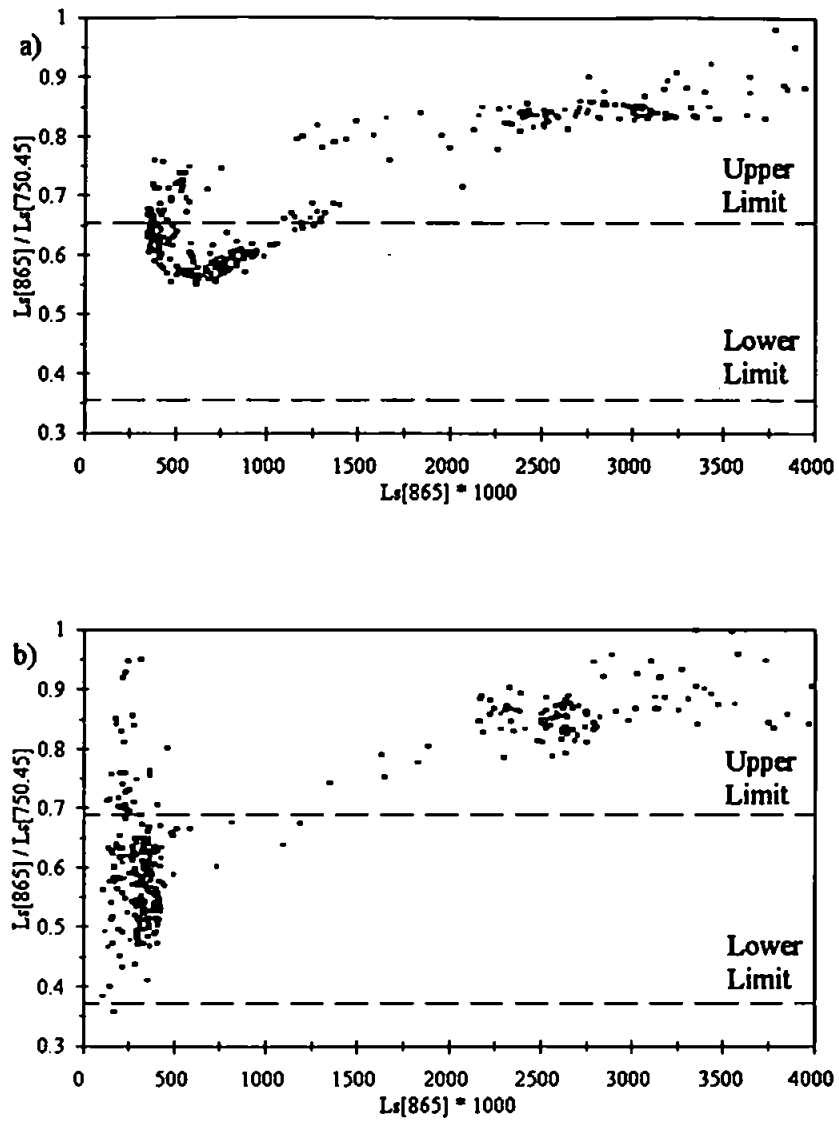


Figure 6-19: Regression of waveband 12 versus the sensor waveband radiance ratio for September Fl a) 2 and b) 9.

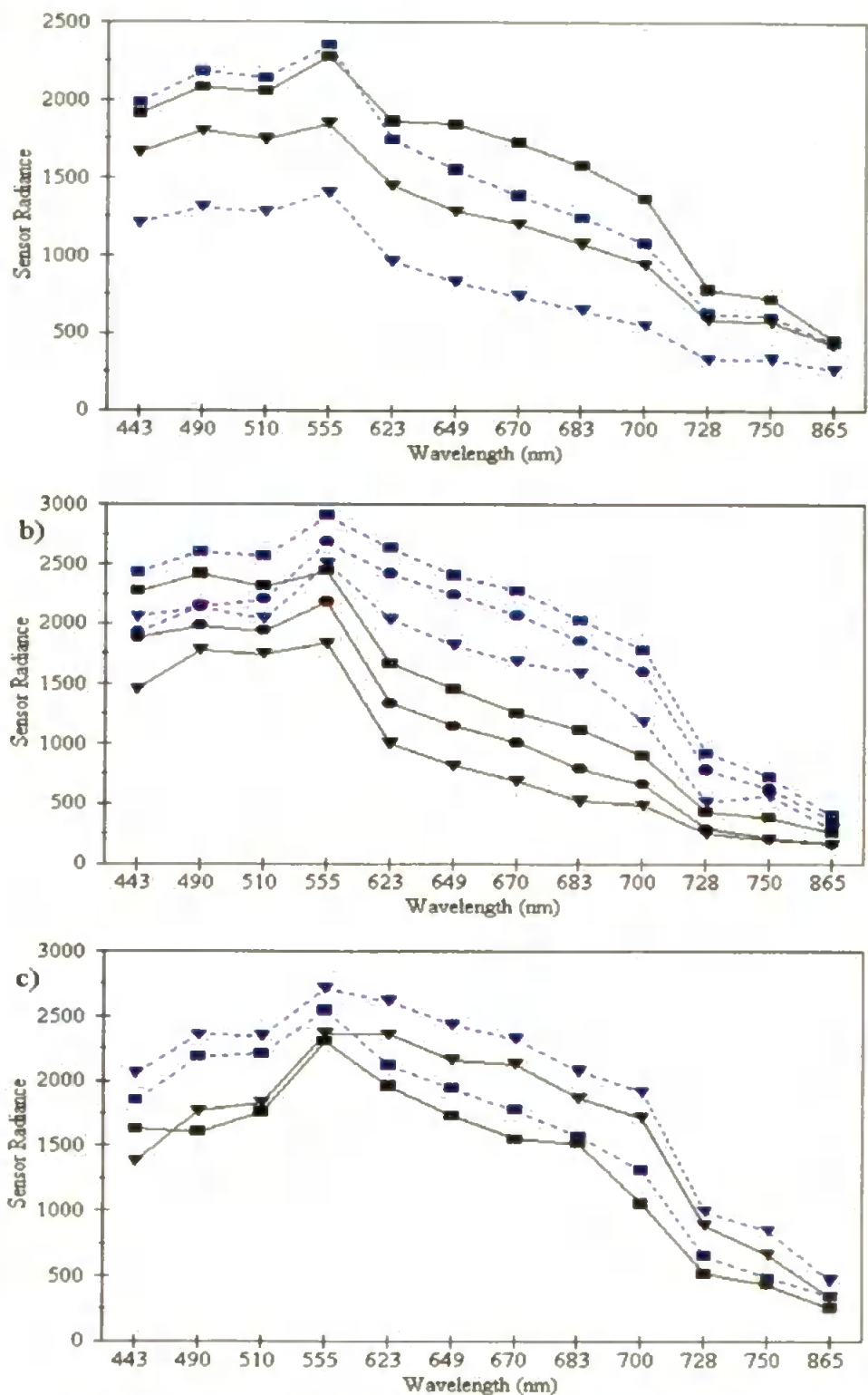


Figure 6-20: Comparison of the wavelength spectra for:

- a) August Flightlines 3 (triangles) and 4 (squares) at 5 km (dotted line) and 10 km (solid line).**
- b) September Flightlines 1 (squares), 4 (triangles) and 5(circles) at 10 km (dotted line) and 15 km (solid line).**
- c) September Flightlines 8 (triangles) and 9 (squares) at 14 km (dotted line) and 18 km (solid line).**

6.4.2 Spectral Radiance Comparison

In this section the spectral components, as opposed to the nadir lines (in Section 6.3.2) will be compared, see Figure 6-21. All three sets of spectra show a peak response at 555 nm (waveband 4). The three near-infrared wavebands have consistently lower levels than the visible. As expected, the greater the altitude the higher the sensor radiance due to the atmospheric signal. This shows that the water to aircraft atmospheric path contributes a greater signal than the solar to water path, due to the aerosol backscattering of the downwelling solar irradiance and much smaller signal leaving the water compared to that which was downwelling. The August, compared to September, spectra have lower water-leaving radiance levels despite the higher SPM values (see Table 6-3 and 6-4) due to the August overcast conditions and hence lower solar irradiance values.

6.5 Discussion

Without an atmospheric correction, the algorithm produces SPM concentration estimates for turbid Case 2 waters, with an SPM range of 200 to 1000 mg/l. Below 200 mg/l the atmospheric compared to water-leaving signal becomes large and so large errors can occur. Above 1000 mg/l the waveband ratio versus SPM relationship flattens off to form an asymptote and so became insensitive, so a cut-off was used at this level with the waveband ratio range exceeding its limits.

When large amounts of aerosols are present, in the atmosphere, the waveband ratio's accepted range will be exceeded and those pixels masked out. However, with thin cloud and in Case 1 water conditions the ratio may reach, but not exceed, the top of the range and so predict erroneously high SPM concentrations.

As the algorithm uses the near-infrared wavelength region, where it integrates the signal arising from a depth of less than 20 cm, it can be assumed that the SPM concentration is homogeneous for this layer. So the SPM maps represent the 'surface' SPM concentrations and the algorithm will work well in 'shallow' areas.

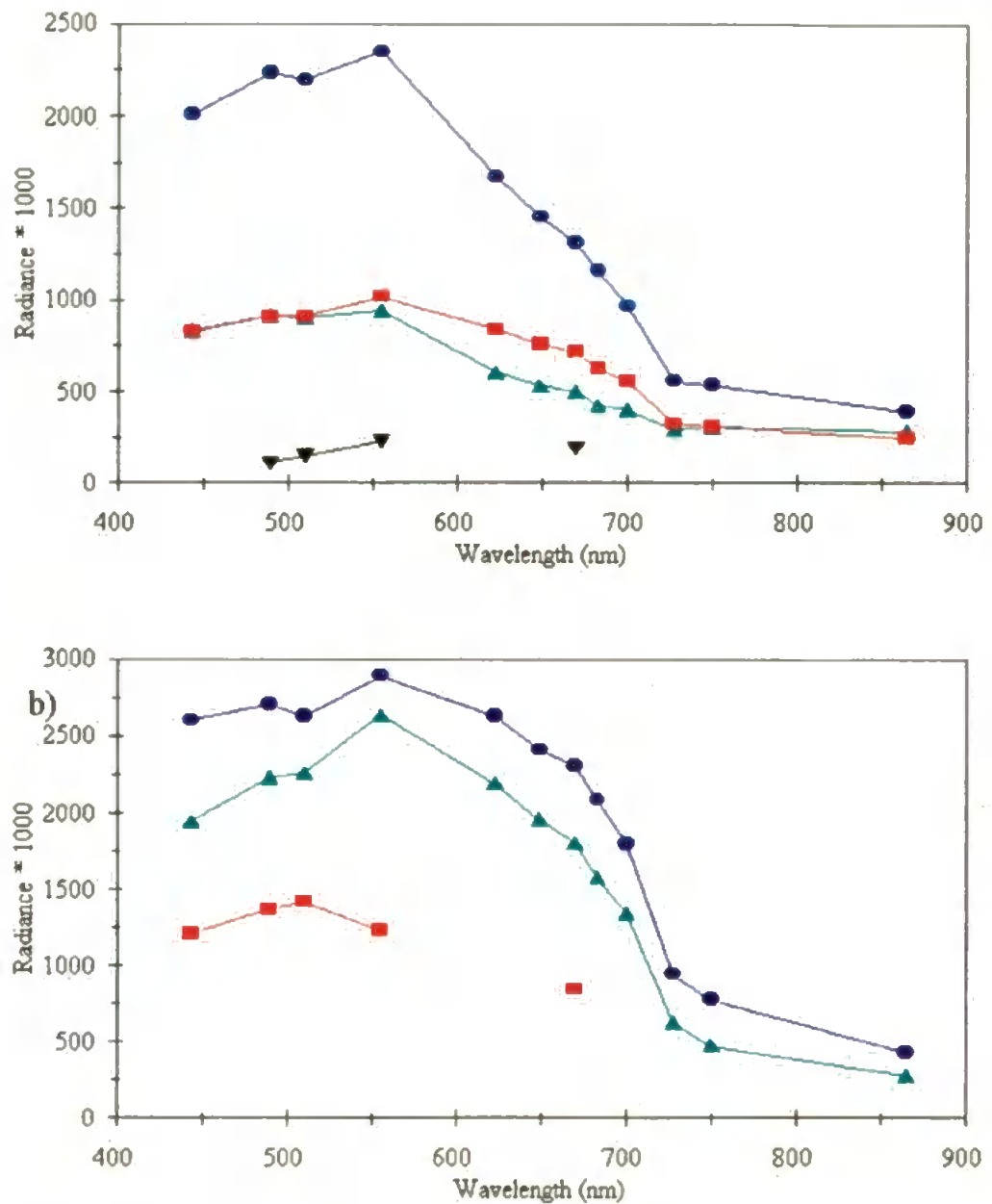


Figure 6-21: Comparison of the wavelength spectra for:

- a) August with measurements at 5000 ft (circles), Fl 8 2000 ft (triangles), Fl 9 2000 ft (squares) and at the sea-surface (upside-down triangles).**
- b) September with measurements at 10000 ft (circles), 5000 ft (triangles) and at the sea-surface (squares).**

7. CONCLUSION AND DISCUSSION

This chapter draws together the earlier chapters and then discusses the application of the SPM algorithm and future research.

7.1 Algorithm Development

The laboratory experiments produced consistent results which showed that over the whole spectral range, there is an increase in reflectance with SPM concentration. In the visible wavelengths, there are different magnitudes of reflectance and spectral shapes caused by different sediment types but in the near infrared only the particle size affects the reflectance signal.

Particle size is very important in determining the amount of backscattered light and affects both the visible and near infrared. In developing the algorithm only the sediment fine fractions were used, as any particles larger than this are unlikely to remain in the top 0.2 m of the water column (the approximate penetration depth for the near infrared wavebands) under normal conditions.

DOM and phytoplankton affect the signal up to about 700 nm, so above this we only have the influence of suspended sediment and water. The near infrared reflectance has a more robust relationship with SPM despite the smaller signal and relative changes than in the visible. By ratioing the two near infrared wavebands (SeaWiFS 7 and 8), a robust relationship with SPM is achieved, which is highly stable for a number of sediment types and reduces the variation due to particle size.

The near infrared waveband ratio to SPM relationship was validated with a simple semi-analytical model, which used data and equations taken from the literature and allowed for the development of a global as opposed to specific algorithm from a regression technique. The model also enables the reflectance equation to be converted to normalized water-leaving radiance, which is the property measured by airborne imagers.

As an atmospheric correction was beyond the scope of this PhD, a correction for atmospheric attenuation was developed and used the ground level solar irradiance measurements. It was shown that the SPM algorithm was sensitive to small changes in the solar irradiance waveband ratio and a full atmospheric correction was needed.

A Case 2 atmospheric correction could utilize the SPM algorithm, as the model can predict the water-leaving radiance in the two wavebands, as opposed to a Case 1 atmospheric correction where it is assumed to be zero. The development of such an atmospheric model is beyond the scope of this thesis, but will be undertaken as further work (see Section 7.4).

7.2 Algorithm Validation

The algorithm worked, without an atmospheric correction, in turbid Case 2 waters (SPM > 200 mg/l) as the suspended sediment signal dominates the atmospheric signal. However, at lower concentrations there is an atmospheric contamination, which is detectable in the across swath direction.

The algorithm can efficiently mask out land and other solid targets, giving a position for the land/sea interface as the algorithm holds in shallow water (greater than 0.2 m in depth). The algorithm can also mask out 'pure cloud' pixels, but fails on 'part cloud' or high aerosol pixels where it predicts high SPM values. Clouds can be removed, prior to the algorithm, using a cloud mask (Darzi, 1992) and high aerosols should be removed with an atmospheric correction.

7.3 *In-situ* Measurements

The transmissometers and nephelometer were not suited to the turbid Case 2 waters found within the Humber Estuary, resulting in a lack of continuous SPM data at concentrations above 200 mg/l. A future substitute for these conditions may be $K_d[550]$ and $K_d[632]$ calculated from the underwater light sensors, which gave structural detail at these higher

concentrations (see Figure 4-13a). There is a need for a large number of bottle samples to calibrate the K_d relationship as it had a large spread of values and will vary with both sediment type and particle size. Despite this spread, both the UOR and PRR produced comparable values and the calculated water-leaving radiance values compared favorably to the sensor radiance values.

The fieldwork experiments highlight the problems in obtaining contemporaneous *in-situ* data and airborne imagery. A possible solution is the use of optical buoys, such as the Humber Flux Curtain (Hadlington, 1995) being utilized within the LOIS experiment and the Plymouth Marine Bio-Optical Data Buoy (PlyMBODY) being used for SeaWiFS validation.

7.4 Further Work

The SPM algorithm must be tested in other areas with different sediment types to check its global applicability, which would make it suitable for a satellite (e.g. SeaWiFS) global algorithm. As the algorithm lacks sensitivity in low SPM concentrations there will be a need for a 'visible band' alternative in Case 1 and low Case 2 waters. The extension into the visible wavelengths may also lead to the development of algorithms which can classify different sediment types. The sediment algorithm can also be incorporated into a more advanced water-optics model which would predict the chlorophyll-*a* and DOM concentrations by deconvolving the spectra.

The SPM algorithm can also be incorporated into a Case 2 atmospheric correction. This work has already been started with the Plymouth Atmospheric Closure Experiment (PACE), which involved contemporaneous measurements using: the Meteorological research flight; NERC aircraft; NRA aircraft; ground based measurements; several vessels. The aim is to measure all the relevant parameters so that the Case 2 atmospheric correction model can be comprehensively validated using multi-height flightlines (see appendix 3).

REFERENCES

- Aiken, J. and Bellan, I. (1990). Optical oceanography: an assessment of towed measurement. In *Light and life in the Sea.*, Eds. Herring, P.J., Campbell., A.K., Whitfield, M. and Maddock, L., Cambridge University Press, 39-57.
- Amos, C.L. and Topliss, B.J. (1985). Discrimination of suspended particulate matter in the Bay of Fundy using the Nimbus 7 Coastal Zone Color Scanner. *Canadian Journal of Remote Sensing*, 11, 1, 85-92.
- Andre, J. and Morel, A. (1989). Simulated effects of barotropic and ozone content upon the estimate of marine phytoplankton from space. *Journal of Geophysical Research*, 94, C1, 1029-1037.
- Anger, C.D., Mah, S. and Babey, S.K. (1994). Technological enhancements to the Compact Airborne Spectrographic Imager (CASI). First International Airborne Remote Sensing Conference and Exhibition, Strasbourg, France.
- Angstrom, A. (1964). The parameters of atmospheric turbidity. *Tellus*, 16, 64.
- Aranuvachapun, S. (1986). The atmospheric optical depth spectrum determined from CZCS radiance. *International Journal of Remote Sensing*, 7, 1, 105-118.
- Aranuvachapun, S. (1985). Satellite remote sensing of ocean colours. International Conference on advanced technology for monitoring and processing global environmental data, London, UK, 513-520.
- Arnett, R. (1991). Estuarine pollution: A Case Study Of The Humber. *Geography*, 76, 67-69.
- Austin, R.W. (1974). The remote sensing of spectral radiance from below the ocean surface. In *Optical Aspects Of Oceanography*, Eds. N.G. Jerlov and E.S. Nielsen, Academic Press, 317-344.

References

Bale, A.J., Tocher, M.D., Weaver, R., Hudson, S.J. and Aiken, J. (1994). Laboratory measurements of the spectral properties of estuarine suspended particles. *Netherlands Journal of Freshwater Ecology*, 28, 3-4, 237-244.

Barr, R., Watson, P.G., Ashcroft, C.R., Barnett, B.E. and Hilton, C. (1990). Humber Estuary - A Case Study. *Hydrobiologia*, 195, 127-143.

Bhargava, D.S. and Mariam, D.W. (1991). Effects of suspended particle size and concentration on reflectance measurements. *Photogrammetric Engineering & Remote Sensing*, 57, 5, 519-529.

Bhargava, D.S. and Mariam, D.W. (1990). Spectral reflectance relationships to turbidity generated by different clay materials. *Photogrammetric Engineering & Remote Sensing*, 56, 2, 225-229.

Bhargava, D.S. and Mariam, J.S. (1991). Light penetration depth, turbidity and reflectance related relationships and models. *ISPRS Journal of Photogrammetry and Remote Sensing*, 46, 217-230.

Bird, E.R. and Riordan, C. (1986). Simple solar spectral model for direct and diffuse irradiance on horizontal and tilted planes at the earth's surface for cloudless atmospheres. *Journal of Climate and Applied Meteorology*, 25, 87-97.

Bricaud, A., Morel, A. and Prieur, L. (1981). Absorption by dissolved organic matter of the sea (yellow substance) in the UV and visible domains. *Limnology and Oceanography*, 26, 1, 43-53.

Bricaud, A., Morel, A. and Prieur, L. (1983). Optical efficiency factors of some phytoplankters. *Limnology and Oceanography*, 28, 5, 816-832.

British Transport Docks Board (1980). Humber Estuary Sediment Flux. Report No. 283.

References

particulate constituents of the Tampa Bay coastal plume. *Photogrammetric Engineering & Remote Sensing*, 59, 3, 339-344.

Carder, K.L., Reinersman, P., Chen, R.F., Muller-Karger, F., Davis, C.O. and Hamilton, M. (1993). AVIRIS calibration and application in coastal oceanic environments. *Remote Sensing Environment*, 44, 205-216.

Choubey, V.K. and Subramanian, V. (1991). Spectral Response Of Suspended Sediments In Water Under Controlled Conditions. *Journal of Hydrology*, 122, 301-308.

Clarke, G.L. and Ewing, G.C. (1974). Remote Spectroscopy of the sea for biological production studies. In *Optical Aspects Of Oceanography*, Eds. Jerlov, N.G. and Nielsen, E.S., New York Academic Press, 389-413.

Collins, M. and Pattiaratchi, C. (1984). Identification of suspended sediment in coastal waters using airborne thematic mapper data. *International Journal of Remote Sensing*, 5, 4, 635-657.

Curran, P.J. (1985). *Principles of Remote Sensing*. Longman Scientific and Technical, London, pp 8-55.

Curran, P.J. (1987). Airborne multispectral scanner data for estimating dye dispersion from sea outfalls. *Proceedings of the Institute of Civil Engineers*, 2, 83, 213-241.

Curran, P.J., Hansom, J.D., Plummer, S.E. and Pedley, M.I. (1987). Multispectral remote sensing of nearshore suspended sediments: a pilot study. *International Journal of Remote Sensing*, 8, 1, 103-112.

Darzi, M. (1992). Volume 7, Cloud screening for polar orbiting visible and infrared (IR) satellite sensors. *SeaWiFS Technical Report Series*, eds. Hooker, S.B. and Firestone, E.R., 104566, pp 1-7.

Davies-Colley, R.J. and Vant, W.N. (1987). Absorption of light by yellow substance in freshwater lakes. *Limnology and Oceanography*, 32, 2, 416-425.

References

- Doerffer, R. (1979). Applications of a two-flow model for remote sensing of substances in water. *Boundary-Layer Meteorology*, 18, 221-232.
- Elterman, L. (1968). UV, visible and IR attenuation for altitudes to 50 km. AFCRL-68-0153, Environmental Research Paper, 285.
- Ferrari, G.M. and Tassan, S. (1991). On the accuracy of determining light absorption by "yellow substance" through measurements of induced fluorescence. *Limnology and Oceanography*, 36, 4, 777-786.
- Gordon, H.R. (1978). Removal of atmospheric effects from satellite imagery of the oceans. *Applied Optics*, 17, 10, 1631-1636.
- Gordon, H.R. (1994a). Equivalence of the point and beam spread functions of scattering media: a formal demonstration. *Applied Optics*, 33, 6, 1120-1122.
- Gordon, H.R. (1994b). MODIS Normalised Water-leaving Radiance Algorithm Theoretical Basis Document. Version 1. NASA MODIS Technical Memo.
- Gordon, H.R., Brown, O.B., Evans, R.H., Brown, J.W., Smith, R.C., Baker, K.S. and Clark, D.K. (1988). A semi-analytical radiance model of ocean color. *Journal of Geophysical Research*, 93, D9, 10909-10924.
- Gordon, H.R. and Castano, D.J. (1987). Coastal Zone Color Scanner atmospheric correction algorithm: multiple scattering effects. *Applied Optics*, 26, 11, 2111-2122.
- Gordon, H.R. and Clark, D.K. (1980). Atmospheric correction in the remote sensing of phytoplankton pigments. *Boundary-Layer Meteorology*, 18, 299-313.
- Gordon, H.R., Clark, D.K., Brown, J.W., Brown, O.B., Evans, R.H. and Broenkow, W.W. (1983). Phytoplankton pigment concentrations in the Middle Atlantic Bight: comparison of ship determinations and CZCS estimates. *Applied Optics*, 22, 1, 20-36.

References

- Gordon, H.R. and McCluney, W.R. (1975). Estimation of the depth of sunlight penetration in the sea for remote sensing. *Applied Optics*, 14, 2, 413-416.
- Gordon, H.R. and Morel, A.Y. (1983). Remote assessment of ocean color for interpretation of satellite visible imagery. Springer-Verlag, New York, Berlin, Heidelberg, Tokyo, pp 19-28.
- Gordon, H.R. and Wang, M. (1994). Retrieval of water-leaving radiance and aerosol optical thickness over the oceans with SeaWiFS: a preliminary algorithm. *Applied Optics*, 33, 3, 443-452.
- Greenpeace Toxics Division. (1982). The Humber estuary, Greenpeace, pp 1-4.
- Gregg, W.W. and Carder, K.L. (1990). A simple spectral solar irradiance model for cloudless maritime atmospheres. *Limnology and Oceanography*, 35, 8, 1657-1675.
- Groom, S.B., Moore, G.F., Aiken, J., Allen, C.M. and Bellan, I. (1989). Proceedings of the NERC Remote Sensing Workshop, Institute of Freshwater Ecology, Windermere, 155-168.
- Guzzi, R., Rizzi, R. and Zibordi, G. (1987). Atmospheric correction of data measured by a flying platform over the sea: elements of a model and its experimental validation. *Applied Optics*, 26, 15, 3043-3051.
- Haardt, H. and Maske, H. (1987). Specific in vivo absorption coefficient of chlorophyll-*a* at 675 nm. *Limnology and Oceanography*, 32, 3, 608-619.
- Hadlington, S. (1995). Muddy secrets of the Humber. *The Independent*, Section 2, 27th June, 14.
- Hamilton, M.K., Davis, C.O., Rhea, W.J., Pilorz, S.H. and Carder, K.L. (1993). Estimating chlorophyll content and bathymetry of lake Tahoe using AVIRIS data. *Remote Sensing Environment*, 44, 217-230.

References

- Humber Estuary Committee (1993). The Quality Of The Humber Estuary. National Rivers Authority.
- Iqbal, M. (1983). An introduction to solar radiation. Academic Press: New York, pp 114-115.
- Jerlov, N.G. (1976). Marine Optics. Elsevier Scientific Publishing Company.
- Kirk, J.T. (1983). Light And Photosynthesis In Aquatic Ecosystems. Cambridge University Press.
- Kirk, J.T.O. (1984). Dependence of relationship between inherent and apparent optical properties of water on solar altitude. Limnology and Oceanography, 29, 2, 350-356.
- Kirk, J.T.O (1994). Estimation of the absorption and the scattering coefficients of natural waters by use of underwater irradiance measurements. Applied Optics, 33, 15, 3276-3278.
- Krijgsman, J. (1994). Optical remote sensing of water quality parameters: interpretation of reflectance spectra, PhD Thesis, Delft, Delft University Press.
- Lathrop, R.G. (1992). Landsat Thematic Mapper monitoring of turbid inland water quality. Photogrammetric Engineering & Remote Sensing, 58, 4, 465-470.
- Leckner, B. (1978). The spectral distribution of solar radiation at the earth's surface - elements of a model. Solar Energy, 20, 143-150.
- Liedtke, J., Roberts, A. and Luternauer, J. (1995). Practical remote sensing of suspended sediment concentration. Photogrammetric Engineering & Remote Sensing, 61, 2, 167-175.
- Land-Ocean Interaction Study. (1992). Science Plan for a Community Research Project. Natural Environment Research Council.

References

- Mantoura, R.F.C & Woodward, E.M.S. (1983). Conservative behaviour of riverine dissolved organic carbon in the Severn Estuary: chemical and geochemical implications. *Geochimica et Cosmochimica Acta*, 47, 1293-1309.
- Mitchelson, E.G., Jacob, N.J. and Simpson, J.H. (1986). Ocean colour algorithms for case 2 waters of the Irish Sea in comparison to algorithms from case 1 waters. *Continental Shelf Research*, 5, 3, 403-415.
- Moore, G. and Aiken, J. (1990). Aircraft multispectral remote sensing of water colour off Heligoland. *Proceedings of the Remote Sensing Society Workshop on Applications and Developments in Imaging Spectrometry*, 18-31.
- Morel, A. (1973). Diffusion de la lumiere par les eaux de mer. Resultats experimentaux et approche theorique. *Optics of the Sea, AGARD Lecture Series. NATO advisory group for Aerospace research and development. No 61, 3.1.32-61.*
- Morel, A. (1974). Optical properties of pure seawater. In *Optical aspects of oceanography*, Eds. Jerlov, N.G. and Nielsen, S.E., Academic Press, London.
- Morel, A. (1980). In-water and remote measurement of ocean color. *Boundary-Layer Meteorology*, 18, 177-201.
- Morel, A. (1988). Optical modelling of the upper ocean in relation to its biogenous matter content (case 1 waters). *Journal of Geophysical Research*, 93, C9, 10749-10768.
- Nanu, L. and Robertson, C. (1993). The effect of suspended sediment depth distribution on coastal water spectral reflectance: theoretical simulation. *International Journal of Remote Sensing*, 14, 2, 225-39.
- Novo, E.M.M., Hansom, J.D. and Curran, P.J. (1989). The effect of sediment type on the relationship between reflectance and suspended sediment concentration. *International Journal of Remote Sensing*, 10, 7, 1283-1289.

References

- Novo, E.M.M., Hansom, J.D. and Curran, P.J. (1989). The effect of viewing geometry and wavelength on the relationship between reflectance and suspended sediment concentration. *International Journal of Remote Sensing*, 10, 8, 1357-1372.
- Palmer, K.F. and Williams, D. (1974). Optical properties of water in the near infrared. *Journal of the Optical Society of America*, 64, 8, 1107-1110.
- Parsons, T.R., Maita, Y. and Lalli, C.M. (1984). A manual of chemical and biological methods for sea-water analysis. Pergamon Press: Oxford, pp 173.
- Petzold, T.J. (1972). Volume scattering functions for selected ocean waters, SIO Ref. 72-78, Scripps Inst. Oceanogr., La Jolla, 79. Condensed as chapter 12 in *Light in the Sea*, Eds. Tyler, J.E., Dowden, Hutchinson & Ross, Troudsberg, 1977, 150-174.
- Plass, G.N, Kattawar, G.W. and Guinn, J.A. (1975). Radiative transfer in the Earth's atmosphere: Influence of ocean waves. *Applied Optics*, 14, 1924-1936.
- Priesendorfer, R.W. and Mobley, C.D. (1986). Albedos and glitter patterns of a wind-roughened sea surface. *Journal of Physical Oceanography*, 16, 1293-1316.
- Prieur, L. and Sathyendrath, S. (1981). An optical classification of coastal and oceanic waters based on the specific spectral absorption curves of phytoplankton pigments dissolved organic matter and other particulate materials. *Limnology and Oceanography*, 26, 4, 671-689.
- Pringle, A.W. (1985). Holderness Coast Erosion And The Significance Of Ords. *Earth Surface Processes And Landforms*, 10, 107-124.
- Quenzel, H. (1970). *Journal of Geophysical Research*, 75, 15, 2915.
- Reitan, C.H. (1963). Surface due point and water vapour aloft. *Journal of Applied Meteorology*, 2, 776-779.

References

- Ritchie, J.C., Schiebe, F.R. and McHenry, J.R. (1976). Remote sensing of suspended sediment in surface waters. *Photogrammetric Engineering & Remote Sensing*, 42, 1539-1545.
- Ritchie, J.C. and Cooper, C.M. (1988). Comparison of measured suspended sediment concentrations with suspended sediment concentrations estimated from Landsat MSS data. *International Journal of Remote Sensing*, 9, 3, 379-387.
- Rollins, I.S. (1992). NERC-EPFS software manual 1 - Spectron SE590 Processing Software. Version 1.1. NERC-Equipment Pool for Field Spectroscopy, University of Southampton, Southampton.
- Shettle, E.P. and Fenn, R.W. (1979). Models for the aerosols of the lower atmosphere and the effects of humidity variations on their optical properties. AFGL-TR-79-0214 US Airforce Geophysics Laboratory, Hanscombe Air Force Base, Mass.
- Sifakis, N. and Deschamps, P. (1992). Mapping of air pollution using SPOT satellite data. *Photogrammetric Engineering & Remote Sensing*, 58, 10, 1433-1437.
- Simpson, J.H. & Brown, J. (1987). The interpretation of visible band imagery of turbid shallow seas in terms of the distribution of suspended particles. *Continental Shelf Research*, 7, 11/12, 1307-1313.
- Singh, S.M. (1992). Accuracy of atmospheric correction algorithm using ATM data. *International Journal of Remote Sensing*, 13, 3, 559-569.
- Slater, P.N. (1980). *Remote Sensing: Optics And Optical Systems*. Addison-Wesley Publishing Company.
- Smith, R.C & Baker, K.S. (1981). Optical properties of the clearest natural waters (200-800 nm). *Applied Optics*, 20, 2, 177-184.
- Stumm, W. and Morgan, J.J. (1981). *Aquatic Chemistry*. 2nd Edition, Wiley-Interscience, pp 780.

References

- Stumpf, R.P and Pennock, J.R (1989). Calibration of a general optical equation for remote sensing of suspended sediments in a moderately turbid estuary. *Journal of Geophysical Research*, 94, C10, 14363-14371.
- Tanre, D., Holben, B.N. and Kaufman, Y.J. (1992). Atmospheric correction algorithm for NOAA-AVHRR products: theory and application. *IEEE Transactions on Geoscience and Remote Sensing*, 30, 2, 231-248.
- Tassan, S. (1988). The effect of dissolved "yellow substance" on the quantitative retrieval of chlorophyll and total suspended sediment concentrations from remote measurements of water colour. *International Journal of Remote Sensing*, 9, 4, 787-797.
- Teillet, P.M. (1990). Rayleigh optical depth comparisons from various sources. *Applied Optics*, 29, 13, 1897-1900.
- Teillet, P.M., Fedpsejevs, G., Ahern, F.J. and Gauthier, R.P. (1994). Sensitivity of surface reflectance retrieval to uncertainties in aerosol optical properties. *Applied Optics*, 33, 18, 3933-3940.
- Tocher, M.D.J. (1992). Investigation into the spectral characteristics of suspended particulate matter under controlled conditions. MSc Thesis, Institute of Marine Studies, University of Plymouth.
- Topliss, B.J. (1986). Spectral variations in upwelling radiant intensity in turbid coastal waters. *Estuarine, Coastal and Shelf Science*, 22, 395-414.
- Vigroux, E. (1953). Contribution a l'etude experimentale de l'absorption de l'ozone. *Annales de Physique (Paris)*, 8, 709.
- Whitlock, C.H., Usry, J.W., Witte, W.G. and Gurganus, E.A. (1977). Laboratory measurements of upwelled radiance and reflectance spectra of Calvert, Ball, Jordan, and Feldspar soil sediments. NASA Technical Paper 1039.

References

Whitlock, C.H., Poole, L.R., Usry, J.W., Houghton, W.M., Witte, W.G., Morris, W.D. and Garganus, E.A. (1981). Comparison of reflectance with backscatter and absorption parameters for turbid waters. *Applied Optics*, 20, 3, 517-522.

Witte, W.G., Whitlock, C.H., Harris, R.C., Usry, J.W., Poole, L.R., Houghton, W.M., Morris, W.D. and Gurganus, E.A. (1982). Influence of dissolved organic materials on turbid water optical properties and remote-sensing reflectance. *Journal of Geophysical Research*, 87, C1, 441-446.

Zibordi, G., Maracci, G. and Schlittenhardt, P. (1990). Ocean colour analysis in coastal waters by airborne sensors. *International Journal of Remote Sensing*, 11, 5, 705-725.

Appendix 1: Acronyms and Symbols

Acronyms

AM	Air Mass
CASI	Compact Airborne Spectrographic Imager
CCD	Charge-Coupled Detector
DOM	Dissolved Organic Matter, defined in Case 2 water as the optically active dissolved organic matter of terrestrial origin. Also known as yellow substance (symbol y) or gelbstoff.
EMR	Electromagnetic Radiation
FI	Flightline
FOV	Field-Of-View
HW	High Water
LOIS	Land-Ocean Interaction Study
LW	Low Water
NERC	Natural Environment Research Council
NRA	National Rivers Authority
PAR	Photosynthetically Available Radiation
PML	Plymouth Marine Laboratory
RACS	River-Atmosphere Coast Study
RH	Relative Humidity
SeaWiFS	Sea viewing Wide Field-of-view Sensor
SFOV	Sensor Field-Of-View
SNR	Signal-to-Noise Ratio
SPM	Suspended Particulate Matter
TTHG	Two Term Henry-Greenstein function

Symbols

Φ	W	Radiant flux of energy (power)
$\beta(\lambda, z, \sigma)$	m^{-1}	Volume scattering function
$\beta^*(\lambda, z, \sigma)$	sr^{-1}	Normalised volume scattering function
$\beta_r(\lambda, \sigma)$		Rayleigh volume scattering function
δ		Depolarisation factor
ϵ	J	Radiant energy
ϕ		Azimuth angle
κ	cm^{-1}	Wavenumber
λ	nm	Wavelength
$\bar{\mu}_d(\lambda, z)$		Average cosine for the downwelling light
θ	$^\circ$	Zenith angle
θ_n	$^\circ$	Nadir angle
θ_r	$^\circ$	Refracted angle
$\rho(z)$		Air density
$\rho(\lambda)$		Fresnel reflectance at the air-sea interface
σ	$^\circ$	Angle of incident radiation
$\tau_a(\lambda, h_0)$	m	Aerosol optical depth due to scattering
$\tau_r(\lambda, h_0)$	m	Raleigh optical depth

Appendix 1 - Acronyms And Symbols

$\tau_r^*(\lambda, h_0)$	m	Normalise Rayleigh optical depth
$\tau_{o3}(\lambda, h_0)$	m	Ozone optical depth
$\tau_{wv}(\lambda, h_0)$	m	Water vapour optical depth
ν	s ⁻¹	Frequency
$\omega_o(\lambda, z)$		Single scattering albedo
$\omega_a(\lambda, h_0)$		Aerosol single scattering albedo
$\zeta(\lambda, z)$	m	Optical depth
A		Angstrom Coefficient
AM		Air Mass
B		Anstrom exponent
C_{o3}	cm	Ozone concentration
C_w	cm	Water vapour concentration
Ch	mg m ⁻³	Chlorophyll- <i>a</i> concentration
$E(\lambda, z)$	W cm ⁻² nm ⁻¹	Vector irradiance
$E_d(\lambda, z)$	W cm ⁻² nm ⁻¹	Downwelling vector irradiance
$E_u(\lambda, z)$	W cm ⁻² nm ⁻¹	Upwelling vector irradiance
$E_o(\lambda, z)$	W cm ⁻² nm ⁻¹	Scalar irradiance
$E_{od}(\lambda, z)$	W cm ⁻² nm ⁻¹	Downwelling scalar irradiance
$E_{ou}(\lambda, z)$	W cm ⁻² nm ⁻¹	Upwelling scalar irradiance
$^{\circ}E_o(z)$		PAR irradiance
$^{\circ}E_{od}(z)$		Downwelling PAR irradiance
$^{\circ}E_{ou}(z)$		Upwelling PAR irradiance
$F_0(\lambda, h_0)$	W cm ⁻² nm ⁻¹	Extraterrestrial solar irradiance
$H_a(h_0)$	km	Aerosol scale height
$H_{o3}(h_0)$	km	Ozone scale height
$H_r(h_0)$	km	Rayleigh scale height
$H_{wv}(h_0)$	km	Water vapour scale height
$K(\lambda)$	m ⁻¹	Diffuse attenuation coefficient
$K_d(\lambda)$	m ⁻¹	Downwelling diffuse attenuation coefficient
$K_u(\lambda)$	m ⁻¹	Upwelling diffuse attenuation coefficient
$K_{od}(\lambda)$	m ⁻¹	Downwelling scalar diffuse attenuation coefficient
$K_{ou}(\lambda)$	m ⁻¹	Upwelling scalar diffuse attenuation coefficient
$K_{o3}(\lambda)$	cm ⁻¹	Ozone attenuation coefficient
$K_{wv}(\lambda)$	cm ⁻¹	Water vapour attenuation coefficient
$L(\lambda, z, \theta, \phi)$	W sr ⁻¹ cm ⁻² nm ⁻¹	Radiance
$L_a(\lambda, \theta, \phi)$	W sr ⁻¹ cm ⁻² nm ⁻¹	Atmospheric path radiance from aerosol scattering
$L_p(\lambda, \theta, \phi)$	W sr ⁻¹ cm ⁻² nm ⁻¹	Atmospheric path radiance
$L_r(\lambda, \theta, \phi)$	W sr ⁻¹ cm ⁻² nm ⁻¹	Atmospheric radiance from Rayleigh scattering
$L_s(\lambda, h_0, \theta, \phi)$	W sr ⁻¹ cm ⁻² nm ⁻¹	Radiance received at the sensor
$L_{sky-g}(\lambda, h_0, \theta, \phi)$	W sr ⁻¹ cm ⁻² nm ⁻¹	Sky-glitter radiance
$L_{sun-g}(\lambda, h_0, \theta, \phi)$	W sr ⁻¹ cm ⁻² nm ⁻¹	Sun-glitter radiance
$L_{t-sky-g}(\lambda, h_0, \theta, \phi)$	W sr ⁻¹ cm ⁻² nm ⁻¹	Total sky-glitter radiance
$L_u(\lambda, z, \theta, \phi)$	W sr ⁻¹ cm ⁻² nm ⁻¹	Upwelling radiance (below the water surface)
$L_w(\lambda, \theta, \phi)$	W sr ⁻¹ cm ⁻² nm ⁻¹	Water-leaving radiance at ground level
$L_{wn}(\lambda, \theta, \phi)$	W sr ⁻¹ cm ⁻² nm ⁻¹	Normalized water-leaving radiance at ground level
$L_{ws}(\lambda, h_0, \theta, \phi)$	W sr ⁻¹ cm ⁻² nm ⁻¹	Water-leaving radiance measured at the sensor
N	M m ⁻³	Number of molecules per unit volume

Appendix 1 - Acronyms And Symbols

P	mb	Atmospheric pressure
P_o	mb	Standard atmospheric pressure (1013.25 mb)
$P^*(\lambda, \theta, \phi)$	sr^{-1}	Single scattering phase function
$P^*_r(\lambda, \theta, \phi)$	sr^{-1}	Rayleigh scattering phase function
$P^*_a(\lambda, \theta, \phi)$	sr^{-1}	Aerosol scattering phase function
$R(\lambda, z)$		Reflectance
$R_{+0}(\lambda)$		Reflectance just above the water surface
$R_{-0}(\lambda)$		Reflectance just below the water surface
$R_a(\lambda, z)$		Reflectance due to aerosol scattering
$R_d(\lambda, z)$		Water-air reflectance for totally diffuse irradiance
$R_o(\lambda, z)$		Scalar irradiance reflectance
$R_r(\lambda, z)$		Reflectance due to Rayleigh scattering
$R_{ra}(\lambda, z)$		Reflectance due to multiple scattering
$R_{rs}(\lambda, z)$		Remote sensing reflectance
RH		Relative humidity
Q		Irradaince-to-radiance ratio
T_d	°C	Dew point temperature
V	km	Visibilty or visual range
$a(\lambda)$	m^{-1}	Total absorption coefficient
$a_{Ch}(\lambda)$	m^{-1}	Chlorophyll- <i>a</i> absorption coefficient
$a^*_{Ch}(\lambda)$	m^{-1}	Normalised chlorophyll- <i>a</i> absorption coefficient
$a_s(\lambda)$	m^{-1}	Suspended sediment absorption
$a_w(\lambda)$	m^{-1}	Water absorption
$a_y(\lambda)$	m^{-1}	DOM absorption
$b(\lambda)$	m^{-1}	Total scattering coefficient
$b_b(\lambda)$	m^{-1}	Backscattering coefficient
$b_{bCh}(\lambda)$	m^{-1}	Chlorophyll- <i>a</i> backscattering
$b_{bs}(\lambda)$	m^{-1}	Suspended sediment backscattering
$b_f(\lambda)$	m^{-1}	Forward scattering coefficient
$b_w(\lambda)$	m^{-1}	Water scattering
$\underline{b}_b(\lambda)$	m^{-1}	Backscattering probability
c	ms^{-1}	Speed of light in a vacuum (see Equation 2-2)
$c(\lambda)$	m^{-1}	Beam attenuation coefficient (in all other occurances)
c_a		
h_0	km	Sensor altitude
k		Extinction index
m		Complex refractive index
n		Refractive index for air
n_r		Refractive index for water
n_w		Refractive index ration for air to water
r	μm	Particle radius
sr		Downwelling solar irradiance waveband ratio
$t_d(\lambda, h_0)$		Diffuse transmittance
wtr		Water-leaving radiance waveband ratio
z	m	Depth
z_{90}	m	Penetration depth

Appendix 2: The IDL Processing System

The casigo processing system is written in Interactive Data Language (IDL), which provides a widget based Windows or UNIX interface. The program is executed from the IDL command prompt using the command **@casigo.bat**. The main module (**casigo**) displays a menu, allowing the importing/loading of CASI imagery and subsequent processing (see Figure A2-1).

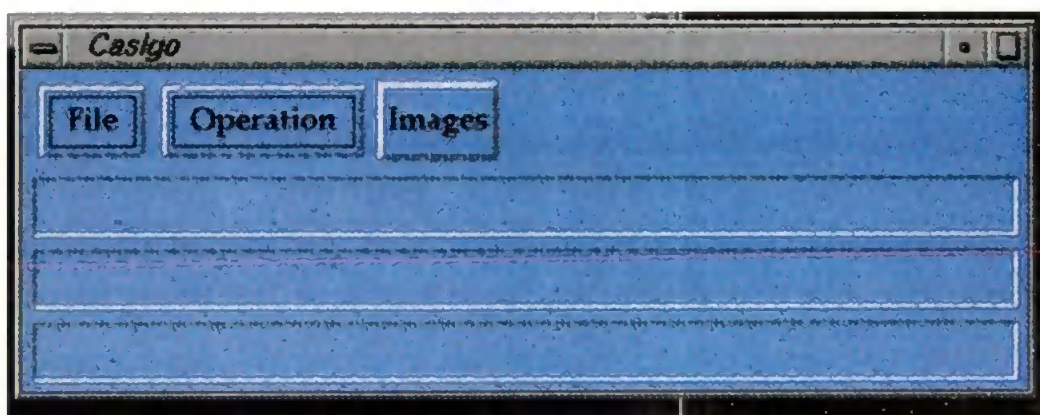


Figure A2-1: Display window for the casigo module.

The CASI imagery (PCI format) is converted to a band sequential file (*.int) and additional ancillary file (*.anc) containing the header information plus additional information, such as the GPS locations of the nadir pixels.

As the system is modular new processing steps can be easily added e.g. atmospheric correction. Intermediate steps can be saved in IDL format, with final images and plots being output as 24-bit TIFF files.

A2.1 Plot Module

The flightline module (**ploter.pro**) not only allows the user to plot a flightline, but also performs the geometric correction (**geom.pro**) which creates a 3D array holding the latitude, longitude and variable from a variable array (e.g. SPM). Examples of flightline plots are Figures 6-2 and 6-3.

The geometric correction was applied to obtain the latitude and longitude for each pixel from the roll corrected imagery and the GPS data in the ancillary file. This involves a series of calculations using the sensor field-of-view (SFOV), altitude of the aircraft, heading (calculated from successive pixels) and the average latitude (*lat*). The equations used can be seen in Figure A2-2.

The x and y dimension of each pixels in degrees of longitude (*x_{inc}*) and latitude (*y_{inc}*) can be calculated from Equations A2-1 and A2-2.

$$x_{inc} = \text{abs}\left(\frac{(x2 - y2) \cdot \cos(lat)}{0.5 \cdot \text{pixels} \cdot 111}\right) \quad \text{A2-1}$$

$$y_{inc} = \frac{y2}{0.5 \cdot \text{pixels} \cdot 111} \quad \text{A2-2}$$

The calculations use normal rather spherical trigonometry as the Earth can be considered flat for aircraft imagery, and no account is taken of the pixel distortion caused by viewing angle.

The boat module (**plotgr.pro**) has an input of a ground truthing file (space separated) and displays the track on a positional plot with the variable e.g. salinity having its magnitude indicated by a look-up table. The background may consist of a bathymetry map which has been digitised and then converted to a regular grid (**bathy.pro**).

A2.2 Colour Composite

This allows the creation of colour composites i.e. 3 wavebands displayed as the red, green and blue components (see Figure A2-3). It is useful for preliminary examining the data. Each waveband can be individually histogram stretched to show the full dynamic range. The resulting images are seen in Figures 6-4 to 6-7.

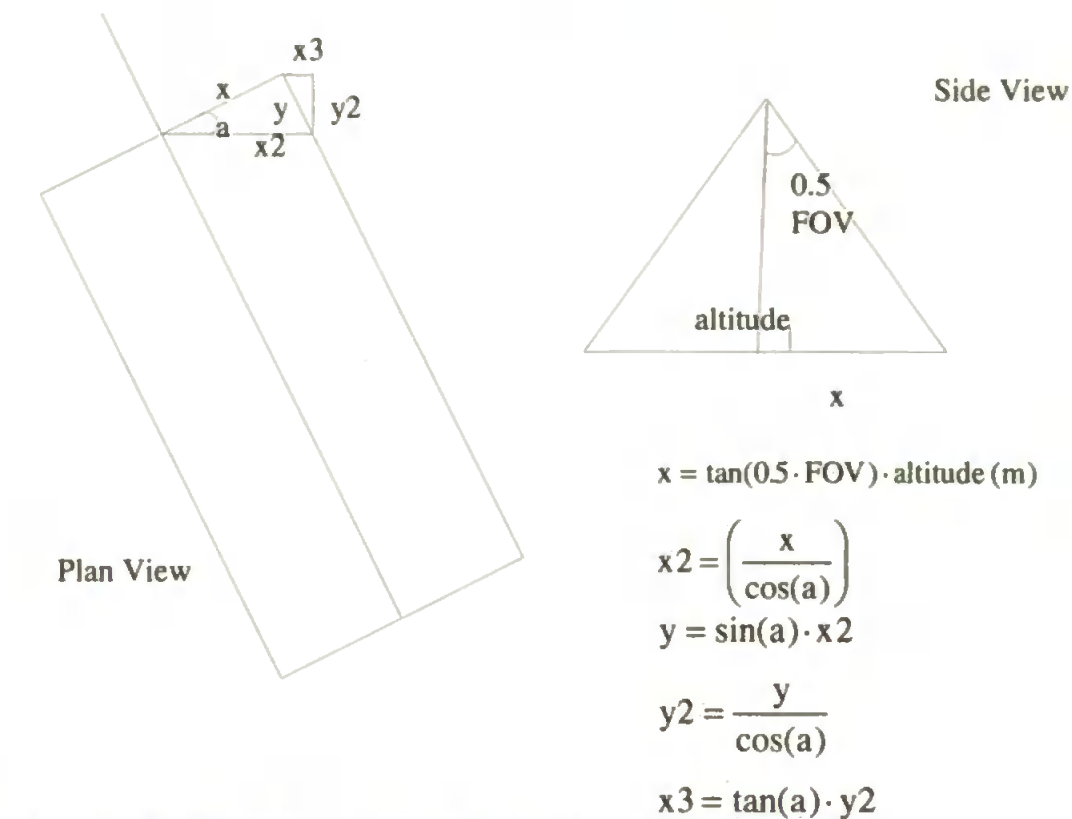


Figure A2-2: CASI Image plan and side views for geometric correction

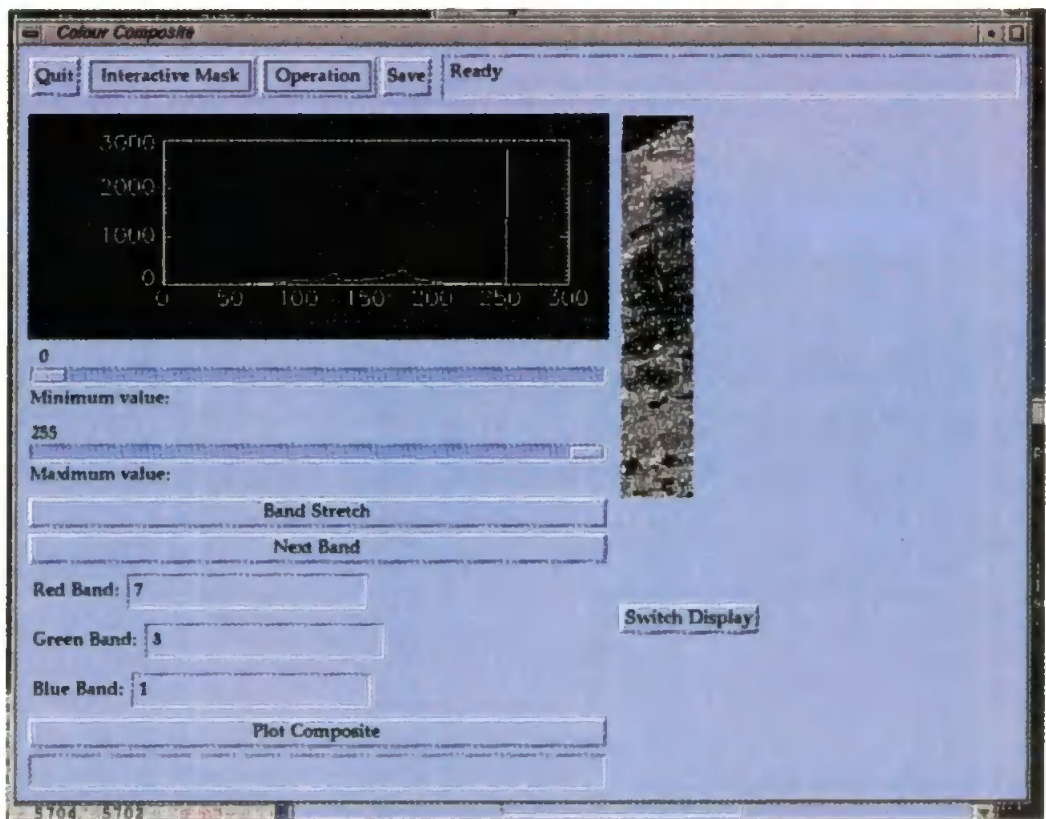


Figure A2-3: Display window for the colour composite module.

A2.3 Masking Module

Wavebands suitable for cloud and land masking are in the near infrared where the water-leaving radiance is comparably smaller than in the visible, and in the visible range it can be assumed that values over $4 \mu\text{W}/\text{nm}/\text{sr}^{-1}$ are not water (see Section 6.2). Once a good dynamic range has been achieved in the required waveband the user can then select an upper cut-off limit, with the pixels having a greater gray scale being masked.

For the SPM algorithm, such masking should not be needed as the near infrared waveband ratio will stray outside the acceptable limits of the algorithm. However, problems occur when we have sub-pixel cloud effects which show up as high SPM concentrations, and certain types of vegetation can have an acceptable ratio. There may also be contamination from surface specular reflectance manifesting as an occasional pixel with a high value.

Three types of data can be output to comma separated files: a spectra for a specified pixel; the full set of wavebands for a swath of pixels; the full set of wavebands for the nadir line. This feature allowed the production of Figures 6-8 to 6-10. The plotting of the data on a multiple x-axis was achieved in a separate IDL program (**multix.pro**).

A2.4 SPM Module

The SPM module (**spm.pro**) has various options for viewing the results: plot nadir line data as either the near infrared waveband ratio or SPM values; plot all the data as waveband 12 radiance versus the near infrared waveband ratio or calculated SPM values. There are several input boxes for changing the axis scaling.

A SPM map is calculated from the pre-loaded image, atmospheric waveband ratio and algorithm constants (see Section 5.4.1 for an explanation of the latter two). An interactive mask is created by **clmask.pro** which can be applied and subsequently removed. Apply a noise removal (median) or smoothing filter or perform an interpolation for missing data either removed by the mask or from the SPM algorithm exceeding the valid range.

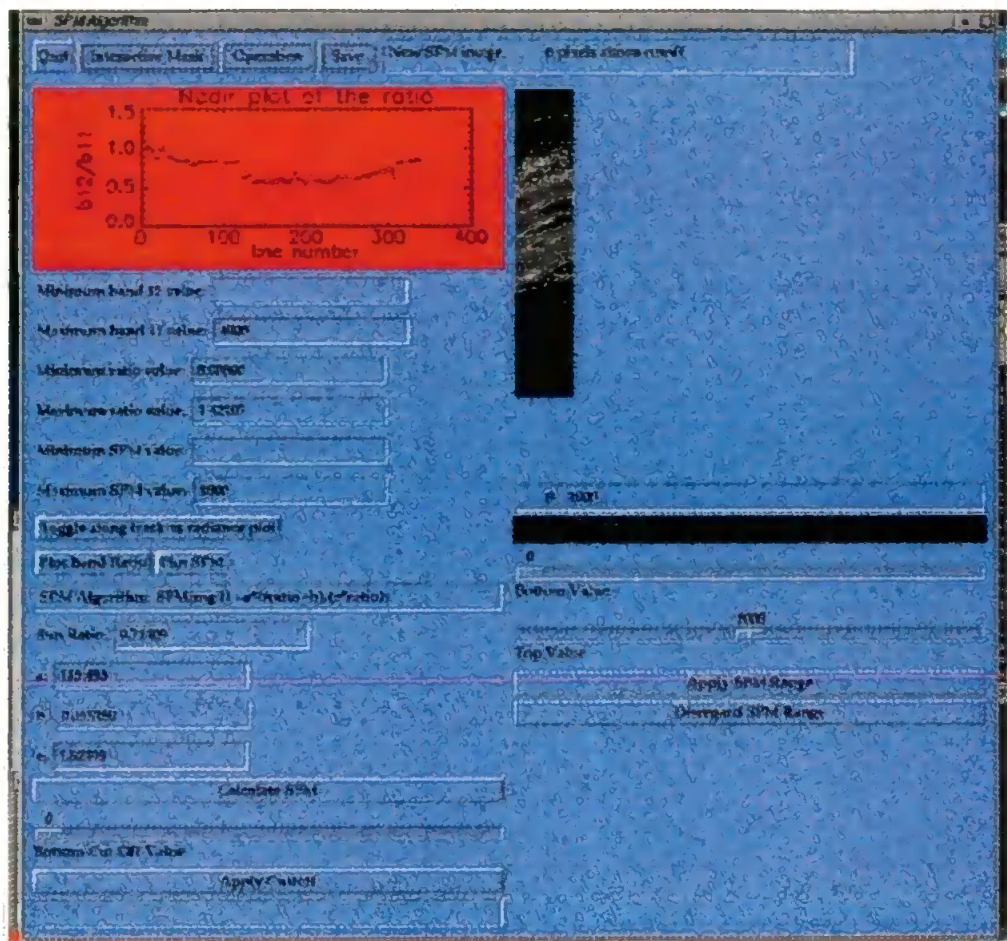


Figure A2-4: Display window for the SPM module

A lower and upper cut-off limit can be applied to waveband 12. The user can also choose an SPM range to be displayed or disregarded from the displayed sediment map. This may be useful when the SPM concentrations are near to the lower limit of the SPM algorithm (about 200 mg/l). Values below this can again give high concentrations because of the increase in the amount of atmospheric signal relative to the water signal.

Appendix 3: Published Papers

Aiken J., Hudson, S.J. and Vessey, J.P. 1994. The measurement of optical attenuation in sea water. *Proceedings of Oceans 94*, Ostates, 2, 689-693.

Bale, A.J., Tocher, M.D., Weaver, R., Hudson, S.J. and Aiken, J. 1994. Laboratory measurements of the spectral properties of estuarine suspended particles. *Netherlands Journal of Aquatic Ecology*, 28, 237-244.

Hudson, S.J., Moore, G.F., Bale, A.J., Dyer, K.R. and Aiken, J. 1994. An operational approach to determining suspended sediment distributions in the Humber estuary by airborne multi-spectral imagery. *Proceedings of the First International Airborne Remote Sensing Conference and Exhibition, Strasbourg*, Vol. III, 3, 10-20.

Hudson, S. 1996. The Plymouth Correction Experiment. Proceedings of the First SeaWiFS Exploitation Initiative (SEI) Team Meeting. NASA Tech. Memo. 104566, Vol. 33, S.B. Hooker E.R. Firestone, Eds., NASA Goddard Space Flight Center Greenbelt, Maryland, 20-22.

The measurement of Optical Attenuation in Sea Water

Dr J Aiken,
Plymouth Marine Laboratory,
Plymouth, UK

S J Hudson
Plymouth Marine Laboratory,
Plymouth, UK

Dr J P Vessey
Chelsea Instruments Ltd
Surrey, UK

1. INTRODUCTION

The high performance of a submersible optical beam transmissometer, such as Chelsea Instruments' Alphatracka, depends on an integrated approach to the design of the electronic, electro-optic, optical and mechanical components, both individually and as a system, to yield both long term stability and a low temperature coefficient (tempco) of calibration. This must be achieved together with an ability to retain the performance when exposed to the full ambient sunlight or when taken to full ocean depth (6000m).

Many of the beam transmissometers currently on the market make measurements at a single wavelength (660nm available from a red LED). As the LED output is not usually corrected for thermal and optical changes with time, it is not a trivial task to change the LED colour used. This paper describes a new instrument with a choice of operational wavelengths of 660, 565 and 470nm using LED sources, which have been stabilised by sophisticated electronic methods. Specimen results from this transmissometer, obtained during rigorous tests, are also presented.

2. BACKGROUND

The beam transmissometer is one of the few, true optical instruments which are used routinely in the oceans to measure the optical properties of the water mass directly. It comprises a light source, focusing optics, lenses etc. and a detector, which measures the loss of signal (attenuation) caused by the volume of water occupying the intervening optical path between the source and detector. When compared to the transmission of pure water, the measurement is normally presented as a percentage transmission. The measurement relates directly to an inherent optical property of the water, the beam attenuation coefficient c . This is the sum of the absorption coefficient a and the scattering coefficient b (all having the units m^{-1}); c is defined as the coefficient of loss of the parallel beam of light passing through 1m of water according to Beer's Law:

$$I = I_0 e^{-c(\lambda)L} \quad (1)$$

where I and I_0 are the measurement for the sample and pure water respectively, L is the beam path length and λ the wavelength of light, denoting that there is a wavelength dependency of c , a , and b .

Note: I_0 is not the transmission signal measured in air, even though air has nearly zero attenuation, since underwater transmissometers have windows and there is a polarisation loss from these in air.

Realising an instrument capable of measuring water transmission is, however, a complex task.

Firstly the instrument requires a well defined (parallel) beam of light. The instrument must be mechanically stable for both laboratory and field applications, and cope with thermal, physical and other environmental changes. Working over a broad range of wavelengths necessitates achromatic optics, lenses, windows etc. Additionally there is the major problem of producing a source of light which is stable in intensity throughout any environmental changes and a detector which has a stable response. The additional requirements imposed by using the instrument underwater, in a hostile corrosive environment, are comparatively minor.

Given these rigorous demands, it is no surprise that there have been few successful developments of underwater transmissometers for the marine environment. The one-off Visibility Laboratory Spectral Transmissometer (VLST) is the only multi-spectral instrument which has been used extensively and successfully in the marine environment. The instrument has a tungsten lamp source (broad spectral range), a filter wheel (5 filters, nominally 440, 492, 522, 551 and 670nm) a folded 1m path length with achromatic and aspheric optics and a photomultiplier detector. The instrument is complex and requires rigorous calibration and general maintenance.

The problem of achromatic optics can be resolved if the instrument is "single wavelength", using a light emitting diode (LED) as source (bandwidth 30-50 nm). A LED source can be intensity stabilised, is small and effectively approximates to a point source. This considerably simplifies both the optical design for a parallel beam and achieving mechanical stability.

The red 660nm LED transmissometer (Bartz et al 1978) has been widely used for transmission measurements in the marine environment for over a decade with path lengths of 100, 25 and 5cm suitable for waters with a wide range of turbidities and opacities.

Interest in the measurement of the beam attenuation coefficient c at several wavelengths arises from the wavelength dependence of a and b . Conversely, measurement of the wavelength variation of c provides information on the major constituents of the water which influenced its colour.

Since a , b and c are inherent optical properties of the water mass, we can expand the relationships into the component parts:

$$\begin{aligned} c(\lambda) &= a(\lambda) + b(\lambda) \\ &= a_w + a_{chl} C_{chl} + a_g C_g + a_{spm} C_{spm} + \\ &\quad a_{ph} C_{ph} + b_w + b_{ph} C_{ph} + b_{spm} C_{spm} \end{aligned} \quad (2)$$

where: a_w , a_{chl} , a_g , a_{ph} and a_{spm} are the absorption coefficients of water, chlorophyll, Gelbstoffe, phytoplankton (accessory pigments) and suspended particulate material respectively (a_{spm} is often summed with a_{ph}); b_w , b_{ph} and b_{spm} are the scattering coefficients of water, phytoplankton and suspended particulate material; and C_{chl} , C_g , C_{ph} and C_{spm} are concentrations of the major constituents.

In open waters there is negligible suspended particulate material (SPM) and only phytoplankton pigments, chlorophyll, accessory pigments and dissolved organic material (DOM) of biogenic origin ($a_g = a_{dom}$, $C_g = C_{dom}$) are significant along with absorption and scattering of water. Scattering from phytoplankton detrital material is generally only significant if coccolithophores or detached coccoliths are present in substantial concentrations. Inshore, in the shallow shelf seas or in estuaries with major fresh water inputs, scattering by suspended particulate material ($b_{spm} C_{spm}$) is the major contribution to $c(\lambda)$ along with absorption by dissolved organic material of terrestrial origin ($a_g C_g$).

The wavelength dependence of these various terms needs to be considered; a schematic of the absorption and scattering spectra of the major components of the water is shown in Figure 1. Chlorophyll-a (the major, ubiquitous, phytoplankton pigment) absorbs strongly at 660nm, very little at 565nm and significantly at 470nm; chlorophyll-b

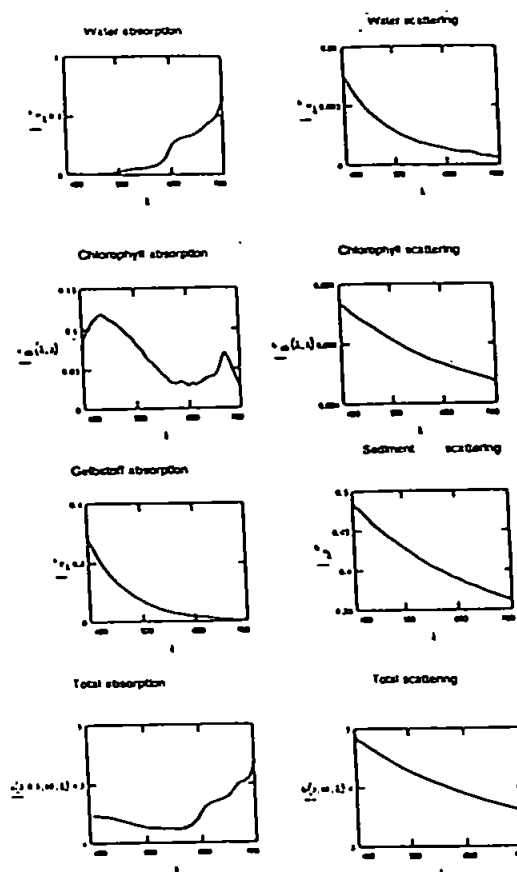


Fig 1: Specific absorption and scattering spectra (left, right) of the major components of marine waters which influence the inherent optical properties; water, chlorophyll, Gelbstoff and suspended particulate material from sediments.

and chlorophyll-c are major absorbers at 470nm. The major accessory pigments carotenoids (both photoprotective and photosynthetic) absorb at 470nm; the photosynthetic carotenoids and other important accessory pigments absorb at 565nm. Dissolved organic material or coloured DOM (CDOM) absorb most strongly in the far blue (400nm) with a well defined exponential decrease to other wavelengths amounting to a small effect at 565nm and is negligible at 660nm. Scattering by all material has an exponential decline from blue to red wavelengths and is significant only when the concentration of scatterers is greater than 10^4 l^{-1} whether phytoplankton cells, phytoplankton detritus (e.g. coccolithophores) or suspended particulate material of inorganic origin from the sediments. In oceanic waters equation (2) can be reduced to:

$$c(\lambda) = a_w + a_{chl} C_{chl} + a_g C_g + a_{ph} C_{ph} + b_w \quad (3)$$

i.e. assuming b_{ph} is negligible. At red (660nm) wavelengths a_g and a_{ph} will also be negligible but at blue wavelengths (470nm) both may be significant.

In turbid estuarine waters, where suspended particulate material dominates, the absorption by chlorophyll (plus other phytoplankton pigments) may be insignificant and equation (2) can be reduced to:

$$c(\lambda) = a_w + a_{chl} \cdot C_{chl} + a_g \cdot C_g + b_w + b_{spm} \cdot C_{spm} \quad (4)$$

At red wavelengths the a_g term may be negligible but not at blue wavelengths.

These considerations are important for interpreting beam attenuation measurements in different bio-optical circumstances.

3. DESIGN CONSIDERATIONS

Electro - Optical

As LEDs are small, low power and mechanically stable, they are well suited for use in a beam transmissometer. The disadvantage of modest long-term output stability and a poor tempco can be overcome by a suitable system design. Photodiodes provide excellent long term output stability, but in a marine transmissometer the tempco of around $0.1\%/^{\circ}C$ requires electronic compensation.

Overall system considerations

Beam transmissometers commonly use a single LED together with a thermistor which compensates both the tempco of the LED output and the photodiode detection efficiency. This does not address the problem of the long-term deterioration of the LED output with ageing which is conventionally compensated by periodic recalibration. For applications requiring "fit and forget" sensors, recalibration is no longer acceptable.

Chelsea Instruments Ltd. uses a ratiometric system design, in which the source beam is split to establish a reference signal. The signal and reference beams are detected with a matching pair of photodiodes, achieving good long term output stability. The photodiodes remain at the same temperature with respect to each other, so no spurious results are obtained when passing through thermoclines.

Electronic design considerations

The Chelsea Instruments' Alphatracka uses a proprietary digitally controlled nulling scheme, in which the feedback from the reference detector is generated in an ADC. The

null is generated at the input of the sample channel preamplifier, which results in a calibration tempco determined primarily by the matching of the photodiodes' (already modest) tempcos.

Such a system allows us to specify the maximum non-linearity as being comparable with that of the highly specified ADC. The signal and reference photodiodes feed into virtual earth amplifiers with considerable loop gain at the carrier frequency. Under short-circuit conditions, the photodiode output currents are linear with optical power over some 8 orders of magnitude. Detailed calculations demonstrate that the overall non-linearity of Alphatracka is determined by the ADC, thereby giving a very high performance.

Mechanical considerations

Precision and stability must be maintained in a deployable instrument. In the standard shallow water Alphatracka the pressure housings at each end of the beam path are made from plastic (titanium is used for the deep sea version, 6000m), which is unaffected by corrosion and is inexpensive. The use of a solid stainless steel chassis (See Figure 2) offers three advantages over the conventional tie-rod system.

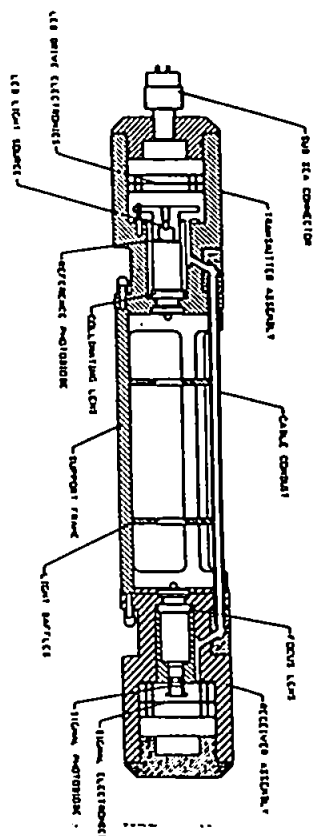


Fig 2: Schematic section of Alphatracka

Firstly, the strong chassis takes all the twisting and shearing strains, without directly passing them to the soft plastic housings. Secondly, the housings have large contact areas with the chassis and thus plastic creep is virtually eliminated. Thirdly, the chassis provides a rigid and well defined cage to which to attach the mounting bracket without putting any strain on the critical pressure housings. In a tie-rod mounted system, there is little choice other than to clamp these pressure housings.

4. RESULTS

Measurements have been made with the blue (470nm) Alphatracka fitted inside Aquashuttle during 3 research campaigns in the Humber Estuary and Plume (HEP, NRA vessel Sea Vigil, June, Aug. and Sept. 1993) and in the North Sea along the east coast from the Tweed to the Wash (LOIS campaign, NERC vessel RRS Challenger, Nov.1993); a chart of the area and the ship tracks are shown in Figure 3.

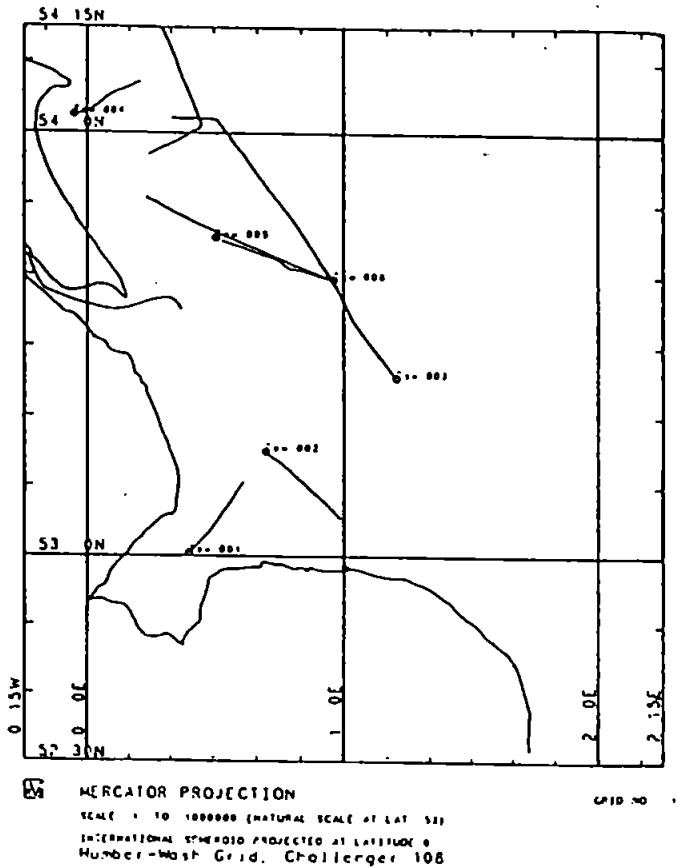


Fig 3: Chart of the Humber Estuary & the East Coast of England, showing the location of Aquashuttle tows

Figure 4 shows examples of the measurements of c_{470} from the Alphatracka in Aquashuttle for: a) a tow into the HEP on 30 June; b) a tow out of the HEP to clear North Sea water on the 4th August 1993; note the measurements are close to full scale, saturation values (i.e. near zero water transmission) in the high turbidity water up the estuary. Figure 4, c and d show the same data converted to equivalent values of SPM, calculated using a relationship derived from all the data from the summer campaign in the HEP, June, August and September 1993; the corresponding discrete measurements for these tows (Figure 4 c and d) are marked on the graphs (solid triangles).

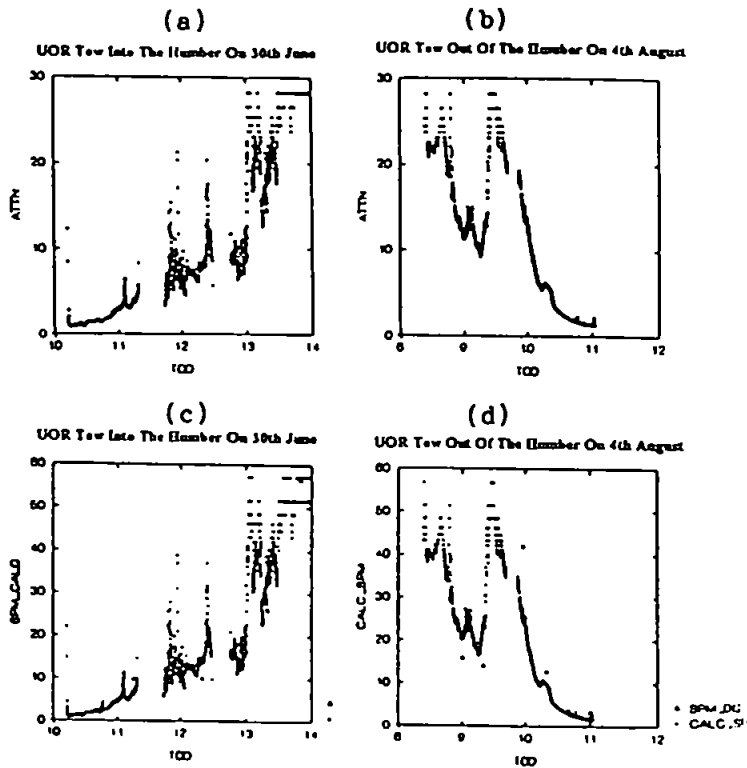


Fig 4: Variation of c_{470} (m^{-1}) versus time of day (TOD, h) for:-
a) tow into the HEP on 30 June;
b) tow out of the HEP on 4 August 1993;

Calculated SPM ($mg\ l^{-1}$) versus time of day (TOD, h) for:
c) tow into the HEP on 30 June;
d) tow out of the HEP on 4 August 1993.

Discrete measurements of SPM from water samples are shown with filled triangles.

The relationship of c_{470} to suspended particulate matter ($mg\ l^{-1}$) is shown in Figure 5 for data up to $100\ mg\ l^{-1}$. This relationship appears to saturate at a value of c_{470} of $30\ mg\ l^{-1}$ and SPM of $60\ mg\ l^{-1}$.

Sediment Calibration

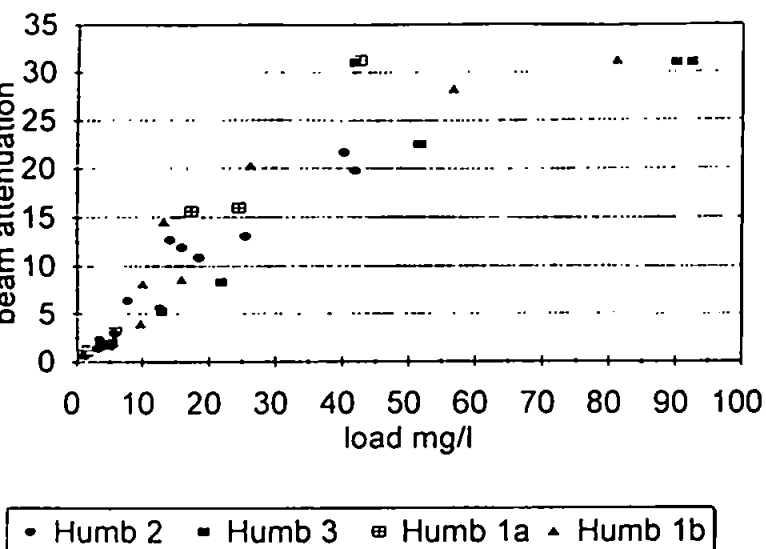
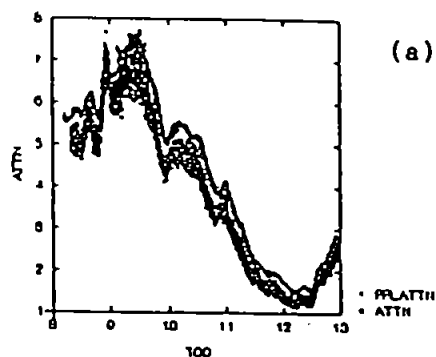


Fig 5: Relationship of c_{470} (m^{-1}) versus SPM ($mg\ l^{-1}$) for all data from the HEP, June, August and September 1993.

The blue Alphasacka in Aquashuttle were towed 9 times in the November campaign. Data on c_{470} from tow 1, from the Wash seawards, is shown in Figure 6a, compared to the data of c_{660} , derived from a red transmissometer, making measurements of surface water, pumped on board RRS Challenger. The two data sets are strongly correlated even though there is some saturation of the measurements at the start of the tow. Results from subsequent tows show even higher correlations between the two measurements (see Figure 6b, tow 3 across the HEP into clear water). The values of c_{660} compared to c_{470} observed for this and subsequent tows, arise, it is suspected, from an observed shift of the air calibration of the red transmissometer.

In 8 months of operations of the new blue Alphasacka, the observed shift of the air calibration has been negligible ($<0.05\%$).

Transmissometer Attenuation Tow 1 On 16th November



Transmissometer Attenuation Tow 3 On 16th November

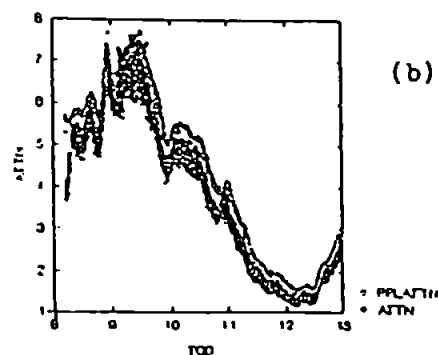


Fig 6: Contemporary measurements of c_{470} Alphasacka of surface pumped water on board RRS Challenger;
a) Tow 1 on 16 November 1993 from the Wash seawards
b) Tow 3 on 16 November 1993 across the Humber Plume into clear water (see Figure 3 for location of tows)

5. CONCLUSION

We have demonstrated the possibility of making optical attenuation measurements at more than one wavelength. The agreement between the results from the red and blue Alphasacka in conditions where there should be minimal wavelength variation of the transmissometer response is very encouraging. A program of work is now planned to compare the results from both the red and blue transmissometers in varying ocean conditions where the different wavelength responses will provide valuable additional data.

REFERENCES

- R Bartz, J R V Zanveld H Pak (1978) "A transmissometer for profiling and moored observations in water", *Ocean Optics*, **60**, 102 - 108

LABORATORY MEASUREMENTS OF THE SPECTRAL PROPERTIES OF ESTUARINE SUSPENDED PARTICLES

A.J. BALE¹, M.D. TOCHER^{1,3}, R. WEAVER², S.J. HUDSON^{1,3} and J. AIKEN¹

KEYWORDS: Suspended particles; spectral properties; estuaries.

ABSTRACT

Laboratory measurements have been made of the spectral reflectance of size-fractionated suspended sediments from two estuarine systems. The results show that reflectance at wavelengths between 400 and 1000 nm increases with decreasing particle size for given sediment masses. Preliminary interpretation suggests that a new factor, target area, which is derived from the volume and number distribution of particles in a suspension, is proportional to the reflectance of the suspension. Reflectance in the near infra-red is shown to be unaffected by other in-water parameters and is also largely independent of the colour or nature of the particles. The relationship between spectral reflectance in the near infra-red and target area therefore provides a means of estimating suspended sediment concentration from remotely sensed imagery if the particle size distribution is known or can be estimated.

INTRODUCTION

Water colour is the visible, water-leaving radiance spectra that results from absorption and back-scattering of a small fraction of incident sunlight by certain constituents of the water. Oligotrophic waters illuminated by sunlight are coloured blue due to the absorption of light by water at red and infra-red wavelengths. However, in coastal and estuarine waters, water colour is modified through absorption by dissolved organic compounds (DOC), chlorophyll and its accessory pigments, and by suspended particles. The complex interactions between absorption and scattering by various constituents of natural waters are well-understood, see for example, JERLOV (1974), MOREL (1974) and KIRK (1989). Because of the modification of the back-scattered, water-leaving radiance spectra by in-water constituents, spectral reflectance ($R\lambda$) measured from aircraft or satellites contains information on the inwater properties and offers the potential to determine quasi-synoptic, spatial distributions of suspended sediment concentration (SSC), phytoplank-

ton and some other water quality parameters in surface waters (GORDON *et al.*, 1988; CURRAN and NOVO, 1988).

Although remotely sensed images often reveal detailed spatial structure, quantification, particularly of SSC has been poor even using 'calibrations' derived from concurrent ground truth measurements (COLLINS and PATTIARATCHI, 1984; CURRAN *et al.*, 1987). The large natural variability in sediment concentration, colour, mineralogy, sorped components and particle size distribution have made the definition of generalized algorithms difficult (CURRAN and NOVO, 1988). Due to this uncertainty, many workers have resorted to laboratory studies to measure reflectance under conditions where many of the variables encountered in the field can be controlled. The particle size distribution, mineralogy and colour of sediments have all been implicated as factors influencing the relationship between SSC and reflectance (NOVO *et al.*, 1989a; CHOUBEY and SUBRAMANIAN, 1991; BHARGAVA and MARIAM, 1990; 1991a).

This paper describes a series of experiments

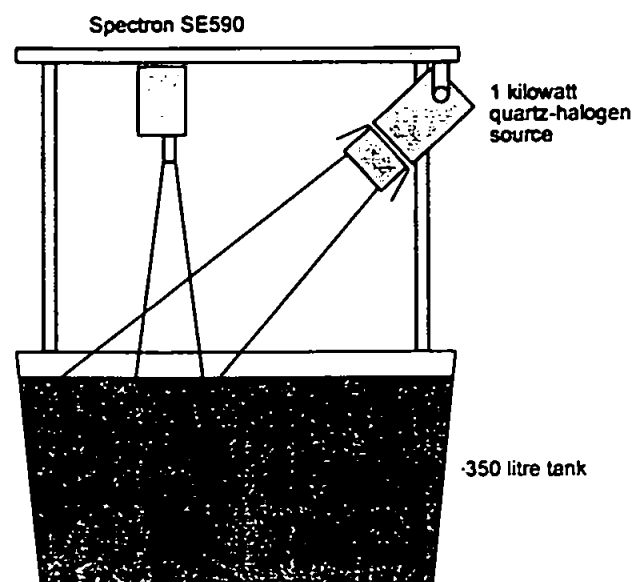


Fig. 1. The arrangement of the apparatus used for the measurement of reflectance spectra. See text for explanation.

carried out under laboratory conditions using a Spectron model SE 590 spectroradiometer to investigate the influence of particle size on the spectral reflectance of natural sediment suspensions.

MATERIALS AND METHODS

The Spectron (Spectron Engineering, Denver CO, USA) incorporates a 256 element photo diode and static diffraction grating giving approximately 2.8 nm resolution (dispersion) over the spectral range 400–1000 nm and signal integration times of the order of milli seconds. The spectrographic range of this instrument compares well with contemporary field systems *e.g.* the Itres Research, Compact Airborne Spectrographic Imager (CASI), capable of measuring over the range 400 to 915 nm with better than 3 nm resolution and the Sea-viewing, Wide Field of view Sensor (SeaWiFS), due to be launched in 1994, with eight bands covering the range 412 to 865 nm (band centres, HOOKER *et al.*, 1992).

The spectroradiometer was mounted in the optimum nadir position (NOVO *et al.*, 1989b) on a rigid gallows over a large (0.7 x 0.8 x 0.6 m deep) container which held 350 l of water and suspended particles (Fig. 1). The depth of water was only marginally less (0.03 m) than that required to avoid reflectance from the bottom of the tank with particle free water (MANTOVANI and CABRAL, 1992). The surface of the tank was illuminated over a circular area of 0.5 m dia. by a 1kW quartz-

halogen lamp (Kaiser, Buchen, Germany) which was mounted on the same gallows at a zenith angle of 45° which is representative of sun elevations over UK waters and optimum for this type of work. At zenith angles of less than 40°, specular reflections from the water surface can interfere with radiance measurements whereas, at angles greater than 50°, surface radiance starts to contribute to water leaving radiance (CURRAN and NOVO, 1988). With a 15° field of view (FOV) the spectroradiometer 'observed' a circle of 0.16 m dia. which was completely and evenly illuminated by the lamp. The internal surfaces of the tank were painted matt black to minimise reflections and a submersible electric pump was used to circulate water within the tank and maintain particles in suspension. Observations were made in a photographic dark room to avoid extraneous illumination.

The spectral response of a calibrated, 0.26 x 0.26 m, PTFE reference panel (Spectralon SRT 4240A made by Labsphere) placed under the spectroradiometer was determined before and after each series of four measurements of the sample. The reference panel completely filled the FOV of the spectroradiometer and, when calibrated to a Lambertian response, defined the incident light spectra (E_d) against which the water-leaving spectra (L_w) were ratioed to determine reflectance (R_λ).

Natural particles were used throughout this work; sediments were collected from the surficial layers of the inter-tidal mud flats of the Tamar and Exe estuaries in the south-west of England. The size distribution of the sediments was determined by a combination of sieve analyses and Malvern laser diffraction of the <63 μm fraction (BALE *et al.*, 1984). Representative portions of each sediment were also size-fractionated using a 1.2 m high, 0.3 m dia. column and sedimentation criteria of 10 min and 3 h, to generate 3 fractions: material settling 1 m within 10 min, material which settled 1 m in 3 h after the 'ten minute' fraction had been removed, and a fraction which had not settled after 3 h. The size distribution of the individual fractions was determined as for the unfractionated sediments and the mass of each fraction was determined gravimetrically. Low sediment (<0.4 mg l⁻¹), organic-rich water for the separate determination of DOC spectra was collected from an upland stream draining peat-rich soils. Spectra of phytoplankton pigments (determined as chlorophyll) were obtained using a mixture of laboratory-cultured algae (principally *Phaeodactylum tricornutum* and *Tetraselmis suecica*) suspended in tap water. As fresh water was used to suspend the algae, chlorophyll determi-

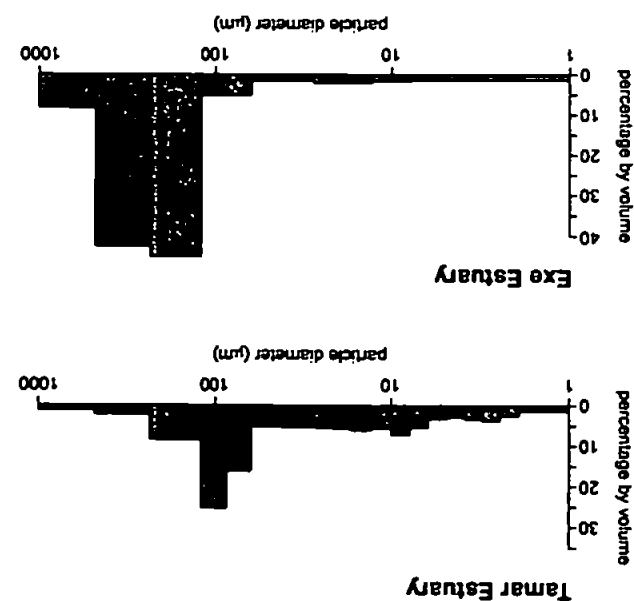


Fig. 2. Particle size distributions of the natural (unfractionated) Exe and Tamar estuary sediments.

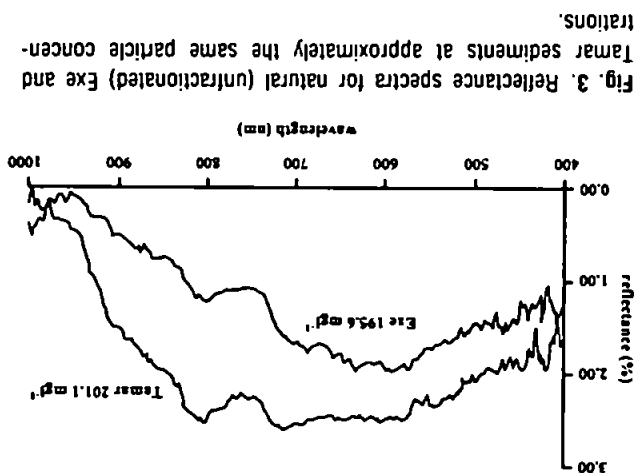


Fig. 3. Reflectance spectra for natural (unfractionated) Exe and Tamar sediments at approximately the same particle concentrations.

fractionated) Exe and Tamar sediments are given in Fig. 3. Reflectance for both sediments rises from 400 nm to maximum between 600 and 700 nm. Both spectra exhibit a minimum at 750 nm co-incident with a water absorption peak, maximum at around 800 nm and then their reflectance values decrease rapidly as water absorption increases in the infra-red (*cf.* Kirk, 1983). The two spectra, while exhibiting broadly similar features, differ in reflectance by values of 0.5% to 1% which is almost a factor of two at 800 nm. The spectra in Fig. 2 for 200 mg l⁻¹ of Tamar sediment is similar in form and magnitude to spectra generated by Novo *et al.*, (1989a) for 100 mg l⁻¹ of white clay where the particle size was described as 1-20 µm; however, if typical, most of the particles would be nearer 1 µm diameter.

RESULTS

Figure 2 shows that the stock sediments from the two sites have quite different particle size distributions. The Exe sample contains a much higher proportion of sand than the Tamar sediment. The differences reflect the location of the sampling sites within the estuaries relative to the gradation from high sand content at the seaward end of the estuary to predominantly silt in the turbid upper reaches. The colour of the two sediments was also visibly different; the Exe sediments were red coloured, particularly in the fine fractions, whereas the Tamar sediments were grey-brown. To some extent, the colour of the estuarine sediments, particularly the clay fractions, echo the colour of the soils within the respective catchments. Reflectance spectra for similar concentrations of natural (un-

fractionated) Exe and Tamar sediments are given in Fig. 3. Reflectance for both sediments rises from 400 nm to maximum between 600 and 700 nm. Both spectra exhibit a minimum at 750 nm co-incident with a water absorption peak, maximum at around 800 nm and then their reflectance values decrease rapidly as water absorption increases in the infra-red (*cf.* Kirk, 1983). The two spectra, while exhibiting broadly similar features, differ in reflectance by values of 0.5% to 1% which is almost a factor of two at 800 nm. The spectra in Fig. 2 for 200 mg l⁻¹ of Tamar sediment is similar in form and magnitude to spectra generated by Novo *et al.*, (1989a) for 100 mg l⁻¹ of white clay where the particle size was described as 1-20 µm; however, if typical, most of the particles would be nearer 1 µm diameter.

Figure 2 shows that the stock sediments from the two sites have quite different particle size distributions. The Exe sample contains a much higher proportion of sand than the Tamar sediment. The differences reflect the location of the sampling sites within the estuaries relative to the gradation from high sand content at the seaward end of the estuary to predominantly silt in the turbid upper reaches. The colour of the two sediments was also visibly different; the Exe sediments were red coloured, particularly in the fine fractions, whereas the Tamar sediments were grey-brown. To some extent, the colour of the estuarine sediments, particularly the clay fractions, echo the colour of the soils within the respective catchments. Reflectance spectra for similar concentrations of natural (un-

fractionated) Exe and Tamar sediments are given in Fig. 3. Reflectance for both sediments rises from 400 nm to maximum between 600 and 700 nm. Both spectra exhibit a minimum at 750 nm co-incident with a water absorption peak, maximum at around 800 nm and then their reflectance values decrease rapidly as water absorption increases in the infra-red (*cf.* Kirk, 1983). The two spectra, while exhibiting broadly similar features, differ in reflectance by values of 0.5% to 1% which is almost a factor of two at 800 nm. The spectra in Fig. 2 for 200 mg l⁻¹ of Tamar sediment is similar in form and magnitude to spectra generated by Novo *et al.*, (1989a) for 100 mg l⁻¹ of white clay where the particle size was described as 1-20 µm; however, if typical, most of the particles would be nearer 1 µm diameter.

Figure 2 shows that the stock sediments from the two sites have quite different particle size distributions. The Exe sample contains a much higher proportion of sand than the Tamar sediment. The differences reflect the location of the sampling sites within the estuaries relative to the gradation from high sand content at the seaward end of the estuary to predominantly silt in the turbid upper reaches. The colour of the two sediments was also visibly different; the Exe sediments were red coloured, particularly in the fine fractions, whereas the Tamar sediments were grey-brown. To some extent, the colour of the estuarine sediments, particularly the clay fractions, echo the colour of the soils within the respective catchments. Reflectance spectra for similar concentrations of natural (un-

fractionated) Exe and Tamar sediments are given in Fig. 3. Reflectance for both sediments rises from 400 nm to maximum between 600 and 700 nm. Both spectra exhibit a minimum at 750 nm co-incident with a water absorption peak, maximum at around 800 nm and then their reflectance values decrease rapidly as water absorption increases in the infra-red (*cf.* Kirk, 1983). The two spectra, while exhibiting broadly similar features, differ in reflectance by values of 0.5% to 1% which is almost a factor of two at 800 nm. The spectra in Fig. 2 for 200 mg l⁻¹ of Tamar sediment is similar in form and magnitude to spectra generated by Novo *et al.*, (1989a) for 100 mg l⁻¹ of white clay where the particle size was described as 1-20 µm; however, if typical, most of the particles would be nearer 1 µm diameter.

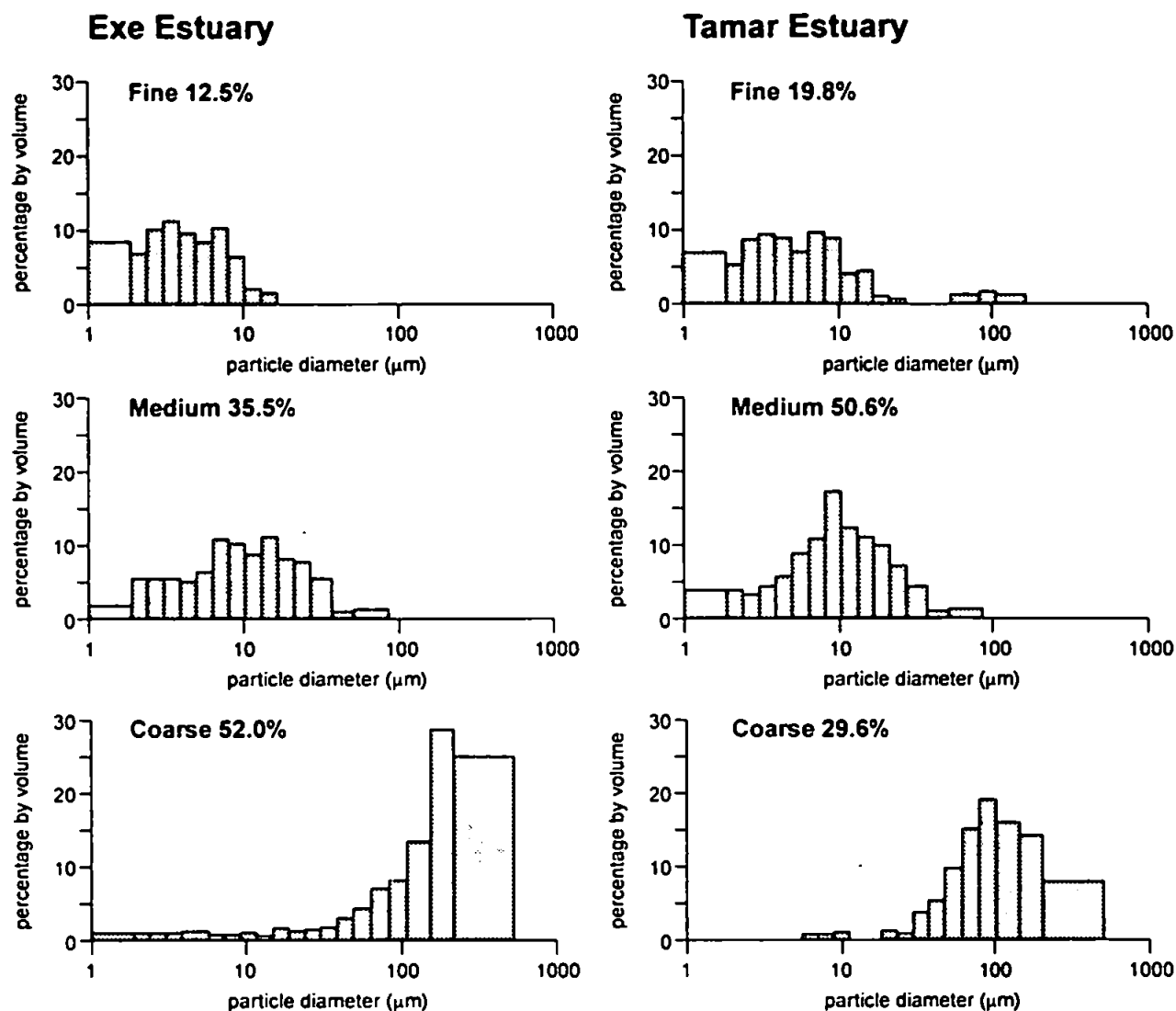


Fig. 4. The size distributions of the three fractions of Exe and Tamar sediments produced by sedimentation for 10 minutes and 3 hours.

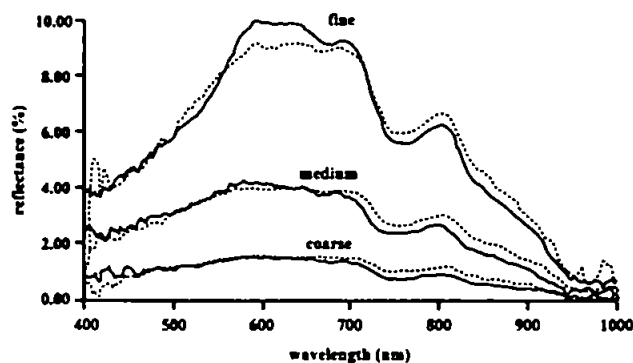


Fig. 5. Reflectance spectra for the three size fractions of Exe and Tamar sediments. Exe spectra are shown with solid lines and Tamar with broken lines. The particle concentrations in mg l^{-1} of the suspensions were as follows: fine Exe = 101.48, fine Tamar = 100.67; medium Exe = 92.73, medium Tamar = 96.45; coarse Exe = 127.32, coarse Tamar = 116.32.

Since identical settling criteria were used to generate the sediment fractions, the particle size distributions of the individual size fractions from both estuaries are very similar (Fig. 4). None of the fractions are cleanly separated by the sedimentation method, particularly the fine and medium 'cuts' where the tails overlap. This is due to the use of natural sediments where the variation in shape and composition of particles gives rise to a spectrum of properties within a given fraction. However, the relative proportions of the fractions within the bulk sediment (given with each size distribution in Fig. 4) are clearly consistent with the overall particle size distribution given in Fig. 2. The reflectance spectra obtained from suspensions of the size fractions obtained from both sediments are shown in Fig. 5. Each of the suspensions contained about the same concentration of particles (approximately

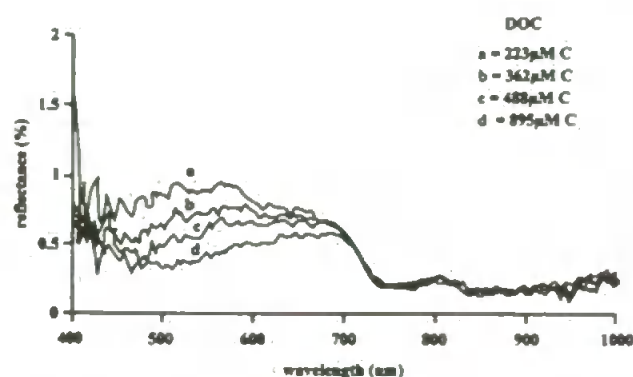


Fig. 6. Reflectance spectra for DOC at four concentrations showing how reflectance in the visible is reduced with increasing carbon but that the influence does not extend above 750 nm.

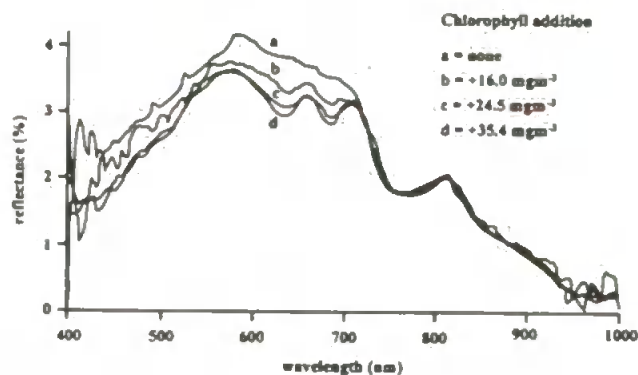


Fig. 7. Reflectance spectra for a sediment suspension with various additions of chlorophyll added also indicating that the influence on the sediment spectra is negligible above 700 nm. The chlorophyll values are only qualitative due to the potential cell lysis induced by fresh water.

100 mg l^{-1}) and the spectra clearly illustrate two points. Firstly, there is a ten-fold increase in reflectance in going from the coarse to the fine sediments for a given SSC. Secondly, except for the fine fractions, where the spectra for Exe and Tamar sediments diverge slightly between 580 and 680 nm, the sediments from both estuaries return very similar reflectance spectra.

In Fig. 6 the spectra of varying concentrations of natural riverine DOC show a small reflectance (maximum 1%) in the region 400–750 nm which reduces with increasing carbon concentration and is consistent with the known absorption characteristics of DOC in natural waters where absorption coefficients are high at blue wavelengths but fall to zero at 700 nm (KIRK, 1983). Fig. 7 shows the spectra obtained from a sediment suspension to which a range of chlorophyll concentrations in the form of phytoplankton have been added. Chlorophyll absorbs strongly in the visible region, particularly at blue wavelengths, thus reducing the reflectance of the sediment in the visible region as chlorophyll

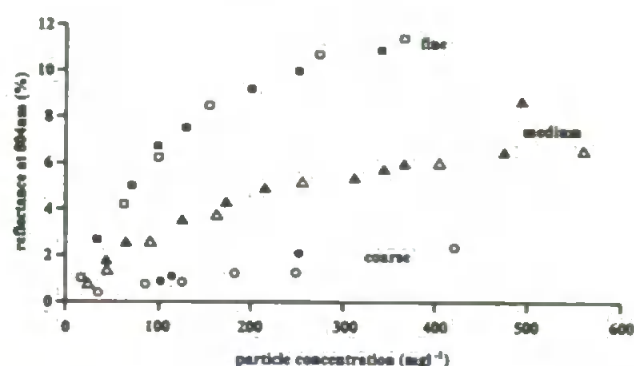


Fig. 8. Reflectance values at 804 nm for three size fractions plotted against particle concentration. Square symbols are fine particles, triangles are medium particles and circles are coarse particles. Tamar sediments are solid symbols, Exe sediments are open symbols.

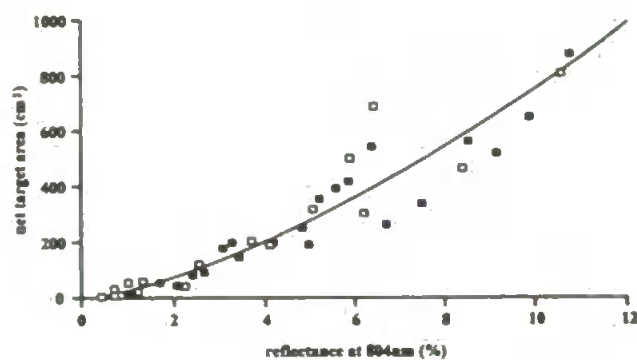


Fig. 9. The reflectance values at 804 nm from Fig. 8 plotted against the target area of the particles in each sample. Tamar sediments are solid squares, Exe sediments are open squares.

concentrations increase. Significantly, in relation to reflectance by sediments, neither DOC nor chlorophyll and its related pigments influence reflectance at wavelengths greater than 750 nm.

Thus it would appear that reflectance in the near infra-red is due almost entirely to the physical presence of particles. Fig. 8 shows the reflectance values at 804 nm for the three size fractions, from both estuaries, plotted as a function of sediment concentration. The choice of 804 nm was made on the basis that it represented a reflectance maximum (water absorption minimum) in a region that was unaffected by DOC, chlorophyll or other pigments. Reflectance, which was shown in Fig. 4 to vary markedly with the size distribution of the particles, is clearly very similar for similar particle size distributions and is independent of the colour and origin of the two sediments sampled. This general conclusion regarding the influence of particle size on reflectance is consistent with the findings of other workers (HOLYER, 1978; NOVO *et al.*, 1989a; BHARGAVA and MARIAM, 1991b).

Towards a general model

Assuming the effect of the atmosphere on remote-sensed reflectance spectra will eventually be corrected adequately, then simple reflectance-SSC relationships obtained from concurrent ground truth measurements, or various transformations of them (CURRAN and NOVO, 1988), might provide a valid means of deriving SSC. However, as described above, particle size has a major effect on the reflectance-SSC response and it would seem that a general model must accommodate, or at least recognise, the influence of the particle size distribution in order to derive SSC in terms of mass per volume.

The data obtained in this work were, therefore, examined in relation to the hypothesis that reflectance varied with the net cross-sectional area of the particle population in suspension. Calculations were made as follows: first, the midpoint of each size interval in the appropriate volume distributions (as shown in Fig. 4) was found and, assuming spherical particles, the cross-sectional area and volume of the particles with diameters equivalent to each mid point were calculated. Secondly, assuming a uniform density of 2.5 g cm^{-3} , the mass of each particle was calculated from its volume. Thirdly, the particle numbers in each size interval were calculated by dividing the mass of particles in each size interval by the mass of the appropriate mean particle. Fourthly, the net target area (TA) of the particles was found by multiplying the particle numbers in each size interval by the cross-sectional area of the appropriate mean particle and summing the values obtained for each size interval. Fig. 9 shows the same reflectance data as in Fig. 8 but plotted against the calculated TA for each suspension. By relating reflectance at 804 nm (R_{804}) to TA rather than to sediment mass, the six data sets representing three size fractions of two sediments, are now distributed along one curve which was described by a power relationship:

$$TA = 25.437 \cdot R_{804}^{(1.466)} \quad (1)$$

A corrected r^2 value of 0.897 indicated that TA could be derived from reflectance (R_{804}) with confidence. As a test, the reflectance values obtained for un-fractionated Exe and Tamar sediments were used to derive TA values over a range of particle concentrations. At the same time the TA for both sediments were also calculated from the particle size distributions shown in Fig. 2. The calculated and derived TA values are compared in Fig. 10 and correlate with a r^2 value of 0.989.

DISCUSSION

The use of TA to normalise the range of reflectance response that occurs with different sized particles for a given sediment mass, may be simplistic. However, this work clearly indicates that the particle size of suspended sediments cannot be ignored in attempting to quantify SSC from optical reflectance measurements and the use of TA has proved to be a practical, albeit empirical, method of 'compensating' for particle size with the materials examined here. Although it could be argued that sedimentation prevents large, dense particles from being entrained in surface waters and aggregation, due to biotic processes and the high ionic strength of saline waters, would tend to remove the smallest particles from suspension, there will still be a spectrum of particle size in the real world. Clearly there is now a need to examine other particle types, shapes, etc. to further test this model. It may then be that light scattering models (*e.g.* MIE, 1908) will provide a more suitable general understanding of light interaction with particles.

Considering the range and complexity of shape of natural sediment particles, the use of spheres to represent particles is a major simplification. However, nearly every form of particle sizing technique, including sedimentation, has necessarily had to adopt the same convention in order to interrelate number, diameter and volume statistics. Using a density of 2.5 g cm^{-3} assumes that all the particles are quartz or similar material, which may be approximately true for the sand type grains within the populations studied here. However, it is well known that most natural particles are actually aggregates of mineral grains and less dense material, with densities considerably less than 2.5 g cm^{-3} . McCAYE (1984) has calculated that marine aggregates, with

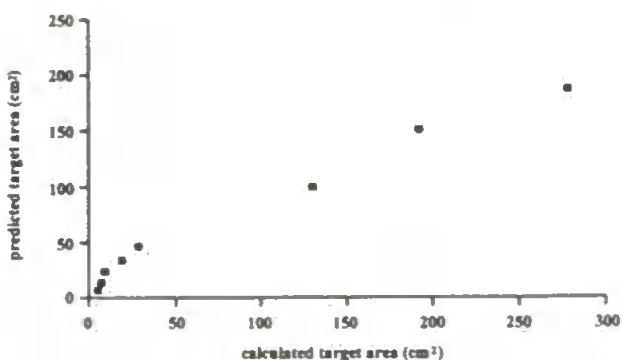


Fig. 10. Comparisons of target area values calculated for natural (unfractionated) Exe and Tamar sediments from their particle size distribution with the target area predicted from their reflectance data.

high water content might display an effective density of little more than water itself. The material used for this work was bed sediment which was physically and chemically disaggregated by the addition of 5% Calgon (sodium hexametaphosphate; 6.25 g l^{-1}). Having measured the size distribution of the sediment fractions generated by settling column in this work, it is possible to place approximate limits on the range of density that would be consistent with Stoke's settling and these range from ~ 1.8 to $\sim 3.0 \text{ g cm}^{-3}$. It should be stressed that these values are very approximate due to the range of particle sizes in each fraction and the long settling time intervals used. Nevertheless, they show that 2.5 g cm^{-3} is not an unrealistic constant to enable mass-volume interconversions for these principally mineral materials.

Having used the relationship between reflectance (R_{804}) and TA to derive the target area of the two complete (unfractionated) sediments, the inversion was taken to its logical conclusion *i.e.* the calculation of their SSC. We already had the particle size distributions (Fig. 2a) of the two sediments. This did not work as well as expected. Although the derived TA values correlated well with TA calculated from the size distributions, the inversion to SSC was not as well correlated ($r^2 = 0.648$). This result is attributed to the stock particles, being principally bed sediments, having a much larger size range than would be found in typical suspensions.

CONCLUSIONS

1. Laboratory studies of natural estuarine particles in suspension have shown that for given sediment concentrations (mass per volume), reflectance is mainly influenced by the particle size structure of the population and increases with decreasing particle size.
2. For the sediments examined in this work, reflectance at 804 nm is closely related to the target area of particles in a suspension (and thus to the sediment concentration and size distribution of a population) and is largely independent of colour and probably mineralogy. Future work must examine more extreme particle types, shapes, surfaces and colours.
3. Information on the nature of particles might be derived from the finest material which is predominantly clay and where small differences in the visible spectra were apparent. Further work is required in this area.

ACKNOWLEDGEMENT

The authors are grateful to Dr E.M. Rollin of the NERC Equipment Pool for Field Spectroscopy for the preparation of the spectroradiometer and for guidance in its use and with subsequent data processing and to Mr A. Miller and Mr A. Pomroy of PML for the DOC measurements and assistance with the chlorophyll analyses, respectively.

REFERENCES

- BALE, A.J., A.W. MORRIS and R.J.M. HOWLAND, 1984. Size distribution of suspended material in the surface waters of an estuary as measured by laser Fraunhofer diffraction. In: W.R. Parker and D.J.J. Kinsman, Eds., *Transfer Processes in Cohesive Sediment Systems*. Plenum Press, New York, p. 75-85.
- BHARGAVA, D.S and D.W. MARIAM, 1990. Spectral reflectance relationships to turbidity generated by different clay materials. *Photogramm. Eng. Rem. Sens.*, 56: 225-229.
- BHARGAVA, D.S and D.W. MARIAM, 1991a. Light penetration depth, turbidity and reflectance related relationships and models. *ISPRS J. of Photogramm. and Rem. Sens.*, 46: 217-230.
- BHARGAVA, D.S and D.W. MARIAM, 1991b. Effects of suspended particle size and concentration on reflectance measurements. *Photogramm. Eng. and Rem. Sens.*, 57: 519-529.
- CHOUBEY, V.K. and V. SUBRAMANIAN, 1991. Spectral response of suspended sediments in water under controlled conditions. *J. Hydrol.*, 122: 301-308.
- COLLINS, M. and C. PATTIARATCHI, 1984. Identification of suspended sediment in coastal waters using airborne thematic mapper data. *Int. J. Rem. Sens.*, 5: 635-657.
- CURRAN, P.J., J.D. HANSON, S.E. PLUMMER and M.I. PEDLEY, 1987. Multispectral remote sensing of nearshore suspended sediments: a pilot study. *Int. J. Rem. Sens.*, 8: 103-112.
- CURRAN, P.J. and E.M.M. NOVO, 1988. The relationship between suspended sediment concentration and remotely sensed spectral radiance: a review. *J. Coast. Res.*, 4: 351-368.
- GORDON, H.R., O.B. BROWN, R.H. EVANS, J.W. BROWN, R.C. SMITH, K.S. BAKER and D.K. CLARK, 1988. A semianalytic radiance model of ocean color. *J. Geophys. Res.*, 93: 10909-10924.
- HOLYER, R.J., 1978. Towards universal multispectral suspended sediment algorithms. *Rem. Sens. Env.*, 7: 323-338.

- HOOKE, S.B., W.E. ESAIAS, G.C. FELDMAN, W.W. GREG and C.R. McCLAIN, 1992. An overview of SeaWiFS and Ocean Colour. NASA Technical Memorandum 104566, Vol 1. Goddard SFC, Maryland, USA.
- JERLOV, N.G., 1974. Significant relationships between optical properties of the sea In: N.G. Jerlov and E. Steeman Nielson, Eds., *Optical Aspects of Oceanography*. Academic Press, London, 77-94.
- KIRK, J.T.O., 1983. *Light and photosynthesis in aquatic ecosystems*. Cambridge University Press, 401 pp.
- KIRK, J.T.O., 1989. The upwelling light stream in natural waters. *Limnol. Oceanogr.* 34: 1410-1425.
- MANTOURA, R.F.C., and E.M.S-WOODWARD, 1983. Conservative behaviour of riverine dissolved organic carbon in the Severn Estuary: chemical and geochemical implications. *Geochim. Cosmochim. Acta*, 47: 1293-1309.
- MANTOVANI, J.E. and A.P. CABRAL, 1992. Tank depth determination for radiometric measurements. *Int. J. Rem. Sens.*, 13: 2727-2733.
- McCAYE, I.N., 1984. Size spectra and aggragation of suspended particles in the deep ocean. *Deep Sea Res.*, 31: 329-352.
- MIE, G., 1908. Beiträge zur optisch trüber Medien speziell kolloidalen Metallösungen. *Ann. Physik.*, 25: 377.
- MOREL, A., 1974. Optical properties of pure water and pure seawater. In: N.G. Jerlov and E. Steemann Nielson, Eds. *Optical Aspects of Oceanography*, Academic Press, London, p. 1-23.
- NOVO, E.M.M., J.D. HANSOM and P.J. CURRAN, 1989a. The effect of sediment type on the relationship between reflectance and suspended sediment concentration. *Int. J. Rem. Sens.*, 10: 1283-1289.
- NOVO, E.M.M., J.D. HANSOM and P.J. CURRAN, 1989b. The effect of viewing geometry and wavelength on the relationship between reflectance and suspended sediment concentration. *Int. J. Rem. Sens.*, 10: 1357-1372.
- PARSONS, T.R., Y. MAITA and C.M. LALLI, 1984. *A manual of chemical and biological methods for sea-water analysis*. Pergamon Press, Oxford, 173 pp.

Addresses of the authors:

1. NERC Plymouth Marine Laboratory, West Hoe, Plymouth, PL1 3DH, U.K.
2. Department of Geographical Sciences, University of Plymouth, Drake Circus, Plymouth, PL4 8AA, U.K.
3. Institute of Marine Studies, University of Plymouth, Drake Circus, Plymouth, PL4 8AA, U.K.

AN OPERATIONAL APPROACH TO DETERMINING SUSPENDED SEDIMENT DISTRIBUTIONS IN THE HUMBER ESTUARY BY AIRBORNE MULTI-SPECTRAL IMAGERY*

S.J. Hudson^{1,2}, G.F. Moore^{2,3}, A.J. Bale², K.R. Dyer¹ and J. Aiken².

¹ Institute of Marine Studies
University of Plymouth
Plymouth, Devon, UK.

² Plymouth Marine Laboratory
Plymouth, Devon, UK.

³ University of Southampton
Southampton, Hampshire, UK.

ABSTRACT

In August and September 1993, the Humber estuary was surveyed using the Compact Airborne Spectrographic Imager (CASI), a multi-spectral (400-900 nm) CCD imager. The CASI was flown in "spatial" mode, utilising 12 wavebands chosen to simulate the SeaWiFS (Sea-viewing Wide Field-of-view Sensor) band set, calculate chlorophyll fluorescence and monitor atmospheric parameters. Supporting ground truth was acquired with towed and profiling in-water radiometric measurements. From in-water measurements, algorithms have been developed to interpret the aircraft imagery as maps of suspended sediment concentration. The interpretation was aided by laboratory measurements of the water leaving spectra from a tank containing suspended sediment, originating from locations around the Humber area. The spectra were averaged into the same wavebands as CASI and then compared with an analytical in-water optics model. The two near infrared bands (simulation of SeaWiFS bands 7 and 8) provide a means of interpreting the airborne imagery for suspended sediment concentration, calculating the water-leaving radiance and provide an atmospheric correction, in Case 2 waters, for the visible bands.

1.0 INTRODUCTION

Measuring the fluxes of sediment within and out of estuaries are of importance in the studies of coastal erosion and sediment budgets. These questions are being addressed by the Land-Ocean Interaction Study (LOIS), which is a UK Natural Environment Research Council (NERC) community research project. LOIS is focused on the Humber estuary (figure 1) with the aim of quantifying the suspended sediment fluxes through a combination of moored measurements, shipborne surveys and remote sensing including airborne and satellite imagery of water colour.

* Presented at the First International Airborne Remote Sensing Conference and Exhibition, Strasbourg, France, 11-15 September 1994.

The tidal dynamics and water movements make it difficult to map the sediment distributions from a vessel in the water, as sediment concentrations vary considerably both spatially and temporally, especially on a tidal time scale. Mapping, using airborne remote sensing, provides a flexible technique of surveying large areas in a short time span. Even though it can provide only measurements of the sea surface, this is extremely valuable when it supplements the other data. However, a knowledge of the target sediment characteristics is required to obtain an accurate algorithm for the interpretation of airborne measurements that can be used on an operational basis. A pilot study was carried out in 1993 to establish the procedures and develop preliminary algorithms prior to the full campaign which started in March 1994. The overflights were carried out simultaneously with extensive sea-truth measurements.

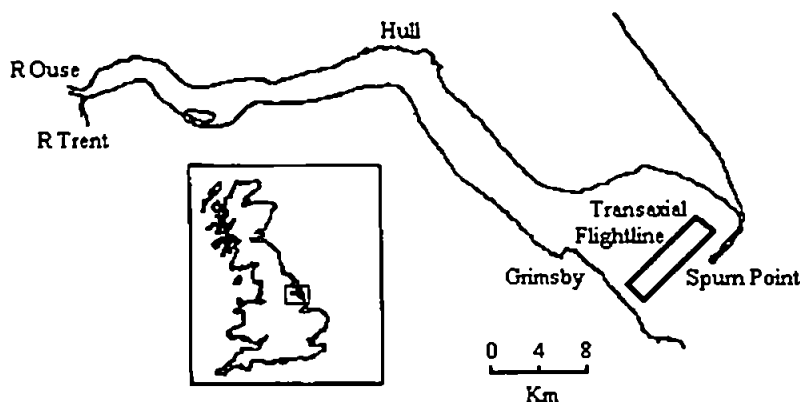


Figure 1. The Humber Estuary

A sediment algorithm needs to take account, of the atmosphere and other in-water constituents, such as Dissolved Organic Matter (DOM) and phytoplankton, as these affect the water leaving radiance to varying degrees throughout the visible spectrum. This paper describes the laboratory study and water-optics model which were used in the development of the suspended sediment algorithm.

2.0 ALGORITHM DEVELOPMENT

The algorithm derived in this paper was developed from laboratory measurements, taken under strictly controlled conditions, and validated through mathematical modelling before being applied to the imagery.

2.1 LABORATORY STUDY

Laboratory tank experiments (set-up in figure 2) were used to characterise the reflectance signals resulting from different suspended sediment types. This approach allowed the concentrations of the various in-water constituents to be carefully controlled and the geometry and illumination conditions to be kept constant. The reflectance spectra were measured using a Spectron spectroradiometer (model SE-590) loaned by the NERC

Equipment Pool for Field Spectroscopy (EPFS). The full experimental methodology is described in Bale *et al.* (1994).

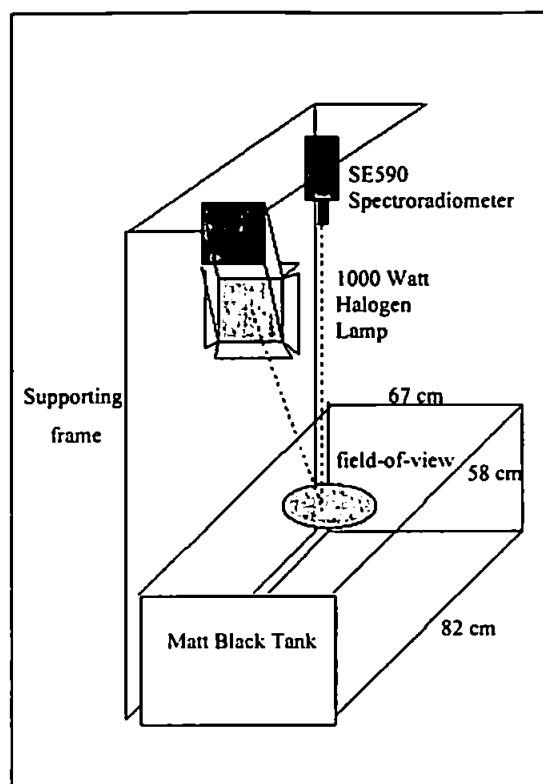


Figure 2. Tank Experimental Arrangement

Sediment samples taken from the surface of inter-tidal areas around the Humber, were added to the tank at concentrations of approximately 10, 20, 40, 60 and 100 mg l⁻¹. At each concentration, four water-leaving radiance spectra were measured and their mean was converted to reflectance using measurements of a calibrated white reference panel and the program supplied with the Spectron.

This data set was then combined with earlier results, which included sediment from the Tamar and Exe estuaries (both in South West England), measured over a wider range of sediment concentrations. The data were pooled, in order to derive an algorithm which gave concentration values for all sediment types. The laboratory measurements of spectral reflectance for the different sediment types showed, in all cases, an increase in reflectance with an increase in concentration (see example in figure 3a). This is in agreement with previous work (Bhargava & Mariam, 1991).

Similar measurements were made with DOM (brackish water from a moorland stream) and chlorophyll (a mixed phytoplankton culture), the concentrations of DOM and chlorophyll in each case were determined by standard laboratory methods of analysis (see Bale *et al.*, 1994). The reflectance spectra clearly showed that these constituents only effect the reflectance signal up to about 700 nm (see figure 3b for DOM and figure 3c for chlorophyll). The main reason for this is the high absorption by water, above this wavelength, which dominates the spectra.

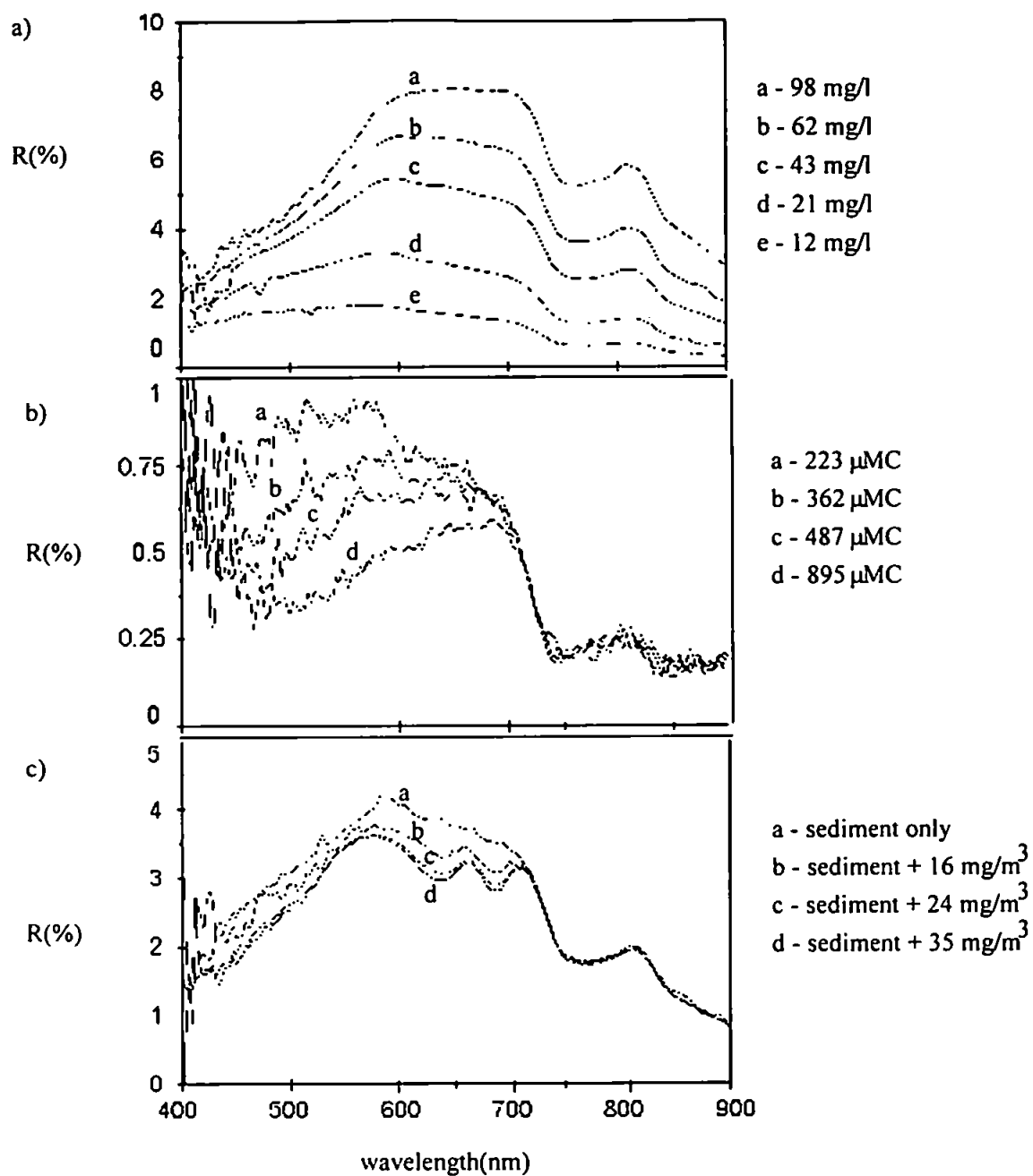


Figure 3. Spectral Reflectance Of a) Humber Sediment, b) DOM and c) Chlorophyll Measured At Differing Concentrations

The high resolution spectra obtained with the Spectron under laboratory conditions were binned over the same wavebands as used with the CASI. In the near infrared, bands 11 and 12 (table 1), the sediment signal was smaller than in the visible and also unaffected by variations in the DOM and chlorophyll concentrations. Bale *et al.* (1994) showed that the reflectance in the near infrared (e.g. 806 nm) was proportional to the suspended particulate matter (SPM) concentration. In this work we showed that, the ratio of these two near infrared bands was related to the sediment concentration.

2.2 WATER-OPTICS MODEL

An analytical water-optics model was developed to validate the tank experiments and derive a general solution. The model was based on the commonly used reflectance equation (Gordon *et al.*, 1975):

$$R_{-0}(\lambda) = 0.33 * \frac{b_b(\lambda)}{b_b(\lambda) + a(\lambda)} \quad (1)$$

Where the total absorption (a) and total backscattering (b_b) coefficients are the sum of the in-water constituents water (w), chlorophyll (chl), yellow substance ($y = \text{DOM}$), suspended sediment (s):

$$a = a_w + a_{chl} + a_y + a_s \quad (2)$$

$$b_b = 0.5 * b_w + b_{bchl} + b_{bs} \quad (3)$$

Water absorption (a_w) values were taken from Smith & Baker (1981), for the wavelength range 400 to 800 nm, and Palmer and Williams (1974) for the near infrared beyond this. It was very important to have the near infrared data as the water absorption in this region cannot be extrapolated from the visible.

The chlorophyll absorption (a_{chl}) equation was taken from Prieur and Sathyendranath (1981):

$$a_{chl} = a_c 0.06 C^{0.62} \quad (4)$$

where a_c is the normalised spectral absorption coefficient of phytoplankton pigments and C is the chlorophyll concentration (mg m^{-3}).

The equation for DOM absorption (a_y) relates the wavelength required to the absorption coefficient at the standard wavelength of 440 nm and the concentration (Y) after Bricaud *et al.* (1981):

$$a_y(\lambda) = a_y(440) \exp(-k(\lambda - 440)) * Y \quad (5)$$

Suspended sediment absorption (a_s) is assumed to be a small constant value of around 0.4.

Water backscattering is accounted for by multiplying the total water scattering coefficient (b_w) by a factor of 0.5 which arises from the symmetrical nature of the volume scattering function (Morel, 1974) i.e. the backscattering and forward scattering are of the same magnitude.

The chlorophyll backscattering (b_{bchl}) used the equation of Gordon & Morel (1983):

$$b_{bchl} = A(\lambda) C B(\lambda) \quad (6)$$

The sediment backscattering (b_{bs}) was calculated from sediment volume scattering functions, by fitting a curve to the experimental data of Petzold (1972) and Whitlock *et al.* (1981).

The model was used to estimate the reflectance resulting from wavebands equivalent to those used with the CASI (table 1) for different concentrations of chlorophyll, DOM and suspended sediment. The near infrared band ratio calculated by this model approximated the equivalent ratio obtained from the tank experiment (figure 4).

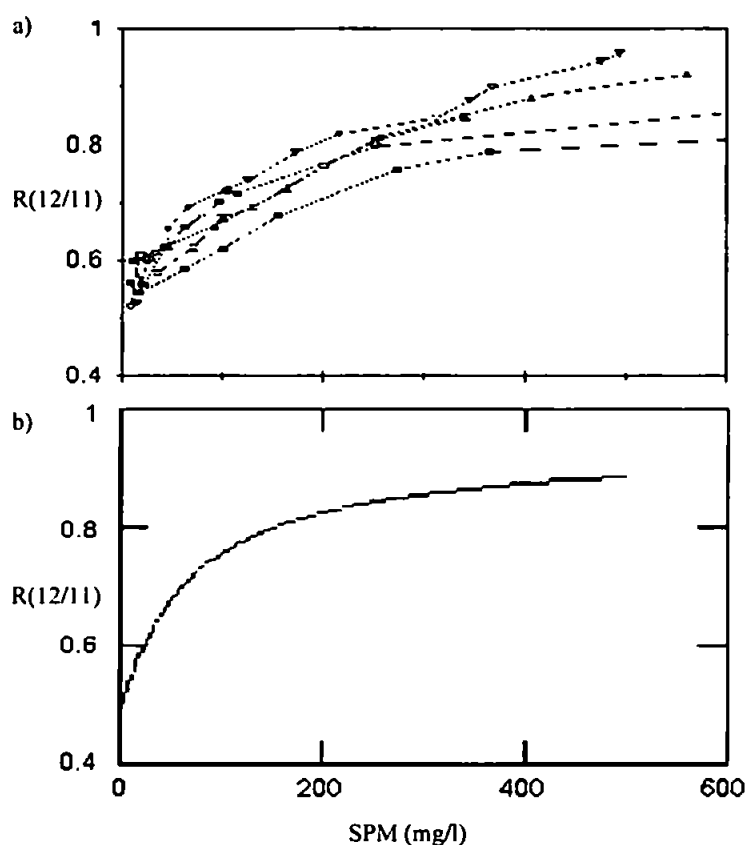


Figure 4. Band Ratio (12/11) Plotted Against SPM For a) The Tank Data-Set With Each Curve Representing A Different Sediment Type And b) The Curve Derived From The Model

Table 1. CASI Wavebands

Bands	Wavelength Range	
1	433-453	SeaWiFS 2, chlorophyll absorption
2	480-500	SeaWiFS 3, pigment absorption
3	500-520	SeaWiFS 4, pigment absorption
4	545-565	SeaWiFS 5, sediment hinge point
5	610-636	Ozone absorption
6	637-660	
7	660-680	SeaWiFS 6, chlorophyll absorption
8	680-685	Chlorophyll fluorescence
9	690-710	Fluorescence Base
10	716-740	Atmospheric water absorption
11	745.1-755.8	First half of SeaWiFS 7, atmosphere
12	845-885	SeaWiFS 8, atmosphere

In order to relate these results to the aircraft sensor, the reflectance equation (1) was replaced by the normalised water-leaving radiance equation (Gordon *et al.*, 1988) which included, in the ratio, the effect of differing amounts of solar irradiance in each band. The algorithm for SPM was derived from the model output for the normalised water-leaving radiance ratio.

3.0 FIELD EXPERIMENT

The Humber estuary is the largest estuary on the east coast of England, with a total drainage area of around 250 000 km² (Arnett, 1991). From the confluence of the rivers Trent and Ouse (at Trent Falls) to the mouth at Spurn Point, the Humber is 62 km long, and the width increases from 1 to 8 km, respectively (Barr *et al.*, 1980). It is a macrotidal estuary with a 7 m tidal range on spring tides, which gives rise to high SPM concentrations and fast flowing currents. At the mouth there are several axial channels which focus the tidal streams, resulting in varying SPM concentrations across the mouth. There are also well defined fronts running parallel to the north and south shores characterised by both salinity and SPM gradients.

In this study the fieldwork and aircraft overflights were concentrated in the mouth and plume areas. The aircraft was flown at heights of 614, 1 534 and 3 068 m along three specific flight lines: an axial line along the estuary, transaxial line across the mouth (figure 1) and Humber approaches line from offshore to the estuary mouth. The different heights result in varying amounts of atmospheric signal, and so provide a means of determining the algorithm's sensitivity to these effects. The Humber approaches flightline was chosen to cover conditions ranging from turbid Case 2 water (in the estuary), to waters approaching Case 1 (about 16 km offshore). This would determine the range of SPM values for which the algorithm is valid for.

Field measurements were taken coincident with the overflights in order to obtain ground truth data. The sampling consisted of a track down the Humber (from Hull) and out into the plume. During the underway period, the vessel continuously measured in-water parameters, such as salinity, temperature, chlorophyll fluorescence and suspended solids (derived from turbidity measurements), and it towed a fixed depth oceanographic recorder

(described by Aiken & Bellan, 1990) which measured similar in-water parameters, upwelling and downwelling irradiance at six wavebands. Bottle samples were taken every half an hour to calibrate the sensor measurements.

During the overflight period, the boat remained stationary and continued to monitor the in-water parameters as well as taking optical measurements. The optical measurements consisted of solar irradiance, including the total Photosynthetically Available Radiation (PAR) and a full spectrum (from 400-900 nm) using the Spectron (SE-590). In-water reflectance was measured, using the profiling reflectance radiometer (Biospherical Instruments model PRR-600) and at a fixed depth by the oceanographic recorder.

4.0 REMOTE SENSING IMAGERY

The instrument used was the Compact Airborne Spectrographic Imager (CASI), flown by the National Rivers Authority (NRA) on a Piper Chieftan aircraft. The instrument had a field-of-view of 35 degrees, covered by 512 pixels, and dynamic range of 12 bits (i.e. a resolution of 1 in 1046 of the saturation radiance).

CASI can be flown in either "spatial" or "spectral" mode. In "spectral" mode the instrument records the full wavelength range (from 430 to 870 nm with a resolution of 2.8 to 2.9 nm) using 288 bands and the operator chooses only 39 of the 512 across track pixels. In its "spatial" mode, the operator has the full set of across track pixels, but selects a limited number of non-overlapping wavebands. "Spatial" mode was selected for this work and 12 wavebands (table 1) were chosen.

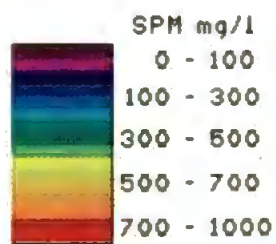
The data was radiometrically calibrated, to units of $\mu\text{W}/\text{cm}^2/\text{sr}/\text{nm}$, before having the algorithm applied.

5.0 RESULTS

The suspended sediment algorithm was applied to the transaxial flightline (figure 1) flown on September 1st, at an altitude of 3 068 m. The structures seen in the water (figure 5) tie up closely to the bathymetry, the areas of high SPM concentration (300 to 1000 mg l^{-1} as indicated by the lighter shades of grey) were situated over the shoals and the lower concentrations (0 to 300 mg l^{-1}) coincided with channels. Low water occurred at 11:52 GMT and the overflight began at 11:17 GMT and took 4 minutes to complete, therefore the higher SPM concentrations appear to be the result of suspension of bed sediment during the ebb tide. The lower SPM values, in the channels, are of a similar magnitude to those measured on the boat as it passed through the area. The boat survey was not able to measure the high concentrations associated with the shallow water regions because of the navigational constraints imposed on the vessel. As can be seen from the mud banks (dark black area at the top of figure 5), the land and other non-water targets are masked out by the algorithm as they produced negative SPM values.

6.0 CONCLUSION

The tank results showed that changes in the suspended sediment concentration affect the reflectance signal in the near infrared (above 700 nm), but this is dependent only on concentration and not variations in sediment type. In addition, the concentration of DOM and chlorophyll do not effect the reflectance signal above approximately 700 nm. A simple analytical model can be used to accurately predict the reflectance signal in the



Humber
Estuary

Kilnsea Flight Line

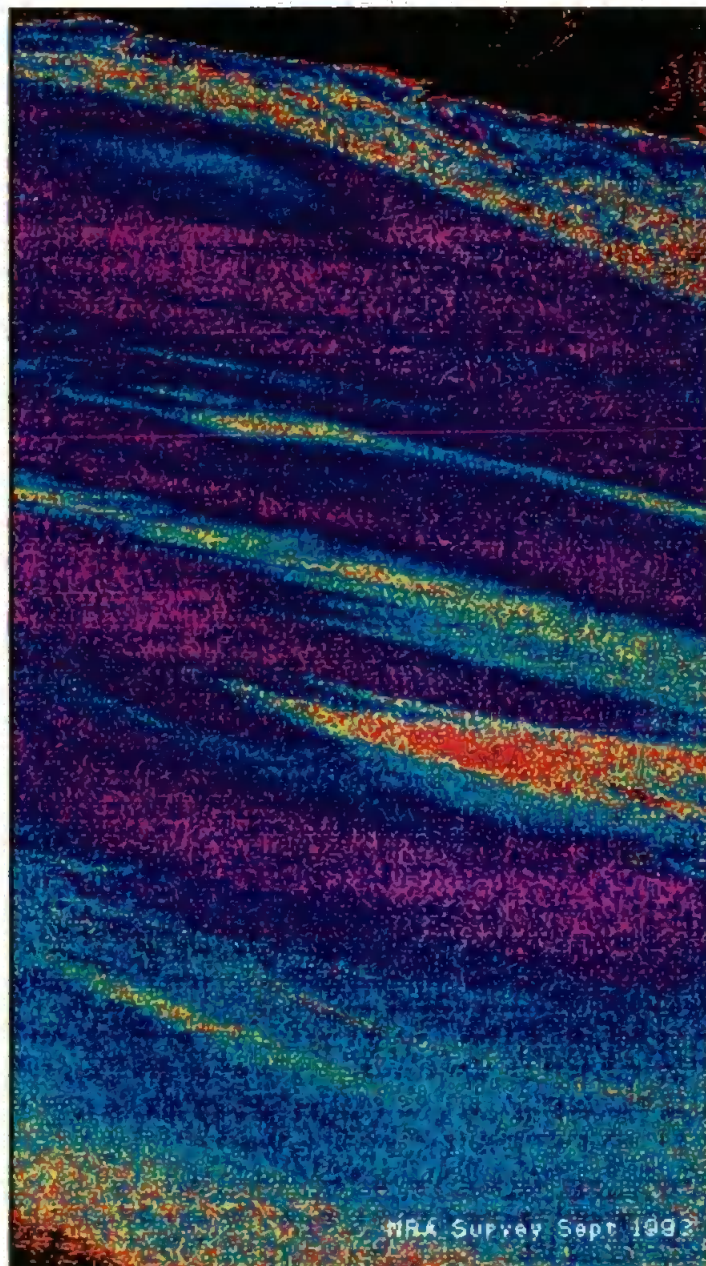


Figure 5: Transaxial Flightline For September 1st.

near infrared region, where sediment scattering is the dominant factor in Case 2 waters. The algorithm produced a sediment map (figure 5), which highlighted fine resolution structures present in the water. These features tie up closely to the bathymetry, and the high SPM values are the result of bed resuspension in shallow areas.

7.0 DISCUSSION

In the work carried out to date, the algorithm works effectively without an independent atmospheric correction (figure 5) when the suspended sediment is the dominant water constituent. Atmospheric effects were taken into account in the design of the algorithm, by ensuring the two near-infra red bands were not situated on atmospheric absorption features. Additionally, the Rayleigh scattering in the near infrared is small and almost constant, and under normal conditions the aerosol scattering effect on the ratio will be approximately 1.0. If there are high amounts of aerosols, such as cloud or haze, the algorithm will mask out these areas.

Further work needs to be carried out on the validation of the algorithm, under differing water and atmospheric conditions. Work, being carried out at present indicates that the small effects in the ratio, due to aerosols, can be separated from the SPM variation. The aerosol contribution can then be input to an atmospheric correction model, and used to correct the visible bands. This will make these bands available for further work on determining chlorophyll and DOM concentration, as well as classifying differing sediment types. Comparisons can then be carried out with mooring measurements being made at four points across the mouth, and sediment fluxes estimated.

8.0 ACKNOWLEDGEMENTS

The authors would like to thank NRA for providing the CASI imagery and the master and survey officer of "Sea Vigil" for their assistance. The research was funded by NERC under the LOIS Community Research Project and Samantha Hudson was in receipt of a NERC Studentship.

9.0 REFERENCES

- J. Aiken and I. Bellan, "Optical oceanography: an assessment of towed measurement." In *Light and life in the Sea*, eds. P.J. Herring, A.K. Campbell, M. Whitfield and L. Maddock, Cambridge University Press, Chapter 3, pp. 39-57, 1990.
- R. Arnett, "Estuarine pollution: A Case Study Of The Humber", *Geography*, Vol. 76, pp. 67-69, 1991.
- A.J. Bale, M.D. Tocher, R. Weaver, S.J. Hudson and J. Aiken, "Laboratory measurements of the spectral properties of estuarine suspended particles", *Netherlands Journal Of Aquatic Biology*, To Be Published.

R. Barr, P.G. Watson, C.R. Ashcroft, B.E. Barnett and C. Hilton, "Humber Estuary - A Case Study", *Hydrobiologia*, Vol. 195, pp. 127-143, 1990.

D.S. Bhargava and J.S. Mariam, "Light penetration depth, turbidity and reflectance related relationships and models", *ISPRS Journal Of Photogrammetry and Remote Sensing*, Vol. 46, pp. 217-230, 1991.

A. Bricaud, A. Morel and L. Prieur, "Absorption by dissolved organic matter of the sea (yellow substance) in the UV and visible domains", *Limnology and Oceanography*, Vol. 26, No. 1, pp. 43-53, 1981.

H.R. Gordon, O.B. Brown, R.H. Evans, J.W. Brown, R.C. Smith, K.S. Baker and D.K. Clark, "A semianalytic radiance model of ocean color", *Journal of Geophysical Research*, Vol. 93, No. D9, pp. 10 909-10 924, 1988.

H.R. Gordon, O.B. Brown and M.M. Jacobs, "Computed relationships between the inherent and apparent optical properties of a flat homogeneous ocean", *Applied Optics*, Vol. 14, pp. 417-427, 1975.

H.R. Gordon and A.Y. Morel, *Remote assessment of ocean color for interpretation of satellite visible imagery: a review*, Lecture Notes on Coastal and Estuarine Studies 4, Springer-Verlag, New York, 1983.

A. Morel, "Optical properties of pure water and pure seawater", In *Optical aspects of oceanography*, eds. N.G. Jerlov and E. Steemann Nielsen, Academic Press, London, pp. 1-24, 1974.

K.F. Palmer and D. Williams, "Optical properties of water in the near infrared", *Journal Of The Optical Society Of America*, Vol. 64, No. 8, pp. 1107-1110, 1974.

T.L. Petzold, *Volume scattering functions for selected ocean waters*, University of California, San Diego, Scripps Institute Oceanography Visibility Laboratory, Ref. 72-78, 1972.

other L. Prieur and S. Sathyendranath, "An optical classification of coastal and oceanic waters based on the specific spectral absorption curves of phytoplankton pigments, dissolved organic matter and particulate materials", *Limnology and Oceanography*, Vol. 26, No. 4, pp. 671-689, 1981.

R.C. Smith and K.S. Baker, "Optical properties of the clearest natural waters (200-800 nm)", *Applied Optics*, Vol. 20, No. 2, pp. 177-184, 1981.

C.H. Whitlock, L.R. Poole, J.W. Usry, W.M. Houghton, W.G. Witte, W.G. Morris and E.A. Gurganus, "Comparison of reflectance with backscatter and absorption parameters for turbid waters", *Applied Optics*, Vol. 20, No. 3, pp. 517-522, 1981.

Plymouth Atmospheric Correction Experiment (PACE)

PACE is designed to give atmospheric closure by contemporaneously measuring the atmosphere and collecting optical imagery, this will initially involve two fieldwork experiments within the Plymouth area: 12th to 23rd June and the 31st July to 11th August 1995. There will be overflights by the Meteorological Research Flight and the Compact Airborne Spectrographic Imager (CASI), to measure atmospheric parameters and simulate SeaWiFS radiance respectively.

Both aircraft will follow a loop of three flightiness around the Plymouth Sound area, including both Case 1 and 2 water conditions (see Figure 1). The overflights will occur at heights of 2000, 5000, and 10000 feet to investigate the vertical atmospheric structure.

The Meteorological aircraft will collect general atmospheric data, such as wind speed and humidity, plus more detailed aerosol measurements continuously over each flight line. Atmospheric parameters such as the total water content and ozone concentration will be useful in determining water vapour absorption and looking at the contribution of tropospheric ozone to the total ozone optical depth. In calculating the aerosol single and multiple scattering phase functions, measurements of the number densities of aerosol particles (PCASP instrument), aerosol light scattering (nephelometer) and aerosol size spectrum (scattering laser spectrometer) will be useful.

Several research vessels and the Plymouth Marine Bio-Optical Data Buoy (PlyMBODY) will provide contemporaneous measurements of the in-water parameters and optical properties. Vessels will tow the undulating oceanographic body (UOR) measuring chlorophyll fluorescence, suspended sediment concentration and the upwelling and downwelling irradiance in six wavebands (412, 443, 490, 510, 550 & 632 nm). At the end of each boat transect and when the aircraft sensor is directly overhead a profiling reflectance radiometer will be lowered into the water to calculate the water-leaving radiance. In conjunction with the optics work the boat will also take samples to classify the in-water parameters and calibrate the sensors.

The atmospheric and in-water information will be position located to the aircraft imagery to perform the atmospheric correction. Atmospheric models will be adapted for use in sediment laden waters using the research that is currently being undertaken at Plymouth and in various atmospheric correction groups around the United Kingdom. The ground truth measurements will also allow the development of algorithms, e.g. chlorophyll and suspended sediment, from the corrected imagery.

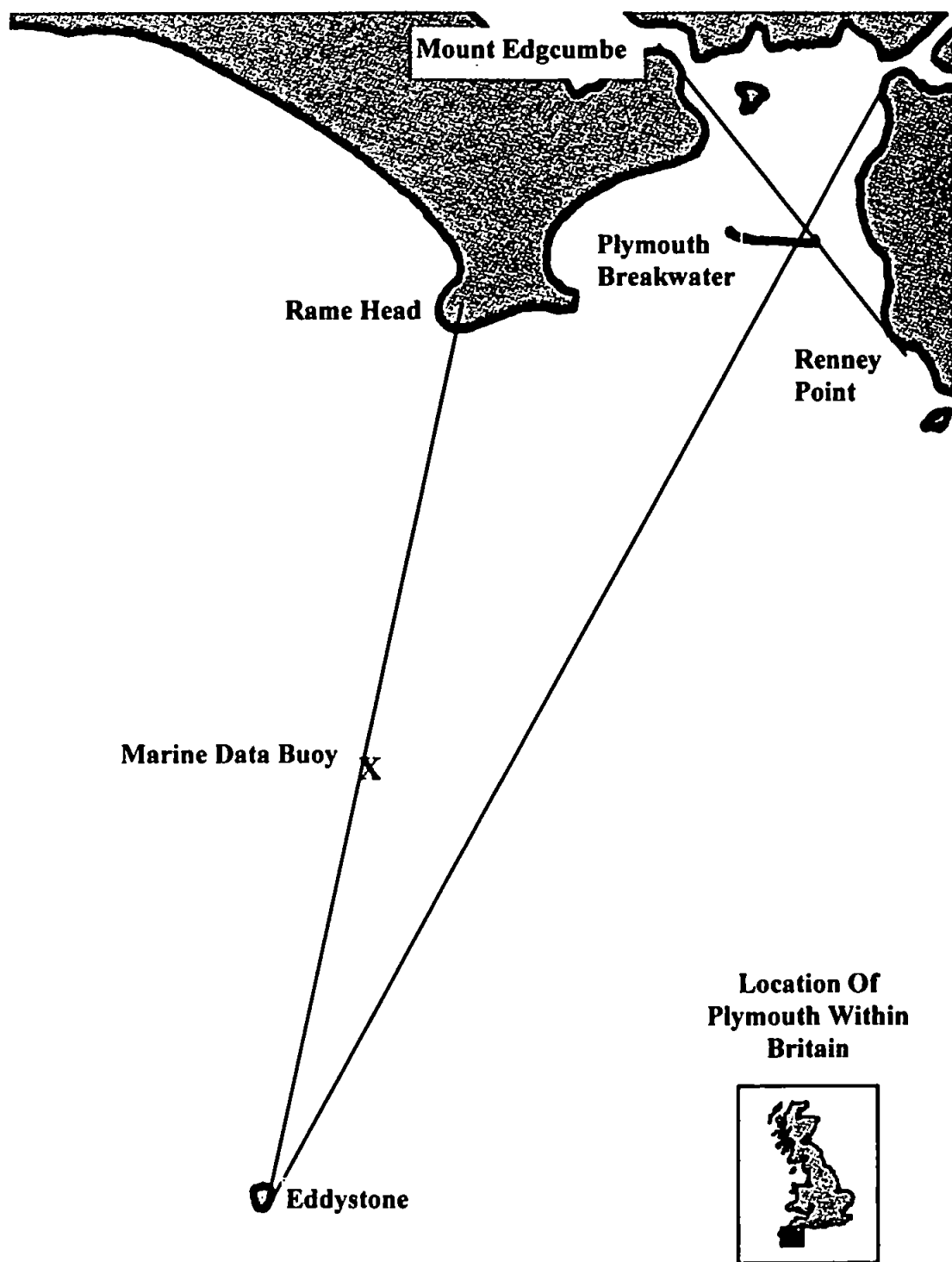


Figure 1: Flightline Positions for PACE